Model identification of a flapping wing micro aerial vehicle

Aguiar Vieira Caetano, Joao

DOI
10.4233/uuid:5311a47f-267e-46b3-9131-5228e22fef8b

Publication date
2016

Document Version
Final published version

Citation (APA)
Aguiar Vieira Caetano, J. (2016). *Model identification of a flapping wing micro aerial vehicle*. [Dissertation (TU Delft), Delft University of Technology]. https://doi.org/10.4233/uuid:5311a47f-267e-46b3-9131-5228e22fef8b

MODEL IDENTIFICATION OF A FLAPPING WING MICRO AERIAL VEHICLE

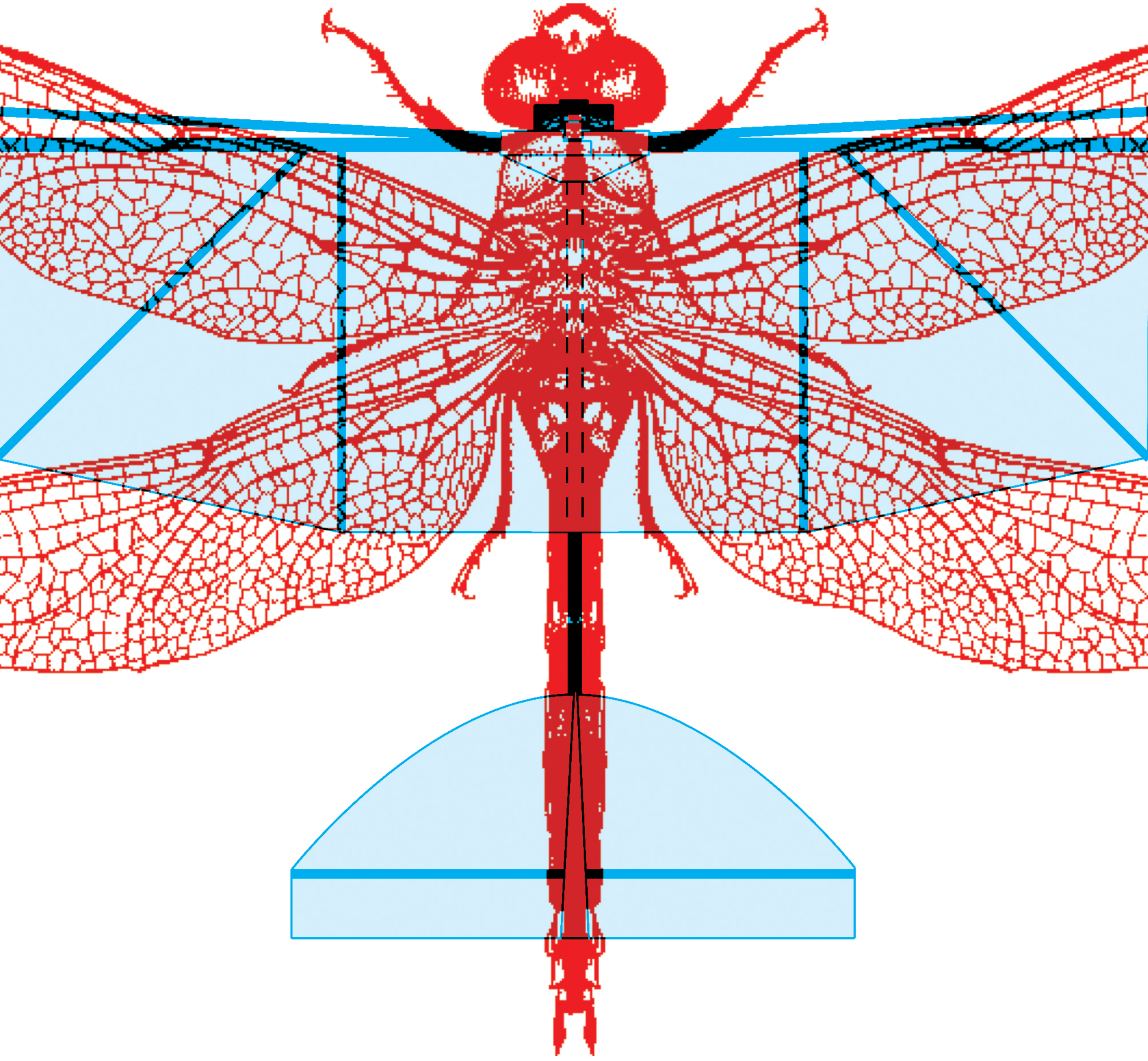

João Vitor Aguiar Vieira Caetano

MODEL IDENTIFICATION OF A FLAPPING WING MICRO AERIAL VEHICLE

MODEL IDENTIFICATION OF A FLAPPING WING MICRO AERIAL VEHICLE

Proefschrift

ter verkrijging van de graad van doctor
aan de Technische Universiteit Delft,
op gezag van de Rector Magnificus prof. ir. K.C.A.M. Luyben,
voorzitter van het College voor Promoties,
in het openbaar te verdedigen op donderdag 13 oktober 2016 om 12:30 uur

door

João Vitor AGUIAR VIEIRA CAETANO

Master of Science in Aeronautical Engineering,
Portuguese Air Force Academy
geboren te Funchal, Portugal

Dit proefschrift is goedgekeurd door de

promotor: prof. dr. ir. M. Mulder
copromotor: dr. ir. C.C. de Visser
copromotor: dr. G.C.H.E. de Croon

Samenstelling promotiecommissie:

Rector Magnificus,	voorzitter
Prof. dr. M. Mulder,	Technische Universiteit Delft
Dr. C.C. de Visser,	Technische Universiteit Delft
Prof.dr. A.J. Preumont	Universiteit Libre Brussel
Prof.dr.ir. L.L.M. Veldhuis	Technische Universiteit Delft
Dr.ir. J.F.L. Goosen	Technische Universiteit Delft
Prof.dr.ir. J.L. Herder	Technische Universiteit Delft
Prof.dr.ir. J.A. Mulder	em.hgl. Technische Universiteit Delft

Keywords: Flapping Wing, Micro Aerial Vehicle, DelFly II, Aerodynamic Modeling, Quasi-steady Aerodynamics, Kinematic Modeling, Simulation, Free-flight, Wind tunnel

Printed by: TBD

Front & Back: J.V. Caetano

ISBN 000-00-0000-000-0

An electronic version of this dissertation is available at
`http://repository.tudelft.nl/`.

To Susana.

"If there is one thing I have learned is that I still have much to learn."
João Caetano

CONTENTS

SUMMARY

Different flapping wing micro aerial vehicles (FWMAV) have been developed for academic (Harvard's RoboBee), military (Israel Aerospace Industries' Butterfly) and technology demonstration (Aerovironment's NanoHummingBird) purposes. Among these, the DelFly II is recognized as one of the most successful configurations of FWMAV, with a broad flight envelope, that spans from hover to fast forward flight, revealing autonomous capabilities in the form of automatic flight and obstacle avoidance. Despite the technological development, very little is known about the dynamic behavior and aerodynamic force generation mechanisms of FWMAVs which, in turn, limits the development of models that could be used for advanced control strategies and flight simulations. The present dissertation contributes to the understanding of the mechanics of flapping flight, using a data-driven systematic approach to the modeling of the DelFly II.

It aims at answering to the following research question:

"How to develop physically representative dynamic models of clap-and-peel flapping wing micro aerial vehicles using free-flight and wind tunnel experimental methodologies?"

This is done through the use of flightpath reconstruction and model identification techniques applied to novel experimental test procedures that encompass automatic flight, wind tunnel and vacuum chamber test setups. This dissertation is divided in two parts: Part I presents the experimental methods and data processing techniques that were used to determine unsteady aerodynamic forces that act on the FWMAV during flight; Part II focuses on the development and identification of the aerodynamic models, by first studying the applicability of linear time-invariant (LTI) model structures, followed by a detailed study of the flapping-wing force generation mechanism using quasi-steady aerodynamic principles.

A version of the DelFly II was programmed to command specific inputs to the control surfaces (flapping frequency, elevator and rudder) for the excitation of the dynamic modes during free-flight testing maneuvers. Its position and orientation in time were recorded at 200Hz by an external visual tracking system that tracked the position of eight retro-reflective markers with sub-millimeter accuracy in 168 flight tests, covering a total of 28 minutes of flight.

After testing different kinematic formulations, it was observed that, for the case of the DelFly II and other platforms of similar configuration, a single rigid body kinematic model represents the kinematics of the FWMAV accurately enough to allow for the acting aerodynamic forces and moments to be determined.

To validate the aerodynamic forces reconstructed from the free-flight data, eight flight conditions of the DelFly were replicated in a wind tunnel setup. Additionally, flapping tests were performed in a vacuum setup, to study the frequency spectrum of the aerodynamic forces and separate aerodynamic contributions from the purely kinematic forces generated during flap. It was observed that numerical differentiation techniques used to obtain the velocities and accelerations from the free-flight data highly affect the quality of the reconstructed forces, through the magnification of the noise and low-pass filtering of the force data at each time differentiation. Furthermore, it was observed that the sampling rate of the tracking system must be at least five times higher than the highest frequency present in the aerodynamic terms that are being reconstructed.

As far as wind tunnel tests are concerned, it was observed that the flapping of the wings can introduce undesired forces in the measurements made on the wind tunnel if the system is not clamped under the average flapping force application point. Especially for the forces acting along the stroke plane (Z force), these can be affected by the vibration of the structure of the FWMAV, due to the excitation of the eigenmodes, as well as by the inertial forces of the wings during flap. As a result, special attention must be paid to the clamping position of the FWMAV in fixed-base experimental methods, and it is recommended that the eigenfrequencies of the system be studied in detail for such cases before testing.

After the unsteady aerodynamic forces and moments were determined, these were used to identify an LTI model of the aerodynamics of the DelFly. This served as a first approach to assess the applicability of relatively simple LTI model structures for the modeling of the DelFly. Two model structures were used: (1) a more complex structure that used all the states reconstructed from the free-flight data; (2) a relatively simple structure that used the states that could be reconstructed from the onboard sensors. The results indicated an accurate modeling of the aerodynamic forces, which suggests the successful use of such linear structures for onboard control strategies of the DelFly II.

The research finalizes with the development of a nonlinear time-varying model of the clap-and-peel mechanism using quasi-steady aerodynamic theory. This model was able to describe the unsteady lift forces with great accuracy. Additionally, a global model of the lift force was developed and validated using the free-flight data. This model represents a considerable expansion of previous models present in the literature, as it provides a physically representative formulation of the clap-and-peel mechanism in the form of a circulatory term, proving to be accurate in predicting the lift force of the FWMAV across a broad flight envelope, from hover to fast forward flight.

The results obtained in this research suggest the use of single rigid body kinematic models for the reconstruction of the forces and moments that act on specific FWMAV, with four-wings configured in ‘X’ and with two wings with single wing-to-body mass ratios below 8% and 2.8%, respectively. Moreover, the high quality position, attitude and force data reconstructed from the free-flight of the FWMAV are shared and fully described in digital format. This allows for further developments in the modeling of FWMAVs with clap-and-peel wing flapping mechanism, which represent one of the most used FWMAV configurations across the community.

To increase the level of fidelity of the models, it is recommended to add an aerodynamic term that accounts for the ’clapping’ motion of the wings. Furthermore, future modeling strategies should account for the tail presence and model wing/tail interactions, using a combination of free-flight data and data from particle image velocimetry (PIV). This would allow a more in-depth understanding of the flow around the tail, especially at reduced flight velocities.

SAMMENVATTING

Recent zijn verschillende klap-vleugel microvliegtuigjes (FWMAV) ontwikkeld voor academische (Harvards RoboBee, TU-Delft DelFly), militaire (Israel Aerospace Industries 'Butterfly'), en technologische demonstratie toepassingen (Aerovironment's NanoHummingBird). Onder deze vliegtuigjes wordt de Delfly II gezien als een van de meest succesvolle FWMAV configuraties, met een brede vlucht envelop die de regionen van de klapwiekende tot de snelle voorwaartse vlucht overspant, en met een unieke capabiliteit op het gebied van de autonome vlucht en het ontwijken van obstakels. Ondanks de technologische ontwikkelingen op het gebied van FWMAV, is er weinig bekend over het dynamische gedrag en de onderliggende mechanismes die aerodynamische krachten opwekken. Op zijn beurt limiteert dit de ontwikkeling van modellen die gebruikt kunnen worden voor het ontwikkelen van geavanceerde regelaars en vlucht simulatoren. Dit proefschrift maakt een contributie in het beter begrijpen van de klapvleugel vlucht door toepassing van data-aangedreven systematische modelleer technieken die werken met vluchtdata van de DelFly II.

Dit proefschrift richt zich op het beantwoorden van de volgende onderzoeksvraag:

"Hoe kunnen fysisch representatieve dynamische modellen ontwikkeld worden van klap-en-pel klapvleugel microvliegtuigjes gebaseerd op vrije vlucht en windtunnel experimenten?"

De gehanteerde aanpak in dit proefschrift maakt gebruikt van vluchtbaanreconstructie en model identificatie technieken die worden toegepast op nieuwe experimentele test procedures bestaande uit automatisch uitgevoerde vrije vlucht manoeuvres, windtunnel, en vacuüm kamer experimenten.

Dit proefschrift bestaat uit twee delen: Deel I presenteert de experimentele methodes en de data processing technieken die gebruikt werden om de niet-stationaire aerodynamische krachten te bepalen die werken op de FWMAV tijdens de vlucht; Deel II richt zich op het identificeren van aerodynamische modellen, eerst door het bestuderen van de toepassing van lineair tijds invariante (LTI) modellen, gevolgd door een gedetailleerde studie van de klappende vleugel krachtopwekkingmechanismen door gebruik te maken van quasi-stationaire aerodynamische principes.

Een versie van de DelFly II was geprogrammeerd om specifieke invoer te genereren voor de verschillende besturingsmechanismen (klap frequentie, hoogteroer, en richtingsroer) om zo de dynamische modes tijdens de vrije vlucht te exciteren. De tijdsafhankelijke positie en oriëntatie van de DelFly II werd gereconstrueerd op een frequentie van 200Hz door met extern optisch volgsysteem de positie van 8 reflectors op sub-millimeter nauwkeurigheid te volgen tijdens 168 vluchtproeven, welke in totaal 28 minuten vrije vlucht besloegen.

Na het testen van een aantal kinematische formuleringen werd geobserveerd dat de kinematica van micro vliegtuigjes met vergelijkbare configuratie als de DelFly II voldoende nauwkeurig beschreven kan worden met een rigide 1-lichaam kinematische for-

mulering, waarmee op zijn beurt de aerodynamische krachten en momenten kunnen worden berekend.

Om de op deze manier berekende waardes van de aerodynamische krachten en momenten te valideren werden acht vliegcondities van de DelFly gereproduceerd in een windtunnel. Daarnaast werden experimenten uitgevoerd in een vacuümkamer met als doel het kunnen separeren van de aerodynamische en inertiale krachten tijdens de klap cyclus door middel van een frequentiedomein analyse.

Er werd gevonden dat de numerieke differentiatie technieken die gebruikt werden om de snelheden en acceleraties te berekenen uit de positiedata een groot effect hadden op de kwaliteit van de gereconstrueerde krachten door de ruisamplificatie en lagedoorlatings filter effecten van de differentiatie. Daarnaast werd gevonden dat de meetfrequentie van het optische volgsysteem tenminste vijf keer hoger moet liggen dan de hoogste frequentie component in de gereconstrueerde aerodynamische krachten.

Een belangrijke bevinding van de windtunnelexperimenten was dat het klappen van de vleugels de waardes van de gemeten krachten sterk beïnvloed wanneer de FWMAV niet precies in het aangrijpingspunt van de klapkrachten is bevestigd op de krachtmeter in de windtunnel. In het bijzonder de metingen aan de kracht die werkt in het vlak van de vleugelslag (Z-as kracht) kan beïnvloed worden door structurele vibraties (eigen bewegingen) geëxciteerd door de vleugelslag samen met de inertiale krachten van de vleugelslag. Deze bevinding leidt tot de aanbeveling dat een gedetailleerde studie van de eigenfrequenties van de FWMAV essentieel is om het bevestigingspunt van een FWMAV in een vaste meetopstelling te kunnen bepalen.

Nadat het bepalen van de aerodynamische krachten en momenten zijn deze gebruikt om een LTI model te identificeren van de DelFly. Deze aanpak diende om de bruikbaarheid van relatief simpele LTI model structuren voor deze toepassing vast te stellen. Twee model structuren zijn gebruikt: (1) een meer complexe structuur die alle gereconstrueerde toestandsvariabelen gebruikt; (2) een relatief simpele structuur die alleen toestandsvariabelen gebruikt die uit boordsensoren gereconstrueerd kunnen worden. De LTI modellen van de aerodynamische krachten en momenten zijn voldoende accuraat bevonden voor gebruik in het regelsysteem van de DelFly.

Dit onderzoek concludeert met de ontwikkeling van een niet-lineair tijdsvariant model van het klap-en-pel mechanisme op basis van quasi-stationaire aerodynamische theorieën. Met dit model was het mogelijk om de niet-stationaire lift krachten met grote nauwkeurigheid te beschrijven. Daarnaast werd een globaal model van de lift krachten ontwikkeld en gevalideerd aan de hand van data van de vrije vlucht. Dit model representeert een aanzienlijke uitbreiding van modellen in de literatuur omdat het een fysiek representatieve formulering bevat van het klap-en-pel mechanisme in de vorm van een circulatie term. Het model is bewezen accuraat te zijn in het voorspellen van de lift kracht werkende op de FWMAV over een groot deel van de vlucht envelop, van de klapwiekende tot de snelle voorwaartse vlucht.

De resultaten die verkregen zijn met dit onderzoek suggereren dat het gebruik van rigide 1-lichaam kinematische modellen voldoende is voor het accuraat reconstrueren van de krachten en momenten die werken op specifieke FWMAVs met vier vleugels in een ‘X-stand’, en met twee vleugels voor een vleugel-lichaam massaratio van respectievelijk 8% en 2.8%. Bovendien zijn de positie-, stand- en krachtdata, gereconstrueerd uit de vrije-vluchtdata van de FWMAV, beschikbaar gesteld in digitaal formaat en volledig beschreven. Hierdoor worden verdere ontwikkelingen toegestaan in het modeleren van FWMAV en met “klap-en-pel” klapvleugelmechanismen, die een van meest gebruikte FWMAV-configuraties is in de gebruikersgemeenschap.

Een aanbeveling voor het verbeteren van de accuratesse van de in dit proefschrift ontwikkelde modellen is om een aerodynamische term toe te voegen die het klappen van de vleugels representeert. Daarnaast is het aanbevolen dat toekomstig werk op dit gebied de aanwezigheid van een staart, en de interactie tussen de vleugel en de staart meeneemt, daarbij gebruik makende van een combinatie tussen van vrije vlucht experimenten, en zgn particle image velocimetry (PIV). Dit zou een diepgaander begrip opleveren van de stroming rond de staart, in het bijzonder tijdens de langzame vlucht.

NOMENCLATURE

ACRONYMS

μAVIARI	Micro Air Vehicles Integration and Application Institute
AFRL	Air Force Research Laboratory
AOA	Angle of attack
BE	Blade Element
CFD	Computational Fluid Dynamics
CG	Center of Gravity
DOF	Degrees of Freedom
EL	Elevator Marker
EOM	Equations of Motion
FEM	Finite Elements Method
FFT	Fast Fourier Transform
FPGA	Field-Programmable Gate Array
FWMAV	Flapping Wing Micro Air Vehicle
GPS	Global Positioning System
HS	Horizontal Stabilizer Marker
IID	Independent and Identically Distributed
IMU	Inertial Measurement Unit
LEV	Leading Edge Vortex
LTI	Linear Time Invariant
LW	Left Wing Marker
MAV	Micro Aerial Vehicle
ML	Maximum Likelihood
NS	Nose Marker

PCC	Pearson Correlation Coefficient
PI	Proportional-Integrative
PID	Proportional-Integrative-Derivative
PIV	Particle Image Velocimetry
PSD	Power Spectral Density
RC	Radio Control
RD	Rudder Marker
RMSE	Root Mean Square of the Error
RW	Right Wing Marker
TE	Trailing Edge Marker
TEV	Trailing Edge Vortex
UVLM	Unsteady Vortex Lattice Method
VS	Vertical Stabilizer Marker

VARIABLES

(e_0, e_1, e_2, e_3)	Quaternion vector
V	Total (absolute) velocity of the FWMAV (norm of (u, v, w))
V_{inf}	Total (absolute) free-stream velocity, same as V
(n_u, n_x, n_y)	Number of inputs u, states x, outputs y
(p, q, r)	Angular velocities in the body frame axes
$(\dot{p}, \dot{q}, \dot{r})$	Angular accelerations in the body frame axes
(u, v, w)	Linear velocities in the body frame axes
$(\dot{u}, \dot{v}, \dot{w})$	Linear accelerations in the body frame axes
(L, M, N)	Aerodynamic Moments in the body axes
(X, Y, Z)	Aerodynamic Forces in the body axes
C_F	Fling coefficient of the quasi-steady model
C_L	Lift coefficient function of the quasi-steady model
C_l	Dimensionless coefficient of translational coefficient function of the quasi-steady model

C_{D_0}	Zero lift drag coefficient of the quasi-steady model
$C_{D_{\frac{\pi}{2}}}$	90°blade pitch drag coefficient of the quasi-steady model
$C_{\{l,F\},global}$	Global coefficients, for global aerodynamic model of lift (l) and fling (F) force contributions
C_{eff}	Effective chord, considers only the peeled part of the wing blade element
$C_{r,global}$	Global coefficients, for global aerodynamic model of rotational force contribution
C_{F_0}	Affine Coefficient
C_{F_s}	Coefficient of a state for a given force or moment
C_r	Dimensionless coefficient of rotational coefficient function of the quasi-steady model
$C_{\theta_{w_0}}$	Affine coefficient for estimated wing pitch angle
$C_{\theta_{w_\zeta}}$	Coefficient of ζ in the pitch angle formula
$C_{\theta_{w_{\dot{\zeta}}}}$	Coefficient of $\dot{\zeta}$ in the pitch angle formula
M_{wing}	Wing mass in quasi-steady model
N	Number of measurement points
N_i	Total number of state observations
R^2	Coefficient of Determination
S	Vector of States
T	Flap period
a_0	Lift curve slope of two-dimensional airfoil
b	Blade element thickness
c	Chord length
$cov()$	Covariance
dr	Width of blade element
f	Flapping frequency
g	Function of the angle between the wing sections

h	Fourier series harmonics number
k	Reduced frequency
m_1	Mass used for inertial force, along the blade element $\boldsymbol{x_w}$
m_2	Mass used for inertial force, along the blade element $\boldsymbol{z_w}$
m_i	Mass of body i
m_{11}	Mass of surrounding fluid being accelerated along the blade element $\boldsymbol{x_w}$
m_{22}	Mass of surrounding fluid being accelerated along the blade element $\boldsymbol{z_w}$
n	Total number of bodies in flapping model
$p_{\{l,F\},i}$	Parameters of global aerodynamic model, for test i
t	Time instant
t^*	Dimensionless time with respect to flap period
v_{x_w}	Velocity of wing blade element along $\boldsymbol{x_w}$
v_{z_w}	Velocity of wing blade element along $\boldsymbol{z_w}$
x_0	Chordwise position of the axis of rotation of the wing section

ARRAYS

$d\boldsymbol{F}$	Total aerodynamic force acting on a single blade element, at each time instant
$d\boldsymbol{F}_{addmass}$	Added mass force acting on a single blade element, at each time instant
$d\boldsymbol{F}_{circ}$	Circulatory force acting on a single blade element, at each time instant
$d\boldsymbol{F}_{inertial}$	Inertial force acting on a single blade element, at each time instant
$d\boldsymbol{F}_{visc}$	Viscous force acting on a single blade element, at each time instant
$\boldsymbol{F_i}$	External acting forces in kinematic model
$\boldsymbol{I_{ij}}$	Product of Inertia of the ornithopter in the $i\ j$ axes

$\boldsymbol{I_i}$	Moment of Inertia of the ornithopter in the i axis
$\boldsymbol{J}$	Cost function of the Maximum Likelihood Method
$\boldsymbol{M_g}$	Moment caused by gravity force on the Body in the kinematic model
$\boldsymbol{M_i}$	External acting moments in kinematic model
$\boldsymbol{Q_j}$	Generalized forces
$\boldsymbol{q}_j$	Array of generalized coordinates
$\boldsymbol{u}_j$	Array of quasi-velocities
$\boldsymbol{v}_i$	Linear velocity of body i in the Body frame in kinematic model
$\dot{\boldsymbol{v}}_i$	Linear acceleration of body i in the Body frame
$\mathbf{R}$	Measurement error covariance matrix
$\mathbf{y}$	Model-predicted system output
$\mathbf{z}$	Measured system output
$\mathscr{R}_{b,I}$	Rotation matrix from Inertial to Body frame, in the Body frame
$\mathscr{R}_{b,w_i}$	Rotation matrix from Body to Wing frame i, in the Body frame
$\mathscr{R}_{w_i,b}$	Rotation matrix from Body to Wing frame i, in the Wing frame

GREEK

(ϕ,θ,ψ)	Euler Angles - Roll, Pitch, Yaw
$(\dot{\phi},\dot{\theta},\dot{\psi})$	Attitude Angle rates
α	Body relative angle of attack of blade element
α_w	Relative angle of attack of blade element
$\boldsymbol{\Gamma_{rot}}$	Rotational Circulation
$\boldsymbol{\Gamma_{trans}}$	Translational Circulation
$\boldsymbol{\Gamma}$	Total Circulation (translational + rotational)
$\boldsymbol{\beta_{ij}}$	Angular velocity coefficient matrix

$\dot{\boldsymbol{\omega}}_{\boldsymbol{i}}$	Angular acceleration of body i in the Body frame
$\boldsymbol{\gamma}_{\boldsymbol{ij}}$	Linear velocity coefficient matrix
$\boldsymbol{\omega}_i$	Angular velocity of body i in the Body frame
$\boldsymbol{\omega}_n$	Natural frequency of the system
$\boldsymbol{\rho}_{b_{wi,h}}$	Vector from CG of wing i to hinge point, in the Body frame
$\boldsymbol{\rho}_{ci}$	Vector from the reference point of a body to its center of mass
$\boldsymbol{\rho}_{h,b}$	Vector from wing hinge point to CG of the main body
$\boldsymbol{\rho}_{w_i,h}$	Vector from CG of wing i to hinge point, in the Wing frame
$\ddot{\boldsymbol{\rho}}_{ci}$	Acceleration of vector $\boldsymbol{\rho}_{ci}$ in the Body frame
δ_e	Elevator angle input
δ_f	Flapping Frequency input
δ_r	Rudder angle input
ϵ	Difference between model-predicted and real output
λ	Dimensionless wing fling angle, θ_{fling}/π
ρ	Autocorrelation function
ρ_f	Fluid density
ω	Angular velocity of the wing during flapping motion
Θ	Set of unknown parameters in the Maximum Likelihood cost function
θ_b	Pitch angle of the FWMAV
θ_l	Pitch angle of lower wing
θ_u	Pitch angle of upper wing
θ_{w_i}	Pitch angle of the wing using chord reference line i
$\hat{\theta}_{w_i}$	Estimated wing pitch angle using chord reference line i
ζ_0	Dihedral of the wings
ζ	Wing angle measured with respect to closed wing position

$\dot{\zeta}$	Wing flap angular velocity
$\ddot{\zeta}$	Wing flap angular acceleration

REFERENCE FRAMES AND SUBSCRIPTS

B	Body Reference Frame
I	Inertial Reference Frame
W_i	Reference Frame of wing i
$_I$	Inertial Frame Subscript
$_b$	Body Frame Subscript
$_w$	Wing Frame Subscript
$(\boldsymbol{x_I}, \boldsymbol{y_I}, \boldsymbol{z_I})$	Unit axes of the Body reference frame
$(\boldsymbol{x_b}, \boldsymbol{y_b}, \boldsymbol{z_b})$	Unit axes of the Body reference frame
$(\boldsymbol{x_w}, \boldsymbol{y_w}, \boldsymbol{z_w})$	Unit axes of the Wing reference frame

1

INTRODUCTION

FLYING species, like birds and insects, have unmatched capabilities as far as locomotion is concerned. Their ability to fly has evolved over the course of millions of years. Driven by the needs for locomotion and survivability, and made possible through the densification of the Earth's atmosphere, different species started to evolve to conquer the remaining mean – the air. An evolution that is dated to have started earlier than 300 million years ago, with a fossil evidence of a 60 cm span dragonfly-like *Meganeura* [BBC, 2015] proves that flying is advantageous for many reasons. Such ability to fly has also been a source of inspiration to mankind. In fact, references of such inspiration date back to Greek mythology, with the legend of Icarus and Daedalus [Graves, 1955]. Later, Leonardo Da Vinci detailed in the Paris Manuscript B the schematics of a flapping mechanism designed for a human being. Despite not reaching completion, such a mechanism was used by João Almeida Torto, in Viseu, Portugal in the first registered attempt to fly like a bird in 1540, by jumping from a church tower, which resulted in the death of the adventurer Lapa [1928], illustrated in Figure 1.1.

Today, the picture is significantly different. It is well understood that flying species exhibit extreme capabilities which, once mastered by humans, could leverage the way we see and experience flight. One can easily foresee such knowledge being applied to the development of highly-maneuverable flying robots that mimic a bird or insect for high risk military or intelligence gathering operations. In this respect, science fiction is not that far from representing the current state of the art.

In an attempt to comprehend the mechanics of flight, three strategies are typically adopted. Firstly, the study of flying species in controlled environments, focusing mainly on the aerodynamics and kinematics of flapping flight of flapping species, with examples of detailed and important studies by Wood [1970, 1972], Weis-Fogh [1972, 1973, 1975], Ellington [Ellington, 1984c,b; Ellington et al., 1996; Ellington, 1999], and Wang [Wang, 2000, 2005; Wang and Eldredge, 2013]; Secondly, the development of computer simulations recurring to physical and phenomenological modeling of a flapping wing system, through a combination of kinematic, inertial and aerodynamic principles, e.g., Gebert and Gallmeier [2002]; Miller and Peskin [2005]; Andersen et al. [2005a]; Ansari

(a) Illustration of the jump with people watching.

(b) Reconstruction of the event at the Air Museum, Sintra, Portugal.

Figure 1.1: Illustration of João Torto jumping from a church tower in Viseu, Portugal (courtesy of *Museu do Ar*, Portugal).

et al. [2006]; Berman and Wang [2007]; Dietl and Garcia [2008]; Bolender [2009]; Pfeiffer et al. [2010]; Su and Cesnik [2010]; Gogulapati and Friedmann [2011]; Kolomenskiy et al. [2011]; Orlowski and Girard [2011]; Nakata et al. [2015]; and thirdly, the actual development of flapping wing systems and the subsequent study of their properties, benefiting from the maturation of technology, which allows for the development of flapping mechanisms and flight capable platforms.

While the former two strategies mainly encompass the study of existent species and are based on physical principles, the latter strategy can, itself, be further divided in two groups, based on the methodology. The first group consists of studies of a sole flapping wing system in a fixed-base setup, with the goal of fundamentally understanding the design parameters and the aerodynamics of flapping wings, e.g., Spedding and Maxworthy [1986]; Dickinson et al. [1999]; Khan and Agrawal [2005]; Lentink and Dickinson [2009]; Hines et al. [2011]; Maniar et al. [2012]; Percin et al. [2012a]; Percin and van Oudheusden [2015]. The second group entails studies on FWMAV, with the focus on wind tunnel and free-flight experiments, e.g., Fearing et al. [2000]; Baek et al. [2011]; Keennon et al. [2012]; Kim et al. [2012]; Ma et al. [2013]; Chirarattananon and Wood [2013]; Nakata et al. [2011]; Karasek et al. [2014]; Caetano et al. [2015c].

It is envisioned that such vehicles will occupy an existing gap in conventional fixed and rotary wing aircraft applications, owing to their agility, broad flight envelope, resilient behavior when in contact with obstacles and promising properties at very low Reynolds numbers.

1.1 FLAPPING WING MICRO AERIAL VEHICLES

Recent technological advances have boosted the development of man-made bio-inspired flapping wing platforms – ornithopters. Especially for FWMAVs, for which flapping is believed to yield most advantages [Ansari et al., 2006; Dickinson et al., 1999; Ellington et al., 1996; Malolan et al., 2004], the small size and mass heavily restrict the range of sensors and processing onboard. With a total take-off weight of only a few grams, descriptive and comprehensive flight dynamic models are still not available, with model identification [Lee and Han, 2012; Lim et al., 2012; Caetano et al., 2013a] and consequent flight control being active areas of research [Keennon et al., 2012; Wood, 2008]. In this respect, a distinction should be made between different flapping wing designs: (1) the ones inspired from birds and most insects, having only one pair of wings (monoplane), which can either move independently or be driven by the same flapping mechanism prescribing the same motion in time; (2) the ones inspired from four-winged insects like the dragonfly and the *locust*, in a biplane or tandem configuration; Within these latter designs, another distinction should be made between the bird-like tailed designs and the insect-like tailless configurations.

Tailless designs, which in general mimic insects, have very small size and weight and offer the possibility of performing highly dynamic maneuvers. Such configurations are lighter, more agile and less prone to suffer from external disturbances, e.g., wind gusts. However, they require active stabilization, as they are statically and dynamically unstable, hence forcing the wing beat to be actively controlled in several degrees of freedom, for lift, thrust and control. In fact, these requirements make them very difficult to design, produce and control. To date, only four tailless FWMAVs have been able to show the ability to perform controlled flight: Aerovironment's Nano Hummingbird [Keennon et al., 2012]; Harvard's Robobee [Ma et al., 2013], Festo's BionicOter and eMotionButterfly [Festo, 2013].

Tailed designs, similar to birds and bats, benefit from being statically stable and therefore do not require active stabilization around a trimmed flight condition. In such configurations wings are mainly used for lift and thrust while other control surfaces, in the tail, are used for active control. This approach simplifies both the flapping mechanisms and the control strategies, typically resulting in a flap mechanism design that has only one active degree-of-freedom – flap around the body of the ornithopter – which is responsible for the passive pitching and lagging motions. Such tailed configurations allow for the research to focus on higher-level problems and implementations, such as altitude control [Baek and Fearing, 2010; de Croon et al., 2012] or obstacle avoidance [de Croon et al., 2012; Tijmons et al., 2013]. However, tailed designs are more sensitive to external perturbations and are hard to control throughout their broad flight envelope, i.e., from hover to fast forward flight, due to dynamic instability at some flight regimes. Hence, active control is still needed to further expand the ornithopter's flight envelope and fully exploit its capabilities. Factors like the complexity of the flapping mechanism and control strategies as well as the very small size of tailless designs motivate researchers to explore bird-like tailed designs for higher level studies. As a result, such configurations are the most common, with examples of successful flight capable FWMAV including the DelFly [de Croon et al., 2009], i-Bird [Baek, 2011], Kinkade Slow Hawk [Grauer et al., 2011], University of Arizona ornithopters [Maniar et al., 2012], Cybird P1 [Lee and Han, 2012], Golden Snitch [Hsiao et al., 2012] and Chiba University MAV [Nakata et al., 2011]

On the one hand, when making a distinction in the platforms with respect to size alone, very small centimeter size flapping robots have only two wings (monoplane) and do not have a tail. Besides the inspiration from insects, these configurations have been shown to be the best for such small sizes, (see top-left section of Figure 1.2 [Ma et al., 2013; Chirarattananon and Wood, 2013; Hines et al., 2014]), as more wings would imply more complex flapping and control strategies and a centimeter size tail would not be efficient. On the other hand, for larger flapping platform designs, the tail offers an effective means for control, thus being present in most of the designs. In such platforms the differences arise in terms of wing shape and configuration. The faster robots typically have one set of two wings, in monoplane configuration, thus being limited in terms of flight envelope, as these are not able to perform hover flight (see top-right section of Figure 1.2). In case of hover requirements, a biplane wing configuration is often selected, either in tandem or 'X' wing configuration, cf. Worth noting are two exceptions to the typical configurations for larger FWMAVs, which represent major achievements in their development: Aerovironment's Hummingbird [Keennon et al., 2012] and Festo's BionicOpter [Festo, 2013].

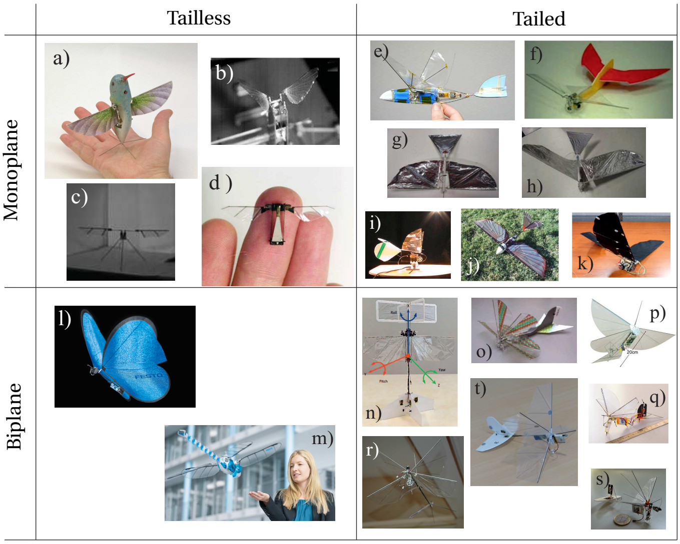

Figure 1.2: Different FWMAV developed in academia and industry. a) Aerovironment's Nano Hummingbird [Keennon et al., 2012]; b) University of Arizona FWMAV [Randall et al., 2012]; c) Carnegie Mellon University FWMAV Hines et al. [2014]; d) Harvard's RoboBee [Wood, 2008]; e) CalTech's MicroBat [Pornsin-sirirak et al., 2001]; f) Tamkang University Golden Snitch [Hsiao et al., 2012]; g) and h) University of Maryland Small Bird [Bejgerowski et al., 2009] and Big Bird [Mueller, 2001]; i) and j) University of Arizona 24cm and 74cm FWMAVs [Lim et al., 2012]; k) KAIST ornithopter [Lee and Han, 2012]; l) Festo's eMotionButterfly and m) Festo's BioniCopter [Festo, 2013]; n) National University of Singapore [Nguyen et al., 2015]; o) Wright-state University MAV [WSU, 2012]; p) Berkeley's i-Bird [Rose and Fearing, 2014]; q) Chiba University FWMAV [Nakata et al., 2011]; r) TUDelft's DelFly I, s) DelFly Micro and t) DelFly II used in this dissertation.

1.2 ON THE MECHANICS OF FLAPPING FLIGHT

The present section provides information on the typical study methods used to better understand the flapping wing mechanics. Furthermore, it describes the parameters involved in the kinematic characterization of flapping wings and presents the most prominent aerodynamic mechanisms that act during the flapping motion.

1.2.1 A WORD ON FLAPPING WING STUDY METHODS

The methods used to study flapping wings can be divided in three categories: (1) experimental and (2) numerical study of flapping wings aerodynamics; (3) dynamic behavior of flapping flight, which includes both the kinematics and the aerodynamics of the entire flyer.

Mainly due to technological limitations, early models of flapping flight focused on the analysis of wake evolution instead of the fluid-structure interaction occurring at the wing level. Notable experimental work from Wood [1970], Norberg [1972a,b] and Weis-Fogh [1972, 1973] in analyzing the flapping kinematics and the mechanisms of flight of different flying species paved the way for the development of a first model of the Weis-Fogh clap-and-fling wing interaction mechanism. In particular, Lighthill [1973] proposed a first model to explain the added lift force present in the *Encarsia Formosa* wasp. Despite being two-dimensional and inviscid, such models were verified experimentally several years later, in the studies of Bennett [1977a], Spedding and Maxworthy [1986] and Sunada et al. [1993]. Using a different approach, ‘wake models’ tried to explain the average force experienced during flapping flight, shedding light on the flapping mechanisms for non-interacting wing kinematics, as seen on insects like the *Drosophila*. Seminal work by Ellington [1978, 1984e] and Rayner [1979a,b] lead to the development of vortex based models by use of the blade-element and actuator disk theories in a complementary fashion. These models determined the lift from the change in momentum from the downward induced stream needed to counter the animal’s weight, calculating the circulation from this force balance. Later ‘local circulation’ methods complemented the average wake models including spanwise and temporal oscillations of induced velocity, with good results, e.g., Zbikowski [2002].

Recent breakthrough analytical studies have shed new light in the mechanics of flapping flight by incorporating phenomenological terms of known fluid dynamics, specifically the noteworthy work by Dickinson et al. [1999], Sane and Dickinson [2001, 2002] and Lehmann [Lehmann et al., 2005; Lehmann, 2007]. Much like the studies mentioned in the previous paragraph, these studies still follow an experimental methodology replicating the wings of flapping species. Nevertheless, such studies differ by using wing replicas with different sizes as of their natural counterparts, and subjecting them to flap tests in specially designed test setups. Such studies generally rely on the dynamics scaling of the actual phenomenon and involve the development of dynamically scaled wings in terms of size, shape, flapping velocity and surrounding fluid properties so as to simulate the flapping of known flying species. A considerable body of work has been done at a more fundamental, level with experimental setups dedicated to the characterization of the flow around the wing under the influence of different wing shapes, wing flexibility, flapping patterns, wing interactions and different free-stream velocities, e.g., Particle Image Velocimetry PIV [Percin et al., 2011, 2014].

In contrast to with the previous methods, computational fluid dynamics (CFD) and numerical simulation studies, e.g., Nagai et al. [2009]; Su and Cesnik [2010]; Nakata et al. [2011]; Kolomenskiy et al. [2011]; Kang et al. [2011]; Zheng et al. [2013], allow for thorough and in-depth analyses when compared to simple phenomenological models. These methods, however, are often too complex and time consuming and, despite being adequate for fundamental understanding of the flapping mechanics, the complexity of the resulting models also leads to an inability to be used for flapping flight simulation and model-based flight control developments.

While the first two methods introduced above addressed fundamental experimental and numerical methods focusing on the characterization of the flow around a flapping wing, they lack on the understanding of the connection between the aerodynamics of the wing and the dynamics of free-flight of the whole flying system, whether be it an insect, bird or a robot. To bridge this gap, a considerable body of work has focused on the identification of models from the free-flight of a specimen of interest. For these methodologies, the typical modeling techniques can be divided in two categories: (1) black-box modeling (e.g., neural networks) when little or nothing is known about the driving physical principles; (2) white or gray-box modeling, for which there exists some physical insight and an initial model structure Grauer et al. [2011]; Lim et al. [2012]; Lee and Han [2012]; Caetano et al. [2015a]. This dissertation focuses on the latter approach, which will be further developed in Section 1.5.4.

Instead of focusing on the aerodynamics of a flapping wing, a considerable body of work is dedicated to the understanding of the influence of the kinematics of flapping wings on both the aerodynamic force generation mechanisms [Berman and Wang, 2007; Lentink and Dickinson, 2009] and on the dynamics of the air vehicle as a whole [Dietl and Garcia, 2008; Orlowski and Girard, 2011; Oppenheimer et al., 2011]. Such studies focus on a higher level understanding of the system as a whole, with the objective of identifying the dynamics of a flight capable FWMAV, paving way for the development of control strategies for such platforms. Furthermore, analysis of flapping wing flight requires a careful combination of flapping wing kinematics and flapping wing aerodynamics, which are addressed separately below.

The section proceeds with the description of the kinematic parameters used to describe flapping flight.

1.2.2 KINEMATICS OF FLAPPING WINGS

Natural flyers have adopted their wing shapes and stroke kinematics, i.e., pure motion considering only internal and inertial forces, having different optimization goals related to their survivability and surrounding environment. Hence, an unquantified number of flapping kinematics can be found in natural species, making it very difficult to fully characterize the motion and wing beat for all existing cases and designed platforms. Parameters like flapping frequency, wing shape and structure, aspect ratio, wing flexibility vary considerably between flyers, cf. Norberg [1975].

Nevertheless, a set of parameters was found to describe the kinematics of flapping wings, and is graphically identified in Figure 1.3. Three types of motion are prescribed in flapping flight: (1) heaving motion, here η, only present in some species and FWMAV, is also know as lagging of the wing during flap, around the $\boldsymbol{z_b}$ axis; (2) pitching motion, here

θ_w, defined by the rotation of the wing around the $\boldsymbol{y_b}$ axis; and (3) sweeping motion, here ζ, corresponding to the largest deflection of the wing, and the main driver of flapping flight – this motion is performed around the $\boldsymbol{x_b}$ axis, and defines the stroke plane;

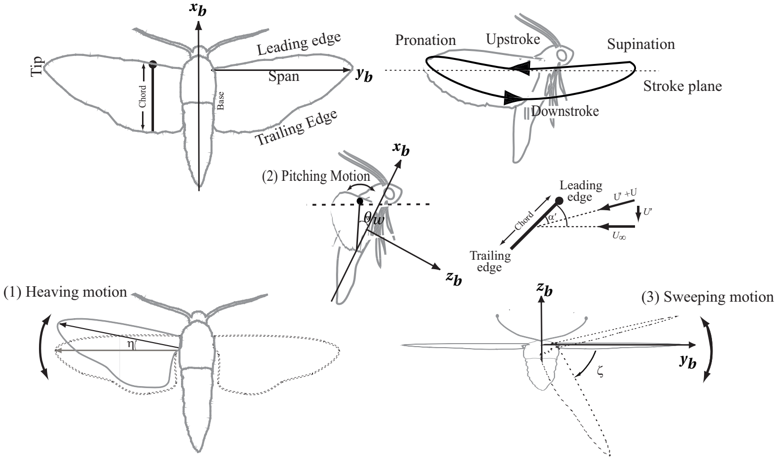

Figure 1.3: Kinematics of flapping wing, based on original schematics by Sane [2003].

1.2.3 AERODYNAMIC FORCE GENERATION MECHANISMS

Unsteady aerodynamic effects have been shown to be dominant factors in flapping flight [Sane, 2003]. Here we address the most important mechanisms of flapping force generation, considering the wing as a very thin flat plate. It is worth noting that aerodynamic concepts and definitions, e.g., the Kutta condition, fluid viscosity, Reynolds number, vortex or unsteadiness are assumed to be understood by the reader, hence building on conventional aerodynamics for the explanation of flapping wing force generation mechanisms.

Adding to the Reynolds number, another non-dimensional parameter that has been shown to affect the aerodynamic modeling of flapping flight is the reduced frequency. This term reflects the unsteadiness in the flapping, being a ratio of the mean chord length of the wing and the wavelength of the shed vortices. It is calculated using:

$$k = \frac{\omega c}{2V}, \tag{1.1}$$

with ω the average angular velocity of the wing in the flapping motion.

The following paragraphs will address the details of six important unsteady aerodynamic mechanisms: (1) Wagner effect; (2) Leading Edge Vortex; (3) Rotational Force; (4) Wing-wake interaction; (5) Added mass; (6) Clap-and-fling. For more information about these mechanisms, the reader is referred to Sane [2003]; Dickinson et al. [1999]; Ellington et al. [1996]; Ellington [1999]; Lehmann [2007].

Wagner Effect

Initially proposed by Wagner [1925], this mechanism explains the delay in the growth of circulation on a translating wing that started moving from rest state. During the impulsive start, the viscous action of the fluid delays the establishment of the Kutta condition. In addition to this, the velocity field that is induced at the trailing edge due to the generation of a starting vortex also counteracts the growth of circulation, hence further delaying the steady-state value. This mechanism is graphically represented in Figure 1.4.

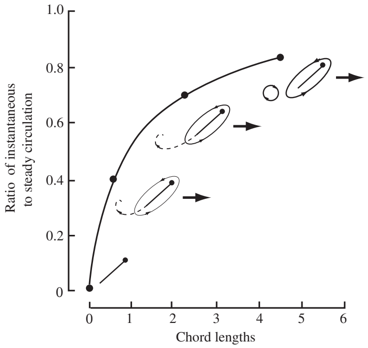

Figure 1.4: Explanation of the Wagner effect: delayed growth of steady state circulation and the generation of a starting vortex, adapted from Sane [2003].

Leading Edge Vortex

This mechanism occurs on wings flapping/moving at an angle of attack (AOA) higher than the stall angle such that the flow separates at the leading edge. This flow separation results in a formation of the leading edge vortex (LEV) which creates a low pressure region and a corresponding suction force. The LEV is formed as a result of the separation but it may stay attached to the wing throughout the motion (a stable LEV), which happens generally for finite wings performing curvilinear motions. For translating wings, the LEV forms but cannot stay attached to the wing and sheds. The time the wing generates high forces before the LEV sheds (so the wing stalls) is the reason to call it also as the ‘delayed stall’. The shedding of the LEV occurs in translating wings, as some stability mechanisms are absent in that case. Such mechanism is used by insects and was shown to be stable for certain conditions in flapping flight by Polhamus [1971]; Ellington et al. [1996] and Dickinson et al. [1999].

When compared to 2-dimensional translation motions, 3-dimensional revolving and rotating wings have the ability of sustaining the LEV during a considerable portion of the flap, whereas a translational motion would result in the consequent growth of the LEV until separation occurs. Figure 1.5 presents the difference in LEV generation and growth for 2-dimensional and 3-dimensional kinematic – here T1 indicates the time instant that captures the initial LEV generation and T2 depicts the instant when final LEV that was ‘captured’ by the 3-dimensional movement. In particular for thin flat wings, the LEV is responsible for the generation of a force that is perpendicular to the wing section, due to the sum of the suction force and the normal force acting on the wing. Since this term is present during translation of the wing, it is typically considered in the translational circulation term of an aerodynamic model.

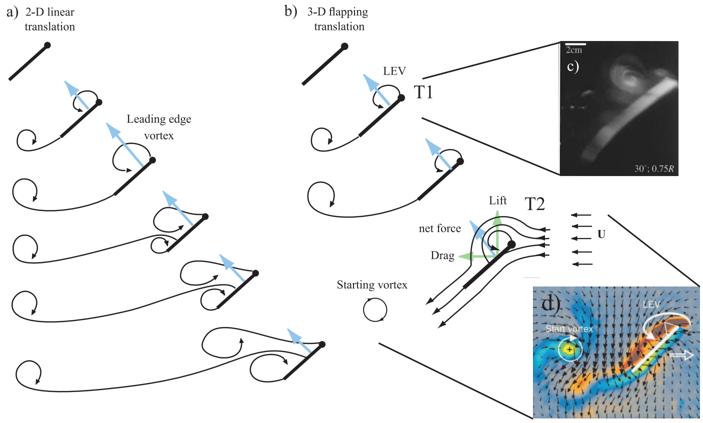

Figure 1.5: Explanation of LEV generation: comparison of (a) a 2-dimension translating motion with (b) a 3-dimension flapping motion, adapted from Sane [2003]; (c) is the experimental visualization of T1, adapted from van den Berg and Ellington [1997]; (d) is the PIV reconstruction of T2, adapted from Lehmann [2007].

ROTATIONAL FORCES

In the context of thin airfoil theory, when a wing rotates about the spanwise axis and translates simultaneously, the stagnation point moves away from the trailing edge, resulting in a transient motion that prevents the Kutta condition from being established. Hence, since this condition must be present at all times, another circulatory term has to be present which adds to the translational circulation (of the LEV, for example). This term, also known as the Kramer effect, was first identified by Kramer [1932] and more recently called rotational circulation [Dickinson et al., 1999]. Such circulatory force will have different signs depending on the direction of rotation: it adds to the translational circulation if the rotation is in the direction of an increase in the angle of attack; conversely, it has an opposite sign if the wing pitches down during rotation.

Ellington [1984c] proposed a simple empirical formula for the rotational circulation of a 2-dimensional wing under the assumption of quasi-steady aerodynamics to be:

$$\Gamma_{rot} = \pi(0.75 - \hat{x}_0)c^2\dot{\theta}_w, \tag{1.2}$$

with $\hat{x}_0$ the dimensionless axis chord of the axis of rotation and $\dot{\theta}_w$ the wing pitch angular velocity, in rad/s. Later, Dickinson et al. [1999] and Sane and Dickinson [2002] verified the formula using experimental data. Given the limitations of quasi-steady aerodynamics, other studies have focused on evaluating the effect of the pitch motion during flap. Numerical studies by Sun and Tang [2002] have allowed for a visualization of the effect of pitch-wise rotation during flap, by comparing pure flapping motion with a combined flap and pitch up motion of a 3-dimensional wing, which is described in Figure 1.6, where solid and dashed lines indicate the positive and negative vorticity. Here, it can be seen that the vortices are stronger during the combined flap and rotation motion, when compared to the pure flapping motion.

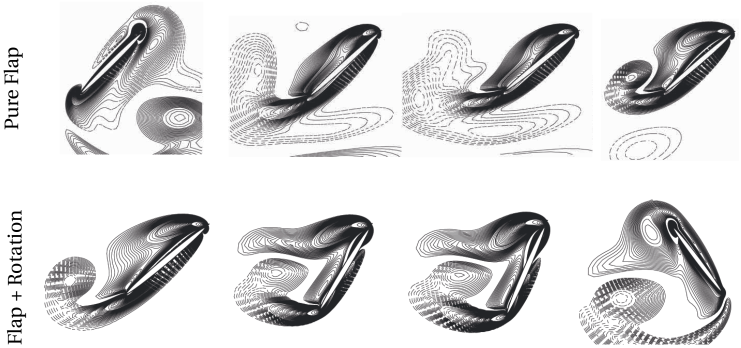

Figure 1.6: Effect of pitch-wise rotation during flapping motion represented with numerically simulated vorticity plots. Top: pure flapping motion; Bottom: a combined flapping and rotation (pitch up) motion. Solid and dashed lines represent the positive and negative vorticity, respectively, adapted from Sun and Tang [2002]

WING-WAKE INTERACTION

As the wing reaches the end of one stroke and reverses the direction of movement, it sheds both the LEV and the trailing edge vortices. This shedding induces an increase in the velocity field at the vicinity of the wing section. Upon reversal, the wing encounters its own shed vortices which are now part of the wake, which can lead to an increase of the generated forces due to a positive addition of locally induced velocities – hence also called 'wake capture'. Such a mechanism was shown to be present in flapping flight, although highly influenced by the stroke kinematics. Dickinson et al. [1999] showed that the force generated through wake capture can be augmented with an advance of the wing rotation with respect to the end of the stroke, stemming from a more energetic wake.

ADDED MASS

When a wing accelerates in a fluid, it experiences a reacting force exerted from the fluid on the wing surface as a result of the inertia of the fluid in the vicinity of the wing – hence also known as 'added mass inertia' [Sane and Dickinson, 2001] or 'virtual mass' [Ellington, 1984d]. This force component is present in both translational and rotational accelerations and at the same time as the circulatory terms, hence making it difficult to measure and estimate in isolation. A way to determine the added mass is to measure all forces acting on a flapping wing and subtract all estimated circulatory and viscous terms, as performed by Sane and Dickinson [2002].

CLAP-AND-FLING

First proposed by Weis-Fogh [1973], this mechanism of force generation occurs upon wing-wing interaction at the end of a half-stroke, for flying species like the *Trialeurodes* *vaporariorum* [Weis-Fogh, 1975], *Thrips physapus* [Ellington, 1984b], and the parasitoid wasp *Muscidifurax raptor* [Miller and Peskin, 2009]. The effect is illustrated in Figure 1.7. Here, the 'clap' part occurs at the end of a stroke, starting (a) when the leading edge of the wings touch each other and (b) as the wings rotate before stroke reversal, the gap formed by the contacting wing sections decreases in size pushing out the air between them in a downward direction. Consecutively, after stroke reversal (c) the wings pronate, and the leading edges start to detach. During this motion, called 'fling' (b to e), a gap is left between the wing sections starting at the leading edge, which increases in size until the wings stop touching each other. During 'fling' the volume that has recently formed between the wings generates a positive pressure differential between this part and the outside, which increases the magnitude of the leading edge vortex and the pressure gradient, resulting in an added net force that points upwards, perpendicular to the stroke plane.

Initially proposed and modeled as rigid wing 'clap-and-fling', it was later observed that the wing flexibility further augments the force generated with this mechanism, being called 'clap-and-peel´ for the case of flexible wings. During the 'clap' there is an increase on the induced velocity at the trailing edge of the wings, which results in an increase in the net lift force; during the 'peel', the flexibility of the wings promotes a reduction of the local angle of attack and an increase on the leading edge vortex, which increases the pressure differential and, therefore, the suction during the initial part of the 'peel'. Furthermore, this mechanism is also believed to attenuate the formation of the starting vortex and, therefore, the Wagner effect, which explains the faster build of circulation during the beginning of the onset stroke.

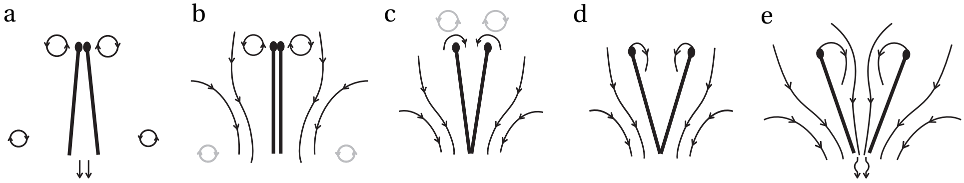

Figure 1.7: Representation of clap-and-fling motion, at different consecutive dimensionless times, from a to e. Arrows show the direction of flow; black and gray lines represent current and previous subfigure vortices, respectively; detached lines are streamlines; circular shapes represent vortices; lines connected to leading edge are starting vortices; lines at trailing edges of subfigure *e* represent the interaction between the beginning of starting vortices and the flow from withing the cleft.

1.3 CHALLENGES IN MODEL IDENTIFICATION OF FLAPPING WING MAV

The characterization of the previous aerodynamic mechanisms and their modeling would allow for the prediction of the behavior of a flapping wing vehicle, as well as pave the way to dynamic modeling of ornithopters. This, in turn, would allow for the development of flapping wing flight simulation and control strategies, as well as new designs, possibly leading to a new generation of flapping air vehicles to have automatic flight capabilities.

Currently, there are representative aerodynamic models devised from nature, e.g., Ellington et al. [1996]; Ellington [1999]; Dickinson et al. [1999], experimental observations, e.g., Pesavento and Wang [2004]; Andersen et al. [2005b]; Berman and Wang [2007] and models developed from CFD. The first tend to be rather simplistic and do not describe nonlinear behavior; the latter are often too complicated for flight simulation or onboard model based control. In a general way, we can divide the challenges of modeling flapping wing systems in two categories: Theoretical and Technical challenges.

Theoretical Challenges Related with the question: 'Which theoretical principles explain the aerodynamics and dynamics of controlled flapping flight?' Natural flyers operate in a considerably broad Reynolds number conditions, from 10 to 10^5 [Dudley, 2000]. Despite mimicking nature's flyers, FWMAVs add to the study possibilities by adding more wing kinematics, wing flexibilities and hence, new possible interactions. The Reynolds number of a flight regime affects the behavior of the flow. At high Reynolds numbers, typically present in large flyers, with wing spans above 25cm, viscous effects have been shown to have only a marginal influence and aerodynamic models can be reduced to inviscid Euler based models. Nevertheless, in these conditions, small perturbations in the flow field accumulate with time and can result in the increase of the unsteadiness of the flow.

At small Reynolds numbers, viscous effects have a greater contribution to the overall evolution of the force generation mechanism, structuring the flow around the wings. As a consequence, and contrary to higher Reynolds regimes, perturbations on the flow are more rapidly dissipated [Sane, 2003]. Furthermore, CFD simulations have shown that the Reynolds number affects the evolution of both lift and drag forces while keeping all remaining flapping parameters the same [Zheng et al., 2013]. Such relations and implications complicate the understanding of the dominance of several aerodynamic mechanisms, hence adding difficulty to the modeling of flapping wing aerodynamics.

Flapping wing kinematics further complicate the understanding of the flow mechanisms. Simple and small changes in one single parameter, e.g., the dimensionless time of the pitching motion of the wing with respect to the flapping motion can significantly affect the vortex generation at the end of the stroke, and also change the rotational circulation bound to the wing [Sane and Dickinson, 2002]. Examples of different wing kinematic profiles can be seen in Figure 1.8.

The combination of aerodynamics with the kinematics of flapping further complicates the process. Besides the impact of the kinematics on the wing aerodynamic forces, other factors have been shown to influence the dominant aerodynamic mechanisms. The reduced frequency, for example, was shown to determine which type of modeling theory can be applied, cf. Table 1.1. Furthermore, the inertia of both the wings and the body of the flyer, also affect the modeling due to the relation between the flapping frequency and the natural frequency of the flyer, especially for hover cases. For example, if the flapping frequency (here ω) is considerably higher than the natural frequency of the flyer, then averaging aerodynamic model structures might be applied, since the time resolved evolution of the force during one flap cycle will not affect the dynamics of the flyer (viz. Dickinson et al. [1999]; Berman and Wang [2007]). Conversely, if the flapping

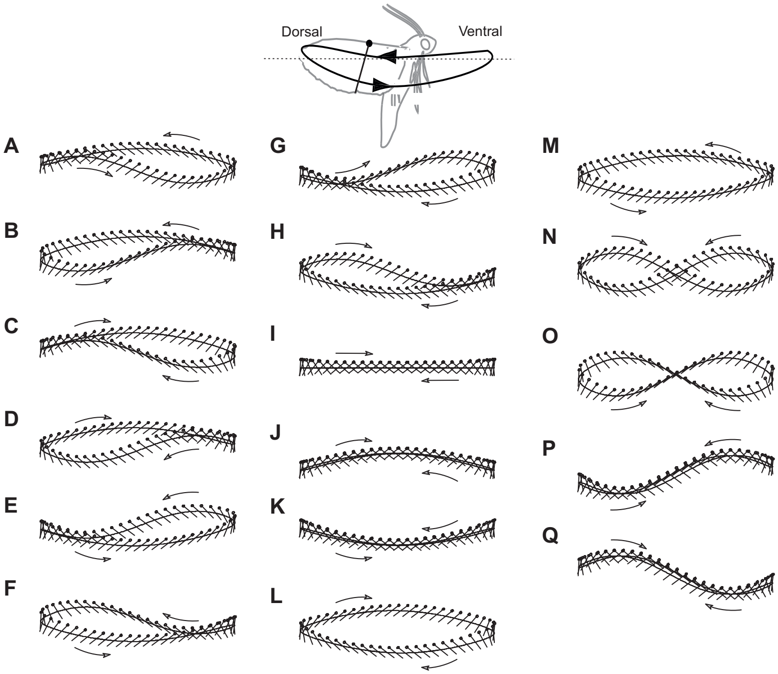

Figure 1.8: Different possible kinematic wing profiles, adapted from Lehmann and Pick [2007].

frequency is of a similar order as the natural frequency of the body modes, the forces acting at each time-step will influence the dynamics of the system, its kinematics and, therefore, also its aerodynamic force generation mechanisms, cf. Table 1.1.

Additionally, even with a profound knowledge of the perturbations affecting the force generation mechanisms, models are not able to analytically predict all possible outputs and influences. As a result, the modeling is subjected to a number of approximations and assumptions, thus limiting their application to a reduced number of meaningful conditions.

Technological Challenges These are predominantly related to the question: 'How to measure and analyze the flight mechanics of flying species?' Depending on the size of the flyer, different methodologies must be employed. Taking the example of the fruit fly *Drosophila Melanogaster*, the small size (≈3mm) and flapping frequency of about 200Hz pose great challenges on recording the fly during flight. Aspects like the image frequency and resolution have been technological bottlenecks in this field. Furthermore, the flight of such species is greatly influenced by the visual, odometric and olfactory information. Larger species pose other types of challenges: beyond the ethics, risks and the requirements needed to nourish and handle larger flyers, the technological bottlenecks are, in general, related to the size of the facilities and the instrumentation of both the room and the flyers, for accurate representation of motion, e.g., Hedenstrom and Johansson [2015].

Instead of testing on natural flyers, several studies focus on the analysis of the flight

Table 1.1: Applicability of existent quasi-steady and proposed models, as function of the reduced frequencies ($k = \frac{\omega c}{2V}$) and the natural body frequencies (ω_n). Adapted from Taha et al. [2012, 2014]. ω is the flapping frequency. UVLM is Unsteady Vortex Lattice Method.

	Hovering		**Forward Flight**		
Criteria	$\frac{\omega}{\omega_n} \gg 1$	$\frac{\omega}{\omega_n} \approx O(1)$	$k > 0.1$ $\alpha > 25°$	$k > 0.1$ $\alpha < 25°$	$k < 0.1$
Modeling Techniques	- Only average forces affect body dynamics - Quasi-Steady Aerodynamics that include LEV, e.g.: - Dickinson et al. [1999] - Berman and Wang [2007] **??**	- Contribution of LEV - Coupling between subflap forces and body dynamics - Numerical methods **??**		- Methods that capture unsteady effects **2D** - Theodorsen [1935] - Peters [2008] **3D** - Jones [1939, 1940] - Reissner and Stevens [1947a,b] - UVLM	- QS Aerodynamics that include forward flight information

mechanics of FWMAV. If, on the one hand, such methods avoid the risks and limitations of contacting with natural species, on the other hand different challenges limit the results. In particular, such methods depend on the existence of a stable and controllable FWMAVs. This requirement is a limitation per se, since FWMAVs are very difficult to produce and controlling one in free-flight is difficult [Grauer et al., 2011; Lim et al., 2012]. In addition, such FWMAVs require advanced and miniaturized technology, as well as considerable technical capabilities for the production and integration of sensors, controllers or an onboard autopilot.

In the presence of the technological limitations presented above, researchers often opt for: tethering the flyer or flapping mechanism, connecting it to a fixed-base by means of a wire [Henningsson and Bomphrey, 2011; Hines et al., 2014], movable clamp with several degrees of freedom [Nakata et al., 2011; Lee and Han, 2012], or rigid clamping [Lin et al., 2006; Muniappan et al., 2005; Mazaheri and Ebrahimi, 2011] in still non-moving air or in a wind tunnel setup [Percin et al., 2014]. Being more advantageous in terms of simplicity than free-flight testing, such methods, however, restrict the motion of the flyer and often represent unrealistic flight regimes, since most of these techniques are applied to non-flight capable flyers or simplified versions of a flapping mechanism.

It is worth noting that these test methodologies are also used in the case of flight capable flyers for more fundamental research, like PIV., viz. Percin et al. [2014]. In addition, CFD and numerical methods can be applied to obtain a more profound insight in the mechanics of flapping wings. These methodologies are, however, limited to the realism of the assumptions, kinematics and physical properties of the flapping wing model.

1.4 THE DELFLY II FLAPPING WING MICRO AERIAL VEHICLE

This Section presents the DelFly II FWMAV that was used in this study. Born in 2006, the 'DelFly' stemmed from a final project of the bachelor program in Aerospace Engineering of Delft University of Technology. Initially with a span of 33cm and a length of 41cm, the first version of the DelFly, named DelFly I, was developed with four wings in an 'X' configuration and an inverted 'V' tail.

Different DelFly configurations have been created, cf. Figure 1.9, with different design goals in mind. The Guinness book of records award winning DelFly Micro is, until the current day, the smallest and lightest member of the DelFly project. It was awarded the smallest air vehicle capable of carrying a camera and broadcasting life video in 2009 [Guinness Book of Records, 2008], with a mass of only 3.07 gram and a wing span of 10cm.

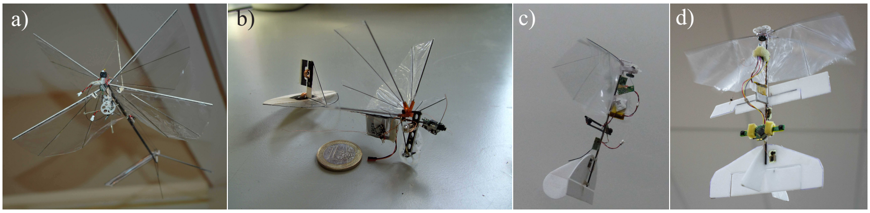

Figure 1.9: Different DelFly versions that have been developed and flown: a) DelFly I; b) DelFly Micro; c) DelFly II with stereo-vision payload; d) DelFly Explorer with ailerons.

The DelFly II is without doubt the most renown and replicated design of the DelFly family, being the platform of study of this thesis. It combines a series of optimizations made from numerous studies, that spanned from wing shape and flapping mechanism re-design [Bruggeman, 2010], wing optimization [De Clercq et al., 2009], CFD simulations [Noyon et al., 2014; Tay et al., 2015], and experimental PIV aerodynamic characterization [Percin et al., 2012a].

The wing configuration, with the four wings displaced in 'X', and small dihedral are close to optimal because: (1) it maximizes lift generation through clap-and-peel aerodynamic mechanism; (2) it simplifies the flapping mechanism, which has only one active degree-of-freedom responsible for the flapping motion; (3) the wing leading edge is the only part of the wing that is mechanically activated by the flapping mechanism, allowing for simple passive rotation of the wings, combining wing flexibility, inertia and aerodynamic forces; (4) the enhancement of lift generation allows for a reduced flapping frequency for hover (≈12Hz) and a reduction in the wing span needed for lift generation; (5) it minimizes the oscillating motion of the body that is induced by the wing flap due to the counteracting movement of the upper and lower wings; (6) the dihedral augments lateral-directional stability. In addition, (7) the tail makes the platform stable in both hover and free-flight configuration.

The wings are made from 10μm Mylar foil, with a 'D' shaped 2 mm section carbon rod, used for the leading edge and main spar, tensioned with two 0.1 mm thin carbon wire stiffeners. The tail can be made from the same Mylar foil, tensioned with carbon rods. However, for durability, ease of assembly and visual cueing the tail is typically made from Styrofoam. Having a dihedral of 15°, the wings open to have a maximum angle of 90° between them, thus having a flap angle (ζ)[1] of 45° per wing. The wing pitch

---

[1] In the course of the dissertation, the flap angle term will replace the previously introduced sweeping term, since we refer to flapping as a combination of sweeping and pitching motions, with the flap angle being defined as ζ.

angle around the leading edge (θ_w) is of ±45°. The elevator (δ_e) and rudder (δ_r) typically deflect up to ±25°and ±40°respectively. Further details of the DelFly are presented in Chapter 2.

1.5 RESEARCH FRAMEWORK

1.5.1 MOTIVATION

Despite the capabilities of the DelFly II and the numerous studies conducted for further optimization, it was developed using a top-down approach. This means the studies focused on the development of the DelFly using a general comprehension of the phenomenological behavior of flapping wings, combined with innovative ideas. The models were tested through trial-and-error and experimentation, being developed with the goal of having a controllable and highly maneuverable platform. The knowledge that was gathered around the platform in terms of wing design, tail configuration and detailed aerodynamic mechanics obtained from PIV [Percin et al., 2011, 2014] and CFD [Noyon et al., 2014; Tay et al., 2015] studies focus on a fundamental understanding of the aerodynamics. Such studies focused on the testing and simulation of specific flapping conditions, with a particular focus of the hover flight condition and neglecting the tail presence, being performed on rigidly attached DelFly models.

Although providing a good insight into the aerodynamic mechanisms of wing force generation of the DelFly, the previous studies did not address the effect of such mechanisms on the dynamics of the DelFly. As a result, the lack of information about the behavior of the DelFly in free-flight limits the development of models that could be used for dynamic simulation and model based control. Furthermore, the knowledge about the interaction between the aerodynamics and the kinematics of flight would allow for the prediction of the impact of different design parameters already at the design phase of a new version of the system.

The DelFly can be flown with relative ease around a trimmed flight condition that is close to hover. It benefits from having a very broad flight envelope, ranging from hover to fast forward flight up to 7m/s, being extremely maneuverable if flown manually by a person. The current lack of knowledge of the system limits both the current use and the development of the DelFly, as it can only be flown automatically around one trimmed condition, where linear proportional-integrative-derivative (PID) controllers are effective.

At an experimental level, the innovative concept of the DelFly complicates the design of proper experimental methodologies that will allow for the understanding of the mechanisms of flight and their connection with the stability and dynamics of the system. As mentioned before, viz. Section 1.3, theoretical and technological bottlenecks limit the studies. Free-flight testing, for example, is limited by a number of conditionings, especially related to the correct design of the inputs that are performed during flight, the data gathering requirements, repeatability and statistic validity of the data, as well as the flight path reconstruction methodologies. In particular, until the beginning of this work, very little was known about the DelFly's flight regimes and envelope, as well as about the system identification requirements of such exotic platform configurations. Regarding the latter, little was known about how inputs and maneuvers should be performed on the DelFly to properly excite the dynamic modes and collect the needed dynamic information for modeling. Moreover, there was no knowledge about the requirements for the tracking system in terms of resolution and sampling frequency, limitations of onboard sensors, e.g., resonating frequency of accelerometers.

Despite the advantages of free-flight testing, such methods are still limited to the technological capabilities of both the flight test arenas and the onboard sensors. Furthermore, extracting forces from free-flight data requires considerable sensor fusion and state reconstruction, which are, in turn, all affected by the kinematic model that is derived or selected to describe the system.

To avoid the technological limitations associated with free-flight testing, other test methodologies can be performed, viz., tethered testing in a wind tunnel and collecting directly measured forces using high sensitivity force balances. However, the previous knowledge of wind tunnel testing is very limited for such flapping platforms, since the cyclic nature of flapping flight induces dynamic oscillations that are not captured in fixed-base experiments, as well as the excitation of the body eigenmodes that can corrupt the collected data. Another limiting factor of bench testing is the lack of knowledge about the test points that represent actual flight conditions of the flyer in free-flight. Such conditions are very difficult to obtain and predict in the absence of free-flight data.

The aerodynamic models of ornithopters created so far are either too complex to be used on board small flapping vehicles or too simple to fully explore the vehicle's potential. Additionally, these models have to be adapted to the physical properties and kinematics of the FWMAV to predict the vehicle's dynamics. This way, the development of a model that could be used for both simulation and for automatic flight control of an FWMAV is much needed. Such a model would allow an FWMAV to be programmed to perform automatic flight and fully explore its capabilities.

1.5.2 RESEARCH OBJECTIVES

The current work addresses the existing knowledge gaps and focuses on the development of dynamic and aerodynamic models of a specific FWMAV – the DelFly II – using system identification and force reconstruction techniques. This poses as an extra challenge since the DelFly FWMAVs are too small to be properly equipped with accurate sensors to measure the states that are needed to completely describe its aerodynamics, e.g., total pressure, velocity, or angle of attack. In addition, as discussed in the previous section, very little was known about the flight envelope the DelFly II and the characterization of the forces and dynamic behavior during free-flight. This thesis, therefore, aims at addressing the previous knowledge gaps by answering to the following research question:

Research Question

How to develop physically representative dynamic models of clap-and-peel flapping wing micro aerial vehicles using free-flight and wind tunnel experimental methodologies?

The research question is further divided in six thesis objectives, which are addressed in each of the dissertation Chapters:

Objective 1 To characterize the flight regimes of the DelFly II FWMAV from free-flight data, using flight path reconstruction techniques and share this high quality data with the community to be used for further modeling and development.

Objective 2 Assess the impact of simple single rigid body kinematics, as opposed to complex multi body kinematic formulations in the reconstruction of aerodynamic forces and moments of an FWMAV.

Objective 3 Compare free-flight with fixed-base wind tunnel testing methodologies for the characterization of the aerodynamic forces acting on a FWMAV and analyze the impact of different force reconstruction methods on the accuracy of the obtained forces.

Objective 4 Assess the applicability of linear aerodynamic model structures in the development of computationally efficient aerodynamic models of the DelFly II.

Objective 5 Develop a physically representative model of the clap-and-peel force generation mechanism of the DelFly II.

Objective 6 Provide recommendations on the methods that should be used to model a general class of clap-and-fling FMWAVs.

1.5.3 RESEARCH SCOPE

The present thesis uses a data driven and system-theoretical approach to the modeling of the dynamics and aerodynamics of the DelFly II FWMAV, from free-flight data and wind tunnel data. It focuses on obtaining a rigorous understanding of the flight envelope of the DelFly II by performing flight path reconstruction of 168 flight tests. The study deliberately focuses on the understanding of the global principles of flapping flight of the DelFly II, viz. flight envelope, multi-rigid body kinematics, global linear aerodynamic modeling and quasi-steady aerodynamic principles, as opposed to the study of particular flapping regimes, complex flexible kinematic models and fundamental aerodynamics, e.g., PIV flow field studies.

Modeling the DelFly kinematics with flexible structure kinematic formulations would result in complex mathematical models of the wings and, consequently, in inefficient and DelFly-specific models. To avoid this complexity and allow for the development of efficient kinematic models, only single and multi-rigid body formulations will be considered in this dissertation, since they still replicate most prominent kinematic parameters of the wing flap, viz. flap angle, wing pitch angle and wing torsion.

Flight path reconstruction techniques will be thoroughly studied and compared to wind tunnel measurements, with the goal of understanding the influence of different state reconstruction techniques, e.g, time vs. frequency differentiation, filter designs, effect of sampling frequency and resolution of the data. In terms of wind tunnel testing, this research focuses on understanding the effects of clamping and natural eigenmodes on the measured forces.

Instead of nonlinear or black-box complex strategies, or fundamental characterization of the flow field, the research on developing global linear aerodynamic models using a gray-box approach, with physical insight and time-resolved nonlinear time-varying models of the DelFly unsteady aerodynamics, using quasi-steady aerodynamic principles.

1.5.4 RESEARCH APPROACH

Three experimental methodologies are used: (1) free-flight testing of the FWMAV in a flight chamber equipped with high-resolution position tracking cameras; (2) wind tunnel testing of the FWMAV at conditions that replicate the flight regime of the DelFly; (3) flapping in vacuum conditions.

The free-flight testing involves specific maneuver input design. This results in a batch of Koehler-like [Malne and Iliff, 1986; Jategaonkar, 1997] identification maneuvers that are pre-programmed into the ornithopter's autopilot to assure repetition of the maneuvers and maximize the dynamic and aerodynamic information. The position, attitude and the control inputs of the FWMAV are recorded by a high precision external visual tracking system and used to compute all the needed states for aerodynamic force and moment reconstruction.

Wind tunnel experimental methods are used to directly measure the time-resolved unsteady aerodynamic forces acting on the DelFly during flapping motion. This methodology involved attaching the FWMAV to a fixed-base and the recording of the aerodynamic forces using a high precision force transducer – ATI Nano17. It allows for the validation of the longitudinal forces that act on the ornithopter and the assessment of the quality of both free-flight and wind tunnel experimental techniques, needed for system identification purposes.

The vacuum experiments are used to further understand the impact of the kinematic and inertial forces on the total forces measured directly using a force transducer. These experiments replicate the flapping frequency of the DelFly in hover, and allows for the characterization of the frequency content of the kinematic and aerodynamic contributions during flapping motion.

After validating the forces obtained from experimental methods, physical insight and recursive methods are used to define a first set of Linear Time Invariant (LTI) aerodynamic model structures. Such structures are divided in two categories: (1) a full model that uses all states reconstructed from free-flight data for simulation purposes; (2) a reduced model that only considers the states that could be obtained from onboard sensors, for onboard model based control purposes. Residual analysis and correlation techniques are used to assess the quality of the models.

To further clarify the flapping force generation mechanisms of the DelFly, quasi-steady aerodynamic principles are used to develop a data-informed nonlinear time-varying model of the longitudinal aerodynamic forces that act during flight. Both a local (per flight regime) and a global aerodynamic (flight envelop applicable) model of the forces are developed. The parameters are identified from the real force data acting on the DelFly using Maximum Likelihood optimization methods, and validated using the free-flight data.

1.6 DISSERTATION OUTLINE

The dissertation is divided in two parts. Part I encompasses Chapters 2, 3 and 4, and concentrates on the experimental methodologies and data processing techniques used to reconstruct the states, inputs and aerodynamic forces and moments that acted on the DelFly II during free-flight. Part II, which includes Chapters 5 and 6, focuses on the aerodynamic modeling the DelFly using the results of Part I. An illustration of the dissertation outline is presented in Figure 1.10. The Chapters 3 to 6 were published in scientific journals and are presented in such a way to allow for the reading as a self-contained study. The Chapters are structured as follows:

Chapter 2 addresses the free-flight experiments that have been conducted. It presents the properties of the two DelFly versions that were used in the free-flight tests, the maneuver input design, and the considerations for free-flight testing of the FWMAV. Furthermore, it discussed the methodology used for the reconstruction of the states and inputs from the position data.

Chapter 3 discusses the impact of the kinematic modeling approach in the reconstruction of the external forces and moments that act during free-flight. It is argued that general aircraft equations of motion, that consider a single rigid body model, might result in incomplete flapping forces being extracted from free-flight data. To understand the impact of such an approach it is compared with a multi-rigid body kinematic formulation. The study indicates that the single rigid body kinematic model is sufficient to extract the aerodynamic forces and moments acting during free-flight, for a group of FWMAV configurations, in which the DelFly II is included.

Chapter 4 further studies the impact of experimental techniques on the forces reconstructed from externally measured 3-dimensional position data. This was done by comparing the forces obtained from free-flight data with the forces directly measured in wind tunnel and vacuum setups at the same flapping frequencies, using a high-resolution force transducer. Specifically for free-flight testing, this Chapter thoroughly studies the impact of data resolution, sampling frequency and numerical differentiation techniques in the final reconstructed forces. Furthermore, considerable changes in the directly measured forces were found for different positions of the clamping of the FWMAV in the wind tunnel experiments. As a result, a thorough study was done to assess the impact of the clamping position and the nature of the different measured forces, before comparing with the free-flight results. It finalizes with detailed considerations on how to perform aerodynamic force reconstruction of both experimental techniques: free-flight and wind tunnel.

Chapter 5 studies the applicability of linear time-invariant data-informed aerodynamic models for the modeling of the aerodynamic forces and moments acting during free-flight. Two models were developed using: (1) all the states and inputs reconstructed from free-flight data; (2) the states and inputs that would be available from onboard sensors. The unknown parameters were estimated using least-squares regression, under the assumption of uncorrelated residuals between the model results and the force data. The models proved to represent the aerodynamic forces with great accuracy. Despite not having the same accuracy, the models showed a good agreement of the aerodynamic moments. Finally, a dynamic simulation of the FWMAV numerically integrated the aerodynamic and dynamic models to propagate the states of the DelFly in time, comparing them with the real free-flight measurement. The results revealed a close approximation of the flight path for only a small period of time (0.5sec), indicating possible use for onboard model based control strategies.

Chapter 6 assesses the applicability of nonlinear time-varying aerodynamic models, addressing the time-resolved unsteady forces at sub-flap time scales using quasi-steady aerodynamic principles. The longitudinal forces resulting from the flapping of the wings are modeled and identified. The model builds on pre-existing theory on flapping wings and further expands it to incorporate both the wing kinematics and the clap-and-fling aerodynamic mechanism, through the inclusion of a fling circulatory term. The model parameters were estimated using a Maximum Likelihood method. Furthermore, a global aerodynamic model is developed using a linear evolution of the estimated parameters across the most important regimes of the DelFly II flight envelope, from hover to 2m/s. The Chapter finalizes with the validation of the model using free-flight forces, concluding that the developed aerodynamic model reproduces the acting unsteady aerodynamic forces with great accuracy.

Chapter 7 addresses the main contributions of the dissertation, by discussing the main findings of each Chapter and answering to the research question. It finalizes issuing a set of recommendations and proposing future work on the area of FWMAV model identification.

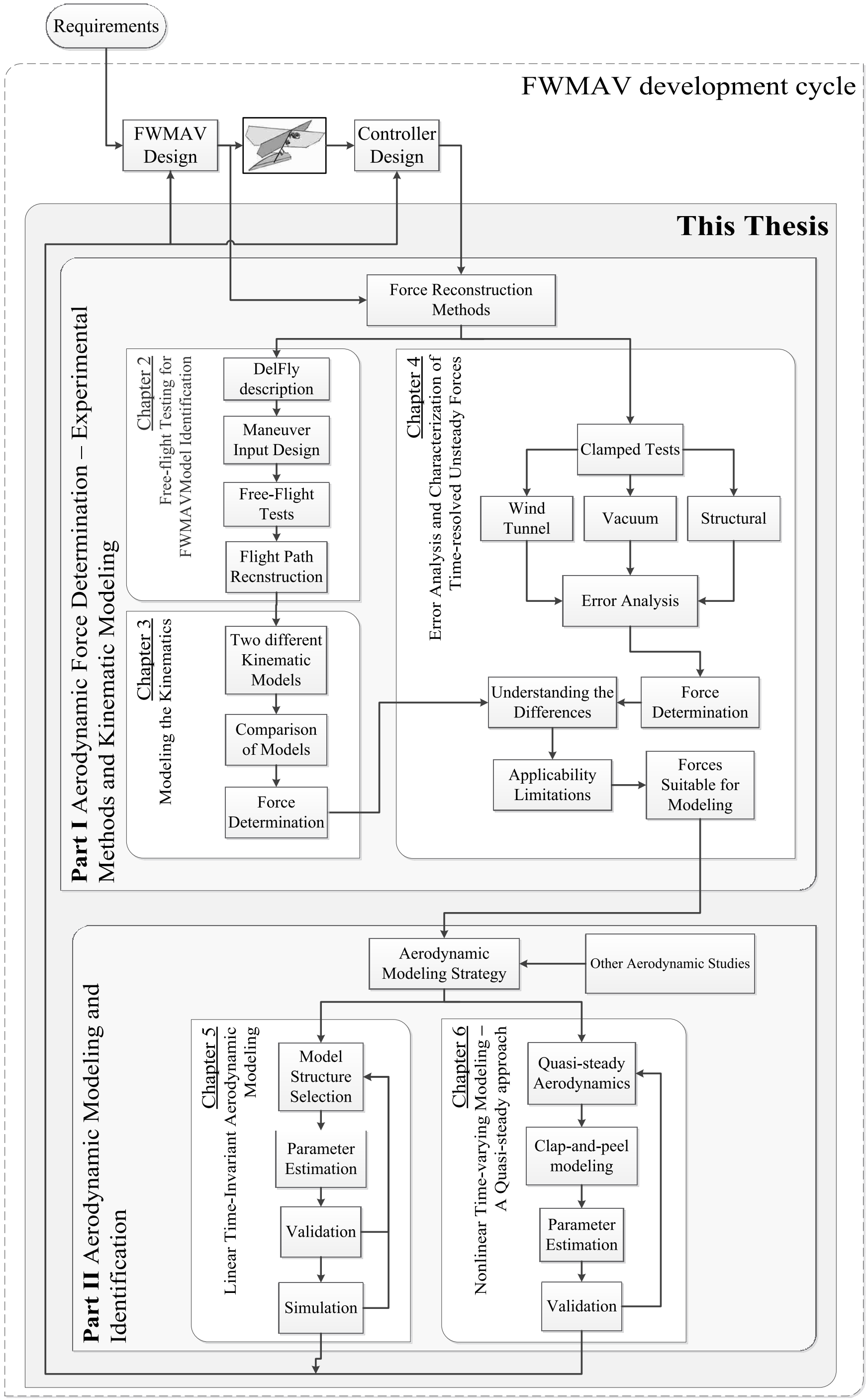

Figure 1.10: Flowchart with the outline and content of the dissertation.

I

AERODYNAMIC FORCE DETERMINATION – EXPERIMENTAL METHODS AND KINEMATIC MODELING

2

FREE-FLIGHT TESTING FOR FWMAV MODEL IDENTIFICATION

To follow a systematic and data driven approach to the modeling of the aerodynamics and kinematics of the flapping wing micro aerial vehicle, it is necessary to first obtain the aerodynamic forces and moments that act on the vehicle during flight. In this regard, the current chapter details the experimental methodology used to perform free-flight tests with the DelFly II. In particular, it presents the FWMAV version, the experimental setup and the design of the input commands that were specifically programmed into the autopilot of the FWMAV to perform free-flight maneuvers inside a flight chamber, which was equipped with a high resolution visual tracking system. Additionally, the flight path reconstruction methods that were used for state and input determination are explained, and a first assessment of the quality of the position data is presented. All position data, reconstructed states, inputs, forces and moments are provided as Matlab loadable files in digital format. Furthermore, an Excel sheet with the description of all tests that were performed in the free-flight experiments is shared along with the data.

This chapter is based on the following three publications: Caetano, J. V., de Visser, C. C., Remes, B. D. W., de Wagter, C., and Mulder, M. (2013b). Controlled flight maneuvers of a Flapping Wing Micro Air Vehicle: a step towards the DelFly II Identification. In *AIAA Atmospheric Flight Mechanics Conference*, number 2013-4843; Caetano, J. V., de Visser, C. C., Remes, B. D. W., de Wagter, C., and Mulder, M. (2013c). Modeling a Flapping Wing MAV: Flight Path Reconstruction of the DelFly II. In *AIAA Modeling and Simulation Technologies*, number 2013-4597; Caetano, J. V., de Wagter, C., Ruijsink, R., Remes, B. D. W., Beran, P. S., and de Visser, C. C. (2016). Free-flight Data of a Flapping Wing Micro Air Vehicle for System Identification. *IEEE Transactions on Robotics*, (submitted).

2.1 INTRODUCTION

Understanding the principles of flight of flapping wing flying species, and applying them to small robots could lead to the systematic design of a new, faster and more agile FW-MAV, capable of extreme maneuvering, stealth flying and perching maneuvers. However, only a very small number of research groups have been able to develop bio-inspired flight capable robots. This is justified by both the inherent difficulty of mimicking nature's fliers, as well as the considerable investment needed for such developments and testing facilities. Furthermore, the reliability of the flight testing and system identification of such robots has been shown to be limited by the inability to perform repeated and automated test maneuvers, since most of the ornithopters have to be flown by a human pilot [Grauer et al., 2011; Lim et al., 2012].

The present Chapter aims at providing the community with flight data of a free-flight capable autonomous flapping wing air vehicle that represents on of the most commonly used design of such robots across the community [Groen et al., 2010; Baek, 2011; Prosser, 2011; de Croon et al., 2012; Nakata et al., 2011; WSU, 2012; Hsiao et al., 2012; Percin et al., 2012b; Deng et al., 2014; Rose and Fearing, 2014; Nguyen et al., 2015]. In particular, this Chapter presents the methodology used to collect the position data of a free-flying DelFly II. It starts by presenting the DelFly version that was used, the experimental setup, the flight chamber details and the maneuver input design. It then progresses with the initial description of the flight path reconstruction techniques that were used to obtain the flight states and inputs from the three-dimensional position data that was recorded during the flight tests. It finalizes with an initial assessment of the accuracy of the data and the presentation of the reconstructed states[1].

2.2 SYSTEM OVERVIEW

2.2.1 THE FLAPPING WING MICRO AIR VEHICLE

A version of the DelFly II was used for data gathering. This robot has a weight of 17 grams and a wing span of 274mm, and is configured with four wings in 'X' form, with a dihedral of 15°. The wings are made from 10μm Mylar foil, tensioned with a leading edge D-shaped carbon rod and two thin mid-wing stiffeners, as shown in Figure 2.1. The geometric data of the wing and tail of the DelFly are presented in Figure 2.2.

The flapping motion is controlled by a small brushless out-runner motor, connected to the flapping gear mechanism made from injection molded plastic placed in front of the ornithopter. During flap, the upper and lower wings perform a motion described as clap-and-peel [de Croon et al., 2012] – a type of motion characterized by the contact of the wings at the end of the in-stroke (clap), followed by a pronation of the wing surface around the leading edge which, aided by the wing flexibility, results in a wing separation that resembles a 'peel'.

Since the initial discovery of this mechanism by Weis-Fogh [1973], other studies, e.g., Ellington [1984a]; Spedding and Maxworthy [1986]; Sane [2003]; Miller and Peskin [2005] have shown that such clap-and-peel wing beats result in an average lift force net gain between 6% and 50% of the force produced by the same wings in a non-interacting motion. In terms of application to FWMAV, such mechanism presents advantages over two-

---

[1] It is worth noting that the detailed free-flight data error analysis is described in Chapter 4

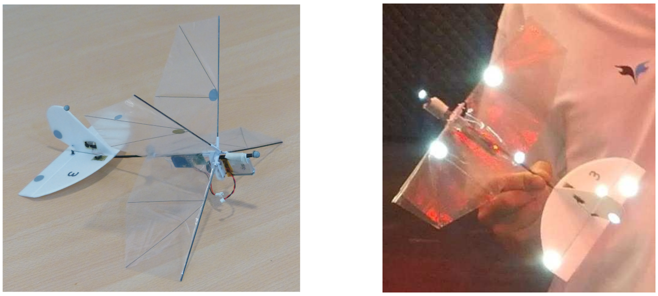

(a) Photograph of the robot with wings in open position.

(b) Retro-reflective markers placed on the robot, with wings closed.

Figure 2.1: DelFly version used in this dissertation – configuration 3, for fast forward flight with battery in front of wings, cf. Table 2.1.

winged robots, namely: a) it reduces the complexity of the wing flap mechanism to only one actively controlled degree of freedom (DOF), which is the flap around the fuselage, and a passive pitching motion around the leading edge; b) it reduces the flapping frequency needed for sustained flight; c) it reduces the flap-induced vibration and body oscillations due to the force balancing movement of upper and lower wings; d) a gain in net lifting force due to the clap-and-peel; e) the dihedral adds lateral and directional stability to the FWMAV in forward flight.

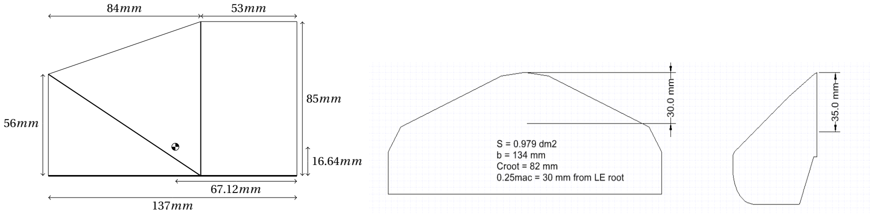

(a) Wing schematic.

(b) Horizontal and vertical tail schematic.

Figure 2.2: Schematic of the DelFly wing and tail. Drawings are not in scale.

The main body of the ornithopter is made from a square 2x2mm section carbon rod. It is configured with a conventional inverted ‘T’ tail, which introduces static stability, as well as a decoupling of the control inputs from the wings, allowing for longitudinal and lateral control directly from the elevator and rudder commands. The tail is made from Styrofoam, for resistance and visual referencing during flight.

In such flying platforms, the velocity envelope at which the ornithopter is still controllable can be adjusted by the location of the center of gravity (CG). In particular, moving the CG forward, closer to the nose, increases the forward flight velocity of the vehicle; moving the CG further back, towards the tail, reduces the average velocity, to the limit of the hover case. This way, a careful selection of the CG is needed to adjust to the type of mission or to the maneuver one wants to perform for system identification purposes .

To cover the full flight envelope of this platform, four CG locations were used, as described in Table 2.1. The configurations change in small aspects like total mass, inertia, distance of tail to the wings and distribution of avionics. The fast forward flight configuration differs from the slow flight one by having a slightly heavier battery placed in front of the wings (cf. Figure 2.1) for the adjustment of the CG and, consequently, a different marker location. In terms of hardware the robots were equipped with: a) an autopilot that used a bi-directional InvenSense IXZ-500 analog gyroscope with a sampling rate of 9kHz – the axes were positioned to measure pitch and yaw rates; b) an Atmel AVR ATMega8PA micro-controller running at 8Mhz, with a 3.3V power supply; and a radio control receiver for manual flying; c) 180mAh 1S Lithium Polymer battery; d) a brushless out-runner motor; e) a 1x1x0.25mm Hall effect sensor for flapping gear rotational speed measurement. The flapping frequency was controlled using a proportional–integral (PI) controller. The presented configurations are capable of performing sustained flight at velocities that range from hover to 7m/s.

2.2.2 EXPERIMENTAL SETUP

A position tracking system was used to capture the position of eight retro-reflective markers (see Figure 2.1), placed on the FWMAV, in free-flight in 3D space at a frequency of 200Hz. The position of the markers was such that no plane of symmetry could exist between them, to avoid the loss of orientation and attitude from the tracking system. The markers that were placed at the nose, wing trailing edge (at the center of the robot) and on the vertical stabilizer were spherical, with a diameter of 5mm. The remaining markers were made of circular flat retro-reflective tape and were placed: a) at the wing stiffener intersection, to be less prone to bend due to wing flexibility; b) at the horizontal stabilizer, near the left extremity and adjacent to the elevator hinge; c) on the elevator, close to the right extremity and adjacent to the elevator trailing edge; d) on the rudder, close to the trailing edge. It is worth noting that the small size of the robot limits the distance between the reflective markers, and only eight were placed on the robot. Using more markers, with a smaller distance between them, would lead to a frequent ‘marker swap’ or ‘marker fusion’ in the tracking system, resulting in unusable data.

The flight chamber[3], presented in Figure 2.3, was equipped with 60 Vicon cameras, displaced in a total volume of (22x17x10)m^3, which allows for submillimeter precision of the position measurements [Caetano et al., 2015c] for such platforms. For more information on the testing facilities, the reader is referred to Laboratory [2015].

2.2.3 EXPERIMENT DESIGN

System identification of flying platforms requires for specific maneuvers to be designed and carefully executed. In particular, step, doublet and triplet (2-1-1)[4] inputs were designed and programmed into the autopilot to be performed during flight for all four

---

[2] CG location is measured from the wing leading edge, at wing hinge, along $\boldsymbol{x_b}$ axis. The Inertia tensor was obtained from a CAD model of the DelFly.

[3] Located at the United States Air Force Research Laboratory Micro Air Vehicles Integration and Application Institute, at Wright-Patterson AFB.

[4] Based on the 3-2-1-1 ‘Koehler’ [Malne and Iliff, 1986] maneuver performed on aircraft.

Table 2.1: Inertia and Geometric Properties of the DelFly used in this dissertation [2].

		Property	**Configurations 1 & 2 Slow Flight** ($V \leq 1m/s$)	**Configurations 3 & 4 Fast Flight** $V \geq 1m/s$
FWMAV		Total Mass (g)	17.4	18.4
	CG 1	CG (x_b, y_b, z_b) [mm]	(-70.4, 0.0, 2.0)	(37.1, 0.1, 0.2)
		x_{CG} [% root chord]	83	44
		(I_{xx}, I_{yy}, I_{zz}) [kgm^2]	(1.340, 6.718, 6.953)E-5	(0.250, 2.498, 7.372)E-4
	CG 2	CG (x_b, y_b, z_b) [mm]	(63.1, 0.0, 2.0)	(-37.1/35.6, 0.1, 0.2)
		x_{CG} [% root chord]	74	42
		(I_{xx}, I_{yy}, I_{zz}) [kgm^2]	(1.23, 9.644, 9.898)E-5	(0.194, 2.872, 7.974)E-4
Single	**Wing**	Mass (single) [g]	0.29	
		Span [mm]	137	
		Root chord [mm]	85	
		Tip chord [mm]	56	
		Surface [dm^2]	1.05	
		Dihedral [°]	15	
		Angle between wings [°]	[0,90]	
Horizontal	**Tail**	Mass (no electronics) [g]	1.22	
		Span [mm]	134	
		Total surface [dm^2]	0.979	
		Elevator chord [mm]	24	
		Distance of LE from nose [mm]	148	137
		Incidence [°]	-3.4	-4.2
		Elevator deflection [°]	[-18,24]	[-21,22]
Vertical	**Tail**	Mass (no electronics) [g]	0.28	
		Height [mm]	54	
		Total Surface [dm^2]	0.275	
		Rudder chord [mm]	34	30
		Distance of LE from nose [mm]	148	137
		Rudder deflection [°]	[-19,46]	[-42,43]

Figure 2.3: Image of flight chamber where the DelFlys were flown.

Table 2.2: Inputs that performed in each control surface.

Longitudinal	**Lateral-Directional**	**Longitudinal-Directional**
Elevator Up	Rudder Right	Elevator Up + Rudder Right
Elevator Down	Rudder Left	Elevator Up + Rudder Left
Throttle Up	-	Elevator Down + Rudder Right
Throttle Down	-	Elevator Down + Rudder Left
-	-	Rudder Right + Elevator Up
-	-	Rudder Right + Elevator Down
-	-	Rudder Left + Elevator Up
-	-	Rudder Left + Elevator Down

robot configurations, for the different control surface inputs, i.e., elevator, rudder, flapping frequency (throttle), with different combined input sequences, detailed in Table 2.2. The inputs were programmed to be performed for the exact duration of 1/3sec per wave for the case of step and doublet inputs, and 2/3sec for the first wave of the 2-1-1 triplet, that would result in a 4/3sec total input duration (cf. Figure 2.4)[5]. A full deflection of the control surface was configured for the elevator and rudder inputs; throttle was set to increase to maximum power or reduce to half-trimmed flight power, for increase and decrease in the throttle, respectively.

It was not possible to perform automated maneuvers for the fast forward flight configuration, as the robot would then cross the room and hit the walls during a longer maneuver. Instead, the robot was flown by hand using a radio controller and different maneuvers were performed, e.g., climb at maximum flapping frequency, descent with very low flap frequency, gliding flight, turns and loopings, for the assessment of performance and characterization of full flight envelope.

2.3 DATA PROCESSING

A total of 233 flight tests were performed, with an average duration of 17sec per test. Tests of more than 30 seconds could result in total information loss, due to a high processing

---

[5] six video files accompany the manuscript showing doublet and triplet maneuvers during the flight tests (camera footage) and flight path reconstruction animations.

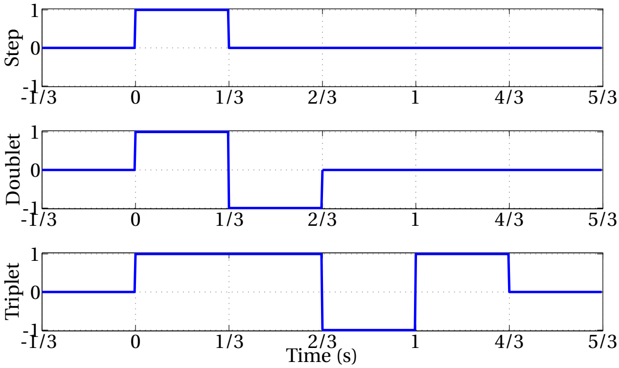

Figure 2.4: System identification commands performed on the control surfaces.

effort of the tracking system. In one of the tests, the DelFly was able to fly for 22 minutes and 33 seconds in a quasi-circular trajectory, covering almost 7 kilometers with a total battery consumption of 0.166Ah. This latter test aimed at determining the flight time for the maximum traveled distance in fast forward flight – the CG was at 44% of the root chord for this test (configuration #3 in Table 2.1). The test was performed continuously but recorded in parts, corresponding to tests #133 to #139 of the shared data.

2.3.1 FLIGHT PATH RECONSTRUCTION

The data contains the position of the eight retro-reflective markers, at 200Hz. From this data it is possible to reconstruct the full flight path of the FWMAV and obtain the states during the maneuvers[6]. Figure 2.5 presents the relative position of the markers after processing the flight data.

Despite the advances on the autopilot equipping the DelFlys, it was not possible to record the information from the onboard sensors. Additionally, it was also impractical to down-link the onboard sensor information and synchronize it with the flight chamber information due to security protocols. As a result, no data fusion was possible for the reconstruction of the states and inputs, hindering the application of more complex and accurate flight path reconstruction techniques. In effect, the states and inputs were reconstructed from the position of the eight markers, using the methods detailed below.

Please note that the current Chapter aims at presenting the flight path reconstruction methodology that was concluded to be the most reliable during this research project. It focuses on introducing the states and inputs that can be reconstructed from high resolution three-dimensional position data, showing only an example of the factors related to the flight regime and maneuver that affect the accuracy of the data. The details about the impact of different criteria and data processing methods, e.g., kinematic model, numerical differentiation scheme, are detailed in Chapter 3 and Chapter 4.

Three right-handed reference frames were defined for state reconstruction and are

---

[6] All processing was done using Matlab2012b.

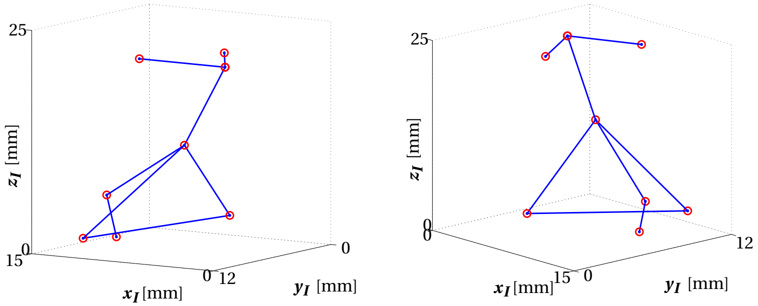

(a) View from bottom-right.

(b) View from top-left.

Figure 2.5: Reconstructed marker position of robot – markers connected by line.

presented in Figure 2.6: (1) Inertial reference frame, $(\boldsymbol{x_I},\boldsymbol{y_I},\boldsymbol{z_I})$, aligned with the flight chamber, with $\boldsymbol{x_I}$ and $\boldsymbol{y_I}$ coplanar with the ground, and $\boldsymbol{z_I}$ pointing up, forming an orthonormal frame; (2) the Body reference frame, $(\boldsymbol{x_b},\boldsymbol{y_b},\boldsymbol{z_b})$, with $\boldsymbol{x_b}$ aligned with the carbon rod of the body of the FWMAV, pointing forward; the $\boldsymbol{y_b}$ axis is defined from the CG to the right wing direction and is coplanar with the tail plane; the $\boldsymbol{z_b}$ axis forms and orthonormal frame, perpendicular to $x_b y_b$ plane, pointing down; (3) the Wing reference frame $(\boldsymbol{x_w},\boldsymbol{y_w},\boldsymbol{z_w})$, similar to the Body reference frame, but rotating with the wing – left wings have the $\boldsymbol{y_w}$ pointing to the left, in the direction of the wing tip and $\boldsymbol{z_w}$ is pointing up.

The orientation of the FWMAV is obtained by transforming the vectors from the inertial to the Body frame, using a 3-2-1 rotation, that follows *yaw* $(\psi) \longrightarrow$ *pitch* $(\theta) \longrightarrow$ *roll* (ϕ) order. The Euler (ϕ, θ, ψ) angles are calculated from the comparison of the entries of Eq. 2.1[7], where the lines of the first matrix are the normalized coordinates of the Body frame written in the Inertial frame coordinates. However, these angles present limitations: a) the pitch angle is only defined from $]-\frac{\pi}{2}, \frac{\pi}{2}[$; b) the values of yaw and roll angles can be misleading at high pitch angles, which results in errors when determining angular rates from Euler angles. To avoid such limitations, new attitude angles $(\phi_r, \theta_p, \psi_y)$ were computed with θ_p defined from $]-\pi, \pi[$ and the body angular rates were computed using quaternions. Detailed results of this conversion are presented in 5.2 in Chapter 5.

Velocities and accelerations (both linear and angular) were calculated by using a 3-point central difference numerical differentiation. This method was shown to be the best option to maximize signal-to-noise ratio and minimize the low-pass filtering effect of numerical differentiation, as demonstrated in Chapter 4 [Caetano et al., 2015c]. Linear velocities and accelerations were obtained from the CG location of the robot and the angular accelerations were determined from the angular velocities. Total angle of attack (α) and side-slip angle (β) were calculated under the assumption of undisturbed air, not considering flap-induced local flows (cf. Figure 2.6). The inputs were reconstructed from the relative marker position. In particular, six inputs were determined: flap angle (ζ),

---

[7] c and s replace the cos and sin functions respectively.

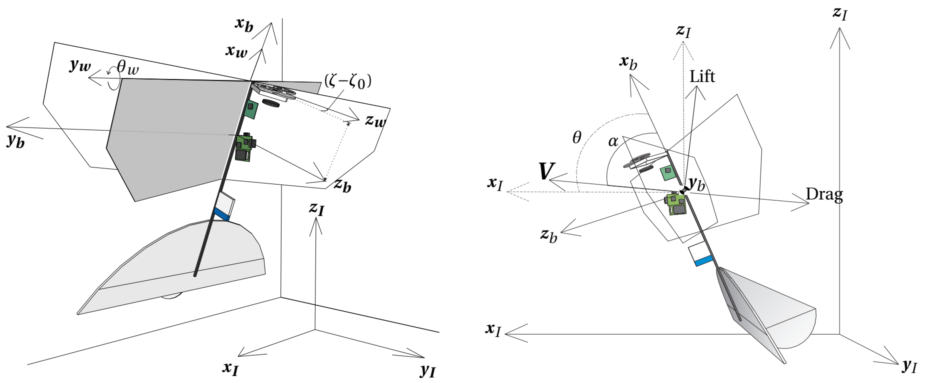

(a) Perspective view.

(b) Lateral view.

Figure 2.6: Schematic of the FWMAV in free-flight with representation of Inertial ($\boldsymbol{x_I}, \boldsymbol{y_I}, \boldsymbol{z_I}$), Body ($\boldsymbol{x_b}, \boldsymbol{y_b}, \boldsymbol{z_b}$) and Wing ($\boldsymbol{x_w}, \boldsymbol{y_w}, \boldsymbol{z_w}$) reference frames, Velocity ($\boldsymbol{V}$), pitch (θ), angle of attack (α), wing pitch (θ_w) and wing flap angle (ζ).

$$\mathscr{R}_{bi} = \begin{bmatrix} i_{b_x} & i_{b_y} & i_{b_z} \\ j_{b_x} & j_{b_y} & j_{b_z} \\ k_{b_x} & k_{b_y} & k_{b_z} \end{bmatrix} = \begin{bmatrix} c\theta c\psi & c\theta s\psi & -s\theta \\ c\phi c\theta c\psi - c\phi c\psi & c\phi c\psi + s\phi s\theta s\psi & s\phi c\theta \\ s\phi s\psi + c\phi s\theta c\psi & s\phi c\psi - c\phi s\theta s\psi & c\phi c\theta \end{bmatrix} \tag{2.1}$$

flap rate ($\dot{\zeta}$), flap acceleration ($\ddot{\zeta}$), flapping frequency (δ_f), elevator (δ_e) and rudder (δ_r) deflection. In the interest of clarity, all reconstructed states are listed in Table 2.3.

Figure 2.7 presents the position of the CG of the robot (Figure 2.7a) and command inputs, in the form of wing flap angle (ζ), as well as the elevator (δ_e) and rudder (δ_r) deflection angles, as a function of time (Figure 2.7b). Figure 2.7a presents the trajectory of the robot for a doublet input on the elevator, representing a sample of four seconds of test #25. The first part shows one second of horizontal leveled flight, followed by an elevator doublet input over $\frac{2}{3}$sec. This induced an oscillation around $\boldsymbol{y_b}$, that was damped after three seconds. The red and magenta parts in Figure 2.7a indicate the elevator deflection up (negative) and down (positive), respectively, as indicated in the middle plot of Figure 2.7b, at time=6sec. The blue star indicates the transition from negative to positive deflection on the elevator. The arrows along the trajectory indicate the $\boldsymbol{x_b}$ (black) and $\boldsymbol{z_b}$ (gray) body axes, being equally spaced of 0.2sec. The flight path is projected with a gray line on the $x_b y_b$ plane for better visualization. The loss of altitude during the maneuver is caused by the transition from forward to hovering flight, with the pitch angle surpassing 90°. This causes a reduction on the generated lift due to the lack of relative wind on the wings and tail. The downwards (positive) deflection of the elevator induces a pitch down movement and, consequently, a recovery in the attitude and altitude through a gain of forward velocity u.

Table 2.3: States and input commands reconstructed from flight data.

Quaternions	**Euler Angles** [rad]	**Attitude Angles** [rad]	**Euler Angle Rates** [rad/s]	**Velocities** [m/s]	**Accelerations** [m/s^2]
e_0	ϕ	ϕ_r	$\dot{\phi}$	u	$\dot{u}$
e_1	θ	θ_p	$\dot{\theta}$	v	$\dot{v}$
e_2	ψ	ψ_y	$\dot{\psi}$	w	$\dot{w}$
e_3					

Angular Rates [rad/s]	**Angular Accelerations** [rad/s^2]	**Flapping**	**Aerodynamic Angles** [rad]	**Inputs** [rad]
p	$\dot{p}$	ζ	$--$	δ_f
q	$\dot{q}$	$\dot{\zeta}$	α	δ_e
r	$\dot{r}$	$\ddot{\zeta}$	β	δ_r

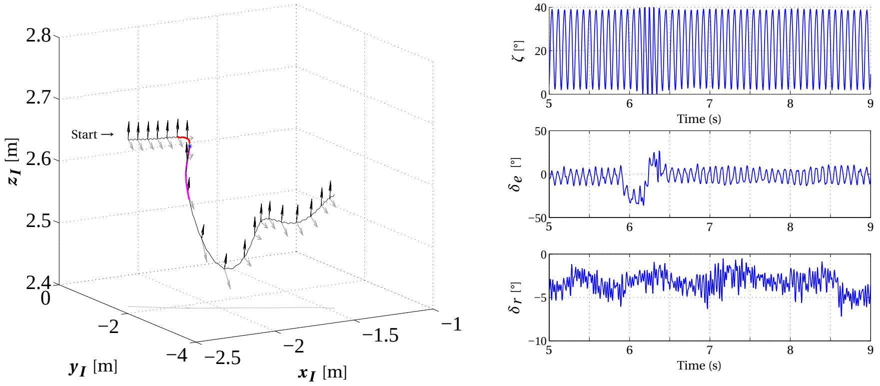

(a) CG position of the FWMAV in the Inertial reference frame during the flight test.

(b) Inputs: flap angle ζ; elevator angle (δ_e) and rudder (δ_r) angles.

Figure 2.7: Position and commanded inputs during elevator doublet maneuver, corresponding to 4sec of flight test #25.

2.3.2 INITIAL ASSESSMENT OF THE ACCURACY OF THE DATA

From the initial data, a total of 168 flight tests were considered valid, which results in a total of 28 minutes of usable flight time, across a multitude of conditions. From these, 147 files (approximately 25 minutes of flight) were recorded using the slow flight configuration, which corresponds to the typical flight regime of the ornithopter. A full description and characterization of each flight test is made available though the '*Flight_Test_Description.xlsx*' file.

An initial assessment of the impact of the flight speed and maneuver type on the accuracy of the system was done by calculating the relative distance between each pair of markers, at each time step, and compare it to the real physically measured[8] distance. It was concluded that the tracking system accuracy and inherent precision is affected by the DelFly's flight speed and attitude rate of change. In particular, fast forward flight velocities and abrupt maneuvers result in the loss of marker position or in a dilution of the precision of markers in 3D space.

Figure 2.8 presents an example of how a maneuver can significantly affect the accuracy of the position data, for three different flight tests – the magenta square in each subfigure indicates the starting point of the flight path. Here all subfigures present the trajectory of the DelFly, with the plot axes in meters. The colored bar below each plot indicates the error in the accuracy, in millimeters, corresponding to the difference between the recorded marker distance and the real physical distance.

Figure 2.8a shows the flight test for a doublet input on the elevator (test #25 of the data), where the velocities were small and there was no sudden attitude change – the errors here were below 1.2mm. However, for other tests some parts of the data were practically unusable, as illustrated in Figures 2.8b and 2.8c, where the speed and the fast maneuvers cause considerable errors, even when all the markers are present in the recorded data file.

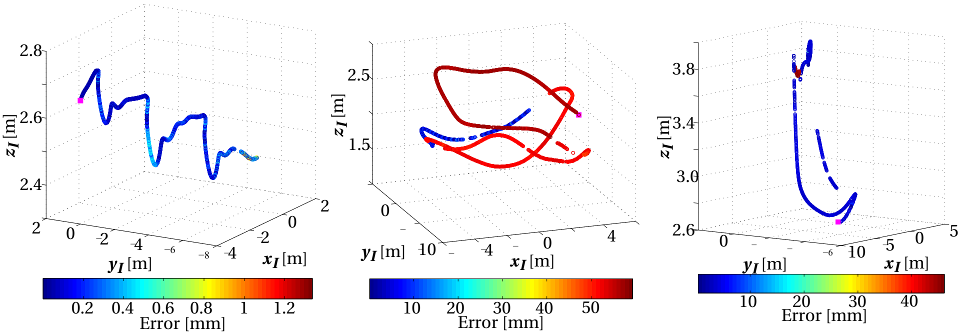

(a) Doublet elevator input; Average velocity of 1m/s; no considerable errors.

(b) Fast forward flight around the room; average velocity of 3.2m/s, with top speed of 4.8m/s when the tracking system loses some of the markers (end part of the dark red flight path).

(c) Fast forward flight with transition to hover; velocity from 3m/s to 4.2m/s before climbing; 0.5m/s at the top of the maneuver and increases to 4.5m/s at the descent (tracking system loses some markers).

Figure 2.8: Initial assessment of tracking system accuracy for three different flight regimes and maneuvers.

---

[8] Measurement was done using a caliper

2.3.3 RESULTS

In the interest of objectiveness, the results of the flight path reconstruction are presented for one flight test. More plots and respective discussion are presented in Appendix A. All outputs can be easily accessed on the *Data* folder provided with the dissertation. A detailed explanation of contents of the data is presented in Appendix F. The code used to calculate the outputs is made available under the *Code* folder. The content of this folder is also detailed in Appendix F.

As an example, a lateral doublet input (right-left) on the rudder is presented and discussed, which corresponds to test #32 . This test has an overall length of 12.9sec, where three similar doublet inputs were commanded. Only one of the input responses is shown, over a sample of 4sec of flight which includes a steady-state of 1sec, followed by the doublet input and 2.3sec of dynamic response, adding to a total duration of 4sec. All reconstructed states and aerodynamic terms presented in the current section were filtered using a Chebyshev type II low-pass filter, with a cut-off frequency of 40Hz, which was shown to maximize the signal-to-noise ratio, while still considering the aerodynamic components needed for system identification both in the time and frequency domain, as demonstrated in Chapter 4 [Caetano et al., 2015c]. Figure 2.9 shows the flight path of the robot during the maneuver, with its 3D position shown in the top plot and a 2D perspective of the height with time on the bottom plot. The blue line represents the flight path; the green and red markers indicate the initial and final position, respectively; the magenta and black lines indicate the rudder deflection to the right and left, respectively.

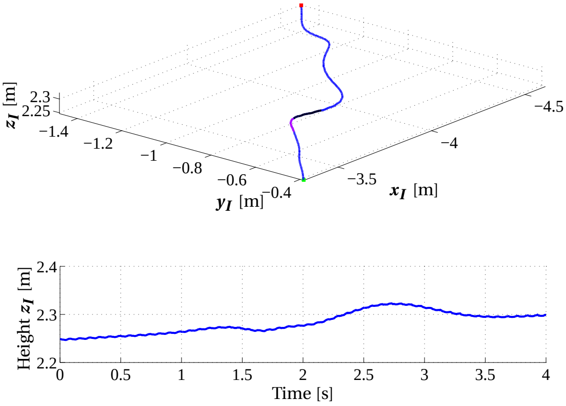

Figure 2.9: Top plot: 3D position of the CG of the DelFly in the Inertial reference frame; Bottom plot: height during the maneuver as a function of time.

Attitude states are computed using Eq. 2.1 and the inputs are computed from the relative position of the markers in the Body frame, in *Rotation_Matrix.m* (provided with the manuscript, cf. Appendix F). The attitude states of this test are presented in Figure 2.10. In Figure 2.10a one can observe that: a) the flapping frequency tends to increase just after the maneuver due to an increase in the relative velocity, which temporarily reduces the power needed to flap, therefore, explaining the increase in height observed after the maneuver. The square wave shape is justified by tracking sampling frequency, which only allows for a small number of samples to be collected per flap cycle ($\frac{200}{16} = 12.5$Hz; $\frac{200}{15} = 13.3$Hz); b) the elevator position is influenced by the flap induced vibrations on the tail and the play between the servomechanism and the elevator link arm, oscillating between [-5,15]°; c) the rudder is less affected by the vibration, and the doublet input occurs between [1.1,1.7]sec of the test. Furthermore, the second part of the input, which corresponds to the deflection to the left, has a smaller duration due to the lag time of the actuator, that takes 70msec to invert the deflection.

Figure 2.10b presents the attitude angles of the robot during the maneuver. The roll (ϕ_r) and yaw (ψ_y) angles present an evolution that resembles an airplane, reacting laterally and directionally to the input. It is worth noting that the rudder has a coupled effect on the pitch (θ_p) angle, induced by the vertical geometric position of the rudder with respect to the CG of the robot. This results in a decrease in the pitch angle just after the inputs, except for the part where the input inverts, at time=1.4sec.

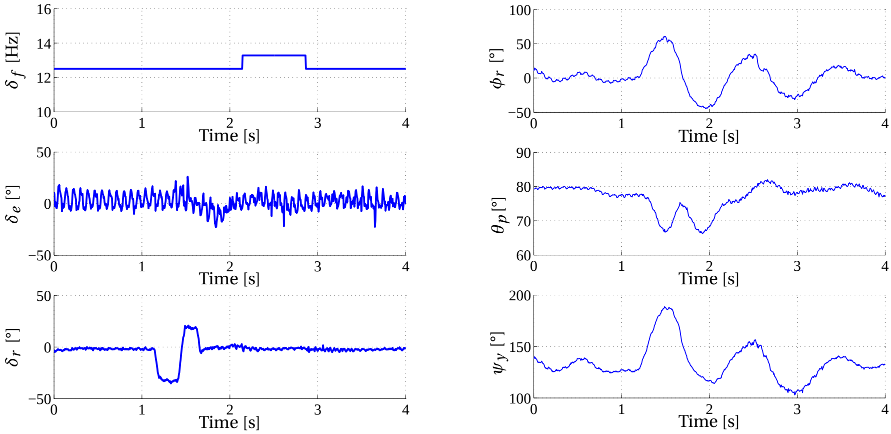

(a) Input commands.

(b) Attitude angles.

Figure 2.10: Inputs and attitude angles, reconstructed from flight data of test #32.

Figure 2.11 presents the reconstructed linear (Figure 2.11a) and angular (Figure 2.11b) velocities of the same test. During the maneuver, the longitudinal velocities do not vary much, with the largest oscillation being the v velocity component, along y_b. As it can be observed, the DelFly exhibits an oscillatory motion that is damped in 2sec. The increase in the peaks of the plots of Figure 2.11a from 2.35sec is justified by the loss of precision of the tracking system, which then propagates into the differentiated states, magnifying the noise-to-signal ratio.

The linear and angular accelerations that were calculated from the time differentiation of the velocities are presented in Figure 2.12. As expected, the terms that are most affected by the rudder deflection are the $\dot{v}$, the $\dot{r}$ and the $\dot{p}$, hence influencing the cor-

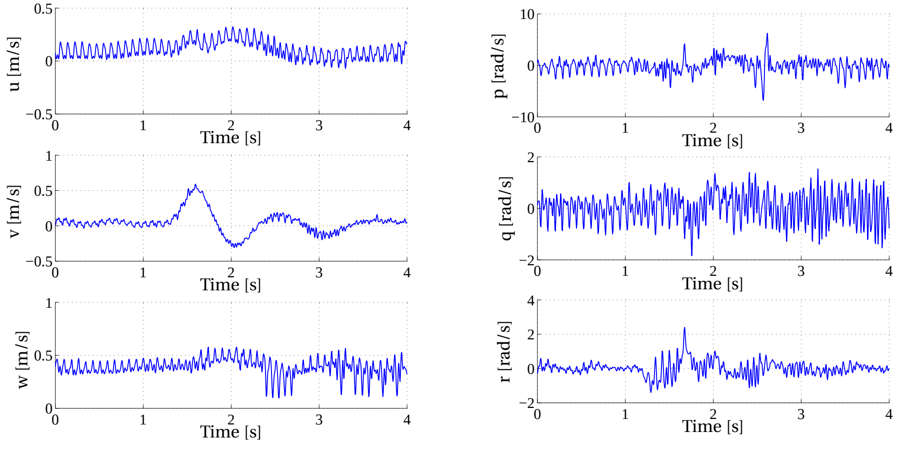

(a) Linear velocities.

(b) Angular velocities.

Figure 2.11: Linear and angular velocities along the body axes for flight test #32.

responding forces and moments that act along their axes. The forces and moments obtained for the flight tests #25 and #32 described here are presented in Appendix B.

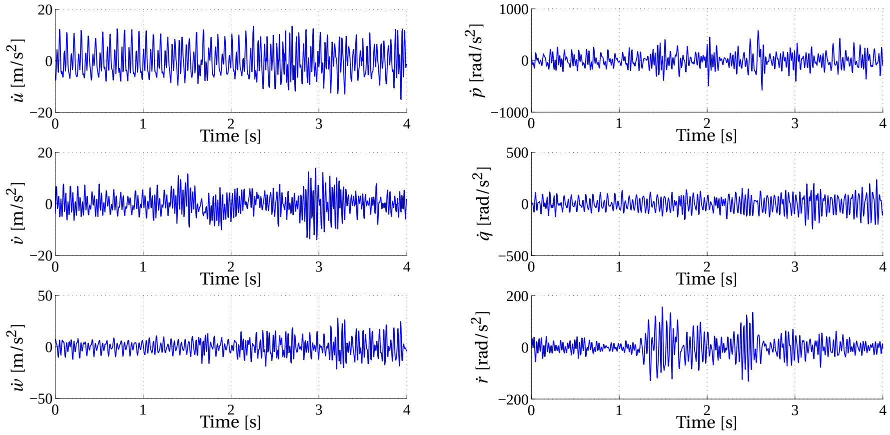

(a) Linear accelerations.

(b) Angular accelerations.

Figure 2.12: Linear and angular accelerations along the body axes for flight test #32[9].

---

[9] Worth noting that the comparison of the forces computed from different kinematic formulations for this specific flight test is presented in Appendix B, and was published in Caetano et al. [2014b].

2.4 CONCLUSION

The flight path reconstruction techniques that were used allowed for the reconstruction of the flight states and inputs. Nevertheless, further analyses are necessary to properly assess the correct flight path reconstruction techniques that should be applied. In particular, the following factors will be analyzed in-depth in the succeeding two Chapters: (a) effect of kinematic model used for force reconstruction (Chapter 3); (b) the numerical differentiation scheme and its impact on the low-pass filtering of the data and noise magnification; (c) the uncertainty that is propagated into the differentiated states; (d) the nature of the error affecting the states; (e) the frequency content of the aerodynamic forces and moments; (f) the filtering frequency and effect of filter type on the data (factors (b) to (f) are addressed in Chapter 4).

The deflections on control surfaces were found to induce a large oscillation on the platform during the execution of the dynamic maneuvers, especially for the longitudinal case which, sometimes, lead to the inversion of the direction of flight (pitch angle greater than 90°). Therefore, it is recommended that further system identification procedures undertaken with this platform consider smaller deflections on the control surfaces. Additionally, considering the recent technological advances made at the autopilot level, future work should consider the recording of onboard sensor data that is synchronized with the external position measuring system. This would allow for the application of sensor fusion flight path reconstruction techniques, resulting in an improved accuracy on the estimated accelerations, forces and moments.

3

MODELING THE KINEMATICS

Several formulations have been proposed to model the dynamics of ornithopters, with inconclusive results regarding the advantages and actual need for complex kinematic formulations. In this chapter, we address the conclusions of Chapter 2 by deriving and comparing two kinematic models of the DelFly: (1) single rigid body Newton-Euler based aircraft equations of motion and (2) virtual work principle derivation for multiple rigid body flapping kinematics. The aerodynamic forces and moments are compared by feeding the states that were reconstructed from the position and attitude data into the dynamic equations of both formulations. To understand the applicability of rigid body formulations to other FWMAVs, six wing-to-body mass ratios and monoplane and biplane wing configurations were studied using real flight data. The results show that rigid body models are valid for the aerodynamic reconstruction of FWMAVs with four wings in 'X' configuration and two-winged FWMAV with a total wing-to-body mass ratio below 24% and 5.6%, respectively, without considerable information loss, for flapping frequencies below 15Hz.

This chapter was published as: Caetano, J. V., Weehuizen, M. B., de Visser, C. C., de Croon, G. C. H. E., and Mulder, M. (2015d). Rigid-Body Kinematics Versus Flapping Kinematics of a Flapping Wing Micro Air Vehicle. *Journal of Guidance, Control and Dynamics*, 38(12). Section II.A. of the publication was removed from the current chapter as it was repeating the information already detailed in Chapter 2 regarding the FWMAV and the experimental setup for the free-flight testing.

3.1 INTRODUCTION

The evolution of FWMAVs has lead to the development of high-end bioinspired robots, such as Aerovironment's Nano-Hummingbird [Keennon et al., 2012], Harvard's RoboBee [Ma et al., 2013], Carnegie Mellon's [Hines et al., 2011] and UC Berkeley's [Baek and Fearing, 2010] FWMAVs and TU Delft's DelFlys [de Croon et al., 2009]. These benefit from having a more extensive flight envelope than conventional fixed or rotary wing platforms, as they are capable of hover, fast forward flight and perching, while making use of efficient lift generation strategies when in forward flight.

To take full advantage of the capabilities of the FWMAV, an accurate dynamic model is needed for automatic control and design improvement. Such model can either relate the inputs and states to the outputs through black-box or nonlinear dynamic inversion approaches, or it can use a white-box phenomenological approach applied to a set of consecutive kinematic and aerodynamic blocks. In the latter approach, the kinematic block is the basis of the dynamic models, which will affect the aerodynamic reconstruction and aerodynamic identification cycle, as presented in Figure 3.1.

There is no consensus on how representative rigid body kinematic models are of flapping wing systems, with several studies arriving at contradicting results. While some authors claim the need for devising complex equations of motion that model the flapping and have used, e.g., Newton-Euler's force principles [Gebert and Gallmeier, 2002], Kane's equations [Bolender, 2009], Lagrange's energy-based methods [Grauer et al., 2011] or d'Alembert's virtual work principle [Orlowski et al., 2010; Orlowski and Girard, 2011], other authors [Dietl and Garcia, 2008; Dietl et al., 2011] have used simple aircraft equations of motion to simulate the behavior of bird-like FWMAV and have demonstrated dynamic model stability, as well as a flying simulation.

Flapping wing kinematic formulations can be complicated to derive [Bolender, 2009; Orlowski and Girard, 2011; Grauer et al., 2011] and are not practical for iterative system development, as new formulations have to be devised for each change in the design of the FWMAVs. This way, rigid body kinematic models would facilitate system identification techniques and the derivation of phenomenological aerodynamic models that could more easily be used for onboard flight control strategies and simulations.

Only a reduced number of studies have used real flying robots for aerodynamic characterization [Grauer et al., 2010, 2011], and none of them focused on comparing the impact of the kinematic formulations in system identification or force simulation. A first comparison between two dynamic formulations that represented a real FWMAV was attempted by Caetano et al. [2014b], but this work only included one degree of freedom (d.o.f.) on the wings and its results only addressed the applicability of each formulation to that particular FWMAV.

The current Chapter aims at better understanding the need for complex kinematic formulations for the aerodynamic identification of FWMAVs by assessing the applicability of rigid body kinematics to bioinspired FWMAV. It is applicable to ornithopters inspired in bird species like the Pomatorhinus Ruficollis or the Coturnix Coturnix [van den Berg and Rayner, 1995] or in insect species like the Schistocerca Gregaria [Taylor and Thomas, 2003] or the Manduca Sexta [Berman and Wang, 2007], in terms of body mass, wing-to-body mass ratio and wing flap frequency, as well as to ornithopters with 'X' wing configuration, used in Academia [WSU, 2012; Rose and Fearing, 2014] and industry.

The study is done through the comparison of the aerodynamic forces and moments reconstructed from real flight data using two different dynamic models: a) simple Newton-Euler's single rigid body general aircraft equations of motion and b) complex Virtual Work Principle multi-rigid body flapping formulation. The analyses are further extended by changing the wing-to-body mass ratios of simulated FWMAVs using the same flight data to predict the effects of wing mass and number of wings on the reconstructed aerodynamic forces and moments. This provides a wing-to-body mass ratio confidence interval for the application of rigid body kinematics to FWMAVs with four and two wings that have a similar configuration to the ornithopter that was used in the flight tests. A description of the present study and its involving framework is presented in Figure 3.1.

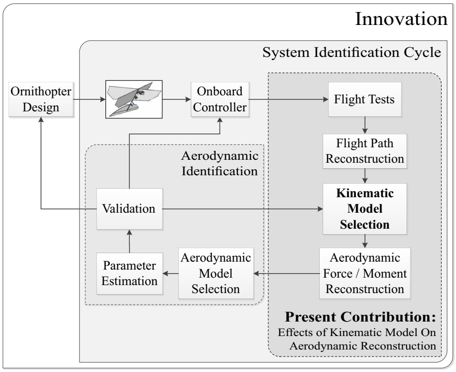

Figure 3.1: Contribution of the current study in the ornithopter Design and Identification cycles.

The Chapter is structured as follows: it starts by presenting the FWMAV kinematic and dynamic formulations in Section 3.2. In Section 3.3 the aerodynamic forces and moments were calculated for the real FWMAV and used to assess the applicability of rigid body kinematics to different FWMAVs. Section 3.4 concludes that rigid body formulations are applicable to FWMAVs within a certain wing-to-body mass ratio.

3.2 MODEL AND DYNAMIC FORMULATIONS

This section presents the mathematical principles and assumptions of the two dynamic formulations that are compared in this study. It starts by presenting the FWMAV model, followed by the two dynamic formulations that were derived for that model.

The formulations have different approaches. The first, typically known as the general aircraft equations of motion, uses Newton-Euler's principle to derive the equations of motion of a rigid non-flapping body. The second uses the Principle of Virtual Work applied to rigid bodies to determine the kinematics of a flapping platform.

The Body reference frame is attached to the main body, with its origin at the CG. The main body carbon rod is aligned with the $\boldsymbol{x_b}$ axis; the $\boldsymbol{y_b}$ axis points out of the right side of the DelFly; the $\boldsymbol{z_b}$ points down, perpendicular to the $x_b y_b$ plane, as indicated in Figure 3.2.

Table 3.1 presents the masses of the composing parts of the DelFly. These will be mentioned further in the article to explain some of the assumptions that were taken.

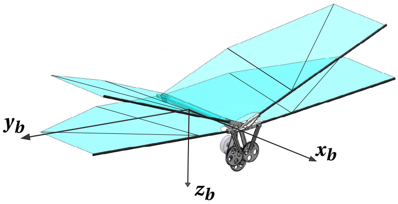

Figure 3.2: Wing configuration and Body frame axis ($\boldsymbol{x_b}$, $\boldsymbol{y_b}$, $\boldsymbol{z_b}$).

Table 3.1: Masses of the Components of the Ornithopter

Component	Mass (g)
Main Rod	0.791
Autopilot	1.454
Battery	5.640
Servo (x2)	0.536
Driving Mechanism	3.182
Horizontal Tail Structure	1.215
Vertical Tail Structure	0.279
Reflector balls (x3)	0.33
Other (glue + wires)	1.48
Body & Tail	16.2
Wing	0.298
Total	17.4
Wing-to-Body Mass ratio	1.8 %

3.2.1 SINGLE RIGID BODY DYNAMIC MODEL

MODEL AND REFERENCE FRAMES

The first model approach considers the DelFly as a rigid body with no moving parts. Six assumptions were taken in this rigid body kinematic formulation: a) non-flapping rigid body; b) constant mass; c) no inertia changes due to flapping or bending; d) symmetric platform; e) stationary atmosphere; f) flat Earth.

MATHEMATICAL FORMULATION

The Newton-Euler based rigid body equations of the DelFly are given by [Stevens and Lewis, 2003]:

$$
\begin{aligned}
X &= m(g\sin\theta + \dot{u} + qw - rv)\\
Y &= m(-g\sin\phi\cos\theta + \dot{v} + ru - pw)\\
Z &= m(-g\cos\phi\cos\theta + \dot{w} + pv - qu)\\[1ex]
L &= I_x\dot{p} - I_{xz}(\dot{r} + pq) + (I_z - I_y)qr\\
M &= I_y\dot{q} + (I_x - Iz)rp + I_{xz}(p^2 - r^2)\\
N &= I_z\dot{r} - I_{xz}\dot{p} + (I_y - I_x)pq + I_{xz}rq\\[1ex]
\dot{\psi} &= (q\sin\phi + r\cos\phi)/cos\theta\\
\dot{\theta} &= q\cos\theta - r\sin\theta\\
\dot{\phi} &= p + (q\ sin\phi + r\cos\phi)tan\theta
\end{aligned}
\tag{3.1}
$$

The first six equations represent the acting aerodynamic forces (X, Y, Z) and moments (L, M, N) along the body axes of the vehicle $(\boldsymbol{x_b}, \boldsymbol{y_b}, \boldsymbol{z_b})$. The translational and angular velocities are represented by (u, v, w) and (p, q, r), respectively, while $(\dot{u}, \dot{v}, \dot{w})$ are the linear accelerations at the CG and the last three equalities relate the Euler angles (ϕ,θ,ψ) and rates $(\dot{\phi},\dot{\theta},\dot{\psi})$ to the body angular velocities.

APPLICABILITY ASPECTS

The previous formulation does not account for any moving parts and considers the inertia tensor as being constant. Moreover, the non-flapping validity region depends not only on the wing-generated evolution of the forces and moments over the flap cycle but also on the wing mass to body ratio and the wing inertia to body inertia ratio.

The rigid body formulation, however, benefits from being easily devised for non-exotic aircraft configurations while still taking into consideration the accelerations and Coriolis couplings of rigid body dynamics. This approach is justified by the wing configuration of the ornithopter that minimizes the CG oscillations over a flap cycle, as the lower wing flap counteracts the upper wing's to a great extent, as shown in Figure 3.3.

Furthermore, Figure 3.3 compares the position of CG of the DelFly with a similar ornithopter that would have only two wings similar to the ones on the test ornithopter. It is known [de Croon et al., 2009] that the 'X' wing configuration maximizes lift and thrust production by more that 150% when compared to a two-winged ornithopter. Hence, this comparison is still conservative, since a two-winged ornithopter would need bigger wings or higher flapping frequency for sustained flight thus inducing larger oscillations on the CG location.

The DelFly is manually built making it not perfectly symmetric around the $x_b z_b$ plane. However, the symmetry assumption is justified by the small moments of inertia around $\boldsymbol{x_b}$ and crossed moments of inertia, making the coupled I_{xy}, I_{yz} negligible, here assumed to be zero.

The last three equalities of Eq. 3.1 are not well defined for pitch angles close to 90° since a small variation in yaw will induce a large oscillation in ψ, resulting in inadequate information in $\dot{\psi}$ and consequently wrong angular velocity r determination. The same

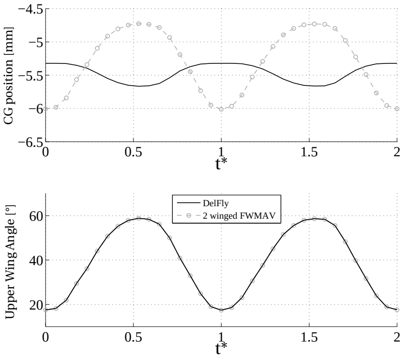

Figure 3.3: Location of the CG with respect to the body carbon rod within two flapping cycles for the DelFly and for a two-winged ornithopter with similar wings and flapping kinematics of the upper wings of the DelFly.

happens to the roll angle, as a rotation around $\boldsymbol{z_b}$ affects the heading angle ψ which, in turn, feeds a rolling miss-information to the Euler angles.

Moreover, the singularity at θ =90° denies the calculation the Euler angles, and hence, the rotational rates (p, q, r). The ornithopter can enter such singularity conditions for certain elevator pitch-up maneuvers. Therefore, to prevent p, q, r from feeding wrong information into the forces and moments equations, new attitude angles were computed, as explained in Chapter 5.

3.2.2 MULTI-RIGID FLAPPING WING DYNAMIC MODEL

MODEL AND REFERENCE FRAMES

The second method models the DelFly as a combination of five rigid bodies - a main body and four wings. The main body includes the carbon rod that connects the parts, the hardware attached to the rod, as well as the vertical and horizontal tails. In the real ornithopter, only the elevator and rudder have one degree of freedom with respect to the rigid body. These surfaces vibrate during flight due to the flapping, given the mechanical play in the small servos – as can be seen in Figure 2.7b. However, their low mass (0.46g for the elevator and 0.15g for the rudder) compared to the total mass of the body (16.2g) associated with the small amplitudes of vibration make their contribution to the kinematics nearly non-existent, which justified the modeling of the components as a single rigid body.

Conversely, the wing bodies, identified as W_1, W_2, W_3 and W_4 in Figure 3.4b, are modeled separately since all of them have different kinematics that will affect the overall kinematic behavior of the ornithopter. The Body reference frame (B) was defined as in the previous rigid body method, and is presented in Figure 3.2. The reference frames and θ_w are shown in Figure 2.6.

Wing Frame (W) A separate reference frame was used for each wing, whose origin is at the hinge point and the $x_w y_w$ plane coincident with the wing surface. The frames are assumed to rotate with the wing around $\boldsymbol{x_b}$ and $\boldsymbol{y_w}$.

Two vectors describe the motion of the CG of all wings in the Body frame: $\boldsymbol{\rho}_{h,b}$ represents the position of the hinge point with respect to the CG of the main body; $\boldsymbol{\rho}_{w,h}$ connects the hinge point to the CG of the wings, as indicated in Figure 3.4a.

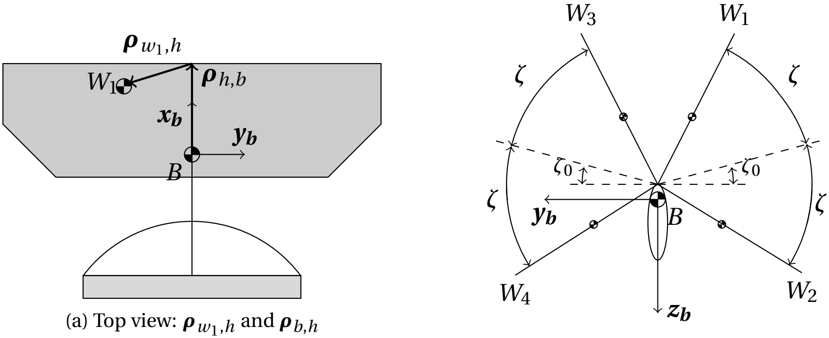

(a) Top view: $\boldsymbol{\rho}_{w_1,h}$ and $\boldsymbol{\rho}_{b,h}$ representation, from the CG of the body to the CG of the wing, with closed wings.

(b) Front view: wings open at angle ζ; dashed line represents the position of the closed wings at ζ_0.

Figure 3.4: Simplified Model with CG, Body (B) and Wing (W1 to W4) reference frames.

Wing Modeling The four wings are modeled as rigid bodies that are geometrically identical to the real wings [Caetano et al., 2014b]. The wing models have two d.o.f.: active rotation around $\boldsymbol{x_b}$ with an angle ζ (Figure 3.4b) and passive rotation around $\boldsymbol{y_w}$ with an angle θ_w (Figure 2.6). The wings are set at a dihedral angle ζ_0 of 13° and the flapping angle ζ is defined from ζ_0 to the wing for all wings, as shown in Figure 3.4b.

For the current model, the wing pitch angle (θ_w) is taken around the $\boldsymbol{y_w}$ axis of the wing as being the angle between the chord line of the wing foil and the $x_b y_b$ plane. This angle will determine the evolution of the CG of the wing during the flap cycle. Figure 3.5 presents the chordwise evolution of the lower wing surface of the real ornithopter during one flap cycle for a section located at 70% of the wing span. It was processed from high speed imagery collected when testing the DelFly in a wind tunnel [Groen et al., 2010]. It is divided in six time-steps: first three subfigures (a, b, c) represent the out-stroke motion; last three subfigures (d, e, f) represent in-stroke motion; $t^* = \frac{t}{T}$ represents dimensionless time, with T being the period of the flap. Bottom wings are assumed to have a mirrored evolution.

It is important to use the real wing pitch angle information in the kinematic modeling. In order to add one d.o.f. to the model (wing pitch angle) and keep the same number of generalized coordinates, the wing pitch angle θ_w of the model has to be a function of the wing flap angle ζ. This allows for the adjustment of the kinematic model to different flapping frequencies as well as a better approximation to the real wing pitch angle.

Figure 3.5a presents two possible model chord distributions indicated by the Wing frame axes $\boldsymbol{x_{w_1}}$ (dashed) and $\boldsymbol{x_{w_2}}$ (dottted). $\boldsymbol{x_{w_1}}$ was obtained by connecting the leading edge of the real foil distribution to the trailing edge; $\boldsymbol{x_{w_2}}$ was obtained in the same way, using a point placed at 50% of the wing foil.

The selection of 50% of the chord is justified by the movement of the wing during the ‘peel’ part of the flap (Figure 3.5a). The leading edge foil separates from the upper wing (‘peel’ motion [de Croon et al., 2012]) while the after part of the foil closer to trailing edge lags considerably behind it until a $t^* = 0.3$. Furthermore, a selection of 50% of the chord conserves the kinematic information, as the dashed line of $\boldsymbol{x_{w_2}}$ will better represent the position of the CG of the wing, presented in Figure 3.4, thus more accurately modeling the kinematic forces that will act on the ornithopter.

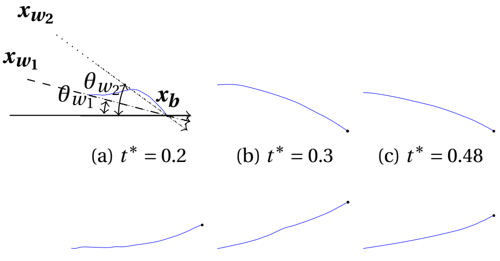

(a) $t^* = 0.2$ (b) $t^* = 0.3$ (c) $t^* = 0.48$

(d) $t^* = 0.71$ (e) $t^* = 0.90$ (f) $t^* = 1$

Figure 3.5: Chordwise evolution of the airfoil during one flap cycle at 70% of the span.

Different functions were used to fit the real wing pitch angle as a function of other states. From comparing the wing pitch angle evolution with flapping in air and in vacuum it was observed that the wing deformation is more influenced by the flapping states than by other states, e.g., the free stream velocity. This way, a function (Eq. 3.2) was fitted to the geometric data used in Figure 3.5, resulting in a model estimated wing pitch angle $\hat{\theta}_w$. This approach also allows for the pitch model to include only kinematic related states, thus separating kinematics from aerodynamics.

$$\hat{\theta}_w = C_{\theta_{w_0}} + C_{\theta_{w_\zeta}}\zeta + C_{\theta_{w_{\dot{\zeta}}}}\dot{\zeta} \tag{3.2}$$

The real wing surface evolution was used to estimate the wing model pitch angle under the following assumptions:

1. the wing pitch angle data for one flap cycle is representative of all flap cycles in flight test data;
2. the wing pitch angle data measured at 70% of the span is applied on the complete span of the wing;
3. deformation of the wing in chord-wise direction is neglected;
4. all four wings have the same evolution.

The coefficients of Eq. 3.2 were estimated using least squares for both θ_w assumptions and are shown in Table 3.2.

The measured wing pitch angle (θ_w) and the estimated pitch angle ($\hat{\theta}_w$) are presented in Figure 3.6 for one flap cycle. The lines in full represent the measured wing

Table 3.2: Estimated Coefficients for Eq. 3.2 using the chord assumptions of 100% and 50% of the wing chord.

Coefficient	$\theta_{w100\%}$	$\theta_{w50\%}$
$C_{\theta_{w_0}}$	0.4476	0.5016
$C_{\theta_{w_\zeta}}$	-1.2946	-1.5849
$C_{\theta_{w_{\dot{\zeta}}}}$	-0.0160	-0.0216

pitch angle (θ_w) for the two chord lines $\boldsymbol{x_{w_1}}$ and $\boldsymbol{x_{w_2}}$ shown before in Figure 3.5a and the dashed lines represent the estimated wing pitch angle evolution, computed using Eq. 3.2.

Unlike the $\boldsymbol{x_{w_2}}$, the chord line $\boldsymbol{x_{w_1}}$ connects the leading edge to the trailing edge, thus not conserving the camber information of the wing, which is responsible for the differences in the recorded pitch angle evolution presented in Figure 3.6.

The inflections on both evolutions of the measured pitch angle are subject to noise from the visual data acquisition, which is more pronounced in $\boldsymbol{x_{w_2}}$, e.g. at $t^* \in [0.25, 0.35]$ and $t^* \in [0.8, 0.9]$. Nevertheless, despite not perfectly following the collected data, the estimated wing pitch angle ($\hat{\theta}_w$) avoids the noisy pitch oscillations and presents an evolution over one flap cycle that avoids kinematic force issues in the formulations that would come from the noisy data.

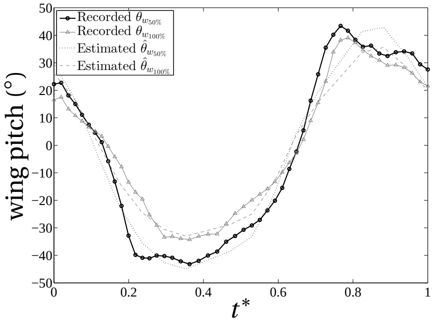

Figure 3.6: Recorded (θ_w) [Groen et al., 2010] and estimated ($\hat{\theta}_w$) wing pitch angles for two chords evolutions.

Body Frame to Wing Frames The transformation from the Body frame to each of the four Wing frames consists of a first rotation around the $\boldsymbol{x_b}$ axis followed by a second rotation around $\boldsymbol{y_w}$, defined as follows for each wing:

$$\begin{aligned}
\mathscr{R}_{w1,b} &= \begin{bmatrix} \cos(\theta_w) & \sin(\theta_w)\sin(\zeta_0+\zeta) & -\sin(\theta_w)\cos(\zeta_0+\zeta) \\ 0 & \cos(\zeta_0+\zeta) & \sin(\zeta_0+\zeta) \\ \sin(\theta_w) & -\cos(\theta_w)\sin(\zeta_0+\zeta) & \cos(\theta_w)\cos(\zeta_0+\zeta) \end{bmatrix} \\
\mathscr{R}_{w2,b} &= \begin{bmatrix} \cos(\theta_w) & \sin(\theta_w)\sin(\zeta_0-\zeta) & -\sin(\theta_w)\cos(\zeta_0-\zeta) \\ 0 & \cos(\zeta_0-\zeta) & \sin(\zeta_0-\zeta) \\ \sin(\theta_w) & -\cos(\theta_w)\sin(\zeta_0-\zeta) & \cos(\theta_w)\cos(\zeta_0-\zeta) \end{bmatrix} \\
\mathscr{R}_{w3,b} &= \begin{bmatrix} \cos(\theta_w) & \sin(\theta_w)\sin(-\zeta_0-\zeta) & -\sin(\theta_w)\cos(-\zeta_0-\zeta) \\ 0 & \cos(-\zeta_0-\zeta) & \sin(-\zeta_0-\zeta) \\ \sin(\theta_w) & -\cos(\theta_w)\sin(-\zeta_0-\zeta) & \cos(\theta_w)\cos(-\zeta_0-\zeta) \end{bmatrix} \\
\mathscr{R}_{w4,b} &= \begin{bmatrix} \cos(\theta_w) & \sin(\theta_w)\sin(-\zeta_0+\zeta) & -\sin(\theta_w)\cos(-\zeta_0+\zeta) \\ 0 & \cos(-\zeta_0+\zeta) & \sin(-\zeta_0+\zeta) \\ \sin(\theta_w) & -\cos(\theta_w)\sin(-\zeta_0+\zeta) & \cos(\theta_w)\cos(-\zeta_0+\zeta) \end{bmatrix}
\end{aligned} \tag{3.3}$$

The position of the CG of each wing is first defined in its own Wing frame (W_1 to W_4) as $\boldsymbol{\rho}_{w,h}$ (Figure 3.4) and then transformed to the Body frame using the transpose of the transformation matrices found in Eq. 3.3, resulting in:

$$\boldsymbol{\rho}_{b_{wi,h}} = \mathscr{R}_{b,w_i}\boldsymbol{\rho}_{w_i,h} \quad \text{with} \quad i = 1,2,3,4 \tag{3.4}$$

Inertial frame to Body frame The transformation from the Inertial frame to the Body frame is done using quaternions and the rotation matrix takes the form [Phillips et al., 2001]:

$$\mathscr{R}_{b,I} = \begin{bmatrix} e_1^2+e_0^2-e_2^2-e_3^2 & 2(e_1e_2+e_3e_0) & 2(e_1e_3-e_2e_0) \\ 2(e_1e_2-e_3e_0) & -e_2^2-e_0^2+e_1^2+e_3^2 & 2(e_2e_3+e_1e_0) \\ 2(e_1e_3+e_2e_0) & 2(e_2e_3-e_1e_0) & -e_3^2-e_0^2+e_1^2+e_2^2 \end{bmatrix} \tag{3.5}$$

The angular velocities in the Body frame can now be determined using:

$$\begin{bmatrix} 0 \\ p \\ q \\ r \end{bmatrix} = 2\begin{bmatrix} e_0 & e_1 & e_2 & e_3 \\ -e_1 & e_0 & e_3 & -e_2 \\ -e_2 & -e_3 & e_0 & e_1 \\ -e_3 & e_2 & -e_1 & 0 \end{bmatrix}\begin{bmatrix} \dot{e}_0 \\ \dot{e}_1 \\ \dot{e}_2 \\ \dot{e}_3 \end{bmatrix} \tag{3.6}$$

Mass, CG Position and Inertia Moments The full FWMAV and wing CG positions in the Body frame were $(x_b, y_b, z_b) = (-70.4, 0.0, 2.0)mm$ and $(x_b, y_b, z_b) = (-16.5, \pm 67, 0)mm$, respectively measured from the hinge point of the wings, located at the nose. This position can be seen in Figure 3.4. The mass and moment of inertia along the main axes of all rigid bodies is presented in Table 3.3.

Only the diagonal terms of the wing inertia tensor were used and transformed to the Body frame using the inverse of Eq. 3.3:

Table 3.3: Mass and Moments of Inertia of Each Modeled Body

	Complete DelFly	Body	Wing (x4)
Mass (g)	17.4	16.2	0.298
I_{xx} $[Kgm^2]$	$1.34E^{-05}$	$5.94E^{-06}$	$4.44E^{-07}$
I_{yy} $[Kgm^2]$	$6.58E^{-05}$	$6.29E^{-05}$	$1.74E^{-07}$
I_{zz} $[Kgm^2]$	$6.95E^{-05}$	$6.27E^{-05}$	$6.18E^{-07}$

$$I_w^b = \mathscr{R}_{b,w} I_w \mathscr{R}_{b,w}^T \tag{3.7}$$

MATHEMATICAL FORMULATION

Generalized coordinates and Quasi-velocities The main body has six d.o.f. in Inertial space which then translate into seven generalized coordinates (q_j) Baruh [1999] given the quaternion-based rotation of Eq. 3.5; the four wings (W_1 to W_4) have two extra d.o.f., ζ and θ_w. However, since θ_w is correlated with ζ by Eq. 3.2 this results in only one added generalized coordinate. Hence, there are eight generalized coordinates to be considered in the kinematic equations: the inertial position of the main body (x, y, z), the quaternion terms (e_0, e_1, e_2, e_3) and the flap angle ζ.

$$\boldsymbol{q}_j = [x, y, z, e_0, e_1, e_2, e_3, \zeta] \tag{3.8}$$

There are also eight generalized velocities, which correspond to the time derivatives of $\boldsymbol{q}_j$. Nevertheless, there are only seven quasi-velocities thanks to one non-holonomic [Baruh, 1999] constraint in the generalized coordinates, caused by the quaternion definition. Consequently, the quasi-velocities are formed by the linear velocities (u, v, w), the angular velocities (p, q, r) and the time derivative of the flapping angle $(\dot{\zeta})$, as follows:

$$\boldsymbol{u}_j = [u, v, w, p, q, r, \dot{\zeta}] \tag{3.9}$$

Velocities The translational velocities for each rigid body written in the Body frame are:

$$\begin{aligned} \boldsymbol{v}_1 &= u\boldsymbol{x}_b + v\boldsymbol{y}_b + w\boldsymbol{z}_b \\ \boldsymbol{v}_i &= \boldsymbol{v}_1 + \boldsymbol{\omega}_1 \times \boldsymbol{\rho}_{h,b} + \boldsymbol{\omega}_i \times \boldsymbol{\rho}_{b_{w_{i-1}},h} \quad \text{with } i = 2,3,4,5 \end{aligned} \tag{3.10}$$

and the angular velocities are defined as:

$$\begin{aligned}
\boldsymbol{\omega}_1 =& p\boldsymbol{x}_b + q\boldsymbol{y}_b + r\boldsymbol{z}_b \\
\boldsymbol{\omega}_2 =& (p+\dot{\zeta})\boldsymbol{x}_b + [q-\dot{\theta}_w cos(\zeta_0+\zeta)]\boldsymbol{y}_b + \\
& [r+\dot{\theta}_w sin(\zeta_0+\zeta)]\boldsymbol{z}_b \\
\boldsymbol{\omega}_3 =& (p-\dot{\zeta})\boldsymbol{x}_b + [q+\dot{\theta}_w cos(\zeta_0-\zeta)]\boldsymbol{y}_b + \\
& [r-\dot{\theta}_w sin(\zeta_0-\zeta)]\boldsymbol{z}_b \\
\boldsymbol{\omega}_4 =& (p-\dot{\zeta})\boldsymbol{x}_b + [q-\dot{\theta}_w cos(-\zeta_0-\zeta)]\boldsymbol{y}_b + \\
& [r+\dot{\theta}_w sin(-\zeta_0-\zeta)]\boldsymbol{z}_b \\
\boldsymbol{\omega}_5 =& (p+\dot{\zeta})\boldsymbol{x}_b + [q+\dot{\theta}_w cos(-\zeta_0+\zeta)]\boldsymbol{y}_b + \\
& [r-\dot{\theta}_w sin(-\zeta_0+\zeta)]\boldsymbol{z}_b
\end{aligned} \tag{3.11}$$

Accelerations Given the previous definitions, the translational and linear accelerations of the main body terms become:

$$\dot{\boldsymbol{v}}_1 = \frac{\partial \boldsymbol{v}_1}{\partial t} + \boldsymbol{\omega}_1 \times \boldsymbol{v}_1 \tag{3.12}$$

$$\dot{\boldsymbol{\omega}}_1 = \frac{\partial \boldsymbol{\omega}_1}{\partial t} = \dot{p}\boldsymbol{x}_b + \dot{q}\boldsymbol{y}_b + \dot{r}\boldsymbol{z}_b \tag{3.13}$$

where $\frac{\partial \boldsymbol{v}_1}{\partial t}$ is the change in speed observed from the rotating Body frame defined in Eq. 3.14. The second term is the acceleration caused by the rotation of the reference frame.

$$\frac{\partial \boldsymbol{v}_1}{\partial t} = \dot{u}\boldsymbol{x}_b + \dot{v}\boldsymbol{y}_b + \dot{w}\boldsymbol{z}_b \tag{3.14}$$

The translational and angular accelerations of wing rigid bodies are defined, respectively, by:

$$\dot{\boldsymbol{v}}_i = \frac{\partial \boldsymbol{v}_i}{\partial t} + \boldsymbol{\omega}_1 \times \boldsymbol{v}_i \quad \text{with} \quad i = 2,3,4,5 \tag{3.15}$$

$$\dot{\boldsymbol{\omega}}_i = \frac{\partial \boldsymbol{\omega}_i}{\partial t} + \boldsymbol{\omega}_1 \times \boldsymbol{\omega}_i \quad \text{with} \quad i = 2,3,4,5 \tag{3.16}$$

Generalized Forces Let Q_j be the generalized forces related to each quasi-velocity u_j, which are defined using the virtual work principle:

$$Q_j = \sum_{i=1}^{n} (\boldsymbol{F_i}\boldsymbol{\gamma_{ij}} + \boldsymbol{M_i}\boldsymbol{\beta_{ij}}) \tag{3.17}$$

with n the number of bodies, j the index of the generalized force, and $\boldsymbol{F_i}$ and $\boldsymbol{M_i}$ the external acting forces and moments respectively. $\boldsymbol{\gamma}_{ij}$ and $\boldsymbol{\beta}_{ij}$ respectively represent the velocity coefficient matrix and the angular velocity coefficient and can be calculated by differentiating the linear and angular velocities of each body with respect to each quasi-velocity, using:

$$\boldsymbol{\gamma}_{ij} = \frac{\partial \boldsymbol{v}_i}{\partial \boldsymbol{u}_j} \tag{3.18}$$

$$\boldsymbol{\beta}_{ij} = \frac{\partial \boldsymbol{\omega}_i}{\partial \boldsymbol{u}_j} \tag{3.19}$$

The forces Q_1, Q_2 and Q_3 are the resultant forces along the Body frame axes, which include gravity and aerodynamic forces (that will be calculated bellow). The weight vector is expressed in the Body frame axes by:

$$\boldsymbol{g_b} = \mathscr{R}_{b,I} \begin{bmatrix} 0 & 0 & g \end{bmatrix}^T \tag{3.20}$$

Hence, the first three generalized forces become:

$$\begin{bmatrix} Q_1 \\ Q_2 \\ Q_3 \end{bmatrix} = \begin{bmatrix} X \\ Y \\ Z \end{bmatrix} + (m_1 + m_2 + m_3 + m_4 + m_5)\boldsymbol{g_b} \tag{3.21}$$

The following generalized forces (Q_4, Q_5 and Q_6) are the moments in the Body frame, which also include gravity ($\boldsymbol{M_g}$) and aerodynamic (L, M, N) terms:

$$\begin{bmatrix} Q_4 \\ Q_5 \\ Q_6 \end{bmatrix} = \begin{bmatrix} L \\ M \\ N \end{bmatrix} + \boldsymbol{M_g} \begin{bmatrix} \boldsymbol{x}_b \\ \boldsymbol{y}_b \\ \boldsymbol{z}_b \end{bmatrix} \tag{3.22}$$

$$\text{with} \quad \boldsymbol{M_g} = \sum_{i=1}^{4} \boldsymbol{\rho_{w_i,b}} \times (m_{i+1}\boldsymbol{g_b}) \tag{3.23}$$

The last generalized force, Q_7, is the moment needed to flap the wings, that represents the motor torque needed to overcome wing kinematic loads (M_m):

$$Q_7 = M_m \tag{3.24}$$

D'Alembert's Method For Rigid Bodies All the previous derivations can now be used to calculate the aerodynamic forces (Eq. 3.21) and moments (Eq. 3.22) acting on the FW-MAV by replacing Q_j in the previous formulations, using d'Alembert's dynamic principle of virtual work [Baruh, 1999]:

$$\sum_{i=1}^{n} [m_i(\dot{\boldsymbol{v}}_{\boldsymbol{i}} + \ddot{\boldsymbol{\rho}}_{ci})\boldsymbol{\gamma_{ij}} + (I_i\dot{\boldsymbol{\omega}}_i + \boldsymbol{\omega}_i \times I_i\boldsymbol{\omega}_i + m_i\boldsymbol{\rho}_{ci} \times \dot{v}_i)\boldsymbol{\beta_{ij}}] = Q_j \tag{3.25}$$

where i is the body index and j is the quasi-velocity or generalized force index, m_i is the mass of each rigid body, I_i the inertia matrices for the rigid bodies and $\boldsymbol{\rho}_{ci}$ is the vector from the reference point of a body to its center of mass. If the reference point of the rigid body is its CG ($\boldsymbol{\rho}_{ci} = 0$) the equation simplifies to:

$$\sum_{i=1}^{N} [m_i\dot{\boldsymbol{v}}_{\boldsymbol{i}}\boldsymbol{\gamma_{ij}} + (I_i\dot{\boldsymbol{\omega}}_i + \boldsymbol{\omega}_i \times I_i\boldsymbol{\omega}_i)\boldsymbol{\beta_{ij}}] = Q_j \tag{3.26}$$

APPLICABILITY ASPECTS

Such flapping wing kinematic model is able to better represent the physical FWMAV when compared to rigid body models. It accounts for mass and inertia distribution changes and separates the kinematic contribution from the aerodynamic forces and moments that are reconstructed, allowing for a more accurate aerodynamic reconstruction. It also avoids the complex differentiations of energy-based methods, e.g., using Lagrange's formulation.

Despite modeling the flexible FWMAV wings as rigid bodies, this formulation still accounts for the two d.o.f. of the wings and uses real wing chord evolution to model the movement of the rigid bodies, thus minimizing the errors between the aerodynamic reconstruction of the model and the real FWMAV. Furthermore, this formulation results in a simpler computational analysis when compared to flexible multi-body formulations, which justifies its application for onboard modeling.

The errors resulting from modeling flexible structures as rigid bodies were considered to be negligible for the assessment of the validity of rigid body formulations for FWMAV aerodynamic reconstruction.

3.3 RESULTS AND DISCUSSION

The current section compares the aerodynamic forces and moments reconstructed from the flight data using the dynamic models derived in Section 3.2. First, the control surface positions of the real FWMAV, as well as the aerodynamic forces and moments reconstructed from each dynamic model are shown. This is followed by an extension of the results to different wing-to-body mass ratios. Finally, the validity regions of the models are discussed.

3.3.1 FORCE AND MOMENT IDENTIFICATION RESULTS

A single part of the flight tests was considered to be representative of the flight conditions, as it covers trimmed flight and abrupt elevator change[1]. The forces and moments presented here correspond to the portion of text #25 that was presented before, in Chapter 2. Figure 2.7a presents a visualization of the trajectory of the FWMAV. It shows one second of horizontal leveled flight, followed by an elevator doublet input over $\frac{2}{3}$ seconds which induced a longitudinal oscillatory movement that was dampened after three seconds. The red and magenta parts in Figure 2.7a represent the elevator deflection to maximum up (negative) and down (positive), respectively, as indicated in the middle plot of Figure 2.7b, at time=6sec. The blue marker indicates the transition from positive to negative. The ornithopter goes over 90° in pitch just before losing altitude. The arrows indicate the $\boldsymbol{x_b}$ (black) and $\boldsymbol{z_b}$ (gray) Body axes along the maneuver and are equally spaced of 0.2sec. The flight patch is projected on the $x_b y_b$ plane for better visualization.

The loss of altitude during the maneuver is caused by the transition from forward to hovering flight, causing the lift to be smaller due to the lack of relative wind on the wings and tail. This effect is then aggravated by the elevator deflection down, which initially causes the FWMAV to lose more altitude, and then contributes to an increase in forward velocity u, that allows the FWMAV to regain altitude and return to leveled flight while

---

[1] The selected flight test can be seen in the video file that accompanies the thesis.

keeping all inputs at trim position.

The influence of the displacement of the wings during flapping (top plot of Figure 2.7b) is visible on the sub-flap oscillations of the elevator (δ_e) and rudder (δ_r) positions, depicted in the middle and bottom plots of Figure 2.7b.

The states that were reconstructed from the position and attitude of the ornithopter for this test are presented in Chapter 5 (Figures 5.2 to 5.5) and in Caetano et al. [2013a] (Figures 4 to 7).

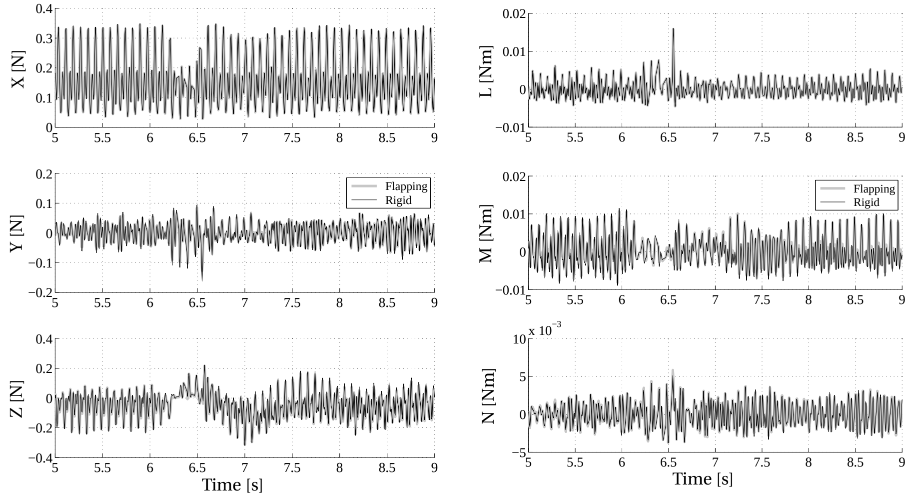

(a) Aerodynamic forces.

(b) Aerodynamic moments.

Figure 3.7: Aerodynamic forces and moments calculated using both kinematic models and physical properties of the real ornithopter.

The evolution of the aerodynamic forces and moments, presented in Figure 3.7, shows that both kinematic derivations lead to very similar aerodynamic forces and moments, even during highly nonlinear maneuvers, like the one shown.

Among the forces, the Z force shows the biggest differences between both methods, while X reveals an almost perfect match. The differences in Z are caused by the deceleration of the wings at the end of the out-stroke, where the flap angle is maximum, since the wing stroke plane is almost parallel to the$\boldsymbol{z_b}$ axis. This results in added pitch inducing forces along $\boldsymbol{z_b}$ which, in turn, induce variations in the pitch moment M between both methods, as observed in Figure 3.7b.

The L moment reveals very similar results between the methods due to the symmetry of the model along the $x_b z_b$ plane. Alike the M moment, the N moment calculated for the flapping kinematics has lower peaks due to separation between the kinematic and the aerodynamic effects of the wings.

The previous results point to the applicability of rigid body models for the aerodynamic force identification of FWMAVs that have symmetric positioning of wings and a single wing-to-body mass ratio under 1.8%, which is the ratio of the ornithopter that was used.

The following section explores the applicability of the kinematic models, testing the identification procedure with different wing-to-body mass ratios and wing configurations.

3.3.2 EXTENSION OF RESULTS TO DIFFERENT WING-TO-BODY MASS RATIOS

METHODOLOGY CONSIDERATIONS

The previous results are extended here to assess the effects of relative wing-to-body mass ratios in the aerodynamic force and moment reconstruction using the same flight data. In particular, other four-winged and two-winged ornithopter kinematics were simulated for different single wing-to-body mass ratios, while keeping the total mass of the FWMAV constant.

Body masses were changed by assuming a uniform distribution of variable density in the bodies. In effect, the inertia tensor was recalculated for each mass ratio and included in the kinematic formulations. It was assumed that the simulated FWMAVs would flap with the same frequency as the DelFly ($\sim 12Hz$).

Root Mean Square of the Error (RMSE) and the Coefficient of Determination (R^2) were used for the quantitative assessment of the applicability of rigid body formulations in both cases. The RMSE (Eq. 3.27) is an indication of the absolute difference between the two signals. A value of zero indicates identical signals. The higher the value, the larger the difference between the signals.

$$RMSE_{F_{flapping},F_{single}} = \sqrt{\frac{\sum(F_{flapping} - F_{single})^2}{N_i}} \tag{3.27}$$

It is worth noting that the aerodynamic forces and moments that were obtained with this method consist of the ones that would have acted on a FWMAV with the indicated mass and inertia properties, had it flown this trajectory. The results will be conservative since higher wing-to-body mass ratios would also induce larger body oscillations during flapping, that are not captured by the flight data. Nevertheless, this method consists of a sensitivity study and is used to predict the effect of kinematic models in aerodynamic reconstruction, thus providing a safety threshold for the application of rigid body kinematics. The fact that it uses real flight data allows for more reliable conclusions than using pure simulated trajectories based on aerodynamic models that are subjective to assumptions and approximations.

The Coefficient of Determination (Eq. 3.28) is the average of the squared error between two signals divided by the variance of the original signal. A value of one means a perfect fit and a value closer to zero means a bigger residual between the signals.

$$R^2_{F_{flapping},F_{single}} = 1 - \frac{\sum(F_{flapping} - F_{single})^2}{var(F_{flapping})N_i} \tag{3.28}$$

FOUR-WINGED FWMAV

The mass of the wings for a four-winged FWMAV is increased to obtain higher wing-to-body mass ratios and the flapping wing model is again compared with the single body model. In particular, the RMSE and the R^2 are calculated for the longitudinal Z force to assess the difference between the methods, as it is the force that presents larger differences.

Table 3.4 shows this analysis for six different single wing-to-body mass ratios, starting from 1.8% (mass ratio of the DelFly) to 15%. The differences between forces and moments grow with a higher wing-to-body mass ratio, observed by the decreasing R^2 and increasing RMSE – from a mass ratio of 8% the R^2 goes below 0.7. This means that the estimated forces and moments from the flapping wing model are very different from the forces and moments estimated from a single rigid body model. Hence, using single rigid body dynamics for higher mass ratios may result in inadequate system identification results.

The forces and moments of both methods that would act on a four-winged vehicle with mass ratio of 8% are shown in Figure 3.8.

Table 3.4: Comparison between Single Body and Flapping Models for four-winged FWMAV.

Test	Body Mass [g]	Single Wing Mass [g]	Mass Ratio [%]	RMSE Z Force [N]	R^2 Z Force
1 (real)	16.2	0.298	1.8	0.0114	0.9806
2	15.5	0.466	3	0.0183	0.9478
3	14.5	0.725	5	0.0284	0.8652
4	13.2	1.05	8	0.0413	0.6992
5	12.4	1.24	10	0.0487	0.5770
6	10.9	1.63	15	0.0639	0.2838

For a better visual interpretation of the values presented in Table 3.4, the residuals in the forces and moments between both kinematic formulations for different wing-to-body mass ratios are presented in Figure 3.9. To maximize figure readability only four ratios are considered.

TWO-WINGED FWMAV

A similar analysis was done for two-winged FWMAVs, where the mass and moments of inertia of wings two and four (bottom wings) were set to zero, thus isolating the kinematic effect of the two top wings, representing a bird-like FWMAV. Given the absence of valid aerodynamic models to adequately simulate the flight trajectories, the flight data of the real ornithopter was used for assessing the effects of varying the wing-to-body mass ratio. Instead of comparing two-winged to four-winged configurations per se, this approach estimates the impact of wing-to-body mass ratio in the difference between the forces and moments obtained by both kinematic models,. Nevertheless, it conserves the impact of the kinematic model in the parametric study and allows for the understanding of the errors of using rigid body kinematics to model a FWMAV of such configuration. For the ease of comparison, the wing-to-body mass ratios used were the same as for the four-winged FWMAV.

The results, presented in Table 3.5, indicate that the differences in the forces and moments increase more rapidly for the same wing-to-body mass ratios – the R^2 takes

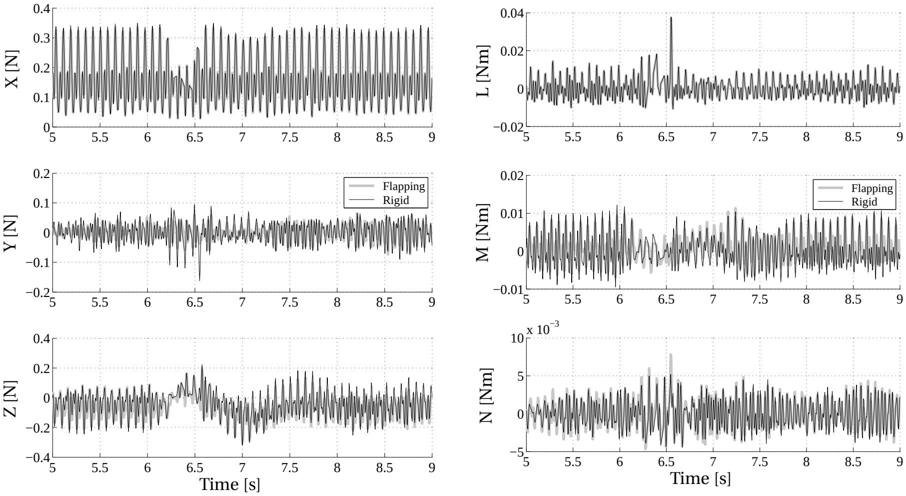

(a) Aerodynamic forces.

(b) Aerodynamic moments.

Figure 3.8: Aerodynamic forces (a) and moments (b) calculated using both kinematic models for a four-winged ornithopter with a single wing-to-body mass ratio of 8%.

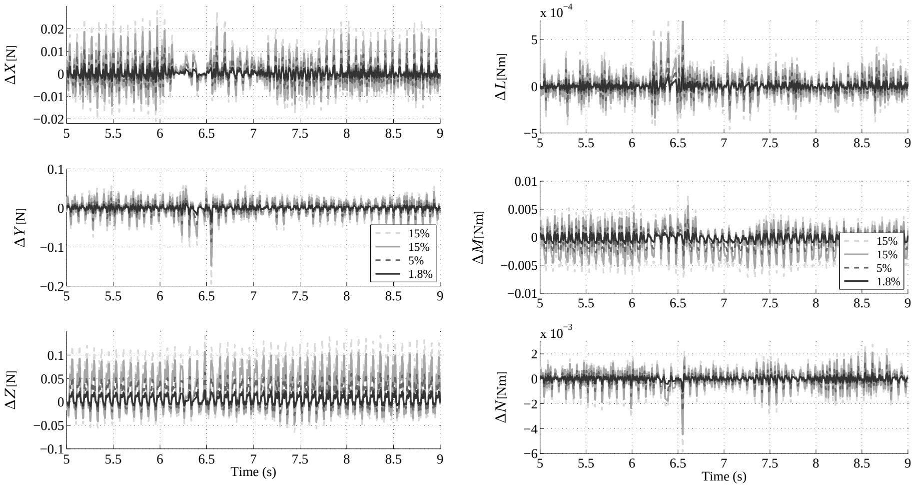

(a) Residuals of aerdoynamic forces.

(b) Residuals of aerdoynamic moments

Figure 3.9: Residuals of the aerodynamic forces (a) and moments (b) between both kinematic models, for different single wing-to-body mass ratios, from 1.8% to 15%, for a four-winged FWMAV.

values lower than 0.8 from a mass ratio above 3%, highlighting the stabilizing effect of a four wing configuration similar to the real ornithopter. The forces and moments acting on a two-winged FWMAV with mass ratio 3% are shown in Figure 3.10. As observed, the

Z force and M moment present the biggest variations among the methods.

Table 3.5: Comparison between Single Body and Flapping Models for two-winged FWMAV.

Test	**Body Mass [g]**	**Single Wing Mass [g]**	**Mass Ratio [%]**	**RMSE Z Force [N]**	**R^2 Z Force**
1	16.8	0.302	1.8	0.0492	0.8182
2	16.4	0.49	3	0.0801	0.6687
3	15.8	0.79	5	0.1287	0.4931
4	15.0	1.19	8	0.1953	0.3468
5	14.5	1.45	10	0.2360	0.2892
6	13.4	2.01	15	0.3268	0.2062

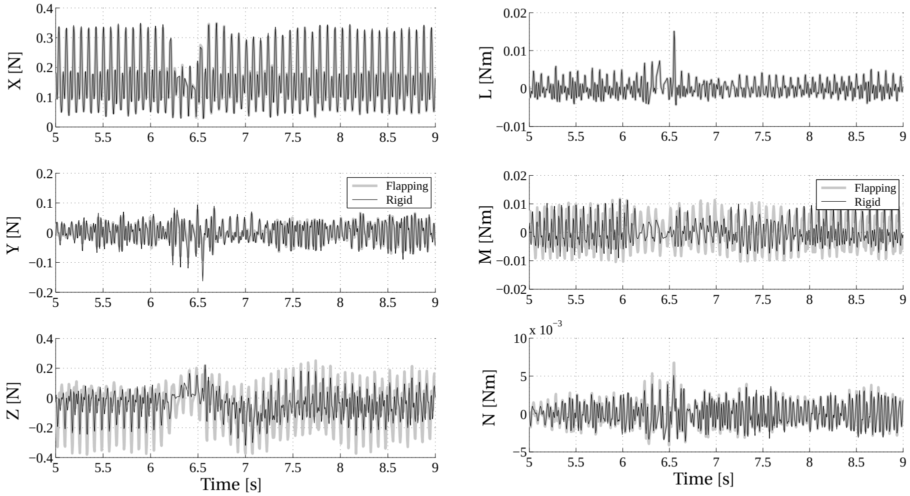

(a) Aerodynamic forces.

(b) Aerodynamic moments.

Figure 3.10: Aerodynamic forces (a) and moments (b) calculated using both kinematic models for a two-winged ornithopter with a single wing-to-body mass ratio of 3%.

The residuals of the aerodynamic forces and moments calculated between kinematic both models of a two-winged ornithopter are presented in Figure 3.11. The magnitude of the residuals shows that small changes in the wing-to-body mass ratios can result in considerable offset of the forces calculated using rigid body model, when compared to a flapping multi-rigid body kinematic model.

3.3.3 DISCUSSION

The values of R^2 presented in Tables 3.4 and 3.5 are shown in the plot of Figure 3.12 for easier comparison. For the current study, an R^2 above 0.7 was considered as being acceptable for the use of rigid body kinematics for FWMAV force reconstruction. Under

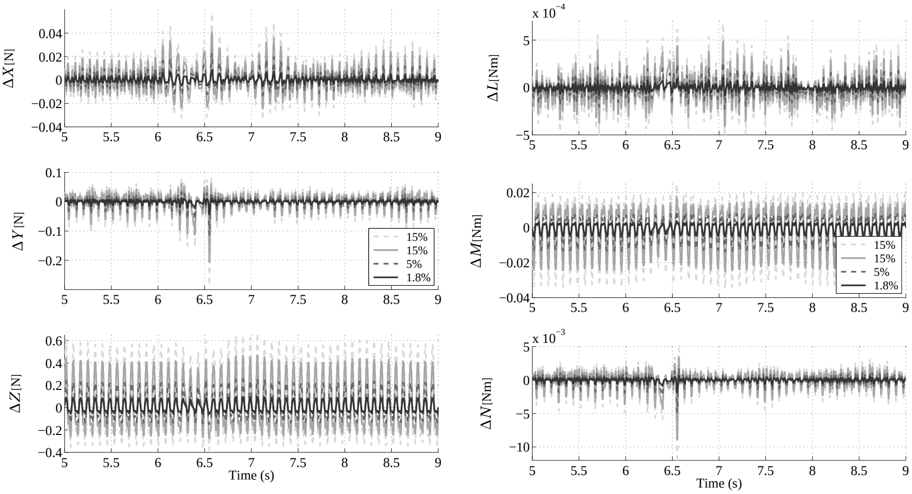

(a) Residuals of aerdoynamic forces.

(b) Residuals of aerdoynamic moments

Figure 3.11: Residuals of the aerodynamic forces (a) and moments (b) between both kinematic models, for different single wing-to-body mass ratios, from 1.8% to 15%, for a two-winged FWMAV.

this criterion, single rigid body equations of motion can be used for force and moment reconstruction of free flying FWMAVs, without considerable information loss, for cases where the flap induced oscillations are small. This is the case of ornithopters with four-wings and also two-winged ones whose single wing mass to body ratios are smaller than < 8% and < 2.8%, respectively (Figure 3.12).

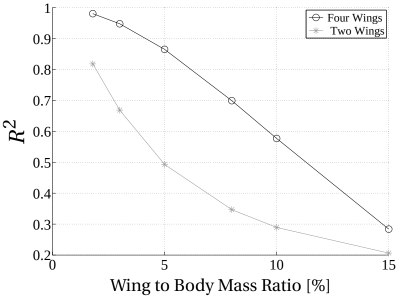

Figure 3.12: Coefficient of Determination of the Z force with mass ration for both configurations.

These results ease the aerodynamic identification procedures since single rigid body kinematics are more easily derived than multi-body ones which subsequently shortens the development time of aerodynamic models.

Despite more complex, detailed multi-body kinematics allow for the direct assessment of control forces and moments over the individual wings and driving mechanisms, with applicability advantages for FWMAVs with active control of more than one d.o.f. of the wings, as the case of insect inspired tailless designs. In the present case, a seventh generalized force Q_7 could be calculated which describes the flapping motor torque.

Multi-body formulations also allow for the separation between kinematic and aerodynamic forces and moments in the identification procedure, thus providing an assessment on the validity regions of rigid body formulations, allowing for more correct system identification in regions where rigid body formulations are not applicable. Furthermore, the use of quaternions has beneficial effects in computational efficiency, as well as in avoiding singularity issues of the Euler angles.

3.4 CONCLUSION

This study compared the aerodynamic forces and moments computed from free flight data using two kinematic formulations devised under different assumptions: a) single rigid body equations of motion, using Newton-Euler formulation, commonly know as the general aircraft equations of motion and b) multi-rigid body flapping wing kinematics using the Virtual Work Principle. In addition, it analyzed the extension of the first method to different Flapping Wing Micro Aerial Vehicles (FWMAVs) that had different wing-to-body mass ratios.

It was observed that more descriptive formulations that use multi-rigid body kinematics are suitable for complex FWMAVs, especially if they have more than one degree of freedom on the wings or are tailless designs, as these formulations allow for control force and moment determination, which is required for active control and dynamic simulation of such configurations. However, single rigid body approaches are simpler to devise, being useful for tailed or passively stable designs and for iterative studies of constantly changing FWMAV configurations, as these formulations still provide correct aerodynamic reconstruction for FWMAVs with low wing-to-body mass ratios without the need for costly derivations.

The results justify the use of single rigid body kinematics, here described as general aircraft equations of motion, for the reconstruction of aerodynamic forces and dynamic behavior of FWMAVs that have a single wing mass to body mass ratio under 8% for ‘X’ wing configurations and under 2.8% for two-winged FWMAVs, equivalent to 24% and 5.6% of total ornithopter mass being at the wings for each configuration, respectively.

These results allow for the understanding of the effects of using simple rigid body kinematic models for force reconstruction of FWMAV and, consequently, ease the characterization of ornithopters with similar configurations [Lim et al., 2012; Rose and Fearing, 2014; Shkarayev and Maniar, 2012; Hsiao et al., 2012; WSU, 2012], or ornithopters inspired in some birds or insect species, e.g., Pomatorhinus Ruficollis, Coturnix Coturnix [van den Berg and Rayner, 1995], Schistocerca Gregaria [Taylor and Thomas, 2003], Manduca Sexta [Berman and Wang, 2007].

4

ERROR ANALYSIS AND CHARACTERIZATION OF TIME-RESOLVED UNSTEADY FORCES

An accurate knowledge of the unsteady aerodynamic forces acting on a flapping wing micro air vehicle is crucial for the correct identification of aerodynamic models. In this regard, this chapter compares the quality of the forces obtained before with forces directly measured in a wind tunnel setup. A comprehensive analysis of various error sources is performed. Effects of different factors, viz. measurement errors, error propagation, numerical differentiation, filtering frequency selection and structural eigenmode interference are assessed. Comparing both methods, it is observed that the force component parallel to the fuselage determined by the two methods are similar for identical flight conditions; however, a significant difference was observed for the forces along the stroke plane of the wings. This was found to originate from the restrictions applied by the clamp to the dynamic oscillations observed in free-flight and from the structural resonance of the clamped FWMAV structure, which generates loads that cannot be distinguished from the external forces. Furthermore, the clamping position was found to have a pronounced influence on the eigenmodes of the structure and this effect should be taken into account for accurate force measurements.

This chapter was pushlied as Caetano, J. V., Percin, M., van Oudheusden, B. W., Remes, B. D. W., de Wagter, C., de Croon, G. C. H. E., and de Visser, C. C. (2015c). Error Analysis and Assessment of Unsteady Forces Acting on a Flapping Wing Micro Air Vehicle: Free-Flight versus Wind Tunnel Experimental Methods. *Bioinspiration & Biomimetics*, 10(5). Worth noting that Sections 2.1 and 2.2 of the publication were omitted for simplicity, as they were repeating information detailed in Chapter 2, regarding the FWMAV and the experimental setup for the free-flight testing.

4.1 INTRODUCTION

Animal flight has been an intriguing and long-standing field of study, in which the forces generated by the flapping wings play a central role. Initially, this mode of flight was poorly understood as studies based on the conventional fixed-wing aerodynamics did not predict a lift force generation sufficient for sustained flight [Demoll, 1919]. Only later, after dedicated investigations, the role of unsteady aerodynamics in the lift generation of small flying animals was uncovered [Ellington et al., 1996; Dickinson et al., 1999; Bomphrey et al., 2005]. Over the years, the scientific community has expanded from the study of flapping wing animals, e.g., Norberg [1972b]; Ellington [1984a]; van den Berg and Rayner [1995]; Ellington et al. [1996]; Dickinson et al. [1999] towards the study of simulated [Gebert and Gallmeier, 2002; Bolender, 2009; Gogulapati and Friedmann, 2011; Orlowski and Girard, 2011; Dietl and Garcia, 2013; Caetano et al., 2014b] and actual bio-inspired flapping wing vehicles – ornithopters [Baek and Fearing, 2010; Dietl et al., 2011; Grauer et al., 2011; Percin et al., 2012a, 2014; Keennon et al., 2012; Hsiao et al., 2012; Ma et al., 2013; Caetano et al., 2013a], which are governed by similar aerodynamic phenomena.

Although ornithopters are seldom designed as direct copies of natural counterparts, they provide a unique opportunity to better understand flapping wing flight by independent and dedicated design adjustments [Wood, 2008; Keennon et al., 2012; de Croon et al., 2012; Lee and Han, 2012; Ma et al., 2013; Karasek et al., 2014]. For instance, different parts of ornithopters, notably their wings, can be changed in a systematic way to study the consequent effects on the aerodynamics and force generation. Wings and other aspects can, thus be optimized for a particular objective, whereas for animals the 'optimization' objectives of evolution are more complicated, inter-related and likely involving other criteria than those applying to man-made designs. The research in the area of ornithopters branches into three main fields of interest: a) mechanics of flight and design, b) stability and control and c) aerodynamics, with well-established connections between them. All of these fields share the same need: the modeling of force generation mechanisms, which can only be obtained if the forces and moments that act on an ornithopter can be accurately determined and explained.

Most studies that have been carried out to characterize the forces acting on an ornithopter follow the procedure where the vehicle is rigidly mounted (clamped) to a load cell or force transducer, testing it either at zero free-stream velocity (hover configuration) [Anderson and Cobb, 2014; Nguyen et al., 2010; Baek and Fearing, 2010; Lin et al., 2006; Khan and Agrawal, 2005] or in a wind tunnel (forward flight configuration) [Lee and Han, 2012; Kim et al., 2008]. This method is a reliable and well established technique for force determination, which is advantageous for its low cost and considerably high resolution and precision. Also, it can be used for the study of isolated flapping wings and ornithopters that cannot fly stably by themselves and which are, hence, not suitable for controlled flight experiments. However, this approach tends to be limited in being representative of real flight conditions as they restrain the degrees-of-freedom of the ornithopter. Furthermore, this may lead to a difficulty in interpreting the forces as well as in relating the tested flight regime with the actual operating conditions of the ornithopter, observed in, e.g., Rose and Fearing [2014].

More recently, with the maturation of technology, it has become feasible to determine the forces acting on an ornithopter from free-flight data reconstruction methods, through the use of external tracking systems that record the position of FWMAV [Rose and Fearing, 2014; Maniar et al., 2012; Kim et al., 2012; Lee and Han, 2012; Lim et al., 2012; Dietl et al., 2011; Grauer et al., 2011]. However, the results of such methods are highly dependent on the position accuracy and time resolution of the tracking system, and can be adversely affected by filtering and discrete time differentiation techniques. Moreover, none of these studies have addressed the impact of the aforementioned factors on their final results. Given the small magnitude of the forces acting on a FWMAV, sometimes lower than 10^{-2}N, it is essential that the above-mentioned inaccuracies of these different force measurement approaches are characterized. Moreover, any possible systematic discrepancies need to be identified, if data from different sources are to be compared. First attempts to compare the forces measured by a force transducer and the forces reconstructed from free-flight position data were reported in Caetano et al. [2014a]; Rose and Fearing [2014]. These studies identified considerable differences in the forces across both experimental methods, but failed to properly explain the causes of the differences, as observed in Figure 8 of Caetano et al. [2014a]. The relevance of the forces acting along the stroke plane can be identified from previous studies: for example, such force measurements have been used to model the Lift for ornithopters that typically fly in forward flight regimes, e.g., Rose and Fearing [2014]; Lim et al. [2012]; Lee and Han [2012]; Maniar et al. [2012]; Baek et al. [2011]; Grauer et al. [2011]; Pfeiffer et al. [2010] or to model the forces needed for the control of two-winged insect inspired FWMAVs that usually fly around hover conditions, e.g., Anderson and Cobb [2014]; Ma et al. [2013]; Nguyen et al. [2010]; Wood [2008]; Khan and Agrawal [2005].

Figure 4.1 presents the contribution of the current study within a typical development cycle that connects the three areas mentioned before, with highlight on the force determination from experimental methods, aerodynamic modeling, model validation and controller development. Failure to properly characterize the flap-cycle resolved forces acting on a FWMAV will negatively affect the development cycle (Figure 4.1), where it forms an input for the aerodynamic flight model selection, supplemented with data from other research approaches, e.g., semi-analytical, computational or experimental. As a consequence, this will negatively affect the development of controllers for automated flight and computational flight simulations.

In this study, we provide a detailed examination of the possible sources of errors and uncertainties in the determination of the flap-cycle resolved forces that act on a FWMAV for free-flight and balance mounted wind tunnel experimental methods. The study focuses on the force components acting in the longitudinal (symmetry) plane, due the their importance in defining the lift, drag/thrust and control forces in FWMAVs. The measurement data are analyzed in detail, referring to data from tests made in vacuum and analysis of natural frequency modes, which allows to identify the causes of differences in the determined forces and to issue recommendations for proper force measuring protocols.

The chapter is organized as follows (see Figure 4.1). Section 4.2 describes the experimental methods used to obtain the forces acting on the ornithopter in free-flight and clamped configurations. Section 4.3 is dedicated to the analysis of the noise and errors affecting the measurements of both experimental methods and provides, at the end, an

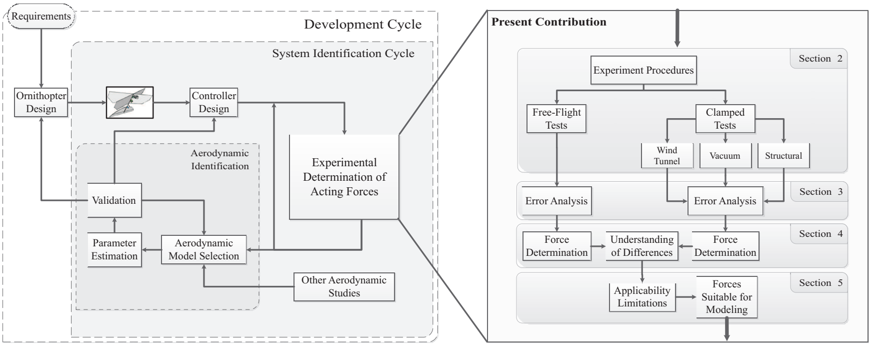

Figure 4.1: Contribution of the current study, including breakdown of the article outline, within a typical development cycle that is focused on determining the forces acting on a FWMAV.

interpretation of the content of the forces in the frequency domain. Section 4.4 explains the differences found in the forces that were acquired by clamping the FWMAV at different positions and compares the temporal evolution of the forces in a flapping cycle for both experimental methods. The impact of this study on the experimental force determination of ornithopters is detailed in the last section (section 4.5), which issues a set of recommendations for future implementations of similar experimental methods.

4.2 EXPERIMENTAL PROCEDURES

The present section describes the experimental procedures that are used to obtain the unsteady forces acting on the FWMAV.

4.2.1 FREE-FLIGHT EXPERIMENTS

The free-flight experimental methods and flight path reconstruction techniques were presented previously in Chapter 2. This section details only the aspects that are necessary to compute the Lift and Drag forces from the free-flight data, as well as the test points that were selected from this data for wind tunnel testing.

Figure 4.2 presents the values of the angle of attack with the total velocity for the flight conditions experienced by the FWMAV. It contains about 330 thousand points (in gray), corresponding to about 28 minutes of recorded flight time. The denser part of the cloud of points consists of the flight conditions of this FWMAV for trimmed automatic flight. The dispersion around the dense area corresponds to maneuvers that were performed for system identification purposes, as presented in Chapter 2. The black markers indicate eight conditions of trimmed flight regimes that were selected for the comparison with the wind tunnel tests.

The Lift and Drag, which are typically more used for aerodynamic studies, can be computed by applying a transformation to the X and Z forces from the Body reference frame to the relative wind reference frame ($\boldsymbol{x_b}$ is aligned with $\boldsymbol{V}$):

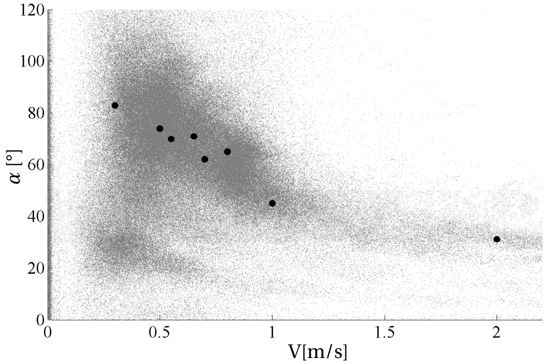

Figure 4.2: Reconstructed angle-of-attack (α) versus total velocity $|\boldsymbol{V}|$. The black markers denote the flight conditions that were selected for wind tunnel comparison.

$$\begin{aligned} Lift &= X\sin\alpha - Z\cos\alpha \\ Drag &= -X\cos\alpha - Z\sin\alpha \end{aligned} \tag{4.1}$$

However, as evident from Eq. 4.1, this representation of forces is affected by the definition of the angle of attack (α), and mixes the X and Z forces that are more readily reconstructed, which could hinder the understanding of the factors that can be of influence in the comparison of experimental data obtained with the two different methods. Consequently, the X and Z forces will be used for the comparison between experimental methods.

4.2.2 CLAMPED EXPERIMENTS

Three different methods were used to broaden the understanding of the factors affecting the forces for obtained from clamped experiments: a) wind tunnel; b) vacuum chamber; and c) assessment of natural structural modes.

WIND TUNNEL EXPERIMENTS

Experiments were performed in a low-speed wind tunnel, capable of delivering stable and laminar flows at speeds as low as 0.3m/s. It has an open test segment, with cross-section dimensions of $(0.6\times0.6)\text{m}^2$. Six components of forces and moments acting on the clamped FWMAV were measured by use of an ATI Nano-17 Titanium force transducer that was attached to a variable pitch mechanism (d) in Figure 4.3). Note that only the two longitudinal components of the captured forces (i.e., X and Z forces) are used for further analysis and comparison with the free-flight estimated forces. The sensor is calibrated to have a resolution of 0.149 gram-force without filtering in all directions. A hot-wire anemometer was used to accurately measure the free-stream velocity, corrected by a thermocouple (Figure 4.3).

A microcontroller system was used to regulate the flapping frequency. It logs the electrical commutations of the brushless motor for high resolution rotational information and reads a Hall sensor signal from the wing driving gear for referencing. A Field-

Table 4.1: Free-flight Test Conditions Replicated in the Wind Tunnel experiments.

Test #	**Velocity V** [m/s]	**Pitch Angle θ**[°]	**Flap Frequency δ_f** [Hz]	**Reduced Freq.** k
1	0.30	83	13.3	0.38
2	0.50	74	12.5	0.32
3	0.55	70	12.5	0.27
4	0.65	71	12.5	0.25
5	0.70	62	11.7	0.23
6	0.80	65	13.3	0.20
7	1.00	45	11.7	0.12
8	2.00	31	10.3	0.06

Programmable Gate Array (FPGA) system of National Instruments was used for data acquisition of the forces and moments, as well as motor phase, voltage and current which were recorded at a rate of 10kHz. The relation between the rotational information captured by the microcontroller system and the phase angle of the wings was assessed by means of high speed image capture syncing. A Photron Fastcam SA 1.1 camera was placed in front of the experimental model to record the spatial positions of the leading edges of both upper and lower wings to determine the stroke angle during the flapping cycle. A series of 1200 images were recorded at 1.2kHz.

The forces were captured for different conditions corresponding to real ornithopter level flight, with the pitch $\theta \in [30, 83]^\circ$ and velocity $|\boldsymbol{V}| \in [0.3, 2]\text{m/s}$. As depicted by the black markers in Figure 4.2, the comparison test points were selected to cover a representative set of the real flight envelope of the ornithopter – the flight conditions of these points are shown in detail in Table 4.1.

To assess the level of contamination of the measured forces by structural resonating modes, the tests were performed for three different clamping positions, defined with respect to the nose of the ornithopter: P1=35mm (under wing clamp); P2=96mm (center clamp); P3=142mm (under tail clamp) – as depicted in Figure 4.4.

VACUUM CHAMBER EXPERIMENTS

In the wind tunnel experiments, the force sensor responds to both the aerodynamic and inertial forces, as well as the mechanical vibrations of the components. As a consequence, proper analysis of the time-history of the aerodynamic forces requires more elaborate investigation to assess the ratio between the aerodynamic and inertial contributions in the measured forces. For this reason, complementary force measurements were performed in a vacuum environment. At a pressure level of 1mbar the ornithopter was clamped to the force sensor approximately at the middle-clamp position (P2). As a general remark, the tests in vacuum are meant to be compared with hover flight condition.

STRUCTURAL ANALYSIS EXPERIMENTS

To further understand the sources of the differences in the collected forces found in the wind tunnel experiments for different clamping positions, the natural vibrational modes of the ornithopter were captured by applying a static impulse-response test of the structure. The impulse was applied at the nose of the ornithopter, for the different clamping

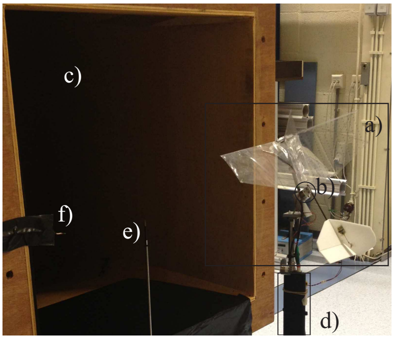

Figure 4.3: Wind tunnel experimental setup: a) DelFly FWMAV; b) ATI Nano-17 force transducer; c) open section wind tunnel; d) actuated strut that allows for attitude changes in pitch and yaw; e) hot-wire anemometer; f) thermocouple for temperature corrections on the hot-wire.

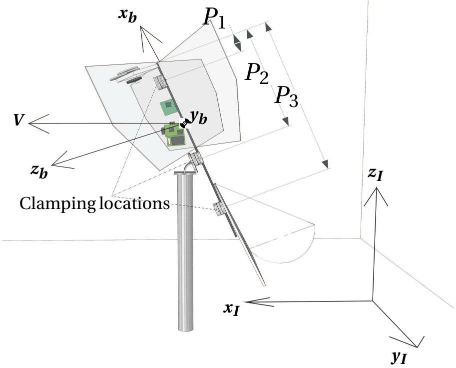

Figure 4.4: Schematic of the ornithopter in wind tunnel testing, with indication of different clamping positions (P1,P2,P3), Inertial ($\boldsymbol{x_I}, \boldsymbol{y_I}, \boldsymbol{z_I}$) and Body ($\boldsymbol{x_b}, \boldsymbol{y_b}, \boldsymbol{z_b}$) reference frames.

positions to determine the dominant natural modes, in particular that of the forward part which is responsible for the force generation (wing section). These experiments are complemented with a finite elements method (FEM) based analysis in CATIA, by modeling a structure with physical properties similar to those of the actual ornithopter. In particular, it incorporates a carbon beam structure and a mass distribution of the components (wings, flapping gear and tail) that is equivalent to the real configuration.

4.3 ERROR ANALYSIS AND ASSESSMENT OF FORCE FIDELITY

This section reports the important characteristics of the experimental data from both free-flight and wind tunnel measurements, notably the error levels and reliability, and explores the impact of the data processing techniques used to calculate the resultant forces. Worth noting that the forces obtained from both the free-flight and the fixed-base experiments contain the aerodynamic and kinematic contributions of the wing flap.

4.3.1 FREE-FLIGHT FORCE DATA

Calculating the forces acting on a FWMAV in free-flight from discrete time position measurements can result in the accumulation of substantial errors to the final force results. Besides the sampling frequency, other factors can negatively impact the reliability of the forces, viz. position measurement errors, propagation of the uncertainties into the differentiated states and the impact of the numerical differentiation scheme. Figure 4.5 shows each process and the need for that step in terms of its specific objective, with each block representing a part of the present Section. The most relevant error sources to be considered are: a) systematic errors that can cause bias in the measured positions of the markers and thus the inferred position and attitude data; b) high noise levels (random errors) and hence low signal-to-noise ratio that may degrade the force reconstruction.

Numerical differentiation of the discrete position data has a twofold effect on the characteristics of the derived state: a) modulation of the signal due to the low-pass filtering effect of the numerical differentiation schemes; b) amplification of the measurement error. The former is of particular interest in the case where the sampling rate of the position data is insufficient with respect to the flapping frequency, since the low-pass filtering effect can attenuate the data in the frequency range of interest. The impact of the latter, on the other hand, depends on the quality of the position information, i.e., error level in the visual tracking measurements.

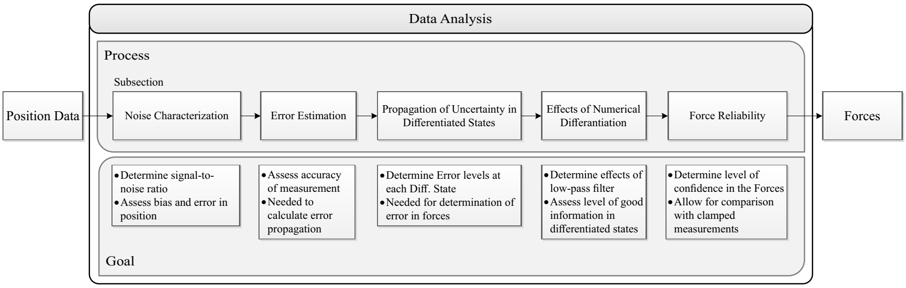

Figure 4.5: Analyses needed for the processing of the position data and assessment of quality of the reconstructed forces, including breakdown of Section 4.3.1.

NOISE CHARACTERIZATION

The estimation of the measurement error level of the visual tracking system is a challenging procedure as it is strongly dependent on the camera layout, the position of the ornithopter in the room, its acceleration and attitude, as well as the retro-reflector size. If the error was found to be non-random, the final reconstructed forces would be unsuitable for the comparison of methods. As the first step in the error analysis, the error in the position measurements is modeled as a random error $v(k)$ [Mettler, 2010]:

$$\hat{x}(k) = x(k) + v(k), \quad \hat{x}(k) \text{ the estimated position; } x(k) \text{ the real position;} \tag{4.2}$$

To quantify the error in the measured states, the measurement error $v(k)$ was assumed to be a zero-mean, independent identically distributed (IID) random variable [Mettler, 2010], i.e., $v(k) \in IID(0,\sigma^2)$; this assumption will be verified along this section. Given the absence of concentrated noise peak in the frequency spectrum of the position measurement, the residual of the measured state was calculated according to:

$$\epsilon(k) = \hat{x}(k) - \hat{x}_{f_c}(k) \tag{4.3}$$

with $\hat{x}_{f_c}(k)$ being the state filtered at a cut-off frequency f_c, by applying a Chebyshev type II low-pass filter design [1]. To confirm the hypothesis of the residual being a zero-mean IID process, the autocorrelation function of the residual, $\rho_\epsilon(k)$, must respect the

---

[1] Implemented in Matlab with the command `design(fdesignhandle,'cheby2','MatchExactly','stopband')`.

95% confidence criterion bounded by the interval of $\pm 1.96/\sqrt{n}$, where n is the number of samples [Brockwell and Davis, 2006]. The autocorrelation function (ρ) of a process can be presented as in Eq. 4.4 [Brockwell and Davis, 2006]:

$$\rho(l) = \frac{\gamma(l)}{\gamma(0)} \tag{4.4}$$

where $\gamma(l)$ is the autocovariance function at the lag l given by:

$$\gamma(l) = cov[\epsilon(t), \epsilon(t+l)] = E[(\epsilon(t)-\mu)(\epsilon(t+l)-\mu)] \tag{4.5}$$

with μ the expected value of the process.

The method used to characterize the random error is affected by the number of samples and autocorrelation lags that are used. For instance, a small number of samples does not allow one to infer the nature of the noise affecting the measurements, as there are no statistical means of assessing the confidence interval; whereas a large number of samples will yield a very small confidence bound determined by $\pm 1.96/\sqrt{n}$, given the large n. The distribution of the correlation function $\rho(l)$ is also influenced by the number of samples (N) and the maximum number or lags (L). Moreover, it was found that including all the samples in a test file would result in the over-estimation of the confidence level as the autocorrelation function will take very small values for high lags between correlated residuals, hence being under the 95% confidence interval.

Box et al. [2008] indicate that the sample size should contain enough points ($N > 50$) and that the lags should be $L \leq \frac{N}{4}$. Based on this, the confidence intervals were assessed with sample sizes N of 300 to 800 samples (corresponding to 0.75sec to 4sec) with $L = \frac{N}{4}$; the selection of L is justified by the need to include enough data for statistical repetition of flap cycles. The number of samples that minimizes the correlation of residuals was found to be 400 samples (equivalent to two seconds of flight), which results in correlation windows of 100 samples (0.5sec) that include, on average, six flap cycles.

The cyclic nature of the flapping motion will cause correlations to occur around the lag times that are correspondent to the flapping frequency. Hence, to suppress this correlation for the assessment of the system noise, the measurement on a static, non-moving, non-flapping ornithopter was used, for which the position of the markers in time was measured and the methodology detailed before was applied. Eq. 4.3 was used to compute the residuals of the states, using a cut-off frequency of f_c =1Hz. A power spectral density (PSD) of the residuals for each position was computed and is presented in Figure 4.6a. If the process was not IID, there would be a correlation between noise values over a given time interval. In a PSD, this would appear as a one or multiple clear peaks. For further clarification, the correlation of the residuals is presented in Figure 4.6b. These results verify the hypothesis of the random error being a realization of an IID process.

The noise analysis on the static marker does not take other influential factors into account, viz. the marker position, the attitude and the acceleration of the ornithopter. Therefore, a similar methodology was applied to free-flight measurements by varying f_c within the interval of $[10, 90]$Hz, with a 1Hz increment and re-calculating Eq. 4.3 in order to assess the characteristics of the measurement noise. This facilitates the selection of the cut-off frequency (f_c) for further analysis, such that the frequency value that minimizes the correlations between the residuals can also be used in the low-pass filtering

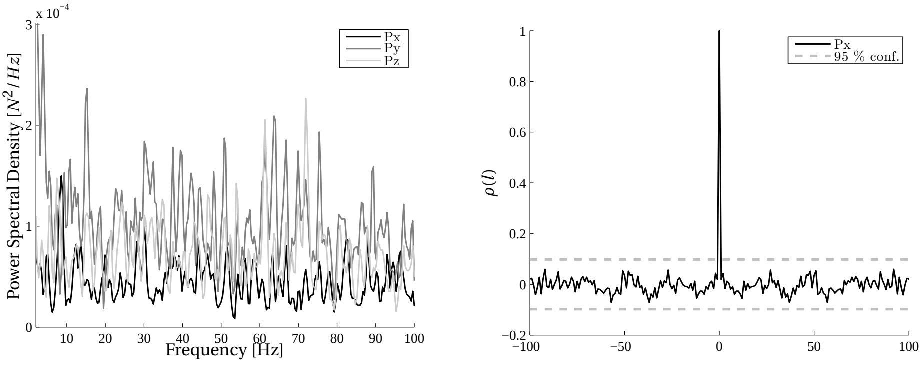

(a) Power spectral density of the position measurements taken in the Inertial frame, over the frequency spectrum.

(b) Autocorrelation plot for the residuals computed using Eq. 4.3, with f_c =1Hz.

Figure 4.6: Confirmation of white noise hypothesis for the noise affecting the position measurements of a static measurement.

of the data to minimize the impact of the measurement noise and hence increasing the signal-to-noise ratio.

For each flight test, the autocorrelation of the residuals of the position measurements in each axis of the Inertial frame was calculated using Eq. 4.4. Similarly, sample sizes of 400 points, with lag windows of 100 samples were used. This is followed by the determination of the percentage of points between the 95% confidence bounds, determined by $\pm 1.96/\sqrt{n}$. The results of the average percentage of points within the confidence bounds for the three position measurements in (x_I, y_I, z_I), respectively (P_x, P_y, P_z), are presented in Figure 4.7a for one of the tests, as an example.

As evident in Figure 4.7a, the percentage of points under the 95% confidence bound is below 95% for all cut-off frequencies. It can also be seen that a higher correlation between the residuals occurs just before the multiples of the flapping frequency, which is revealed by the dips occurring prior to the vertical dashed lines of Figure 4.7a. This is explained by the higher signal-to-noise ratio around each multiple of the flapping frequency. These results condition the selection of the cut-off frequency of the low-pass filter that will be used for the comparison of the wind tunnel and the free-flight reconstructed forces, as explained further down in this Section.

Figure 4.7b presents the autocorrelation values of the residuals for the position measured along $\boldsymbol{x}_I$, computed using Eq. 4.3 with a $f_c = 40Hz$, as it corresponds to one of the frequencies with the highest percentage of uncorrelated points. For this case, 92% of the autocorrelation points were within the confidence bounds, close to the theoretical 95%. A higher percentage of uncorrelated points could not be obtained due to the correlations that occur in the vicinity of the lags equal to multiples of $record_{freq}/flap_{freq}$, which for the case shown is equal to 16 time steps. An assessment of the noise affecting the measurements that is based only on the autocorrelation study may lead to wrong conclusions about any trending or correlation in the data [Shalizi, 2013], and should be done together with trend assessment based on the correlation between the residuals at each lag. Such analysis was performed and is presented in Appendix C. It was concluded that the correlations only existed in the vicinity of the lags mentioned before (lag = 1, 16,...). Combining the results, it is concluded that the noise affecting the measurements can be considered a realization of an IID process.

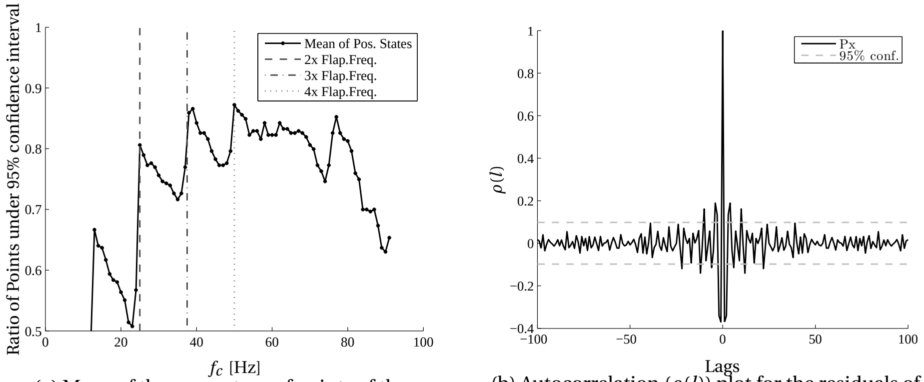

(a) Mean of the percentage of points of the position states (P_x, P_y, P_z) under 95% confidence interval, at different cut-off frequencies f_c.

(b) Autocorrelation ($\rho(l)$) plot for the residuals of the position in $\boldsymbol{x}_I$ (P_x) computed using Eq. 4.3, with f_c =40Hz.

Figure 4.7: Example of Autocorrelation of the residuals of the position measurements for one of the free-flight tests: test #3.

ESTIMATION OF ERROR IN POSITION DATA

Given the absence of additional sensors to perform flight path reconstruction, the uncertainty in the position of each marker was assessed by comparing the relative distances between the markers during free-flight with the actual geometric distance, which was measured using a caliper before the flights. This procedure was carried out for all markers, including those placed at the moving parts of the ornithopter (wings, elevator and rudder). This way, the uncertainty in the position of the markers will include all error sources associated with, e.g., streak line precision loss (motion blur at each sample of the tracking system), centroid determination and random process noise in the system.

The standard deviation of the difference between the relative distance of the markers measured by the tracking system and the real physical distance was used to estimate the uncertainty in the absolute position of each marker, as measured by the tracking system. As an example, let NS and TE represent the position of the markers placed at Nose and Trailing Edge of the FWMAV (see Figure 2.1b) and $\overline{NSTE}_{tracker}$ be their measured relative distance during the flight test, whereas $\overline{NSTE}_{real}$ is the actual distance measured with a caliper. We have:

$$Error_t = \overline{NSTE}_{tracker_t} - \overline{NSTE}_{real} \tag{4.6}$$

as the error of the tracking system at time t. By defining the standard deviation of $Error_t$ as σ_{Error} and assuming that the errors in the position of both markers are uncorrelated exhibiting equal standard deviation, it results that this position uncertainty [Bohm and Zech, 2010] is equivalent to:

Table 4.2: Position Uncertainty Affecting Marker Position Measurement as Standard Deviation of Half of Relative Marker Distance Error. Nose (NS), Trailing Edge (TE), Right Wing (RW), Left Wing (LW), Horizontal Stabilizer (HS), Vertical Stabilizer (VS), Elevator (EL), Rudder (RD).

		Position Uncertainty [mm]									Attitude Angle Uncertainty [°]
	Marker →	NS	TE	RW	LW	HS	VS	EL	RD	Mean	
Test	1	0.14	0.14	0.27	0.35	0.16	0.17	0.07	0.10	0.13	0.16
	2	0.08	0.08	0.10	0.31	0.08	0.12	0.05	0.10	0.09	0.09
	3	0.09	0.09	0.22	0.21	0.09	0.14	0.05	0.12	0.10	0.10
	4	0.08	0.08	0.32	0.44	0.19	0.12	0.15	0.08	0.12	0.09
	5	0.23	0.23	1.79	0.33	0.15	0.23	0.73	0.12	0.28	0.25
	6	0.12	0.12	0.84	0.40	0.20	0.17	0.16	0.09	0.14	0.14
	7	0.09	0.09	0.28	0.16	0.16	0.13	0.13	0.09	0.12	0.10
	8	0.17	0.17	0.25	0.33	0.19	0.19	0.15	0.06	0.16	0.17
Pair Relation		TE	NS	NS	NS	TE	TE	HS	VS	—	—

$$\sigma_{NS} = \sigma_{TE} = \frac{\sigma_{Error}}{2} \tag{4.7}$$

It was previously observed in Chapter 2 and Caetano et al. [2013c] that the uncertainty in the position of the markers is a function of the flight velocity, attitude rate of change and the area of the flight chamber where the measurements are taken. The method used for the uncertainty analysis described in this Section accounts for all these factors in a statistical a-posteriori manner, allowing for the consequent calculation of the uncertainties propagated into the differentiated states. This approach was generalized to provide error estimates for all markers by grouping them in pairs, such that the uncertainty in the position of the markers placed on the wings and control surfaces can be determined by relating them to markers that are rigidly attached to the body of the FWMAV. Table 4.2 presents the uncertainty in the position of the markers using the method explained above. The pairwise marker relation is presented in the last row of Table 4.2, under the following convention for the marker locations: Nose (NS), Trailing Edge (TE), Right Wing (RW), Left Wing (LW), Horizontal Stabilizer (HS), Vertical Stabilizer (VS), Elevator (EL), Rudder (RD). Such pair relation was selected in detriment of other methods such as full marker combination, as it results in a more conservative confidence bound for the comparison between methods. The values of the position uncertainties calculated for each marker agree with the velocity and acceleration that affect them. Particularly, the uncertainties are higher for the markers on the wings (RW, LW), due to the fast wing flap. The last column of Table 4.2 presents the uncertainty in the calculated attitude angle of the FWMAV. It was assumed to be equal for all (ϕ, θ, ψ) angles since it only uses the markers that are rigidly attached to the body, and calculated using:

$$\sigma_{\phi} = \sigma_{\theta} = \sigma_{\psi} = \arctan\left(\frac{\sigma_{NS} + \sigma_{TE}}{\overline{NSTE}_{real}}\right) \tag{4.8}$$

PROPAGATION OF ERROR INTO DIFFERENTIATED STATES

A discrete time differentiation method was selected for the calculation of the states necessary for the evaluation of Eq. 3.1 from position data, instead of fitting the position data with continuous functions, e.g., splines, as the latter method tends to add information to the dataset and mask the dynamics of the platform. Nevertheless, the selected method can add considerable errors to the differentiated rates whose magnitudes depend on the number of points used in the differentiation and sampling frequency. The uncertainty in the differentiated states, and consequently in the forces, can be determined using the following error-propagation expression, as indicated in Bevington and Robinson [2003]:

$$\sigma_f^2 = \sigma_x^2\left(\frac{\partial f}{\partial x}\right)^2 + \sigma_y^2\left(\frac{\partial f}{\partial y}\right)^2 + \ldots + 2\sigma_{xy}^2\left(\frac{\partial f}{\partial x}\right)\left(\frac{\partial f}{\partial y}\right) + \ldots \quad \text{for } f = f(x, y, \ldots) \tag{4.9}$$

As the errors in different states are shown to be uncorrelated, the cross-variance term in Eq. 4.9 can be omitted. This assumption was validated by comparing it with a statistic calculation of the expected value of the uncertainty propagated into the differentiated state, by distributing the uncertainty in the original state between zero and σ_{state}, with a random number generator, for an analysis with 10^6 calculations. The difference between the methods was under 2%.

EFFECTS OF NUMERICAL DIFFERENTIATION

Concerning the numerical differentiation methods, a non-central two-point finite difference scheme, either forward [2] or backward, will result in a time shift of the data and amplify the error levels by a factor equal to the sampling frequency used, viz. 200. Higher Kernel methods, like the five point Lagrange, have shown to remove dynamics from the data, due to smoothing. Therefore, a three-point central difference (Eq. 4.10) was found to be better suited, as it reduces error amplification by a factor of two when compared to two-point methods, as well as not introducing time lags nor significant smoothing. A more extensive study on the fundamental characteristics of these methods for such data can be found in Marble et al. [1981].

Table 4.3 presents the errors affecting each differentiated state for the three different differentiation methods mentioned – non-central two-point (2Pt), central three-point (3Pt) and central five-point Lagrange (5Pt) – for four free-flight tests using Eq. 4.9.

Determining the forces from free-flight position measurements (from Eq. 3.1 that) involves the differentiation of several quantities: velocities (u, v, w) by differentiation of the discrete time-series position data with respect to time once and accelerations $(\dot{u}, \dot{v}, \dot{w})$ by differentiating the data twice. For this purpose, the common practice is to use finite difference algorithms that can approximate the continuous derivative values. In the present study, a second-order accurate three-point central difference algorithm is used for the calculation of time-derivative of the discrete time-series position and angle data:

$$\dot{x}_t = \frac{x_{t+1} - x_{t-1}}{2\Delta t} \tag{4.10}$$

---

[2] indicated in supplementary material, available online

Table 4.3: Position Uncertainty Propagated into the Reconstructed States and Forces.

Test	Diff. Method	Velocity [m/s]			Acceleration [m/s^2]			Ang. Vel. [rad/s]			Forces [N]	
		u	v	w	$\dot{u}$	$\dot{v}$	$\dot{w}$	p	q	r	X	Z
3	2Pt	0.026	0.034	0.034	7.23	9.49	9.46	0.53	0.50	0.02	0.128	0.167
	3Pt	**0.013**	**0.017**	**0.017**	**1.79**	**2.40**	**2.40**	**0.26**	**0.25**	**0.05**	**0.031**	**0.041**
	5Pt	0.017	0.022	0.023	3.21	4.30	4.32	0.35	0.34	0.02	0.057	0.075
6	2Pt	0.034	0.025	0.025	9.58	7.12	7.22	0.79	0.65	0.13	0.169	0.126
	3Pt	**0.017**	**0.013**	**0.013**	**2.42**	**1.80**	**1.80**	**0.40**	**0.33**	**0.13**	**0.042**	**0.031**
	5Pt	0.023	0.017	0.013	4.27	3.22	3.22	0.53	0.43	0.09	0.075	0.057
7	2Pt	0.025	0.025	0.025	7.30	7.22	7.21	0.51	0.50	0.005	0.127	0.125
	3Pt	**0.013**	**0.013**	**0.013**	**1.80**	**1.78**	**1.77**	**0.26**	**0.25**	**0.19**	**0.032**	**0.031**
	5Pt	0.017	0.017	0.0172	3.26	3.22	3.27	0.35	0.34	0.003	0.058	0.056
8	2Pt	0.048	0.017	0.02	13.6	4.80	4.73	0.56	0.77	0.25	0.255	0.093
	3Pt	**0.024**	**0.009**	**0.008**	**3.40**	**1.20**	**1.17**	**0.27**	**0.38**	**0.34**	**0.063**	**0.026**
	5Pt	0.032	0.012	0.011	6.18	2.19	2.14	0.37	0.52	0.17	0.115	0.043

where $\dot{x}$ is the time-derivative of the data, x, t is the index for discretized time and Δt is the time between two data points. The main reasons behind the selection of this scheme can be counted as: a) its higher order of accuracy (smaller truncation error) compared to forward and backward differencing schemes; b) non-existent time-shift of the resultant force data; c) relatively favorable measurement error amplification characteristics compared to first-order accurate schemes. When forward or backward difference algorithms are used, the standard deviation of a differentiated quantity ($\sigma_{\dot{x}}$) equals to $\sqrt{2} \times \sigma_x \times f_{daq}$ with σ_x being the standard deviation of the measured quantity (e.g., position) and f_{daq} being the data acquisition frequency. In the case of three-point central difference scheme, it reads $\sigma_x \times f_{daq}/\sqrt{2}$, which is two times smaller.

It could also be considered to use more points for the calculation of the derivatives; however, the sampling frequency of the measurements (i.e., 200 Hz) compared to the nominal flapping frequencies during the flight (9-13 Hz) will result in excessive smoothing of the data and thus loss of information in the resultant force oscillations. Still, the three-point central difference algorithm also acts as a low-pass filter, the influence of which should be identified for the proper analysis of the data. For this purpose, an analytical analysis was performed on a generic sinusoidal signal ($x(t) = \sin(\omega t)$, where ω is the angular frequency) to calculate the ratio of the amplitudes of the numerically-differentiated and true derivatives [3]. For the three-point central difference algorithm, this ratio reads (cf. Appendix C for derivation.) [Bahill et al., 1982]:

$$\left| \frac{\dot{X}_{d,c}(\omega \Delta t)}{\dot{X}(\omega)} \right| = \frac{\sin(\omega \Delta t)}{\omega \Delta t} \tag{4.11}$$

For a two-point forward difference algorithm, this ratio is:

---

[3] the reader is referred to Appendix C for the detailed calculations.

$$\left|\frac{\dot{X}_{d,f}(\omega\Delta t)}{\dot{X}(\omega)}\right| = \frac{\sqrt{2}\sqrt{1-\cos(\omega\Delta t)}}{\omega\Delta t} \tag{4.12}$$

By use of Eq. 4.11 and 4.12, the frequency characteristics of the central and forward difference algorithms can be calculated. In the free-flight measurements, the sampling frequency was 200Hz (Δt=0.005s) so that the maximum frequency component that can be captured without aliasing is 100Hz according to Nyquist-Shannon sampling theorem. The effect of numerical differentiation on the frequency components is simulated in Figure 4.8.

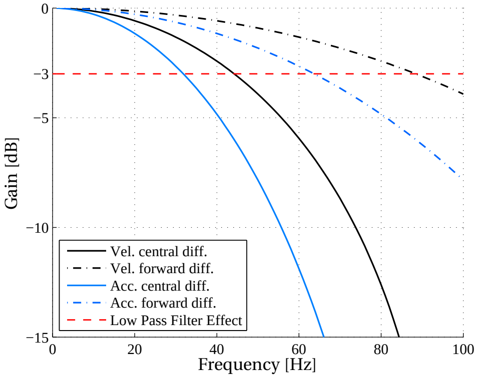

Figure 4.8: Attenuation of the magnitudes of the frequency contents in the calculation of velocities and accelerations by use of central and forward difference schemes. Red dashed line indicates attenuation of -3 dB, equivalent to a half amplitude low pass filter effect.

In the calculation of velocities from the measured marker positions, it is evident that the central difference algorithm attenuates the signal by 3dB at 44Hz, which occurs at 88 Hz for the case of forward-difference methods. For the accelerations, it is at the frequency of 32Hz and 64Hz for the central and forward difference methods, respectively. It becomes clear that first-order accurate algorithms have more favorable frequency response characteristics because of the smaller time interval used in the calculation of the derivative. However, the use of these algorithms introduces a phase lag in the data and result in a time-shift in the calculated forces, which is the main reason not to utilize first-order forward and backward difference schemes.

Assessment of Information Lost due to Differentiation To quantify the information that is lost due to filtering effect of the discrete numerical differentiation scheme in time, the accelerations were also calculated by differentiating the velocity data in the frequency domain. In free-flight it is not possible to assure that the ornithopter flies parallel to one of the horizontal axis of the Inertial reference frame, which results in a spread of the position information over all directions in that frame. As a consequence, this changes the frequency spectrum of the signal along each measurement axis, making frequency domain differentiation infeasible in general for real-life application. Such differentiation in the frequency domain is done by performing a Fast Fourier Transform (FFT) ($\mathscr{F}$) on the velocity data, multiplying it by $j\omega$, and performing an inverse of the FFT ($\mathscr{F}^{-1}$) to these values. This is shown in Eq. 4.13, where a, $\boldsymbol{V}$, F_s stand for the acceleration, velocity and sampling rate, respectively. As a general note, such method should only be applied to de-trended data, which was the case for the velocities in the Body reference frame.

$$a = \mathscr{F}^{-1}[(\mathscr{F}(V)/F_s) \times j\omega \times F_s] \tag{4.13}$$

The amount of information that is filtered by the second discrete differentiation in time applied to the velocities is presented in Figure 4.9 in terms of PSD decay of the differentiated states. The full and dashed lines represent the PSD of the accelerations calculated using central difference algorithm and differentiation in the frequency domain, respectively. The decay of the amplitudes for the case of numerical differentiation in the time domain is considerable for frequencies that are higher than three times the flapping frequency (third peak in the spectrum, not considering the peak of 1Hz caused by the steady-state values of the time domain), compared to the case of differentiation in frequency domain. However, since the latter adds energy at higher frequencies due to the multiplication by $j\omega$ (Eq. 4.13), the real non-filtered PSD is considered to be between between both curves. For lower frequencies, up to the three times the flap frequency, the filtering effect of time differentiation can still be considered marginal.

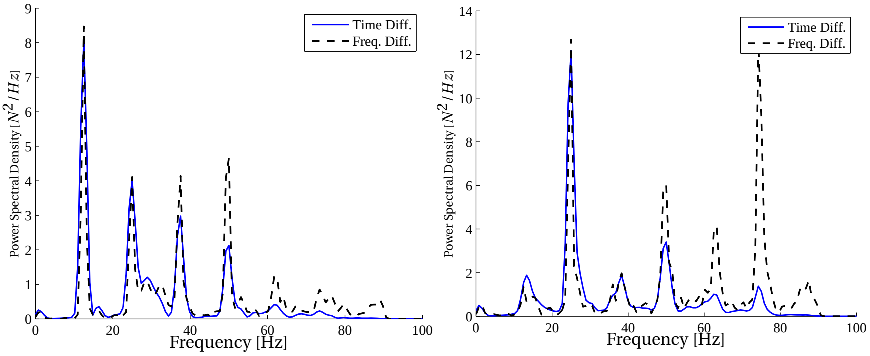

(a) Acceleration along $\boldsymbol{x}_b$, $\dot{u}$

(b) Acceleration along $\boldsymbol{z}_b$, $\dot{w}$

Figure 4.9: Power spectral density of the longitudinal accelerations calculated using discrete time central difference (solid blue) and frequency domain differentiation (dashed black), for test #1, δ_f = 13.3Hz. There is no considerable loss in the energy of the signal for frequencies below 40Hz (three times the flapping frequency).

Figure 4.10 compares the temporal variations of the forces calculated for test #1 (δ_f = 13.3Hz) using the numerical differentiation in time domain (solid blue) or frequency domain (dashed black) in the determination of accelerations. A low-pass cut-off frequency of 40Hz (just above three times the flap frequency) was applied to the force data to maximize the uncorrelated residual results identified in Figure 4.7a, as well as guarantee a high signal-to-noise ratio, seen in Figure 4.9 at 40Hz. The amount of information filtered by the time differentiation method is small, compared with the time evolution of the forces and considered to be marginal for the effect of comparing free-flight with wind tunnel measured forces.

As a general remark, one should be aware of the significant filtering effects which the numerical differentiation algorithms may introduce in the calculation of time-derivatives of the discrete measurement data. For instance, for the specific test conditions considered in this case, a sampling frequency of 100Hz with three-point central difference scheme would result in a cut-off frequency of 16Hz, which is just above the flapping frequency, hindering the determination of valid accelerations and, consequently, forces.

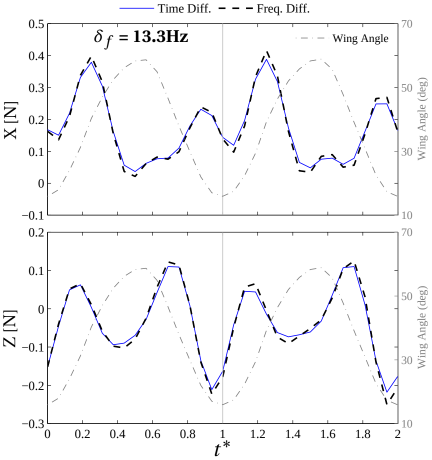

Figure 4.10: Evolution of forces calculated using discrete time central difference (solid line) and differentiation in the frequency domain (dashed line), for test #1. Both forces are low-pass filtered, with cut-off frequency equal to 40Hz. The similar evolutions indicate time differentiation contains all important flapping force information. Dash-dot gray line indicates upper wing angle

RELIABILITY OF THE RECONSTRUCTED FORCES

The nature of flight testing with a real flying ornithopter does not yet allow for optimal attitude and velocity reference tracking, thus causing oscillations around the desired flight regime. These oscillations depend on factors such as ornithopter battery voltage decay and unsteady fluid-structure interactions. Given the absence of closed loop control with the tracking arena, attitude, altitude and velocity tracking was not enforced actively by the controller, causing deviations from the reference parameters in time.

In order to assess the impact of these uncertainties on the free-flight forces and, consequently, on the comparison with the wind tunnel measured forces, the three most important states are plotted for ten consecutive flap cycles, to show the deviation from the reference condition that was used in the wind tunnel tests. In this regard, Figure 4.11 presents, on the left, the time variation of the states for test condition #1, which gives clear evidence of a cyclic variation component induced by the wing flap. The right part of the figure shows the forces of the ten cycles displayed over a two-flap cycle window. The real flight reconstructed forces for individual cycles are represented by the dotted lines, with the phase-average force shown as a solid line, contoured by the uncertainty propagated into the forces (method detailed previously) in the form of error bars. The dashed-dotted line indicates the upper wing flap angle, for the interpretation of the wing stroke phase.

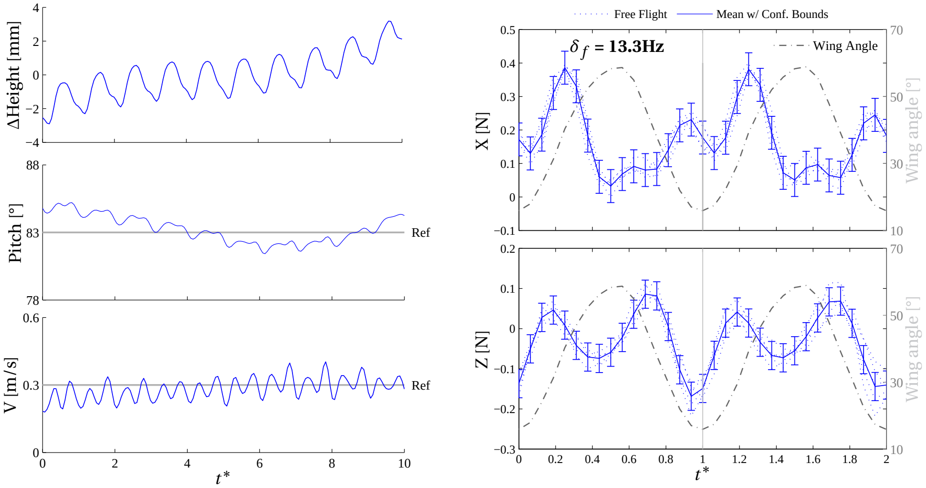

(a) Height variation (top); Pitch angle (middle) and Velocity (bottom) for 10 consecutive flap cycles with indication of reference that corresponds to wind tunnel measured condition. The ornithopter oscillates around the reference given the cyclic nature of the flight and the absence of active reference tracking.

(b) X force (top); Z force (bottom). Dotted lines represents actual evolution, reconstructed from free-flight states corresponding to flight regime in (a). Solid line represents mean value with vertical bars indicating the confidence bounds. Dotted lines fall within the confidence bounds indicating data reliability.

Figure 4.11: Assessment of free-flight data repeatability, with ten consecutive flap cycles, for sample test #1.

To further assess the validity of the confidence bounds determined by uncertainty propagation, the 95% confidence interval was calculated using the ten samples and compared with the uncertainty bounds. The 95% confidence bound was obtained assuming a normal distribution around the mean value at each time-step of the flap cycle, and can be calculated using Eq. 4.14 and Eq. 4.15:

$$95\%_{conf} = \pm t_{dist}\,\sigma_e \tag{4.14}$$

$$\sigma_e = \frac{\sigma_{t^*}}{\sqrt{N}} \tag{4.15}$$

where t_{dist} is the t-distribution with the degrees of freedom $df = N-1$, with $N = 10$ (number of cycles), σ_e is the standard deviation of sample means. It was found that the propagated uncertainty (plotted as vertical bars in Figure 4.11b) is less conservative of the error than the 95% confidence interval of ten cycles, and was assumed to be indicative of force confidence bounds for the remaining parts of the article.

Data repeatability is confirmed to stay within the confidence bounds established by the uncertainty propagated into the forces, validating the method for comparison with wind tunnel forces.

4.3.2 CLAMPED FORCE DATA

While the previous Section covered the techniques used to process the free-flight data, the current Section addresses the factors affecting the fidelity of the force data measured in the clamped experiments. In addition to the aerodynamic and kinematic contributions, the forces measured in the wind tunnel also contain contributions from the structural vibrations of the FWMAV.

AIR VS. VACUUM MEASUREMENT COMPARISON: EXPLAINING FREQUENCY CONTENT IN THE FORCES

The comparison of the frequency spectrum of the forces measured in clamped tests in air (with zero free-stream velocity) and in vacuum provides information about the frequency content of the measured forces under these different conditions, with the objective of identifying the aerodynamic and structural contributions. This result can subsequently assist in selecting a suitable cut-off frequency and filter design to extract the aerodynamic component.

The analysis starts by comparing the power spectral densities of the X and Z forces, shown in Figure 4.12. In the spectrum of the X force, it is clear that the first (fundamental frequency) and the second harmonics of the flapping motion only appear for the measurements in air, which strongly suggests that they can be attributed to the aerodynamic forces. Basically, the second peak can be related to the force generated by the translating motion of both wings that occurs twice in one complete stroke (during the in-stroke and out-stroke phases) [Percin et al., 2014]. Furthermore, the first peak is related to clap-and-fling motion, which can be regarded as a force enhancement mechanism, occurring only once during stroke reversal from in-stroke to out-stroke in a flapping cycle of the FWMAV. The third harmonic has an equal amplitude in-air and in-vacuum conditions suggesting a force contribution associated to flapping motion inertia or mechanical vibrations. The third, fourth and sixth harmonics have appreciably higher amplitudes in vacuum conditions whereas they are damped in the case of flapping in air. This suggests that these peaks likely correspond to wing structural mode excitations.

Analysis of the Z force in hover condition is more difficult as, in principle, the forces generated by the wings moving in opposite phase mostly (not completely due to dihedral angle of the wings) cancel each other resulting in relatively small net Z force production. Comparison of the Z force in air and in vacuum conditions by means of power spectral densities reveals that the first harmonic is the only component that has a pronounced higher amplitude in air conditions, pointing to an aerodynamic contribution. Similar to the X force case, the fourth and fifth harmonics contain considerably more power in vacuum conditions and are dampened in air conditions.

The free-stream velocity, present in the tests performed in the wind tunnel, has shown to influence the evolution of the forces, particularly on the Z force component (as most of the flight conditions considered in this study are the cases of slow forward flight at high angles of attack), thus creating significant difference between the flow conditions

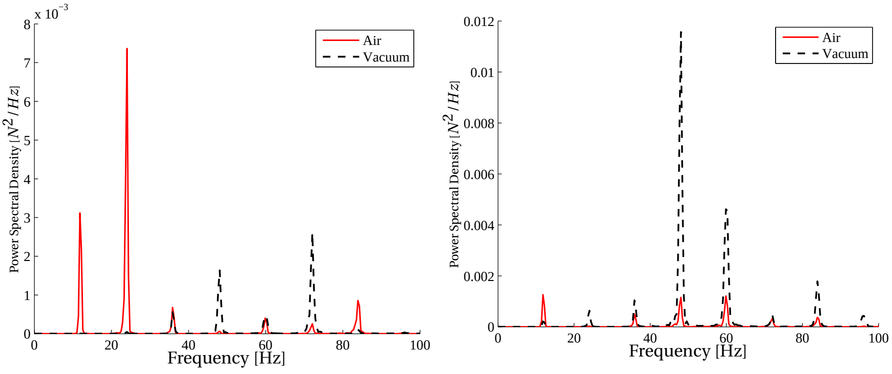

(a) X force

(b) Z force

Figure 4.12: Power spectral densities of X and Z forces measured at $V = 0m/s$, in air (solid red) and in vacuum (dashed black) conditions, for a flapping frequency of 12Hz.

experienced by the lower and upper wings. Therefore, assuming that only the first harmonic of the measured Z force is associated with the aerodynamic forces, as in the case of the hovering flight, will be erroneous. For the X force, however, it is more plausible to assume that the first two harmonics are associated with the aerodynamics since the same force generation mechanisms are dominant in the production of the X force with free-stream, although the magnitudes can be different. As a subsequent conclusion, one needs to conserve the information up to the second harmonic of the flap frequency in the aerodynamic force studies.

RELIABILITY OF THE MEASURED FORCES

The errors affecting the measured forces on the clamped experiments were assessed by applying the same methodology as the one used in Section 4.3.1. In particular, the measurement error was estimated using a fixed, non-oscillating calibrated mass on the sensor. The random-error was found to be zero-mean independent and identically distributed throughout the spectrum, being on the order of 1% of the mass.

Similarly to the free-flight case, the oscillatory nature of the measured forces does not allow for the accurate assessment of the error affecting the measurement due to correlation of residuals. Furthermore, a random error analysis does not suffice to determine the errors of this type of measurements, as there are several sources of errors, e.g., flapping wing frequency oscillations and structural vibrations. This way, data repeatability was checked by calculating the mean and standard deviation of the mean over ten flap cycles, in a method much similar to the one used before (in Section 4.3.1): the 95% confidence intervals were computed for each test using Eq. 4.14, having a mean value of 0.004N. Given the high accuracy of the measurements, the results of only one test are presented, in Figure 4.13, which indicates the measurements (dotted line) and the mean (solid line) with respective confidence bounds.

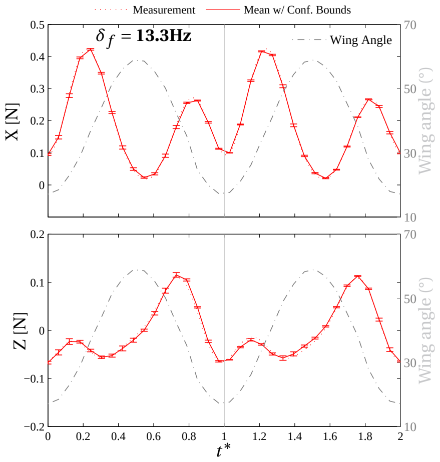

Figure 4.13: Assessment of wind tunnel data repeatability for ten consecutive flap cycles, plotted over a two flap cycle window: X force (top); Z force (bottom). Dotted lines represent actual measured evolution and solid line represents mean value with bars corresponding to confidence bounds, for test #1.

4.3.3 CONSIDERATIONS ON LOW-PASS CUT-OFF FREQUENCY OF THE FILTER

Both free-flight and fixed base wind tunnel experimental methods compared in this study are subject to different measurement errors, which should be identified prior to comparison. For the free-flight experiments, the forces are mainly affected by measurement position data uncertainty, which is amplified by the numerical processing of the data, and propagation of uncertainty. The forces measured from the clamped experiments are mostly contaminated by the body mode natural vibration.

The cut-off frequency of the filter applied to the forces was selected to minimize the noise content in the compared forces, while assuring that no relevant aerodynamic or kinematic information was filtered out. In particular, the cut-off frequency was selected based on: a) minimization of autocorrelation between residuals (Section 4.3.1); b) minimization of propagated uncertainty by selecting three point central difference differentiation scheme (Section 4.3.1); c) low-pass filter effect of discrete time differentiation (in Section 4.3.1) and d) the conclusions of wind tunnel and vacuum chamber comparison (Section 4.3.2), in the following manner:

From a) and d) it was concluded that there is still considerable information about the aerodynamic forces up to twice the flapping frequency and that considering the information up to 40Hz (3 times the flapping frequency) would conserve the contributions of kinematic forces that occur when the ornithopter flaps in air. By combining this with b), c) and d) one can conclude that a cut-off frequency just above three times the flap frequency will result in the maximization of the information content, i.e., maximum signal-to-noise ratio for force comparison. Hence, all data presented in the following section was filtered with a cut-off frequency of the integer number just above $3\times\delta_f$ [Hz], applied to a Chebyshev type II zero-phase lag filter design strategy.

4.4 RESULTS AND DISCUSSION

This section presents the most important results of the study, divided into two parts. Firstly, the effects of the clamping position of the ornithopter are analyzed, which includes the assessment of structural natural resonating modes, and secondly factors affecting the differences between the forces determined from the clamped and free-flight experiments are explained. The effects of the free-stream velocity on the time-resolved unstready forces is present in Appendix D.

4.4.1 EFFECTS OF CLAMPING POSITION IN THE FORCE DETERMINATION

In addition to limiting the free body motions, clamping the FWMAV to the force transducer has another important consequence associated to the dynamics of the structure, as its fuselage can be viewed as two cantilevered beams of square section $(2 \times 2)\text{mm}^2$ hollow carbon rod on both sides of the force sensor clamping point. Due to the oscillatory nature of ornithopter flight, the structural modes of the beams can be excited, consequently causing the resonance of the structures, which influences the forces that are recorded by the force transducer. Conversely, such a mechanism is not present in the free-flight experiments. Here, the coupling between the kinematic forces and the unsteady, aperiodic, fluid-structure interactions occurring in free-flight hamper the possibility of determining the body natural modes and frequencies from the free-flight data. Moreover, other studies on this FWMAV have identified the presence of a longitudinal dynamic oscillatory mode of the FWMAV with a frequency close to 1Hz [Caetano et al., 2013b,a].

In the wind tunnel experimental model, the nose section accommodates the brushless motor, the driving system and flapping wings, which are all mounted on the main frame. These components have a total mass of 6.4g and connected to the fuselage at the nose, while the tail side carries only the 3.9g tail structure. The location of these structures are of importance in terms of structural dynamics, which will depend on the clamping position of the fuselage. The nose section of the fuselage is the critical part as the unsteady forces generated by the flapping wings and high frequency vibrations originating from the driving system are exerted primarily on this side. On the other side of the clamp, the tail is the only source of force production, which also displays vibratory behavior because of its interaction with the unsteady wake of the flapping wings and transmission of upstream vibrations having a small impact on the final result in the wind tunnel tests. The temporal evolutions of X force and Z force components for four tests representing each flapping frequency that was used are shown in Figure 4.14, for the three different clamping positions.

As observed in Figure 4.14a, the X forces present similar evolutions for all clamping positions. These results are very comparable in terms of the overall shape and phase of the oscillations with the largest differences being in the magnitude of the force peaks, namely for the peak at the outstroke ($t^* = 0.23$), with maximum relative difference of 7% between the maxima of the middle clamp and tail clamp. Contrarily, the Z forces differ substantially between different clamping positions, in terms of phase, magnitudes and

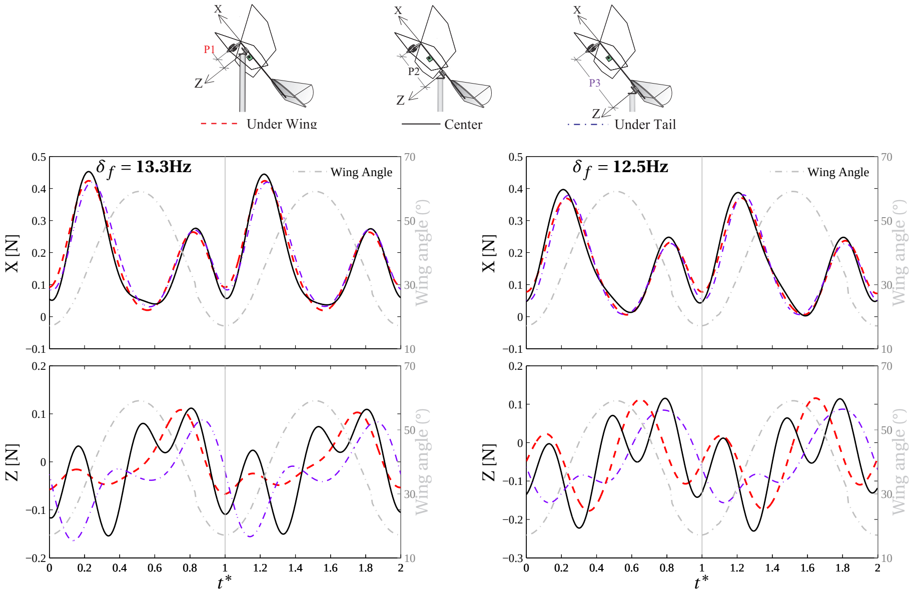

(a) Test #1, δ_f = 13.3Hz, V = 0.3 m/s and θ = 83°.

(b) Test #4, δ_f = 12.5 Hz, V = 0.65 m/s, θ = 71°.

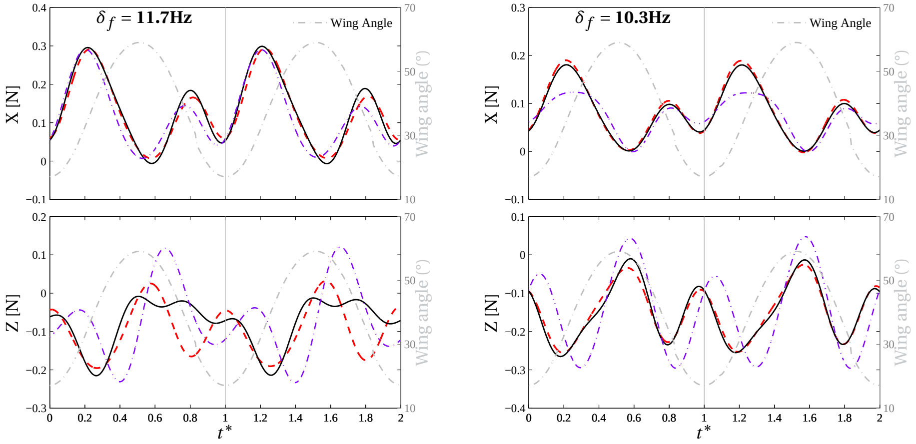

(c) Test #7, δ_f =11.7 Hz, V = 1 m/s, θ = 45°.

(d) Test #8, δ_f = 10.3Hz, V = 2 m/s, θ = 31°.

Figure 4.14: Temporal variations of the force components for different clamping positions on the fuselage plotted for two periods of the flapping motion and complemented with the variations of the upper wing angle (dash-dotted gray).

total number of local maxima in a period of flapping motion. Given the complex flow conditions (i.e. the ornithopter flapping at an angle to the free-stream flow), it is not straightforward to interpret the results and decide on the correct measurement.

Figures 4.14b and 4.14c display the X and Z force variations for slightly faster forward flight conditions. Similarly to the previous case, the X forces have a good correlation for different clamping positions with a maximum relative difference of 16% between the instroke peak forces of middle clamp and tail clamp positions. The small differences observed in the variations of the X force can be attributed to slightly different experimental conditions for different clamping positions, e.g., variation of the interference characteristics between the FWMAV and the balance strut and slight differences in the angles between the body $\boldsymbol{x_b}$ axis and the $\boldsymbol{x}$ axis of the force transducer. The Z force, however, does not follow a common trend for the different cases of clamping locations. However, these factors do not explain the disparities identified in the Z forces.

Interestingly, Figure 4.14d presents a force evolution profile where both the X and Z forces present similar evolutions for clamping under wing and center clamp, revealing a dependency on the flight condition. To verify the presence of structural resonance that might justify the differences in the measured forces, the eigenfrequencies of the wing section of the ornithopter structure determined by the two methods detailed in section 4.2.2 are presented in Table 4.4.

Table 4.4: Natural Frequencies of the Ornithopter Acquired by Mechanical and FEM Analysis, for different clamping positions, in Hz.

	Natural Frequencies [Hz]		
	Under Wing (P_1)	Center Clamp (P_2)	Under Tail (P_3)
Mechanical analysis	270	47	27
FEM analysis	271	42	24

Noting that the first two structural modes observed in the FEM analysis are essentially pitchwise and lateral bending deformations of the body of the ornithopter with equal eigenfrequencies, this explains why the X force component remains invariant with respect to the clamping position. It is clear that, in the case of the tail clamp, the frequency of the first structural eigenmode is very close to the first harmonic of the flapping frequency. During the flapping motion, this mode is excited, which results in structural vibrations that interfere with the forces associated with the flapping wing motion.

Likewise, for the middle-clamp case, the eigenfrequency lies in the range close to the second harmonic of the flapping frequency, especially for high flapping frequency cases, so that clamping at this position poses risk for Z force measurements. Conversely, the nose clamp case presents an eigenfrequency which is considerably higher than the frequency range of the considered force components. This can be attributed to a relatively short beam length and, in turn, relatively short distance between the clamping point and application point of force oscillations. These results advise the need for proper study of the clamping point of the ornithopter or flapping wing prior to force measurement

4.4.2 COMPARISON BETWEEN FREE FLIGHT AND CLAMPED WIND TUNNEL FORCES

The results presented in the previous sections have justified the methodology underlying the force comparison. A proper comparison between the forces reconstructed from free-flight and the forces measured directly by the force transducer in the wind tunnel tests can now be performed. In this regard, four of the eight test points are presented and compared in this subsection. This selection covers the full flight envelope of the ornithopter, from slow flight with high flap frequency, to forward flight with lower flap frequency, and the conclusions taken from these results are representative of the remaining tests.

Figure 4.15 presents the results for the X and Z forces determined from both experimental techniques – the solid line (blue) represents the free-flight forces with the propagated uncertainty, the dashed (red) line indicates the wind tunnel forces and the dashed-dotted (gray) line depicts the upper wing angle, for wing stroke phase relation and comparison. The figure (and respective subfigures) is ordered in a decreasing wing flapping frequency.

There is a good agreement between the X forces of both experimental techniques. The forces measured in the wind tunnel experiments present an evolution that is similar to the forces calculated from the free-flight data, with both forces presenting similar phases and corresponding peak times. Moreover, the X force from the wind tunnel falls within the uncertainty bounds established by the bars around the mean free-flight force, thus increasing the confidence in the comparison of results.

In contrast, the Z forces exhibit different temporal evolutions for the different methods, presenting different phases, as well as non-corresponding force peak occurring times – as seen at $t^* = 0.95$ and $t^* = 1.18$ in Figures 4.15b and 4.15c. Nevertheless, the results reveal a tendency for the forces to become more similar with the decrease in the wing flap frequency, i.e., for 13.3Hz the Z forces present very dissimilar evolutions, while revealing a similar evolution for $\delta_f = 10.3$Hz.

The behavior observed in the Z forces is attributed to two factors: a) the lower loads along the stroke plane at lower flap frequencies and the b) weaker interaction between the inertial loads and the structural eigenmodes in the clamped wind tunnel tests for low flapping frequencies. The natural frequency of the aft-part of the ornithopter (tail) when clamped under wing is comparable to the lowest natural frequency found on the tail clamp (27Hz – in Table 4.4), due to similar structures and mass distributions of both parts. The natural mode occurring at this frequency range will be excited by more energetic faster flap frequencies, around 13.3Hz and 12.5Hz, as the first harmonic of the flap frequency, corresponding of two times the flap frequency, will match the natural frequency of the tail section, causing structural forces to contaminate the measurements, even for the best clamp position[4], corresponding to the clamp under the wing.

In the free-flight tests, the ornithopter oscillates around an average (reference) pitch attitude within one flap cycle. In this case, the tail acts as a natural damper by producing aerodynamic loads. These loads, that are not present in the clamped test experiments, could be a further source of the differences found between both experimental methods. Consequently, detailed analysis is necessary when using fixed-base force measurements for flapping force characterization, as these methods do not include body dynamics and can be contaminated by structural resonances.

---

[4] This assumption was supported by the observation of significant vibrations of the tail section. For visualization of vibrations of the tail, consult the media supplied with the dissertation.

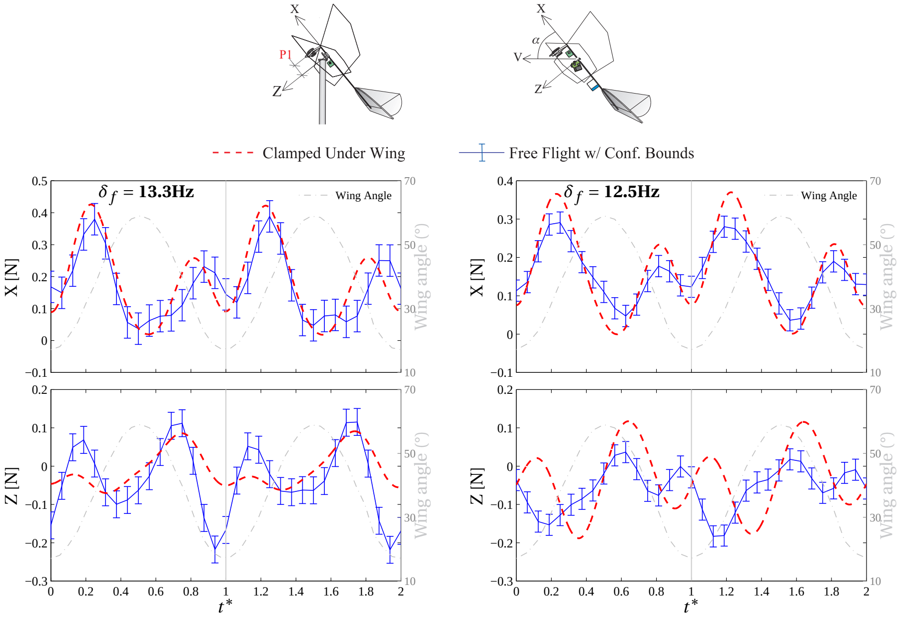

(a) Test #1, δ_f = 13.3Hz, V = 0.3m/s, θ=83°. (b) Test #4, δ_f = 12.5Hz, V = 0.65m/s, θ=71°.

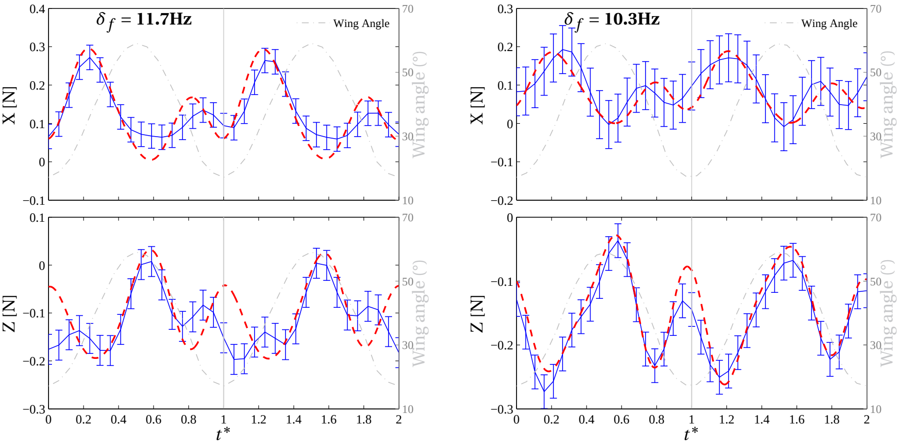

(c) Test #7, δ_f = 11.7Hz, V = 1m/s, θ=45°. (d) Test #8, δ_f = 10.3Hz, V = 2m/s, θ=31°.

Figure 4.15: Temporal variations of X force (top) and Z force (bottom) for both experimental techniques for slow flight conditions; free-flight in solid blue, wind tunnel in dashed red and upper wing angle in dashed-dotted gray.

4.5 CONCLUSION

A thorough study on the factors that can affect the reliability of determining the forces acting on a Flapping Wing Micro Air vehicle (FWMAV) was carried, in which two experimental techniques were compared: a) free-flight in a high fidelity motion tracking chamber; b) clamped wind tunnel direct force measurement, using a force transducer at flight conditions that represent the flight envelope of the ornithopter.

The characterization of the forces acting on a FWMAV computed from free-flight data measured using an external position tracking system should take into account the nature of the error affecting the position measurements. Given the usual method of force determination through the application of discrete time differentiation of the position states, the errors and uncertainties that are propagated into the forces can assume values that are in the order of magnitude of the forces themselves. For example, a standard deviation of the position error of the markers on the ornithopter above 0.5mm will result in the confidence interval to be of the size of the force magnitude, thus suppressing any reliable force extraction. Furthermore, for ornithopters with less than 30cm of wing span the accuracy of the position measurements should be higher that ±0.2mm to allow for suitable force reconstructions.

Filter design also has a considerable effect on the final forces determined from free-flight. Depending on the numerical differentiation scheme, the differentiated states are low-pass filtered already in the state determination phase, which will decrease the signal-to-noise ratio. To conserve the time resolved aerodynamic information present in the frequency spectrum at multiples of the flapping frequency, it is recommended to sample the flight at a frequency of at least five times the wing flap frequency due to the numerical differentiation of the position. This is often not taken into account, e.g., Grauer et al. [2011]; Rose and Fearing [2014]; Lim et al. [2012] and should be considered under the risk of hindering any conclusions from the free-flight forces.

The ornithopter used in this study has a wing configuration that minimizes asymmetric inertial loading along the stroke plane, which is parallel to the z_b axis. This reduces the amount of unwanted factors affecting the force measurements in the wind tunnel. In this regard, a special attention is necessary for experimental studies of two- or single-winged winged setups, as the wing configuration can further add loads that will increase the magnitude of the structural modes in the clamped tests, as well as increase the amplitude of the oscillations of the ornithopter in free-flight. If not taken into account properly, these effects may lead to a incorrect determination of the force component along the stroke plane direction, which is very important for controllability of such two-winged ornithopters. Furthermore, such factors will be a function of wing beat frequency and wing-to-body mass ratio, becoming more pronounced in ornithopters with the increase of any of the latter.

From the analysis of the possible sources of the differences identified in the Z forces measured at different clamping positions, which contrasted with the similar X force evolution throughout the clamping points, it was concluded that the natural eigenmodes of the ornithopter structure interfere with the results, leading to erroneous measurements and incorrect FWMAV force characterization. The natural frequency of the ornithopter is highly affected, not only by its mass and materials, but most importantly by the clamping point, given the cantilever system that results from rigidly attaching the structure. It was concluded that the only suitable clamping point of the ornithopter structure is near the mean aerodynamic and inertial force application point. For the experimental studies that involve measuring the forces acting on the ornithopter directly from a high accuracy force transducer, e.g., Rose and Fearing [2014]; Lee and Han [2012]; Nguyen et al. [2010];

Kim et al. [2008] it is recommended to thoroughly study the natural frequencies of the system for the different possible clamping positions, prior to force measurement to determine if the eigenfrequencies of any of the components are close to the first harmonics of the driving force.

II

AERODYNAMIC MODELING AND IDENTIFICATION

5

LINEAR TIME-INVARIANT AERODYNAMIC MODELING

This chapter presents a first approach to the development of simple aerodynamic models of the DelFly II to be used in simulations and for onboard flight control strategies. For simplicity, linear time-invariant model structures are selected and the model parameters are identified using the free-flight forces and moments reconstructed in the previous chapters, under the assumption of uncorrelated residuals. Two model structures were selected: (1) one that uses all the states reconstructed in the previous chapters; (2) the other uses only the states that can be estimated from onboard sensors, for the prediction of the fidelity of aerodynamic models that could be used for onboard control. It is shown that the approach leads to aerodynamic models that can predict the aerodynamic forces with considerable accuracy. Despite less accurate, the predictions of the aerodynamic moments still follow the general trend of the measured moments. Dynamic simulations based on the identified aerodynamic models show flight trajectories that closely match the real flight path of the DelFly, spanning a number of flapping cycles.

This chapter was published as: Caetano, J. V., de Visser, C. C., de Croon, G. C. H. E., Remes, B. D. W., de Wagter, C., Verboom, J. L., and Mulder, M. (2013a). Linear Aerodynamic Model Identification of a Flapping Wing MAV Based on Flight Test Data. *International Journal of Micro Air Vehicles*, 5(4):273–286. Sections 2 and 3.1 of the publication were removed from the present chapter, as these were repeating the content of Chapter 2 and 3.

5.1 INTRODUCTION

It is envisioned that FWMAVs will occupy an existing gap in conventional fixed and rotary wing aircraft applications thanks to their agility, broad flight envelope, interesting behavior near obstacles and promising properties at very low Reynolds numbers. Especially for nano FWMAVs, for which flapping is believed to yield most advantages [Ansari et al., 2006; Dickinson et al., 1999; Ellington et al., 1996; Malolan et al., 2004], the small size and mass heavily restrict the range of sensors and processing onboard. With a total take-off weight of only a few grams, attitude determination and flight control are still active areas of research [Wood, 2008; Keennon et al., 2012].

The main reason for the current absence of model-based nonlinear control is the difficulty of designing a reliable model for FWMAVs. This derives from the not yet fully understood unsteady aerodynamics [Ellington, 1984a; Percin et al., 2011, 2012a] associated with flapping wing flight. Furthermore the flapping of the wings complicates the model structure as their added inertia effects contribute to the dynamics of the ornithopter [Orlowski and Girard, 2011]. A simple approach was taken by Dietl and Garcia [2008]; Dietl et al. [2011] that modeled the dynamics of a flapping wing aircraft using the general aircraft equations of motion and resulted in a simulated linear time-invariant alternative for the attitude control. This has its advantages due to simplicity since, on the other hand, a complete modeling approach [Bolender, 2009; Orlowski and Girard, 2011] typically results in a complex nonlinear time-variant multi-body representation of the ornithopter that is not suitable of being used onboard.

On the experimental side, Grauer et al. [2010, 2011] succeeded in devising the kinematic equations of motion and was able to determine the Lift and Drag aerodynamic coefficients acting on a two wing bird-like ornithopter using experimental flight data.

The previously mentioned theoretical approaches lack, however, a practical validation in the form of flight testing [Bolender, 2009; Orlowski and Girard, 2011; Dietl and Garcia, 2013, 2008; Dietl et al., 2011], as the models are limited to computational environments. Moreover, the experimental studies [Grauer et al., 2010, 2011] lack the repeatability of the data because the platform was not able to hover or stay aloft for enough time to perform specific flight test maneuvers that are necessary to perform system identification. More recently Caetano et al. [2013b] have been able to program a FWMAV to perform automatic maneuvers for system identification purposes and calculate the aerodynamic forces and moments that act on the FWMAV, using flight path reconstruction techniques and general aircraft equations of motion [Caetano et al., 2013c].

This study aims at bridging the gap between theoretical and experimental approaches and presents a set of benchmark linear aerodynamic models for the DelFly II FWMAV that were devised by applying aircraft system identification techniques and further extending them to flapping wing platforms. These linear aerodynamic models can be used to simulate DelFly flight and form the basis of a future full flight envelope nonlinear control system for the DelFly. Our approach for the development of the aerodynamic models is presented in Figure 5.1. Two linear aerodynamics models were devised and compared: (1) a *full* model that incorporates state variables reconstructed from the tracking system and (2) a *reduced* model that only includes state variables that may be measured or calculated directly from the existing onboard sensors, should this date be directly available (Section 5.3). Section 5.4 presents the validation methodology, using verification maneuvers and a dynamic simulation. The final conclusions are drawn in Section 5.5.

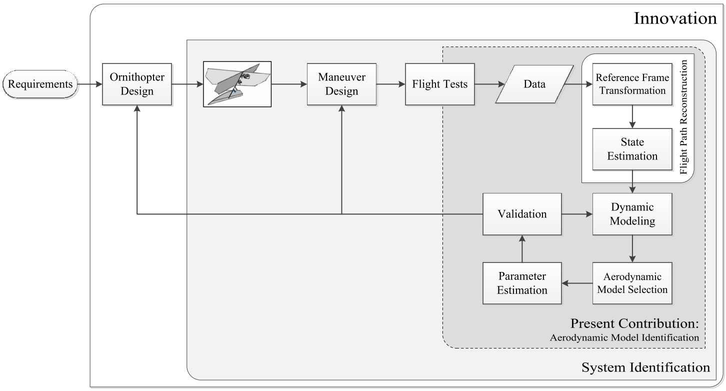

Figure 5.1: Flowchart of current contribution and associated framework.

5.2 FLIGHT PATH RECONSTRUCTION

The evolution of the states around an elevator step input performed in test #23[1] are presented in Figure 5.2 to Figure 5.5. These are somewhat constant before the input, being damped after the input ceases. The elevator was deflected upwards, during $\frac{1}{3}$sec (Figure 5.2). Here the rudder oscillation (middle plot) is related to the rotation and bending of the tail induced by the flapping vibrations, as no input over the rudder was performed by the autopilot. The abscissa axes are defined in seconds with its interval selected to present the response of the DelFly to a step input on the elevator.

In order to keep the Euler relations valid to be used in the general aircraft equations of motion (EOM) Etkin and Reid [1996]; Caetano et al. [2013c]; Stevens and Lewis [2003], the Euler angles were converted to new attitude angles ϕ_r (roll), θ_p (pitch) and ψ_y (yaw) that can count above 90° in pitch. This allows the dynamic equations to be defined for pitch angles in the interval $]-\pi;\pi[$ not needing alternative formulations in terms of, e.g., quaternions. The developed routine evaluated the change in the computed Euler angles: if the ψ and ϕ angles rotated of values close to 180°(thus too big to be caused by a turn) and the $\boldsymbol{z_b}$ was pointing upwards in the inertial frame the θ_p would be equal to $(\pi+\theta)$, while assuming ψ_y and ϕ_r to be equal to the de-rotated initial value that caused the detection of the inverted flight regime.

To decrease the influence of the high oscillatory modes induced by the flapping frequency, the states were filtered using a 3^{rd} order zero-phase lag Butterworth low-pass filter with cut-off frequency of 30Hz, thus conserving the information up to the second flapping frequency harmonic.

Figure 5.3 presents the evolution of the velocities in the body frame: the velocity component u decreases to a negative value as the DelFly loses lift and height. The w component varies due to the pitch angle oscillation – when w goes to negative means

---

[1] More information about this test in presented in `Flight_Test_Description.xlsx`

the DelFly is flying in the opposite direction, in inverted flight. As expected, v does not suffer considerable variations during the longitudinal maneuver. Figure 5.4 presents the Euler (red) and the attitude (blue) angles around the maneuver. The angular velocities in the body frame are depicted in Figure 5.5 – here one can see the considerably high oscillatory behavior of the DelFly caused by the flapping frequency due to its low mass and inertia.

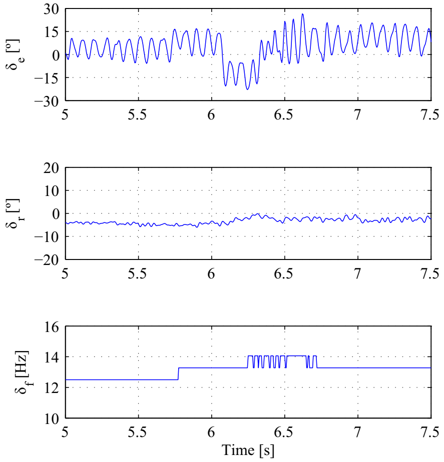

Figure 5.2: Control surface inputs for a part of test #23: elevator (top) and rudder (middle) deflection angles, defined as positive down and left, respectively; flapping frequency (bottom), with step variations due to discrete time calculations.

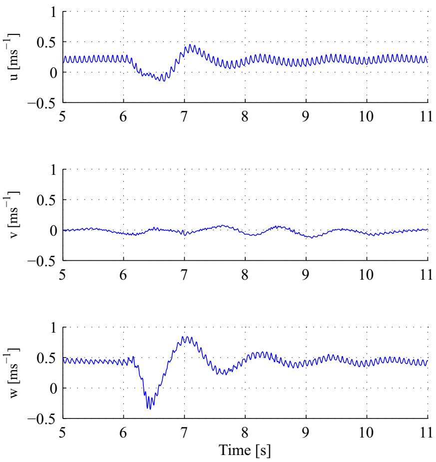

Figure 5.3: Velocities for a part of test #23 written in the body reference frame $(\boldsymbol{x_b}, \boldsymbol{y_b}, \boldsymbol{z_b})$. The velocities' oscillations due to the input are dampened in less than 5 seconds.

The upcoming section will present the assumptions used when devising the aerodynamic model structure. It will also address the different considerations that had to be taken into account to assure that the model is simple enough to not require computationally expensive onboard state estimation algorithms, by means of using only the direct sensor outputs.

5.3 AERODYNAMIC MODELING

The second step in the system identification framework is aerodynamic model identification. This identification aims at creating a model that relates the control inputs to the resulting aerodynamic forces and moments. This way the aerodynamic models can then be used in model-based flight control systems.

5.3.1 AERODYNAMIC MODEL STRUCTURE SELECTION

Several linear model structures of the form of Eq. 5.1 were devised. Here the left-hand side term F_i represents the forces and moments obtained from the Newton-Euler equa-

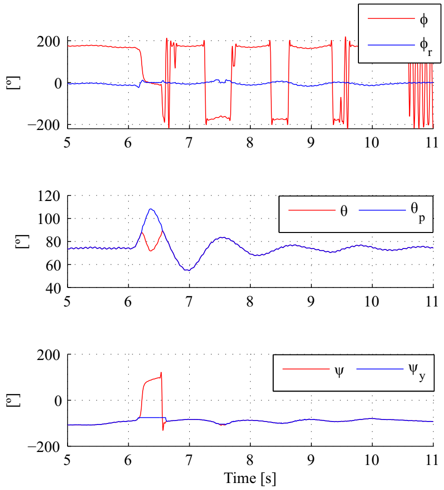

Figure 5.4: Euler angles (red) and attitude angles (blue) around the maneuver of test #23.

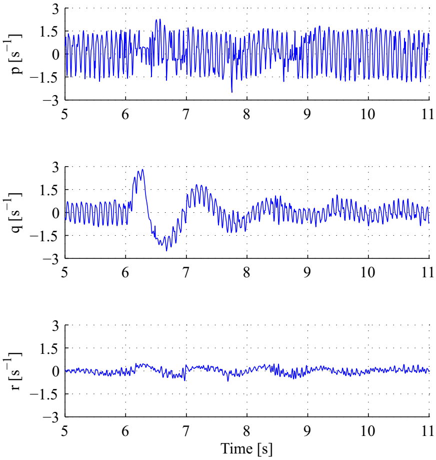

Figure 5.5: Angular velocities in the body frame around the maneuver of test #23.

tions of motion (detailed in Chapter 3); the first term on the right-hand side, C_{F_0}, is the affine coefficient; S represents a state and C_{F_s} the state's coefficient or parameter for a given force or moment F_i. The flight test data was divided into identification and validation sets. The identification set is used to estimate the aerodynamic parameters; the validation set is used to verify if the estimated model is able to represent the aerodynamic forces and moments.

The *full* model structure was defined such that each of the aerodynamic forces (X, Y, Z) and moments (L, M, N) is a linear function of all the states, as in Eq. 5.1. The *reduced* model structure was defined such that it requires only states that are measurable using onboard sensors, with the goal of using it in a nonlinear flight controller. In particular, the coefficients of Eq. 5.1 were substituted in the *reduced* model equation, presented in Eq. 5.2.

$$F_i = C_{F_0} + \sum_{s=1}^{n} C_{F_s}.S \qquad with \qquad S:\{\phi_r,\theta_p,\psi_y,u,v,w,p,q,r,\alpha,\beta,\delta_f,\delta_e,\delta_r\} \tag{5.1}$$

$$\begin{aligned} X &= X_0 + X_q q + X_\theta \theta + X_{\delta_e}\delta_e + X_{\delta_f}\delta_f \\ Y &= Y_0 + Y_p p + Y_\phi \phi + Y_{\delta_r}\delta_r + Y_{\delta_f}\delta_f \\ Z &= Z_0 + Z_q q + Z_\theta \theta + Z_{\delta_e}\delta_e + Z_{\delta_f}\delta_f \\ L &= L_0 + L_\theta \theta + L_{\delta_r}\delta_r + L_{\delta_f}\delta_f \\ M &= M_0 + M_\theta \theta + M_{\delta_e}\delta_e + M_{\delta_f}\delta_f \\ N &= N_0 + N_\theta \theta + N_{\delta_r}\delta_r + N_{\delta_f}\delta_f \end{aligned} \tag{5.2}$$

5.3.2 PARAMETER ESTIMATION

An ordinary least squares estimator was used to estimate the parameters of the linear models. Eq. 5.4 is an example for the estimation of the parameters of the aerodynamics for X, with the regression matrix $\mathbf{R}$ containing a total of N_i observations:

$$\begin{bmatrix} \hat{X_0} \\ \hat{X_q} \\ \hat{X_\theta} \\ \hat{X_{\delta_e}} \\ \hat{X_{\delta_f}} \end{bmatrix} = (\mathbf{R}^\top \mathbf{R})^{-1} R^\top X \qquad (5.3) \qquad \text{with} \qquad \mathbf{R} = \begin{bmatrix} 1 & q(1) & \theta(1) & \delta_e(1) & \delta_f(1) \\ 1 & q(2) & \theta(2) & \delta_e(2) & \delta_f(2) \\ \vdots & \vdots & \vdots & \vdots & \\ 1 & q(N) & \theta(N) & \delta_e(N) & \delta_f(N) \end{bmatrix} \qquad (5.4)$$

Hence, the models' parameters were estimated for a total of five longitudinal maneuvers that covered step, doublet and triplet inputs on the elevator for near-hover and slow forward flight regimes ($V \approx 0.5 m/s$). It is interesting to notice that despite the different maneuvers, the estimated aerodynamic coefficients were found to have very similar values, with best results for the *reduced* model. The average value and standard deviation on the parameter for each model and force are presented in Table 5.1. Furthermore, the analysis of the covariance matrix showed that the coefficients with higher variances also had the higher standard deviations across the maneuvers. This proximity between the estimated coefficients allows for a single aerodynamic model to be used for similar flight regimes, with beneficial consequences in the control strategies.

5.4 RESULTS

The models were validated using two different approaches: (1) by means of validation maneuvers in which the parameters that were estimated in the identification cycle were used to predict the aerodynamic forces and moments of other maneuvers; (2) using a dynamic simulation, where the identified aerodynamic models were used in a nonlinear dynamics simulator to reconstruct the DelFly's flight path and states and then compare them with the original flight path and states that were recorded in the flight tests.

VALIDATION MANEUVERS

This subsection presents the estimated aerodynamic forces and moments for both the *full* and the *reduced* models. In the interest of objectiveness, the estimated aerodynamic forces and moments will be presented for the test case described in Figures 5.2 to 5.5. Hence, Figure 5.6 presents the graphical evolution of the filtered forces (Figure 5.6a) and moments (Figure 5.6b) for the validation part of the system identification cycle. The blue lines represent the forces and moments calculated using the aircraft EOM; the red lines depict the full linear model's evolution; whereas the green lines describe the behavior of the *reduced* model.

Both the *full* and the *reduced* models were able to predict all three aerodynamic forces (Figure 5.6a). The variation in the curves for the peak in the X force results from the fact that the X force that was computed from the EOM is highly affected by the vertical velocity component w, which goes to negative values when the DelFly flies inverted. As for the X force, the models are able to predict the Z force with a high accuracy. Moreover, the Y force does not vary considerably in the (longitudinal) maneuver, as no rudder input was present and, despite some punctual differences, it is also well predicted by both models.

However, none of the models predict the aerodynamic moments (Figure 5.6b) as well as they did for the forces. Nevertheless, the most important moment for longitudinal dynamic analysis, the pitching moment, is the most accurately predicted. Despite these

Model	**Force or Moment**	$\mathbf{C}_0$		$\mathbf{C}_{\phi_r}$		$\mathbf{C}_{\theta_p}$		$\mathbf{C}_{\psi_y}$		$\mathbf{C}_u$		$\mathbf{C}_v$		$\mathbf{C}_w$		$\mathbf{C}_p$	
		Avg	Std. Dev.	Avg.	Std.Dev.	Avg.	Std.Dev.	Avg.	Std.Dev.	Avg.	Std.Dev.	Avg.	Std.Dev.	Avg.	Std.Dev.	Avg.	Std.Dev.
Full	**X**	0.1538	0.1131	0.0110	0.0194	0.0483	0.0431	-0.0100	0.0221	-0.049	0.0246	-0.1095	0.1114	-0.0027	0.0358	5.4100E-4	0.0018
	Y	0.0225	0.028	0.0055	0.0316	-0.0205	0.0245	-0.0274	0.0006	8.9522E-4	0.0169	-0.0614	0.0540	-0.0158	0.0331	-0.0073	0.0029
	Z	-0.2861	0.0297	-0.0097	0.0132	0.1699	0.0168	-0.0030	0.0094	0.0014	0.0084	-0.0134	0.0478	-0.0047	0.0121	-4.4929E-4	0.0007
	L	9.6231E-4	0.0004	-8.4256E-5	2.970E-5	-6.9285E-4	0.0002	1.4884E-5	3.660E-5	-1.8120E-4	0.0006	7.9049E-5	0.0004	-6.1030E-4	0.0007	-2.1300E-5	5E-6
	M	0.0414	0.0191	0.0033	0.0056	-0.0203	0.0078	0.0041	0.0019	-0.0054	0.0044	0.0014	0.0084	-0.0144	0.0059	-0.0021	0.0006
	N	-0.088	0.0134	-0.0017	0.0012	0.0011	0.0047	-4.3412E-4	0.0011	-2.2278E-4	0.01678	-0.0155	0.0166	0.0011	0.0269	1.2782E-4	0.0002
		$\mathbf{C}_q$		$\mathbf{C}_r$		$\mathbf{C}_\alpha$		$\mathbf{C}_\beta$		$\mathbf{C}_{\delta_f}$		$\mathbf{C}_{\delta_e}$		$\mathbf{C}_{\delta_r}$			
	X	0.0067	0.0024	0.0067	0.0093	0.0108	0.0019	-0.1252	0.0430	0.0829	0.0037	-0.0035	0.0160	0.0039	0.1243		
	Y	3.6187E-4	0.0014	-0.0014	0.0091	0.0265	0.0244	0.0124	0.0237	0.0018	0.0008	-0.0011	0.0021	0.021	0.0008		
	Z	-0.0018	0.0010	-0.0051	0.0049	-0.0065	0.0005	0.0519	0.0240	-0.0100	0.0013	4.2333E-4	0.0081	-0.0012	0.0343		
	L	7.4992E-5	5.16E-5	1.3582E-5	7.86E-6	1.9198E-4	0.0007	1.0647E-4	0.0004	-7.0396E-5	1.18E-6	6.5270E-6	8.14E-5	-5.5306E-6	2.118E-5		
	M	0.0013	0.0005	5.5157E-4	0.0014	-6.6045E-4	0.0002	-0.0478	0.0181	5.1973E-4	0.0007	-3.1036E-4	0.0035	-1.6626E-4	0.0148		
	N	2.7412E-4	0.0008	-0.0019	0.0003	1.9530E-4	0.0245	0.0280	0.0162	0.0033	0.0003	4.2332E-4	0.0032	-2.4090E-4	0.0011		
		$\mathbf{C}_0$		$\mathbf{C}_{\phi_r}$		$\mathbf{C}_{\theta_p}$		$\mathbf{C}_{\psi_y}$		$\mathbf{C}_u$		$\mathbf{C}_v$		$\mathbf{C}_w$		$\mathbf{C}_p$	
Reduced	**X**	0.1385	0.0254			0.0354	0.0007										
	Y	-0.0353	0.0184					-0.0412	0.0231							-0.007	0.0019
	Z	-0.2437	0.0224			0.1650	0.0022										
	L	1.0851E-5	0.0001			9.1882E-6	3.66E-5										
	M	-0.0067	0.0191			-0.0031	0.0032										
	N	0.0016	0.0057			-7.1896E-4	0.0016										
		$\mathbf{C}_q$		$\mathbf{C}_r$		$\mathbf{C}_\alpha$		$\mathbf{C}_\beta$		$\mathbf{C}_{\delta_f}$		$\mathbf{C}_{\delta_e}$		$\mathbf{C}_{\delta_r}$			
	X	0.055	0.0009							-0.017	0.0019	0.0093	0.0023				
	Y									0.0028	0.0015			-0.0059	0.0077		
	Z	0.0016	0.0014							-0.0012	0.0019	-0.0055	0.0024				
	L									-4.0721E-6	5.26E-6			-5.9233E-4	6.68E-6		
	M									8.007E-4	0.018	0.0023	0.0039				
	N									2.7054E-5	0.0003			0.0208	0.0004		

Table 5.1: Average and standard deviation of the estimated coefficients for both the *full* and the *reduced* models for a total of 5 elevator input maneuvers. The C_{F_s} form in Eq. 5.1 was replaced by a more general C_s for convenience of representation.

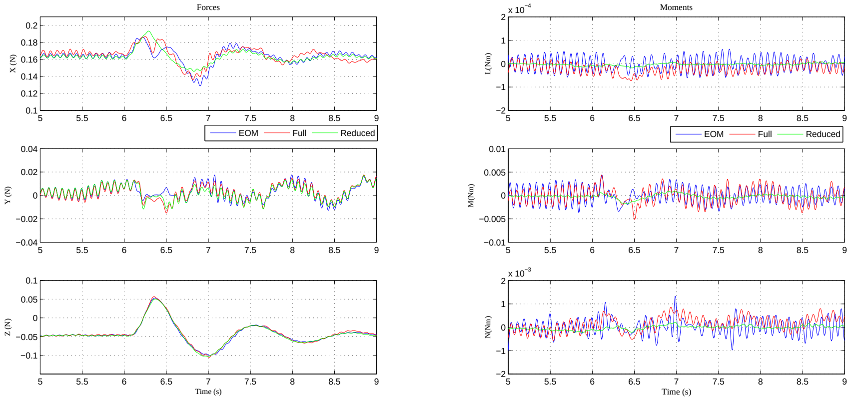

(a) Aerodynamic Forces.

(b) Aerodynamic Moments.

Figure 5.6: Reconstructed (blue) versus estimated forces and moments for both the *full* (red) and *reduced* (green) models, around the elevator step input maneuver. The aerodynamic forces are very well estimated; the aerodynamic moments are still able to follow the calculated moments with a similar behavior, presenting the same evolution and tendency, despite punctual changes.

less than optimal results, the predicted moments show a cycle averaged behavior that is similar to that of the moments calculated directly from the data using the EOM's. This points to a possible application for onboard control, using online filtering of the states or a more refined linear model.

A quantitative measurement of the performance of the model is given by calculating Pearson's correlation coefficient between each of the model's estimations and the forces and moments that were computed from the EOM. The correlation coefficient captures how two signals vary with respect to their means and is defined as $PCC = \frac{\mathrm{cov}(X_{EOM}, X_{estim})}{\sigma(X_{EOM})\sigma(X_{estim})}$. The best performance would be the highest correlation of $PCC = 1$, while completely uncorrelated signals would give $PCC = 0$. Table 5.2 shows the correlation coefficients for the *full* model and *reduced* model. It can be seen that the predicted forces X, Y, and Z are closely correlated to the calculated forces with $PCC \in [0.85, 0.99]$. The moment predictions are still reasonably correlated for the *full* model with $PCC \in [0.39, 0.62]$, but only slightly correlated for the *reduced* model with $PCC \in [0.14, 0.43]$.

Pearson's Correlation Coefficient

Forces and Moments	**X**	**Y**	**Z**	**L**	**M**	**N**
Full Model	0.88	0.97	0.99	0.39	0.62	0.46
Reduced Model	0.85	0.95	0.99	0.14	0.43	0.21

Table 5.2: Pearson's Correlation Coefficient between each of the linear models and the forces and moments that were calculated from the aircraft EOMs.

DYNAMIC SIMULATION

The second model validation method involved the reconstruction of the ornithopter's flight path. Here the identification coefficients (presented in Table 5.1) were used to calculate the aerodynamic forces and moments that were input in the nonlinear equations of motion to compute the new state derivatives, which were integrated, resulting in the new states. The method is very well documented in other sources, i.e., Stevens and Lewis [2003](p.110) and uses the general aircraft EOM.

The control surface deflections that were recorded during the flight tests were used as inputs to the simulation. The initial time was selected to assure low inputs and small rates in the initial states, as well as to be coherent with the time-frame that was presented in Figures 5.2 to 5.6. The initial states and inputs are presented in Table 5.3.

Despite the good predictions obtained for the aerodynamic forces and moments, presented in Figure **??**, the numerical results point to instability in the method for simulations of more than 0.5sec. In particular, the *full* model is able to predict the flight path of the DelFly for half a second but the *reduced* model starts diverging after the first flapping cycle.

Figures 5.7 and 5.8 present the dynamic simulation results. The first (Figure 5.7) presents the real trajectory of the DelFly in the inertial frame versus the trajectories that were reconstructed using both the *full* and the *reduced* models, for two different lapsed times: 0.5 and 0.8 seconds. Here the difference in the trajectories of the *reduced* model (green) and real recorded one (blue) is clearly noticeable. Nevertheless, the *full* model is able to follow the trajectory with minor errors for around half a second.

The small differences in the aerodynamic forces and moments influence the evolution of the states, especially the angular velocities and, consequently, the Euler angles. Figure 5.8 presents the first half of a second of the evolution of the inputs and states, where the reconstructed states diverge away from the real states, especially at t=6.1sec (the time at which the elevator input moves the platform away from the equilibrium). As before, the *full* model was able to follow evolution of the states more closely than the *reduced* model.

Keeping in mind that the motivation behind the current approach was the limited onboard computational resources and that the linear model was intended for onboard control purposes, this study points to the possibility of onboard control of the DelFly (or a similar passively stable platform) using a linear aerodynamic model, given the fact that the states are being updated in real time to the controller.

Axis	**Euler Angles [rad / °]**	**Velocities** (ms^{-1})	**Angular Body Rates** [s^{-1}]	**Aerodynamic Angles [rad / °]**	**Position in Inertial Frame [m]**	**Inputs**
x	-0.1944 / -11.1383	0.1612	-0.2889	1.2113 /69.4024	1.5231	0.0000 (rad)
y	1.2895 /77.88	-0.0357	-0.6007	-0.0777 / 4.4519	0.1314	-0.0939 (rad)
z	-1.6361 / 93.7416	-0.4295	-0.1412		2.3784	13.2813 (Hz)

Table 5.3: Initial states and inputs for the states reconstruction and dynamic simulation, at $t = 5.85sec$.

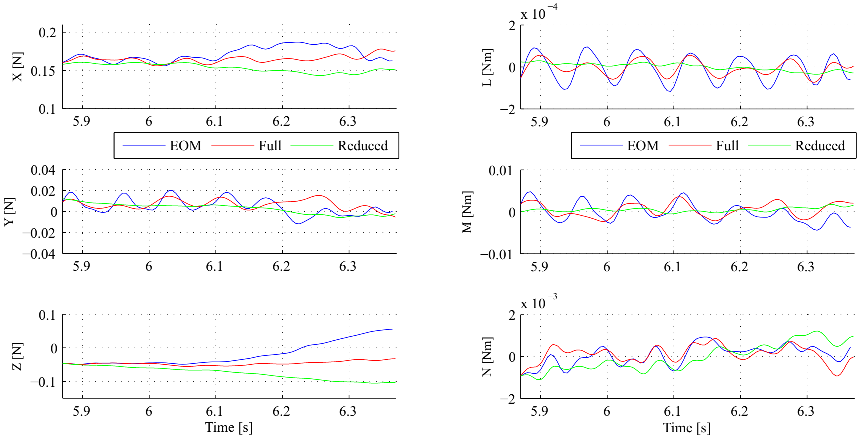

(a) Aerodynamic Forces.

(b) Aerodynamic Moments.

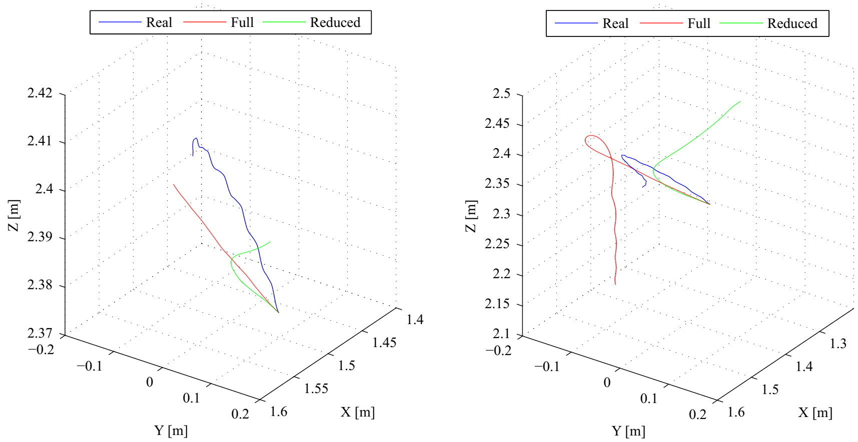

(a) Duration of 0.5 seconds.

(b) Duration of 0.8 seconds.

Figure 5.7: Reconstructed flight path using the *full* (red) and *reduced* (green) models' coefficients compared to the original (blue) recorded path. The *full* model is able to predict the flight path of the DelFly for approximately half a second, whereas the *reduced* model starts to diverge at the first iterations.

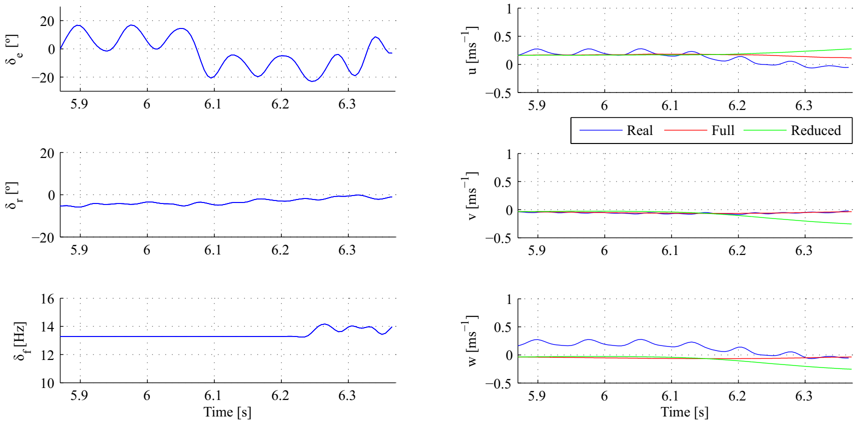

(a) Control surface inputs sequence used to computed the aerodynamics forces from the coefficients.

(b) Evolution of the velocities in the body frame.

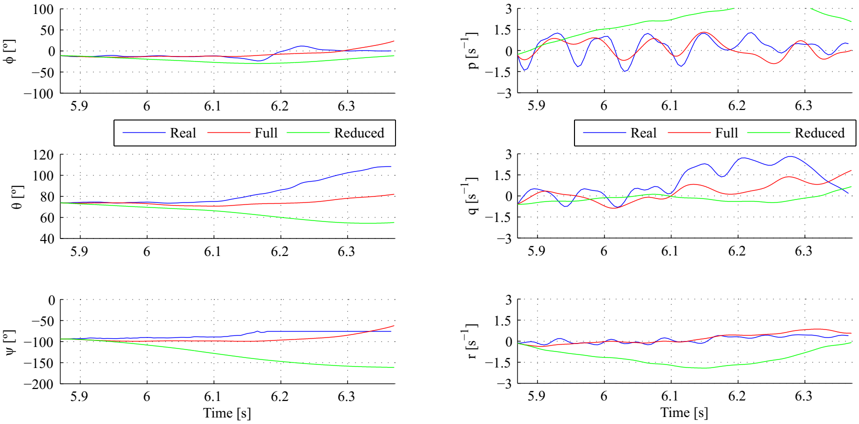

(c) Evolution of Euler angles' evolution

(d) Angular velocities during the simulation

Figure 5.8: Simulated states (in subfigures 5.8b to 5.8d) that were computed using the input sequence (in subfigure 5.8a) for *full* (red) and *reduced* (green) models versus the real (blue) captured states. Inputs and initial states from test #23.

5.5 CONCLUSION

System Identification techniques were used to create a nonlinear flight dynamics model of the DelFly II FWMAV. For this, two linear aerodynamic models were devised and tested in the framework. The more complex model used a total of eleven states and three inputs, whereas the *reduced* model used only the states that could be measured by the onboard sensors and the three inputs. After the estimation of the models' parameters it was seen that both of them were able to predict the aerodynamic forces with great accuracy, showing correlation factors that ranged from 0.85 to 0.99. The results were less optimal for the aerodynamic moments, where the correlations where smaller. However, both models were still able to follow the cycle average evolution described by the calculated aerodynamic moments.

The models were then used to predict the new states of the ornithopter in a nonlinear dynamic simulator. This simulator used the real inputs sequence to predict the DelFly's new states, based on a real initial condition. The results showed that it was possible to reconstruct its flight path and attitude with considerable accuracy for the initial parts of the simulation. However, the small differences between the real and predicted aerodynamic forces and moments cause the nonlinear simulation to diverge from the ground-truth within 0.5 seconds.

These results point to the possible use of linear aerodynamic models for model based onboard flight control. However, for flight simulation purposes of longer periods of time the aerodynamic forces and moments have to be predicted more accurately. Furthermore, the model of the moments is not accurate enough to be used in nonlinear simulations. This is expected, firstly because the angle rates suffer from noise amplification due to the time differentiation of the states, and secondly because the moment estimation correlation coefficients are low, often even below 0.5. Concerning the estimation of the forces it can be seen that the assumption of no-flapping is likely to account for a lot of the remaining model errors. In this regard, the following Chapter will ficus on time-resolved nonlinear time varying model structures that capture the aerodynamic mechanisms of flapping flight using quasi-steady aerodynamic theory.

6

NONLINEAR TIME-VARYING MODELING – A QUASI-STEADY APPROACH

Flapping-wing aerodynamic models that are accurate, computationally efficient and physically meaningful, are challenging to obtain. Such models are essential to design flapping-wing micro air vehicles and to develop advanced controllers, consequently enhancing the autonomy of the developed vehicles. Given the inability of the linear time-invariant approach to model unsteady forces, in this Chapter, the previous models are further developed and a phenomenological model of the time-resolved unsteady aerodynamic forces is derived. The model is based on quasi-steady theory and accounts for inertial, circulatory, added mass and viscous forces. It extends existing quasi-steady approaches by: (1) including a fling circulation factor to account for unsteady wing-wing interaction; (2) considering real platform-specific wing kinematics and different flight regimes. The model parameters are estimated from wind tunnel measurements conducted on the real flapping wing micro aerial vehicle. The comparison to wind tunnel data shows that the model predicts the lift forces on the test platform accurately, and accounts for wing-wing interaction effectively. Additionally, validation tests using real free-flight data show that lift forces can be predicted with considerable accuracy in different flight regimes. Furthermore, a complete parameter-varying model is developed to represent a broad set of flight conditions. It is computationally simple, physically meaningful and requires few measurements, therefore, being potentially useful for both control design and preliminary conceptual studies for developing new platforms.

This chapter was published as: Armanini, S. F., Caetano, J. V., de Croon, G. C. H. E., de Visser, C. C., and Mulder, M. (2016a). Quasi-steady aerodynamic model of clap-and-fling flapping mav and validation using free-flight data. *Bioinspiration & Biomimetics*, 11(4):046002.

6.1 INTRODUCTION

Insects and birds have unmatched flying capabilities. This unique skill has evolved over the course of millions of years, enabling them to improve their survivability, evade predators and carry food. Aside from the development at a neuromuscular level, flying species have optimized their wing shapes and beats to provide them with enhanced performance and lift when required. An example of such evolution is the 'clap-and-fling' mechanism that typically occurs during the dorsal stroke-reversal of two-winged insects and specific birds, such as the pigeon [Nachtigall, 1982]. This mechanism can be seen as the (near) touch of the wings, which begins when the leading edges of the wings touch at the end of the dorsal outstroke (clap) and proceeds with the evolution of the point of interaction between the wings down the chordwise axis of the wings as they pronate around their trailing edges, and fling apart (cf. Figure 4 of Sane [2003]). Since the first description of this mechanism by Weis-Fogh [1973], several studies have identified variations of this motion to be present in many other species: *Trialeurodes vaporariorum* [Weis-Fogh, 1975], *Thrips physapus* [Ellington, 1984b], and the parasitoid wasp *Muscidifurax raptor* [Miller and Peskin, 2009]. Larger insects, such as *Lepidoptera* [Norberg, 1972b] and locusts [Cooter and Baker, 1977] also exhibit similar behaviors.

This particular flapping motion has been shown to augment the generation of lift during one flap cycle and is believed to be used by flapping flyers whose wing stroke capabilities are limited by their sweeping angle [Lehmann, 2007]. Adding to the observations of Weis-Fogh [1973], Ellington [1984b] further suggested that the *Chrysopa Carnea* uses clap-and-fling for lift augmentation, steering and flight control. Several experimental studies tried to prove these hypotheses by developing flapping mechanisms that promote wing interaction [Bennett, 1977a; Spedding and Maxworthy, 1986; Sunada et al., 1993]. More recently, experimental work [Lehmann et al., 2005; Lehmann, 2007; Groen et al., 2010; Percin et al., 2011; Nguyen et al., 2014] and numerical simulations [Mao and Xin, 2003; Miller and Peskin, 2005; Arora et al., 2014] concluded that the clap-and-fling mechanism can enhance lift production by 6% [Groen et al., 2010] to 50% [Kawamura et al., 2008] of the net average force, with most of the studies reporting lift gains of 15% to 25% [Lehmann, 2007; Nguyen et al., 2014].

Inspired by the evolution of natural flyers, such clap-and-fling mechanisms have been mimicked and implemented in a multitude of FWMAV with four wings [Groen et al., 2010; Baek, 2011; Prosser, 2011; de Croon et al., 2012; Nakata et al., 2011; WSU, 2012; Hsiao et al., 2012; Percin et al., 2012b; Deng et al., 2014; Rose and Fearing, 2014; Nguyen et al., 2015]. Reasons for choosing a four-wing design include: (1) lift augmentation, allowing the FWMAV to carry more payload, compared to their non-wing-interacting counterparts Lim et al. [2012]; (2) reduced complexity of flapping mechanisms with two degrees of freedom per wing, compared to multi-degree-of-freedom mechanisms of other designs [Keshavan and Wereley, 2007; Keennon et al., 2012]; (3) reduced flapping induced oscillations due to mutual cancellation of opposed forces caused by countermotion of opposed wings, which facilitates inertial measurement unit (IMU) and vision payload integration; and (4) for tailed FWMAV, the tail introduces static stability and simplifies the onboard control strategies.

Despite the significant maturation of technology, such FWMAVs still have very limited onboard processing capabilities, which, in turn, limit the use of complex control strategies for automatic and autonomous operations. These control strategies are typically characterized by simple PID controllers [Verboom et al., 2015], which limit the flight regime to conditions very close to the linearized model, e.g., the one presented in Chapter 5. More complex strategies, like nonlinear dynamic inversion or unsteady aerodynamic models working atop kinematic information, are currently too computationally expensive for onboard control. To avoid this complexity, some studies suggest the use of free-flight system identification for estimation of low-order ‘brute-force’ models [Grauer et al., 2011; Caetano et al., 2013a; Armanini et al., 2015] or the use of Fourier series for the complete modeling of the aerodynamic forces of an existing FWMAV, which is presented in Appendix E [Armanini et al., 2016b, 2015]. However, such methods are only possible if the FWMAV is already flight capable and typically involve expensive sensoring facilities, thus they are not applicable for the prediction of the aerodynamic, and consequently, the dynamic behavior of FWMAVs during the design phase.

As pointed out by many studies [Dickinson et al., 1999; Sane and Dickinson, 2002; Pesavento and Wang, 2004; Khan and Agrawal, 2005; Percin and van Oudheusden, 2015; Caetano et al., 2015a], in some cases a good compromise can be obtained through the use of quasi-steady aerodynamic models. These closely represent the aerodynamic forces of single non-interacting wings, with results matching experimental and numerical results with great approximation. Such models offer elegant solutions for the limitations identified above. However, for the specific case of lift-augmented clap-and-fling FWMAV, the quasi-steady models devised so far are lacking in three aspects: (1) quasi-steady aerodynamic representation of the added lift from wing-wing interaction during clap-and-fling; (2) accurate modeling of the wings, typically modeled as rigid flapping plates without consideration of spanwise torsion or of the added benefits of wing flexibility shown to be responsible for most of the lift gain [Miller and Peskin, 2009; Percin et al., 2011]; (3) providing model parameters for flight conditions other than hover, hence impeding their application to other flight conditions, where active control is more necessary.

The present study addresses the three aforementioned gaps and presents a simple phenomenological model for flapping-wing aerodynamics, which provides a suitable first approximation of the aerodynamic forces acting on a clap-and-fling FWMAV. The model expands current quasi-steady theory to include additional circulation terms that are present during and shortly after clap-and-fling. The parameters of the model are estimated from the force data of a real FWMAV, obtained from high resolution wind tunnel measurements, considering the real wing kinematics of the specific platform (the DelFly II [de Croon et al., 2012]) in different flight conditions. A global function of the parameters for different trimmed flight conditions is provided, which allows for fast computation of the aerodynamic parameters for a multitude of flight regimes, ranging from close to hover to fast 2m/s flight. Furthermore, the model is validated by comparing the force estimation in different flight regimes with real free-flight data of the FWMAV, ensuring additional closeness to the real physical system. The proposed model is simple, computationally fast and requires few input measurements, therefore potentially highly useful for control applications, being applicable as predictor already at the design stage. The main addition of the model developed in this Chapter over others in literature is presented in Table 6.1 for clarity.

The chapter continues with a comparison of existent quasi-steady models, a theoretical background of the clap-and-fling mechanism and a discussion of the proposed model in Section 6.2. Section 6.3 presents the experimental methods used to obtain the force data and wing kinematics, from both wind tunnel, free-flight testing and PIV measurements. This is followed by the results, discussion and validation of the estimated aerodynamic model in Section 6.4. Section 6.5 summarizes the most important conclusions and contributions to the community.

6.2 AERODYNAMIC MODELING

6.2.1 REVISITING QUASI-STEADY AERODYNAMIC MODELS

As identified by Sane [Sane, 2003], four unsteady mechanisms are present in flapping flight: 1) build-up of a starting vortex from the growth of a trailing edge vortex (TEV), i.e., Wagner effect; 2) delayed stall and leading edge vortex (LEV); 3) rotational circulation around a rotating surface, i.e., Kramer effect; 4) capture of the wake of the previous stroke by the subsequent one, i.e., wake capture. In addition to these, 5) inertial effects due to circular motion; 6) added mass effect due to accelerating wings and 7) wing-wing interaction are also important force generation mechanisms [Pesavento and Wang, 2004; Weis-Fogh, 1973].

Under the assumption of a quasi-steady development of the aerodynamics, the instantaneous forces acting on the wing are equivalent to the forces that would act during a steady uniform motion of the wing at the same free-stream velocity and angle of attack [Ellington, 1984a]. This way, a kinematic pattern can be divided into a number of consecutive time steps at which the forces are calculated, and the time history of the forces is obtained. Despite not considering some of the mechanisms mentioned above, viz. Wagner effect, wake capture and wing-wing interaction, and being initially derived for low angles of attack under thin airfoil theory, quasi-steady models of flapping wings have been shown to represent the aerodynamic forces with great approximation [Dickinson et al., 1999; Pesavento and Wang, 2004; Khan and Agrawal, 2005; Taha et al., 2014; Percin and van Oudheusden, 2015].

The applicability of quasi-steady models is limited by two aspects, as clarified by Table 6.1. On the one hand, for hovering flight regimes, quasi-steady models are applicable if the flapping frequency is considerably higher than the natural frequency of the flapper. When this is the case, the time scale of the flapping is so much smaller than that of the body dynamics, that cycle-averaged aerodynamic forces are sufficient for most types of analysis, and mostly these are not affected by the flow dynamics. On the other hand, for forward flight, the reduced frequency ($k = \frac{\omega c}{2V}$) should be lower than 0.2 for quasi-steady modeling to be applicable. When flow velocity is significantly higher than flapping frequency, unsteady effects are increasingly less dominant. As observed in Table 4.1, the reduced frequency values of the FWMAV range from 0.06 (for fast forward flight) to 0.38 (for close to hover) which begins to fall outside of the quasi-steady theory requirements. Nevertheless, the proposed model builds on quasi-steady principles and extends their applicability to account for clap-and-peel.

Table 6.1: Applicability of existent quasi-steady and proposed models, according to reduced frequencies ($k = \frac{\omega c}{2V}$) and natural frequencies (ω_n). Adapted from Taha et al. [2012, 2014].

	Hovering		**Forward Flight**		
Criteria	$\frac{\omega}{\omega_n} \gg 1$	$\frac{\omega}{\omega_n} \approx O(1)$	$k > 0.1$ $\alpha > 25°$	$k > 0.1$ $\alpha < 25°$	$k < 0.1$
Modeling Techniques	- Only average forces affect body dynamics - **QS Aerodynamics** that include LEV, e.g.: ∘ Dickinson et al. [1999] ∘ Berman and Wang [2007] - **Proposed Model**	- Contribution of LEV - Coupling between subflap forces and body dynamics - Numerical methods		- Methods that capture unsteady effects - UVLM ∘ Theodorsen [1935] ∘ Peters [2008]	- **QS Aerodynamics** that include forward flight information - **Proposed Model**

6.2.2 UNDERSTANDING THE CLAP-AND-PEEL MECHANISM

Following the initial description by Weis-Fogh [1973], for most species the clap-and-fling mechanism starts at the end of a half-stroke – at dorsal stroke reversal, cf. subfigure A in Figure 6.1. As the wings touch, the cleft that is formed closes under the point of contact of the wings in a 'clap'-shaped movement. During this phase, the air in the cleft is pushed down, which is believed to generate extra momentum [de Croon et al., 2012]. After the clap (B in Figure 6.1), the wings pronate and move away from each other, rotating about their trailing edges, which generates a rapid growth of a new cleft between the upper parts of the wings, as they 'fling' apart (C and D). At this phase, air rushes around the leading edge of each wing into the cleft, in what was observed as an augmented LEV [Percin et al., 2011]. As the flap continues, the LEV continues to grow and when the trailing edges separate, a starting trailing vortex starts to form (E).

The example case represented in Figure 6.1 is based on theoretical assumptions found in the literature [Weis-Fogh, 1973; Lighthill, 1973; Ellington, 1984a], complemented with experimental results of important studies in the field [Sane, 2003; Mao and Xin, 2003; Miller and Peskin, 2005; Percin et al., 2011; de Croon et al., 2012]. Several studies have focused on replicating this mechanism through mathematical [Lighthill, 1973], physical [Spedding and Maxworthy, 1986; Sunada et al., 1993; Lehmann et al., 2005] and numerical simulation [Mao and Xin, 2003; Kolomenskiy et al., 2011] to further conclude on the force augmentation mechanisms. All verified instantaneous and net force augmentation. However, two generalizations were present in these studies: 1) the wings were modeled as rigid; 2) the fling phase was modeled as a pure rotation about the trailing edges of the wings, without translation.

Recent observations concluded that in some cases the mechanism is better explained and replicated by a flexible 'peel' that replaces the described fling phase. It is believed that flexibility allows for a reconfiguration of biological structures, which results in reduced Drag [Miller and Peskin, 2009] and wake-capture mechanisms [Percin et al., 2011]. In this updated description, the upper parts of the wings 'peel' apart, while the lower parts are still 'clapping', due to a translatory motion induced by the wing flap reversal along the stroke plane. This reduces the effect of the clap, while promoting the generation of stronger LEV and a decrease of the adverse effects of added mass, due to the reduction of the effective portion of the wing that is accelerating during the outstroke.

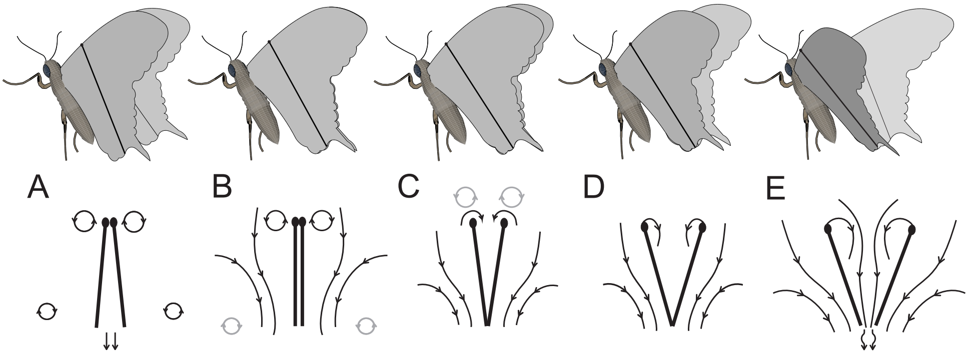

Figure 6.1: Clap-and-fling mechanism represented for a butterfly model with rigid wings. Arrows represent direction of flow; lines in black and gray represent current and previous subfigure vortices, respectively; detached lines are streamlines; circular shapes represent vortices; lines connected to leading edge are starting vortices; arrows at trailing edges of subfigure E represent the interaction between the beginning of starting vortices and the flow from withing the cleft.

Furthermore, this mechanism ensures a considerable reduction – and sometimes cancellation – of the trailing edge vorticity shed by each wing on the consequent stroke (during 'peel'), which promotes the growth of circulation, due to the absence of both the Wagner and Kramer effects – also considered to be one of the reasons for force augmentation [Sane, 2003].

6.2.3 PROPOSED AERODYNAMIC MODEL

Compared to other modeling techniques such as CFD or unsteady vortex lattice methods (UVLM), quasi-steady models gain from their physical insight, relatively simple form and low computational cost (cf. Table 6.2), suitable for physical understanding of the force generation mechanisms, design of FWMAV, control and simulation. Nevertheless, none of the existing quasi-steady models include the contribution of wing-wing interaction, thus failing to predict both the instantaneous and the time-averaged Lift augmentation present in clap-and-peel mechanisms.

Table 6.2: Comparison between existent and proposed models. The focus is on non-CFD methods, as CFD models are not phenomenologically insightful or applicable for on-board control. Adapted from [Taha et al., 2014].

	Dickinson et al.	Berman & Wang	Peters et al.	Khan & Agrawal	UVLM	Ansari et al.	**Proposed model**
# degrees of freedom	low	low	low	low	high	high	low
LEV	✓	✓	-	✓	-	✓	✓
Rotational circulation	✓	✓	✓	✓	✓	✓	✓
Added mass	✓	✓	✓	✓	✓	✓	✓
Viscous effects	-	✓	-	✓	-	-	✓
Wake capture	-	-	-	-	✓	-	-
Wing flexibility	-	-	-	-	-	-	✓
Clap-and-peel	-	-	-	-	-	-	✓
Validated in forward flight	-	-	-	-	-	-	✓
Applicability to onboard control	low	high	low	low	low	low	high

The proposed model builds on existent quasi-steady models to include the effects listed in Section 6.2.1, as items (2) to (7). An extensive survey was performed to understand the applicability and compare the (dis)advantages of the formulations across the literature.

GENERAL FORMULATION

The baseline of the proposed model consists of the combination of quasi-steady aerodynamics with blade element theory [Pesavento and Wang, 2004; Berman and Wang, 2007; Whitney and Wood, 2010]. The forces acting on a wing are divided into blade elementary forces, that are integrated along the spanwise direction to obtain the time history of the forces. The forces acting on a single blade element (BE), at each time instant, take the form:

$$d\boldsymbol{F} = d\boldsymbol{F}_{inertial} + d\boldsymbol{F}_{circ} + d\boldsymbol{F}_{addmass} - d\boldsymbol{F}_{visc} \tag{6.1}$$

which accounts for the inertial, circulatory, added mass and viscous effects, respectively. Note that initial TEV shedding (Wagner effect) was not considered because: a) this effect has different contributions to the forces, depending on the Reynolds number (Re) of the system; a) there is no apparent agreement on the effectiveness of such mechanisms in flapping wings [Lehmann, 2007]; c) clap-and-peel mechanisms considerably attenuate the starting TEV; d) mathematical simplicity.

The inertial term is present in the model: a) because forces are being computed in a rotating coordinate frame [Berman and Wang, 2007] and b) to account for the inertial forces of the mass of fluid which act normal to the wing surface, estimated from two-dimensional theory of a plate moving in an inviscid fluid [Andersen et al., 2005b] – cf. our final model formulation in Eqs. 6.12 and 6.13. While the inertial forces are not a strictly aerodynamic effect, we chose to include them because our experimental setup allowed us to measure only the total forces generated by the wings and, as pointed out in the literature [Sane, 2003], it is highly challenging to separate the aerodynamic forces from the inertial forces in experimental measurements. This term is not discussed further. The other three terms we discuss in detail, in the remainder of this section, progressively building up our model until the final formulation is obtained in Section 6.2.3.

CIRCULATORY TERM

The circulatory term ($d\boldsymbol{F}_{circ}$ in Eq. 6.1) results from a combination of the translatory circulation (Γ_{trans}), and the rotational circulation (Γ_{rot}). Both are included to satisfy the Kutta condition (cf. Figure 2 in Sane [2003]). For single, non-interacting wings (in this case, blade elements) Γ_{trans} includes the contribution of free-stream circulation and LEV; while Γ_{rot} accounts for the added circulatory term needed to maintain the Kutta condition for a rotating blade element. These take the form:

$$\Gamma = \Gamma_{trans} + \Gamma_{rot} = \frac{1}{2} C_L c(r)|V| + \frac{1}{2} C_R c^2(r)\dot{\theta}_w \tag{6.2}$$

where C_L is the Lift coefficient, $|V|$ is the magnitude of the velocity (vector) perceived by the element, C_R is the rotational coefficient, $c(r)$ is the chord as function of the spanwise radius and $\dot{\theta}_w$ is the pitch rate of the wing element.

Several C_L and C_R formulations were studied from literature: viz. for C_L Figure 2 in Dickinson et al. [1999], Eq. 2.16 in Berman and Wang [2007], Eq. 31 in Wang and Eldredge [2013] and Eq. 17 in Taha et al. [2014]. The values for the parameters in each formulation were optimized (as explained below), and similar results could be obtained with all formulations by adjusting the parameters. Hence, we recommend:

$$C_L = C_l \sin(2\alpha) \quad \text{or} \quad C_L = \frac{\pi AR}{2(1+\sqrt{(\frac{\pi AR}{a_0})^2+1})}\sin(2\alpha) \tag{6.3}$$

with the former [Berman and Wang, 2007] for simplicity, the latter [Taha et al., 2014] for preliminary design purposes, to include the aspect ratio (AR) of the wing. C_l is the Lift coefficient magnitude, a_0 is the Lift curve slope of a two-dimensional airfoil, and α is the angle of attack at the blade element. The rotational coefficient C_R takes the form observed in Dickinson et al. [1999] and in Sane and Dickinson [2002]:

$$C_R = C_r(0.75 - x_0) \tag{6.4}$$

with C_r the coefficient, and x_0 the chordwise position of the axis of rotation of the wing section.

The final circulatory term used in the model is derived in the next section, where clap-and-peel effects are discussed and incorporated in the formulation.

INCLUDING CLAP-AND-PEEL

Despite a lack of agreement on how to model clap-and-peel, some aspects have been observed across multiple studies: (1) increased growth of circulation during clap-and-fling [Weis-Fogh, 1973; Lighthill, 1973; Ellington, 1984c; Kolomenskiy et al., 2011]; (2) prolonged effect of clap-and-fling on Lift augmentation, still noticeable after the fling until half-way of the wing stroke [Mao and Xin, 2003; Lehmann et al., 2005]; 3) contribution of wing flexibility to increase in Lift augmentation and significant reduction in Drag [Miller and Peskin, 2009; Noda et al., 2014]. These points are detailed below.

Lighthill suggested the force augmentation mechanism could be described mathematically by a circulatory term of the form [Lighthill, 1973; Kolomenskiy et al., 2011]:

$$\Gamma = g(\lambda)\dot{\theta}c^2 \tag{6.5}$$

with $g(\lambda)$ being a function of the angle between the wing sections ($\lambda = \theta_{fling}/\pi$). A similar theoretical formulation was later introduced by Edwards and Cheng [1982] and Wu and Hu-Chen [1984], who added circulatory terms to the initial formula, with no considerable changes in the outcome. In their study, Spedding and Maxworthy [1986] verified the formulation by performing a wing-wing interaction experiment with pure rotation around the trailing edge, obtaining discrete values for $g(\lambda)$ for different wing separation angles. They concluded the function $g(\lambda)$ to be different from the previous theoretical formulations, taking a somewhat constant value (≈2) up to θ_{fling}=30°, and then increasing linearly with the increase of the separation (cf. Figure 17 in Spedding and Maxworthy [1986]). Moreover, Sunada et al. [1993] also obtained similar results for different wing shapes. These results point to the coherence of the initial circulatory formulation of Eq. 6.5, indicating that after 30° other circulatory terms seem to dominate.

Furthermore, during fling the trailing edges of interacting wings are in contact, which considerably attenuates the generation of TEV, known as starting vortices, thus reducing the delay in bounded circulation growth [Sane, 2003; de Croon et al., 2012; Sane, 2011]. This force augmentation was found to be present also in the case of interacting wings that initiate a translatory motion after the fling [Mao and Xin, 2003; Lehmann et al., 2005]. In particular, it was demonstrated that the clap-and-fling force augmentation still produces effects as late as mid-stroke, after the fling has occurred, suggesting that this mechanism may be distorting the spatio-temporal structure of the wake of the previous stroke, in what could be considered wake-capture. Such phenomenon was later observed experimentally by Percin et al. [2011], who showed the Lift enhancing wake-capture in clap-and-fling mechanisms was possible due to wing flexibility and consequent peel instead of fling. The same study also revealed that during peel a stronger LEV forms, which continues to grow after the peel phase, during wing translation. This is in line with numerical results of Miller and Peskin [2009] and Noda et al. [2014] who observed a considerable Lift increase and surprising Drag reduction due to the inclusion of flexibility in the model.

Conversely, others suggested different theoretical formulations for the force augmentation. Ellington [1984c] proposed a circulation dependent on the velocity of the ‘unzipping’ of the wings ($u_z(t)$) during a modeled ‘flat peel’:

$$\Gamma = u_z(t) x_e f(\theta_{fling}), \quad f(\theta_{fling}) \approx \left(\theta_{fling} - \frac{\pi}{2}\right)^2 + 2 \tag{6.6}$$

with x_e being the effective chord length exposed (‘flung part’). This formulation was tested also in our model; however simpler alternatives were found to yield effective results while requiring less complex computation, e.g., avoiding the calculation of wing ‘unzipping’ velocity. Hence Eq. 6.6 was not used for the final formulation, which presented below in Eqs. 6.12 to 6.14.

Furthermore, actuator disk and conservation of mass theories were suggested to explain additional force observed during clap-and-fling: Bennett [1977b] proposed a formulation based on the conservation of mass around the leading edge, suggesting the fling to promote the growth of induced velocity in the cleft between the wings. He showed this induced velocity was considerably higher in the presence of a mirror wing. Under similar assumptions we have concluded the induced velocity to be a function of the wing flap angle (ζ), flap rate ($\dot{\zeta}$), wing pitch angle (θ_w)[1] and pitch rate ($\dot{\theta}_w$). This approach, however, results in complex formulas that were tested against the method suggested below with no considerable improvements, and hence was not considered for implementation.

The previous observations support the following hypothesis, which addresses the three aspects (1 to 3) mentioned in the beginning of this section:

As opposed to rigid wing clap-and-fling, the flexible clap-and-peel mechanism is dominated by both the translation and the rotation of the wings around the leading edge. Hence, its dominant effects can be explained by a combination of translatory and rotational circulation, defined as functions of wing flap rate ($\dot{\zeta}$) and wing pitch rate ($\dot{\theta}$). After

---

[1] θ_w is the angle between the blade element and the $y_b z_b$ plane; cf. Figure 2.6

the peel phase, the peel rotational circulation ceases when the wing stops rotating ($\dot{\theta}$=0), giving place to a rotational circulation needed to establish the Kutta condition after the trailing edges peel apart.

Hence, clap-and-peel is included in the model by adapting the circulation equation (Eq. 6.2) to the hypothesis in the form of a piecewise function: the first piece acts during the peel phase, until the wing reaches a constant pitch angle (pitch rate $\dot{\theta}=0$) and the second piece equals the circulation of Eq. 6.2:

$$\Gamma = \begin{cases} \frac{1}{2}C_L c(r)|V| + \frac{1}{2}C_F c^2(r)\dot{\theta}_{fling} & \text{if} \quad t^* \geq 0 \quad \text{and} \quad \dot{\theta}_{fling} \geq 0 \\ \frac{1}{2}C_L c(r)|V| + \frac{1}{2}C_R c^2(r)\dot{\theta}_w & \text{else} \end{cases} \tag{6.7}$$

where C_F is the fling coefficient, $t^* = t/T$ is the dimensionless time per flap cycle (period T) and $\dot{\theta}_{fling} = -\dot{\theta}_w$. The above equation thus replaces Eq. 6.2 in the final model.

Different formulations were tested and Eq. 6.7 was found to be the simplest and still physically meaningful formulation to model clap-and-peel, as it considers: a) circulation to be a function of wing flap (translatory circulation) and pitch angles as demonstrated in conservation of mass theory; b) different circulatory terms for each part of the motion; c) cancellation of TEV and the Kramer effect during peel. The clap part was not considered, since for flexible wings its contribution is reduced [Lehmann, 2007]. Thus, the circulatory force contribution in Eq. 6.1 can now be obtained from:

$$d\boldsymbol{F}_{circ} = \begin{bmatrix} dF_{circ_x} \\ dF_{circ_z} \end{bmatrix} = -\rho_f \Gamma \begin{bmatrix} v_{z_w} \\ -v_{x_w} \end{bmatrix} dr \tag{6.8}$$

where ρ_f is the density of the surrounding fluid.

ADDED MASS

The added mass term ($d\boldsymbol{F}_{addmass}$ in Eq. 6.1) originates from the surrounding fluid during blade element acceleration. For a section of size $c \times b \times d_r$, with c the chord, b the thickness, d_r the infinitesimal length, it takes the general form:

$$d\boldsymbol{F}_{addmass} = \begin{bmatrix} dF_{addmass_x} \\ dF_{addmass_z} \end{bmatrix} = -\begin{bmatrix} m_{11}a_{x_w} \\ m_{22}a_{z_w} \end{bmatrix} dr \tag{6.9}$$

6

where m_{11} and m_{22} are the mass of the surrounding fluid being accelerated along the axes of the wing section. These are obtained from the two-dimensional theory of the Joukowski foil profile [Korotkin, 2009]. Here, we consider the wings to be thin flat plates[2] with thickness b:

$$m_{11} = \frac{1}{4}\pi\rho_f b^2, \quad m_{22} = \frac{1}{4}\pi\rho_f c^2_{eff}(r) \tag{6.10}$$

Note that Eq. 6.10 accounts for an effective chord ($c^2_{eff}(r)$), by only considering the 'peeled' part of the chord for added mass purposes – failing to consider this may result in errors in the final model outcome.

---

[2] Formulas for other airfoil shapes can be obtained using Equation on p. 38 of Korotkin [2009], with wing profile information from, e.g., Abbott and Doenhoff [1959]

VISCOUS EFFECTS

Viscous effects (term $\boldsymbol{dF}_{visc}$ in Eq. 6.1), arising from fluid viscosity and friction, are modeled as Drag force acting at each section. Similarly as for the C_L terms, several forms were revisited, viz. Dickinson et al. [1999]; Berman and Wang [2007]; Wang and Eldredge [2013]. After parameter estimation, all forms were found to lead to approximate results. One particular aspect of the model (Eq. 32) in [Wang and Eldredge, 2013] was that it should only be applied in the initial phase of the stroke. Due to singularities present in other formulations, the following was used [Pesavento and Wang, 2004; Berman and Wang, 2007; Taha et al., 2014]:

$$\boldsymbol{dF}_{visc} = \begin{bmatrix} dF_{visc_x} \\ dF_{visc_z} \end{bmatrix} = \frac{1}{2}\rho_f c(r) C_D |V| \begin{bmatrix} v_{x_w} \\ v_{z_w} \end{bmatrix} dr, \quad \text{with} \quad C_D = C_{D_0}\cos^2\alpha_w + C_{D_{\frac{\pi}{2}}}\sin^2\alpha_w \tag{6.11}$$

where C_{D_0} and $C_{D_{\frac{\pi}{2}}}$ are the Drag coefficients for zero and 90°angle of attack of the wing, respectively; v_{x_w} and v_{z_w} are the relative velocities of the blade elements at each wing, along the $\boldsymbol{x}_w$ and $\boldsymbol{z}_w$ axes, respectively; and α_w is the element relative angle of attack, computed from $\arctan(-v_{zw}/v_{x_w})$.

FINAL PROPOSED MODEL

The aerodynamic forces acting along the $\boldsymbol{x}_w$ and $\boldsymbol{z}_w$ axis of each wing blade element can now be formulated as the following equations, in conjunction with Eqs. 6.7, 6.10 and 6.11:

$$\begin{aligned} \boldsymbol{dF} &= \boldsymbol{dF}_{inertial} && + \boldsymbol{dF}_{circ} + \boldsymbol{dF}_{addmass} - \boldsymbol{dF}_{visc} \\ dF_{x_w} &= [m_1 v_{z_w}\dot{\theta}_w && -\rho_f \Gamma v_{z_w} - m_{11} a_{x_w}]dr - dF_{visc_x} \qquad (6.12) \\ dF_{z_w} &= [-m_2 v_{x_w}\dot{\theta}_w && +\rho_f \Gamma v_{x_w} - m_{22} a_{z_w}]dr - dF_{visc_z} \qquad (6.13) \end{aligned}$$

$$m_1 = \frac{c(r)}{\bar{c}R} M_{wing} + m_{22}, \quad m_2 = \frac{c(r)}{\bar{c}R} M_{wing} + m_{11} \tag{6.14}$$

where M_{wing} is the wing mass and ρ_f is the fluid density. The equation terms are arranged in the same order as in Eq. 6.1, which is shown again here for better clarity.

This model is extendable to flapping species and ornithopters with: a) two or four wings; b) dorsal, or dorsal and ventral wing interaction; c) flight conditions different from hover; d) dihedral on the wings. Hence, the infinitesimal forces acting along the body reference frame can be calculated for each blade element using:

$$\begin{aligned} dF_{x_b} &= dF_{x_w}\sin\theta_w + dF_{z_w}\cos\theta_w \\ dF_{z_b} &= (dF_{x_w}\cos\theta_w - dF_{z_w}\sin\theta_w)\cos\zeta \end{aligned} \tag{6.15}$$

The total force is then computed by numerically integrating the forces acting on each blade along the span of the wing (from Eq. 6.15), considering the wing shape, real flapping kinematics, pitch and velocity of the FWMAV and relative wind perceived by each wing element. Finally, the total Lift and Drag forces can be obtained from the known body pitch attitude θ, which in the wind tunnel setup corresponds to the body angle of attack:

$$\begin{aligned} Lift &= F_{x_b}\sin\theta - F_{z_b}\cos\theta \\ Drag &= -F_{x_b}\cos\theta - F_{z_b}\sin\theta \end{aligned} \tag{6.16}$$

6.3 MATERIALS AND METHODS

The two experimental techniques detailed in Chapter 4 were used for model identification. Additionally, PIV data was used to improve the kinematic model of the relation between the flap angle to the wing pitch angle, presented in Chapter 3, Eq. 6.17. In the interest of objectiveness, the free-flight and wind tunnel experimental procedures will not be re-stated in this Chapter. The parameters of the aerodynamic model were identified using the wind tunnel forces, and validated using the free-flight data.

6.3.1 MODELING THE KINEMATICS OF THE WING

The wing kinematics are obtained from experimental data, using a combination of high-speed cameras, motor rotation sampling and PIV measurements [Groen, 2010; Caetano et al., 2015c]. The wing has one active degree-of-freedom (DOF), characterized by the flapping motion along the stroke plane that is perpendicular to the body of the FWMAV. Here, this DOF is represented by the so-called flap angle, ζ, measured as the angle between the wing leading edges and the position of closed wings, ζ_0. Passive pitching is a consequence of wing flexibility, kinematic and aerodynamic forces. As an example of the real wing foil motion, Figure 6.3 presents the shape of the wing foil at 70% of the wing span (see Figure 6.2a) throughout one flap cycle, for 11Hz flapping frequency and hover conditions ($V_{inf}=0$) [Groen, 2010].

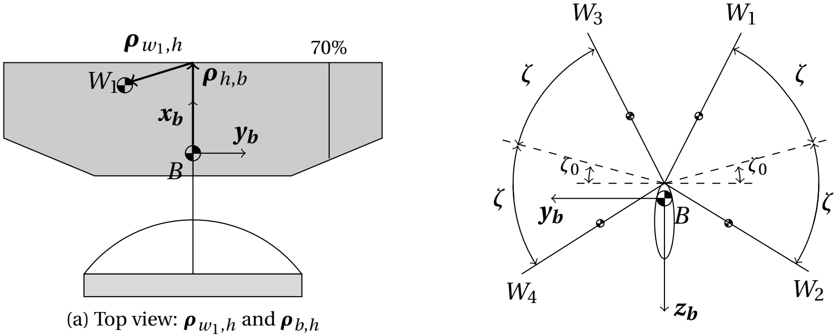

(a) Top view: $\rho_{w_1,h}$ and $\rho_{b,h}$ representation, from CG of the body to CG of the wing, with closed wings.

(b) Front view: wings open at angle ζ; dashed line represents position of the closed wings at ζ_0.

Figure 6.2: Simplified model with CG, Body (B) and Wing (W1 to W4) reference frames. Gray areas represent moving parts.

This information was used to compute a mathematical relation between wing shape, flap angle (ζ) and flap angle rate ($\dot{\zeta}$) using Eq. 6.17 in Matlab. Please note that this Eq. was further improved from Eq. 3.2 to include the $\dot{\zeta}^2$ term.

$$\hat{\theta}_w = \frac{\pi}{2} + C_{\theta_{w_0}} + C_{\theta_{w_\zeta}}\zeta + C_{\theta_{w_{\dot{\zeta}}}}\dot{\zeta} + C_{\theta_{w_{\dot{\zeta}^2}}}\dot{\zeta}^2 \tag{6.17}$$

Despite not considering in-flight deformations from turbulence and unsteady effects, this formulation relates the wing shape to the wing flap phase, reducing the DOF of the model, and hence its complexity, while still maintaining real kinematic properties. The coefficients were obtained through least-squares estimation and are presented in Table 6.3.

Table 6.3: Estimated coefficients for Eq. 6.17 using the distribution in time of the entire chord.

Coefficient	**Value**
$C_{\theta_{w,0}}$	0.3139
$C_{\theta_{w,\zeta}}$	-1.1382
$C_{\theta_{w,\dot{\zeta}}}$	-0.0179
$C_{\theta_{w,\dot{\zeta}^2}}$	-0.0002

Wing torsion was verified to have a close to linear evolution in spanwise direction throughout the flap cycle. It was linearly interpolated, in spanwise direction, between zero wing pitch angle (θ_w) at the wing root and the wing pitch angle at 70% of the span, observed from PIV [Groen et al., 2010]. The different relative wind perceived by each blade element is a function of the spanwise location of that element (r), the pitch angle of the body (θ) and forward velocity of the ornithopter (V_{inf}), wing dihedral (ζ_0), wing flap angle (ζ), wing flap rate ($\dot{\zeta}$), and wing pitch axis of rotation (d) along the chord (c), which is parallel to y_w. Lateral movement of the ornithopter is neglected. Hence, the relative velocity perceived by the upper and lower wing elements, neglecting downwash and unsteady effects (e.g. LEV) is given by:

$$\begin{aligned} v_{x_{w_u}} &= r_i\dot{\zeta}\cos\theta_w - V_{\text{inf}}\cos(\theta_u) \quad \text{and} \\ v_{z_{w_u}} &= -r_i\dot{\zeta}\sin\theta_w - dc(r)\dot{\theta}_w + V_{\text{inf}}\sin(\theta_u)\cos(\zeta_0+\zeta) \end{aligned} \tag{6.18}$$

$$\begin{aligned} v_{x_{w_l}} &= r_i\dot{\zeta}\cos\theta_w + V_{\text{inf}}\cos(\theta_l) \quad \text{and} \\ v_{z_{w_l}} &= -r_i\dot{\zeta}\sin\theta_w - dc\dot{\theta}_w - V_{\text{inf}}\sin(\theta_l)\cos(\zeta_0-\zeta) \end{aligned} \tag{6.19}$$

where $\theta_u=\theta-\theta_w+\frac{\pi}{2}$ and $\theta_l=\theta+\theta_w-\frac{\pi}{2}$, and $d=0$ for the present case. The acceleration of each wing element is obtained by differentiating the previous formulations in time – worth noting that d should be equal to 0.5 to compute the acceleration for the added mass effect. Furthermore, the effective chord used in Eq. 6.9 varies linearly between 0, at the beginning of the fling ($t^*=0$), and 1, when the blade elements peel apart ($t^*\approx 0.17$).

The wing flap angle (ζ) was captured at 1kHz in the tests. While the high frequency makes the state more accurate, the numerical differentiation of this state introduces considerable error magnification, as seen in Chapter 4 [Caetano et al., 2015c], which adds to discontinuities in the differentiated state. Furthermore, the wing flap motion takes more time to completely perform the outstroke than the instroke, due to the fling suction and latency in the motor torque. For these reasons, a biased wing beat formula was used that considers this split cycle evolution with constant period [Oppenheimer et al., 2011].

$$\phi_{up}(t^*) = -A_{amp}\cos((\omega-\kappa)t^*)+\vartheta \tag{6.20}$$

$$\phi_{down}(t^*) = -A_{amp}\cos((\omega+\sigma)t^*+\xi)+\vartheta \tag{6.21}$$

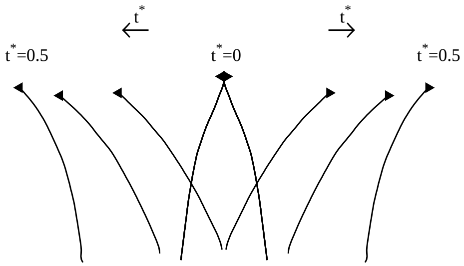

(a) Chord evolution of beggining of outstroke, nondimendional time $t^* \in [0, 0.5]$

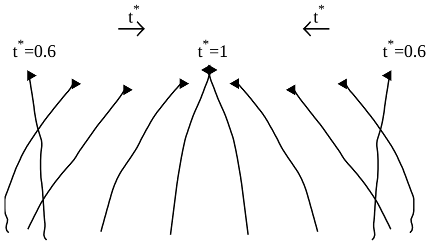

(b) Chord evolution for instroke, $t^* \in [0.6, 1]$

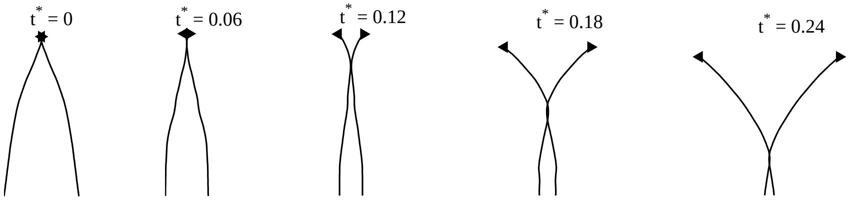

(c) Detailed chord evolution for first part of outstroke, nondimensional time $t^* \in [0, 0.24]$

Figure 6.3: Chord evolution during one flap cycle, for two flexible wings displaying clap-and-peel interaction. Subfigure (c) is a detailed representation of the chord evolution between the first and second time frames in subfigure (a).

where ω is the fundamental frequency, ϑ is the wing bias, κ is the split-cycle parameter, $\sigma{:=}\kappa\omega/(\omega-2\kappa)$, $\xi{:=}-2\pi\kappa/(\omega-2\kappa)$, and A_{amp} adjusts the values to the amplitude of the flapping. The coefficients of the formula were identified as: $A_{amp}=0.34, \kappa=0.35, \vartheta=0.34$. More details on this approximation can be found in Oppenheimer et al. [2011].

6.3.2 TIME-RESOLVED FORCE DATA

Figure 6.4 presents the forces in $\boldsymbol{x}_b$ and $\boldsymbol{z}_b$ direction (X and Z) for a two-flap cycle window and different trimmed flight conditions. For clarity, only four out of the eight test conditions are represented, as there were only four different flapping frequencies in the wind tunnel tests and previous Chapter 4 [Caetano et al., 2015c] showed that, for this ornithopter, flapping frequency has the most noticeable effect on the evolution of the forces. The figure presents the forces determined from both experimental methods. The plot on the left shows the evolution of the forces acting on the FWMAV in free-flight computed using single rigid body kinematics (Chapter 3) – the forces from rigid body kinematics are shown for a better fit with the wind tunnel forces, since both capture inertial and aerodynamic effects. The plot on the right shows the forces obtained from the force transducer in the wind tunnel. The arrows indicate the direction of lowering flapping frequency and increasing total velocity. It is worth noting that the forces from the wind tunnel present a smoother evolution given the direct force measurement and the much higher sampling frequency, as compared to the forces obtained from free-flight, which are significantly more challenging to obtain, as seen in [Caetano et al., 2015d].

As shown in Chapter 4, the raw forces obtained from both experimental methods are not easily processed, due to the significant noise at high frequencies. Particularly in the forces determined from free-flight data, the signal-to-noise ratio reduces considerably due to the double time-differentiation used to compute the accelerations. To reduce the noise, both free-flight and wind tunnel obtained forces were filtered using a zero-phase lag low-pass filter. A cut-off frequency of 40Hz (just above the second harmonic of the flapping frequency) was found to provide sufficient detail for a comparison between wind tunnel and free-flight forces, as well as an accurate evolution of the forces. However, this filters out some details of the aerodynamic force production mechanisms. In particular, the clap-and-fling peak is filtered out, while it is clearly recognizable when higher cut-off frequencies are used. Figure 6.5 shows the wind tunnel forces low-pass filtered at 67Hz (just above the fourth harmonic of the flapping frequency): here the clap-and-fling peak can be seen in the shaded area at the beginning of the flap cycle. By contrast, in the 40Hz-filtered data, this additional peak is merged with the following one, so that while the resulting force augmentation is still recognizable, some details of the force evolution are lost. Lower cut-off frequencies also filter out the initial part of the stroke reversal for non-dimensional cycle times $t^* \in [0.58, 0.70]$. One significant limitation of a higher filter cut-off, however, is that in the current free-flight tests, frequency content above three harmonics was not clearly recognizable and distinct from noise [Caetano et al., 2015c]. For this reason, higher filter cut-offs were only considered further for the wind tunnel data.

The X forces obtained from both experimental methods exhibit a very similar evolution, with phase and peak amplitude decreasing with decreasing flapping frequency and increasing total velocity, as clarified by the large arrows in Figure 6.4b. Moreover, the

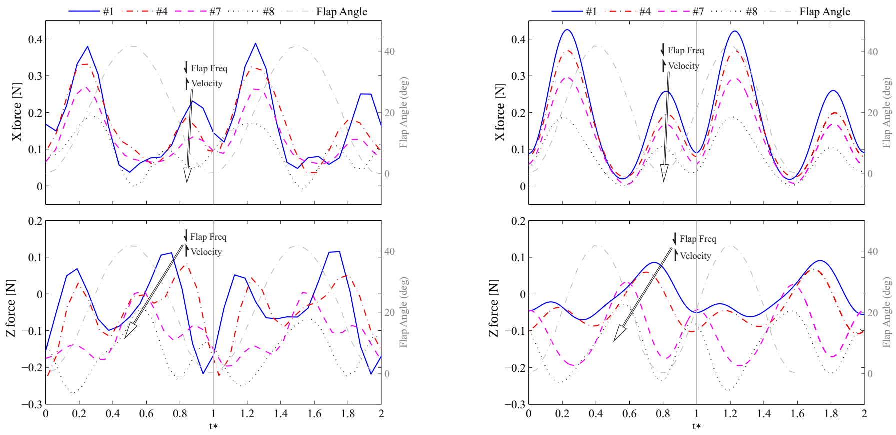

(a) Forces determined from free-flight tests, using single rigid body kinematics.

(b) Forces determined from wind tunnel experiments.

Figure 6.4: Forces acting on the FWMAV, filtered at 40Hz, for test conditions #1, #4, #7 and #8 – cf. Table 4.1. The large arrows indicate the direction of peak phase and amplitude changes with decreasing flapping frequency and increasing total velocity.

sub-flap level behavior of the X forces is similar for all test conditions, and characterized by a nearly constant cycle phase and a peak amplitude that varies with the flapping frequency, as mentioned. The data suggest that in a typical steady flight condition, the X force is the main component sustaining the flight. By contrast, the Z forces vary more between the two experimental methods and between different test conditions. This is due to the restriction imposed by the clamping in the wind tunnel. In free-flight there is an oscillatory motion around the $\boldsymbol{y}_b$ axis, which is more pronounced at higher flapping frequencies, whereas in the wind tunnel this motion is suppressed.

For our modeling, we chose wind tunnel data over flight data for several reasons. Firstly, the wind tunnel measurements have a higher resolution thanks to the significantly higher sampling frequency, and allow for unsteady effects to be clearly visualized, and thus for the obtained models to be evaluated more thoroughly. Secondly, there are fewer external disturbances acting during wind tunnel testing, and a wide range of test conditions can be selected and maintained very effectively. These conditions can be considered realistic, if they are selected to correspond to existing free-flight conditions. Finally, wind tunnel testing allows for the wing aerodynamics to be separated from tail effects. The proposed quasi-steady model accounts only for the aerodynamic forces produced by the wings, thus it is more accurate, on a theoretical level, to use force measurements conducted on the wings alone for model identification. The discussed differences between free-flight and wind tunnel data do have to be considered, however they were found to be negligible for the X force component, which is the main contributor to Lift. Given that Lift is the main component of interest, this limitation was considered acceptable.

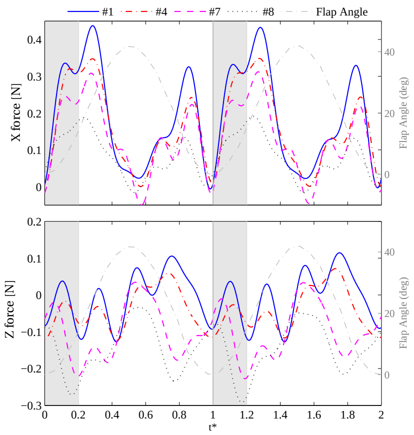

Figure 6.5: Forces acting on the FWMAV, measured in the wind tunnel and filtered at 67Hz, for test conditions #1, #4, #7 and #8 – cf. Table 4.1. Shaded areas indicate the clap-and-peel phase.

6.3.3 PARAMETER ESTIMATION APPROACH

To apply the proposed model (Eqs. 6.12-6.13), the unknown parameters flowing into it ($\Theta = \left[C_l\ C_r\ C_{D0}\ C_{D\frac{\pi}{2}}\ C_F \right]$, cf. Eqs. 6.3, 6.4, 6.7, 6.11) must be determined. These parameters were estimated using a Maximum Likelihood estimator [Jategaonkar, 2006; Klein and Morelli, 2006]. The estimation maximizes the probability of an observation z occurring at a measurement instant k, given a set of parameters Θ. The cost function for this type of problem can be expressed as:

$$J(\boldsymbol{\Theta},\mathbf{R}) = \frac{1}{2}\sum_{k=1}^{N}\left[\mathbf{z}(k)-\mathbf{y}(k)\right]^{T}\mathbf{R}^{-1}\left[\mathbf{z}(k)-\mathbf{y}(k)\right] + \frac{N}{2}\ln\left(\det(\mathbf{R})\right) + \frac{Nn_y}{2}\ln(2\pi), \qquad (6.22)$$

where $\mathbf{R}$ is the measurement noise covariance matrix, N is the number of data samples, n_y is the number of output variables, and $\mathbf{z}(k)$ and $\mathbf{y}(k)$ are the measured and model-predicted outputs, respectively, at measurement time k. The noise covariance matrix $\mathbf{R}$ is estimated in each iteration step using a relaxation technique.

A Gauss-Newton algorithm was used to minimize the cost function. Initial guesses for the parameters, required to initialize the estimator, were based on values in the literature [Andersen et al., 2005b; Berman and Wang, 2007], and are presented in cf. Table 6.4. However, testing showed that the result was not sensitive to the choice of these values. The output equation was obtained via integration from Eqs. 6.12 and 6.13, which represent the forces over a single blade element. The measurements required for this model are the flap angle and its derivative, the wing pitch angle and its first and second derivatives, the flapping frequency, and the forward flight velocity. All of these could be obtained from the wind tunnel tests.

Different estimation setups were investigated, as detailed in Section 6.4.1. Depending on the case, the output $\mathbf{z}$ includes one or both of the aerodynamic forces X and Z,

Table 6.4: Initial guesses for the model parameters, based on values in the literature [Andersen et al., 2005b; Berman and Wang, 2007].

Parameter	Initial value before estimation
C_l	1
C_r	1.6
C_F	1
C_{D0}	0
$C_{D\frac{\pi}{2}}$	π

which is in each case a function of a different set of parameters (out of those available, mentioned above) and measurements.

6.4 RESULTS AND DISCUSSION

This section presents the parameter estimation methodology, and compares the results of the forces obtained from the clap-and-fling model, compared to previously developed base-line models. Worth noting that further comparisons were established between a quasi-steady model (with a formulation that is less complex than the model presented in this Chapter) and a Fourier-series based model, which are presented in Appendix E.

6.4.1 PARAMETER ESTIMATION PROCEDURE

Preliminary tests were conducted to establish the most plausible and effective identification approach. This involved estimating different subsets of the available parameters (cf. Table 6.4), while fixing other parameters at predefined values, and using the X force, Z force, or both as outputs within the estimation process. Worth noting that the parameters were estimated using Maximum Likelihood method, detailed in Section 6.3.3 and in Appendix E.

The chosen setup uses X as sole output measurement, and estimates the parameters C_l, C_r and C_F. It was found that estimating C_{D_0} and $C_{D\frac{\pi}{2}}$ together led to an accurate output but implausible values for these two parameters. This is most likely because these parameters do not have a significant effect on the X force component and hence cannot be identified effectively from X force data. C_{D_0} is also typically very small and thus difficult to estimate reliably. Hence, these parameters were fixed *a priori* at literature-based values (cf. Table 6.4) to ensure physically realistic results.

The X force was selected as output because it is the main contributor to Lift in typical flight regimes, and hence of more interest. Moreover, as discussed in Section 6.3, the Z forces measured in the wind tunnel are significantly affected by the clamping and, therefore, are not a realistic representation of the forces occurring in free-flight. Similarly, the Z component of the forces is considerably affected by the tail of the FWMAV. This again introduces a difference between wind tunnel and free-flight measurements, and additionally implies that the current model, which considers only the wings, is inadequate for a complete representation of the Z forces.

All results presented refer to the outlined setup. In the interest of clarity, results are shown in terms of Lift and Drag forces, as defined in Eq. 6.16. Furthermore, to al-

Table 6.5: Evaluation of computed models

	Lift			**Drag**		
Test #	**RMSE [N]**	**RMSE [%]**	**PCC**	**RMSE [N]**	**RMSE [%]**	**PCC**
1	0.05	13	0.97	0.03	23	0.66
2	0.04	13	0.97	0.05	43	0.25
3	0.04	13	0.97	0.04	36	0.34
4	0.05	15	0.96	0.05	48	0.04
5	0.04	17	0.96	0.05	52	0.30
6	0.05	18	0.94	0.05	64	0.24
7	0.05	50	0.92	0.04	43	0.90
8	0.05	32	0.85	0.04	47	0.72
avg.	0.04	21	0.94	0.04	44	0.43

low for validation with free-flight data, the model is compared to 40Hz-filtered data (cf. Section 6.3.2). A more detailed evaluation that also compares to 67Hz-filtered data is provided for one test case as an example, in Section 6.4.3. Here details of the higher-frequency force evolution are considered.

6.4.2 MODELING RESULTS

Figure 6.6 shows the model-predicted Lift and Drag for four different test cases, in comparison with the corresponding wind tunnel measurements. Results are shown for the same example test cases discussed previously, which represent each of the four different flapping frequencies considered in the testing. For comparison, the plots also show one of the baseline models from the literature [Berman and Wang, 2007], which does not consider clap-and-fling effects. Note that the coefficients of the baseline model were estimated in the same way as those of the proposed model.

Overall, the models replicate the Lift force measurements with considerable accuracy. The shape of the force evolution is captured effectively, with both force peaks in the 40Hz-filtered data being reproduced and the phase alignment and peak amplitudes close to the measured ones. The visual evaluation is confirmed by the low RMSE values (~ 0.04N) and output correlation coefficients up to 0.97 (cf. Table 6.5).

While all metrics indicate a satisfactory performance, results are most accurate for flight conditions close to hover; the correlation coefficient deteriorates slightly for increasing forward velocity and decreasing flapping frequency. This may be partly because a number of assumptions made in the modeling process (cf. Section 6.2 and 6.3.1) refer to either the hover case or a typical flight condition (close to hover, $\delta_f \approx 12$Hz), thus the more the test conditions differ from these cases, the more error is introduced into the model. Additionally, with decreasing pitch attitude, the contribution of the Z force to the Lift increases, and as discussed, the proposed model does not accurately predict the Z forces captured in the balance measurements. Nonetheless, even for test #8, which is characterized by a high forward velocity, the model provides an adequate approximation. While the focus of this study lies on the instantaneous forces, Figure 6.6 shows that the cycle-averaged Lift is also predicted accurately. It is interesting to note that the model yields accurate results also for flight regimes where quasi-steady approaches are not considered applicable, i.e. Test #1–4, where $\frac{\omega}{\omega_n} \approx O(1)$, $k > 0.1$ and $\alpha > 25°$ (cf. Table 6.1). However, the current model does not include the flow dynamics, which are likely to have

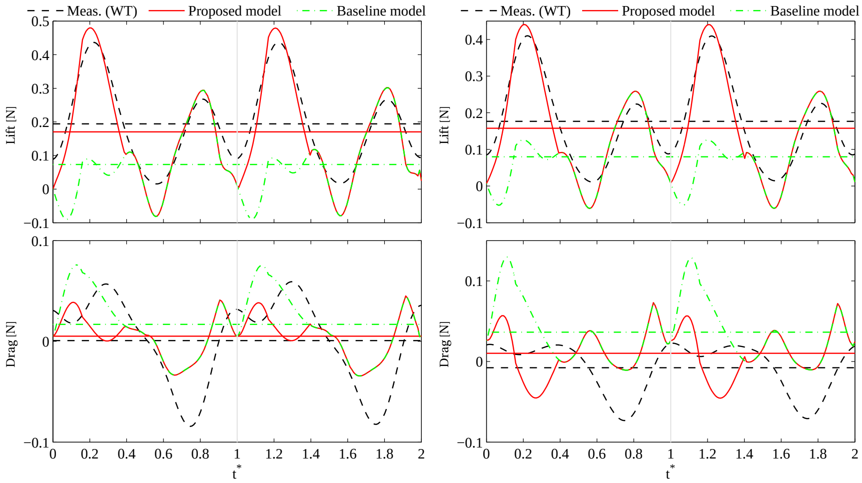

(a) Test condition # 1 (b) Test condition # 4

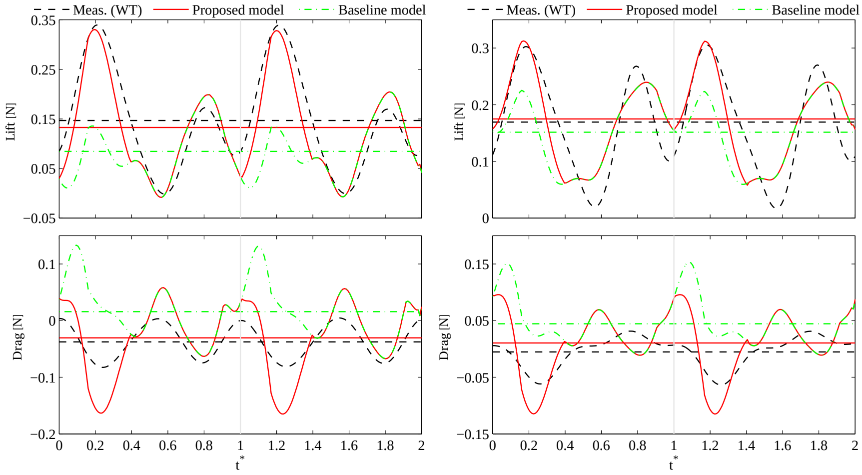

(c) Test condition # 7 (d) Test condition # 8

Figure 6.6: Wind tunnel measurements and models estimated from wind tunnel data for test conditions # 1, # 4, # 7, #8. Cycle averages are also indicated for each force time history (horizontal lines).

an influence in this regime, hence further evaluations are required to draw general conclusions in this regard.

The accuracy of the model is partly due to the added fling term, which substantially affects the force evolution during the first part of the flap cycle. Comparing the model to available quasi-steady models in the literature that do not include clap-and-fling effects, e.g., Berman and Wang [2007] (cf. Figure 6.6), clearly highlights the impact of the supplementary term in the proposed model. The comparison also shows how unsteady effects predominantly occur while the wings are interacting, during the first part of the flap cycle (outstroke). Without the fling term, the model can replicate the second part of the flap cycle, after the wings have separated (here, for $t^* > 0.4$), with accuracy. However, it underestimates the Lift during wing-wing interaction, which leads to instantaneous forces that differ significantly from experimental observation and, consequently, also to a reduced cycle-averaged Lift force prediction. Hence, there is a strong need to account for clap-and-fling for accurate modeling of ornithopters relying on such mechanism.

It can be observed in Figure 6.6, particularly for test conditions #1 and #4, that there is a singularity at around $t^* = 0.4$ of the flap cycle. Due to the definition of circulation as a piecewise function (cf. Eq. 6.7), at the switching point $\dot{\theta}_{fling} = 0$ only zero-order continuity is ensured. For control applications this discontinuity could cause problems and hence it is advisable to enforce continuity and ensure a smooth transition. However, for modeling purposes, the current formulation is considered adequate and more easily interpretable as it shows clearly where fling stops being effective.

In contrast to the Lift forces, the Drag forces are not predicted very accurately, and there is a considerable difference between different results, as highlighted by the output match in Figure 6.6 and the comparatively high RMS values (relative to the magnitude of the measurements). Output correlation coefficients range from 0.04 to 0.90, indicating that the model cannot be relied on to provide an accurate prediction. However, this result was expected, as it is predominantly the Z force component that contributes to Drag. Firstly, as shown in Chapter 4, the Z forces measured in the wind tunnel are significantly affected by the clamping and are thus not a realistic representation of the forces occurring in free-flight. Secondly, the Z force is considerably affected by the tail, so that the current model is in any case inadequate for a complete representation. Thirdly, the Z forces are highly influenced by the kinematics, i.e., the assumptions made on wing shape and torsion (cf. Section 6.3.1). Finally, and indeed *because of* these factors, the model parameters were optimized based on the resulting X force, further constraining the achievable accuracy of the Z and, consequently, Drag force prediction. Despite these limitations, Figure 6.6 shows that the model captures at least a part of the Drag forces, and, more importantly, that it predicts cycle-averaged values that are close to the measurements. For many (control) applications, instantaneous values for Lift are of more interest than ones for Drag [Baek, 2011; Rose and Fearing, 2014; Nguyen et al., 2015].

The parameter estimates, shown in Table 6.6, are in a plausible order of magnitude and the translatory and rotational circulation coefficients approximately agree with similar results in the literature [Andersen et al., 2005b; Sane and Dickinson, 2002]. Correlations between parameters were mostly found to be low (below 0.5), and estimated errors (Cramér-Rao lower bounds) were low (cf. Figure 6.8), suggesting an effective estimation process and reliable results. A correlation was observed between parameters and

Table 6.6: Parameters estimated from each set of estimation data.

Param.	Test #1	Test #2	Test #3	Test #4	Test #5	Test #6	Test #7	Test #8	Avg.	St. dev.
C_l	0.89	1.22	1.20	1.24	1.43	0.90	1.37	2.02	1.28	28%
C_r	1.49	1.45	1.45	1.44	1.39	1.39	1.41	1.57	1.45	4%
C_F	1.69	1.57	1.55	1.58	1.61	1.66	1.43	0.67	1.47	23%

flight regimes. In particular, C_l increases with lower flapping frequencies and higher forward velocities, which can be explained by the increased airflow over the wings leading to increased Lift production, whereas C_F increases with higher flapping frequencies and lower forward velocities, which can be explained by the prevalence of unsteady wing-wing interaction effects closer to hover. While the similar order of magnitude of the parameters over different flight regimes suggests that the initial model structure already partly adjusts the model to the specific test condition, the observed trends further suggest that the final accurate result is attained partly through the parameters. These trends also suggest that with a smaller number of parameters, common to all flight conditions, a global model of the flapping aerodynamics could be obtained that covers all flight regimes. This is discussed in Section 6.4.4.

6.4.3 FREQUENCY CONTENT EVALUATION

Figure 6.7 provides an example of how the model compares to the less filtered wind tunnel data (67Hz cut-off) including five harmonics of frequency content. This allows for a closer evaluation. Note that the Drag force contains significantly higher-frequency content, which is difficult to distinguish from noise. In view of this, and previous observations on the limitations of the Drag modeling, further evaluations are focused on the Lift component.

Firstly, it can be observed that the model cannot fully capture the fling effect. In particular, the additional fling-related force peak occurring in the 67Hz-filtered data at the beginning of the flap cycle (until $t^* \approx 0.17$, cf. Section 6.3.2) is not reproduced. From this perspective, the model follows the 40Hz-filtered data more closely. Here the fling peak is no longer visible, however its effect can be recognized in the phase shift of the first force peak, which, in this case, incorporates the first two peaks of the 67Hz-filtered data. The peaks of the model are approximately aligned with the 40Hz-filtered data, and the amplitudes comparable to those in the data. Hence, while there are limitations connected to the quasi-steady approach, the introduced fling term clearly accounts for a significant part of the overall fling effect.

Secondly, it can be seen that in certain details of the force evolution, the model is closer to the 67Hz-filtered data than to the 40Hz-filtered data. The troughs of the model, for instance, are closer to those of the 67Hz-filtered data, dipping to lower values than those of the 40Hz-filtered data. The model also seems to echo the hint at a peak occurring in the 67Hz-filtered data at $t^* \approx 0.4$ of the flap cycle, corresponding to the time when the wings have moved apart (black circumference in Figure 6.7a). It must be noted that this effect may be enhanced by the discontinuity discussed previously, although an additional peak was found to be present also in the baseline model without clap-and-peel term.

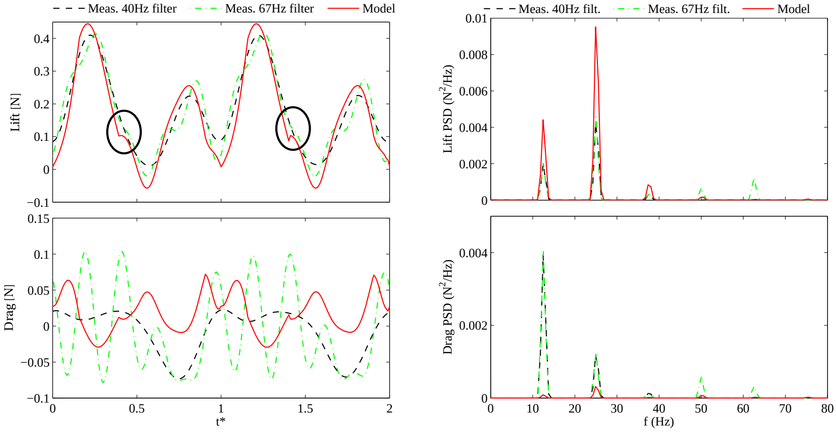

(a) Time domain.

(b) Frequency domain.

Figure 6.7: Model-predicted forces, and forces measured in the wind tunnel filtered at 40Hz and 67Hz, respectively, and corresponding power spectral densities, for test # 4. The circle in Figure(a) highlights one of the additional peaks visible in the data filtered with a higher, 67Hz cut-off.

The right hand side plot in Figure 6.7 shows the power spectral density (PSD) estimates of the model and the corresponding wind tunnel measurements. Here it can be seen that, while the Lift model contains predominantly frequency content up to the third harmonic, there is still some higher-frequency content, at least up to the fifth harmonic. However, at these high frequencies the data are highly affected by noise, and a comparison to data filtered at 3 harmonics already provides a nearly complete evaluation of the model, as also shown in Caetano et al. [2015c].

6.4.4 GLOBAL APPLICABILITY AND VALIDATION WITH FREE-FLIGHT DATA

The results discussed so far were obtained using different model parameters for each flight condition. This restricts the applicability of the model to the specific flight conditions used in the modeling process, for which data was available. Particularly from an application perspective, however, it is of interest to consider different conditions, ideally covering the flight envelope of a system. This is a crucial requirement for control and simulation applications, if the operating domain of a platform is not to be restricted, and also advantageous for design and performance studies, in order to make complete evaluations. In this context, an investigation was made into possibilities to apply the devised model globally, i.e., in different flight conditions, based on the currently available data.

For a model to be applicable in arbitrary conditions, any model parameters must be either constant for all conditions or a function of measurable input variables. To identify global applicability options for our model, we thus consider the parameters (C_l, C_r, C_F, cf. Eqs. 6.3, 6.4, 6.7) estimated from the different available datasets (cf. Section 6.4.2). As remarked previously, trends were observed between the estimated parameters and the flight regime of the data used to estimate them. These correlations are highlighted in Figure 6.8. As forward velocity and body pitch attitude are highly correlated ($R^2 = 0.94$), only the latter variable is shown.

It can be seen that C_l decreases with increasing flapping frequency and decreasing body pitch angle (hence, increases with increasing forward velocity), while C_F displays opposite trends. The trends are approximately linear, particularly in relation to the flapping frequency. There are some slight outliers, mostly corresponding to flight regimes that can be considered outliers (e.g., test condition #6, unusually high flapping frequency for the resulting velocity), but also suggesting that the parameters are correlated to *both* the flapping frequency and the pitch angle (or velocity). Indeed, in Table 4.1 it can be seen that with the same flapping frequency it is possible to fly at different pitch attitudes (e.g., 65° in test condition #6 versus 83° in test condition #1). C_r, by contrast, does not vary significantly across the conditions considered (4% standard deviation, cf. Table 6.6). Sensitivity studies confirm that changes in C_r within the range covered by the parameter estimates from the current tests have a negligible effect on the final result.

These trends suggest that the model can be adapted to cover a significant part of the flight envelope with only a small number of global parameters, rather than a different set of local parameters (C_l, C_r, C_F) for each flight regime. Based on the observations made, a 'global' model was computed by keeping C_r fixed at the average of the results from all test conditions (cf. Table 6.6), and approximating C_l and C_F as a function of the flapping frequency δ_f and the body pitch attitude θ_b. Least squares parameter estimation was applied to compute this function, and a first-order polynomial was found to yield adequate results, while entailing a low computational load and simple model structure:

$$C_{\{l,F\},global} = C_{\{l,F\},global}(\delta_f, \theta_b) = p_{\{l,F\},1} + p_{\{l,F\},2}\delta_f + p_{\{l,F\},3}\theta_b, \quad C_{r,global} = \frac{1}{n}\sum_i^n C_{r,local,i} \tag{6.23}$$

where i indicates the test condition number as defined previously and n is the total number of test cases, in this case $n=8$. The model that results from substituting the respectively relevant part of Eq. 6.23 into Eqs. 6.3, 6.4 and 6.7 is parameter-varying, with two of the original model parameters being a function of the states. Results can thus be computed in any arbitrary condition. However validation is required to evaluate the effectiveness of these results, and especially to verify whether it is acceptable to extrapolate to conditions outside the range considered in the original tests (e.g. $V > 2m/s$). Figure 6.8 shows the model parameters computed from the above equation ('global') compared to the original parameters estimated from separate sets of estimation data collected in different flight conditions ('local'). It can be seen that the two sets of values are close (<8% difference between corresponding parameters).

The obtained 'global' model was first evaluated in the test conditions considered in the wind tunnel. Figure 6.9 compares the output of the global model to wind tunnel data, as well as to the corresponding local model identified specifically in the considered test condition (cf. Section 6.4.2). The figure additionally presents free-flight data collected in conditions approximately corresponding to those recreated in the respective wind tunnel test. As the final goal is to represent a free-flying vehicle, it is of interest that the model should be able to represent the behavior occurring during flight. Before

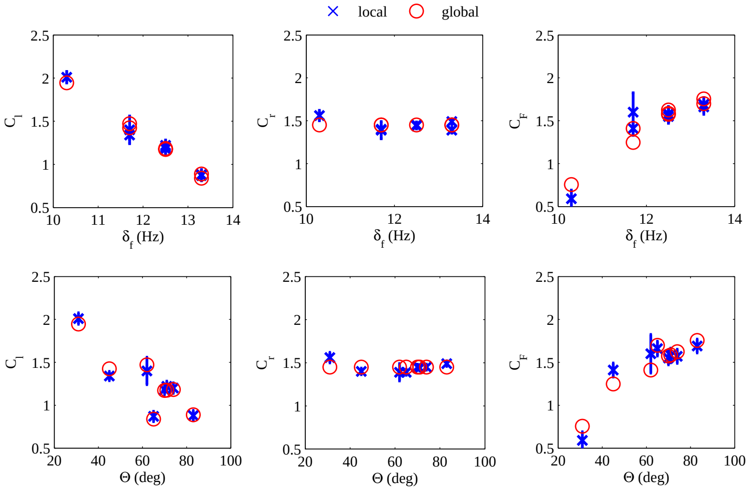

Figure 6.8: Model parameters (C_l, C_r, C_F) (i) estimated from each set of identification data (local, blue crosses), with corresponding estimated error bounds, and (ii) computed from the flapping frequency and body pitch attitude according to Eq. 6.23 (global, red circles).

being compared to free-flight data, the model was filtered after the third harmonic. On the one hand, the current free-flight measurements yield no reliable information beyond the third harmonic (Chapter 4), so it was considered more accurate and meaningful to validate a filtered version of the model with the filtered free-flight forces. On the other hand, the higher-frequency content (above 40Hz) is very limited (cf. Section 6.4.2 and Figure 6.7), so that from a practical point of view using the filtered or unfiltered model is approximately equivalent.

Figure 6.9 shows that the forces predicted by the global model are very close to those predicted by the separate local models for each flight condition. We also observe that the model can approximate the free-flight Lift, albeit not as accurately as the wind tunnel Lift. In this regard, it must be considered that, as discussed in Section 6.3.2, the free-flight and wind tunnel measurements differ somewhat. Hence, regardless of the theoretical quality of the model, its performance cannot be equally effective when it is applied in a free-flight situation, having been identified using wind tunnel data and not accounting for the tail. This limitation mainly affects the Drag component, for which the model cannot be considered to provide reliable information beyond the average force, but also has some effect on Lift: we see for instance that the free-flight Lift in Figure 6.9(a) has significantly smaller peaks than the wind-tunnel Lift. Lastly, Figure 6.9 shows the output of an ‘average’ model, where all parameters are set to an average from the previous test results rather than computed from Eq. 6.23. It is clear that, to cover a wider range of conditions, the suggested parameter-varying approach yields more accurate results. Nonetheless, if a quick and approximate result is desired, or if only a small range is considered, an average model may also be an acceptable solution, requiring even less effort to implement.

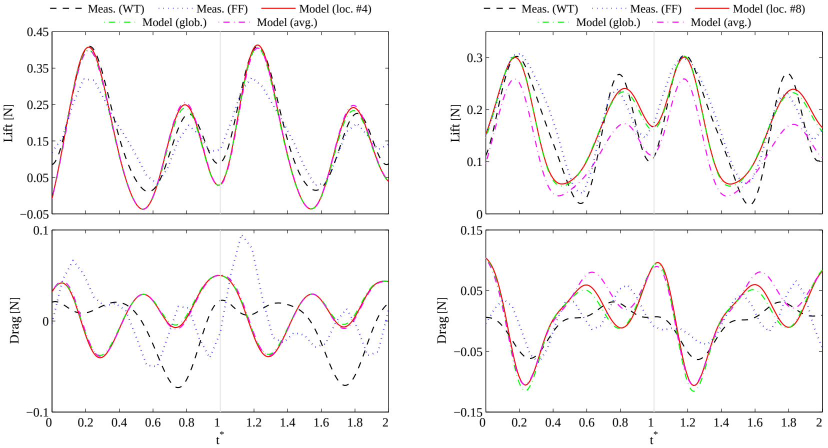

(a) Test condition # 4

(b) Test condition # 8

Figure 6.9: Global model evaluation in comparison to the two local models for test conditions #4 and #8. Wind tunnel (WT) and free-flight (FF) measurements versus model-predicted forces obtained from the 'local' models identified from each separate dataset, and from the 'global' model based on Eq. 6.23.

The final stage in evaluating the model consists in validation with free-flight data collected in flight regimes that were not replicated in the wind tunnel and hence not considered at any stage of the modeling process. Figure 6.10 shows two examples of this. The Lift is still predicted with some accuracy, in terms of both sub-flap evolution and cycle-averaged values. There are some discrepancies, e.g., the model displays larger peak amplitudes, but it is likely that these reflect differences between wind tunnel and free-flight measurements, rather than shortcomings of the model. It can be noted in particular, that the free-flight Lift has slightly larger peaks in the higher-velocity condition in Figure 6.9b than in the lower-velocity one in Figure 6.9a, while an opposite trend was observed in all wind tunnel tests. These observations suggest that the free-flight Lift would be predicted more accurately if the model coefficients were identified from free-flight data. However, in this case additional effects should be considered, particularly the tail, and higher-quality measurements would be required. Nonetheless, the current model gives a first approximation and accurate cycle average also for the free-flight case. At this stage, no suitable data was available to evaluate conditions outside the chosen test range ($V > 2m/s$): this will be investigated in future research.

6.5 CONCLUSION

Quasi-steady models for flapping-wing aerodynamics available in the literature were extended to provide accurate modeling of the lift forces on clap-and-fling ornithopters. The proposed model accounts for inertial, circulatory, viscous, added mass, and wing-wing interaction effects. Key additions to previous quasi-steady modeling approaches

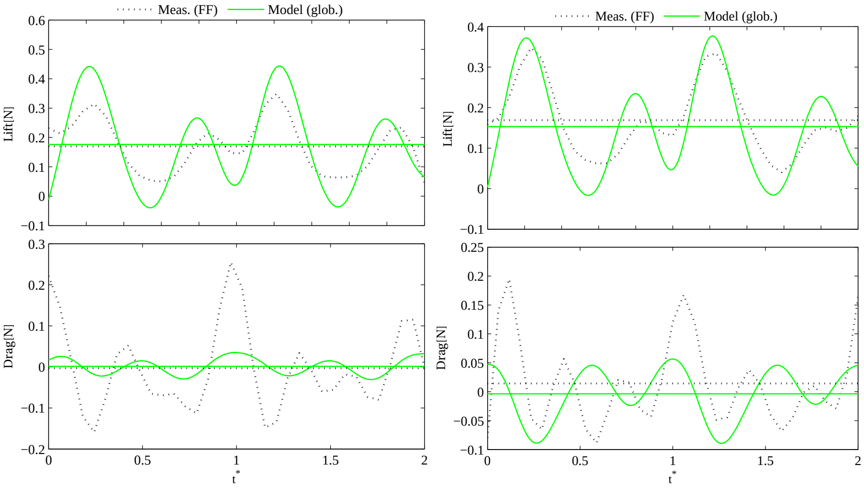

(a) Flight condition:
$\theta = 79°, V = 0.44 m/s, \delta_f = 13.3 Hz$

(b) Flight condition:
$\theta = 59°, V = 0.86 m/s, \delta_f = 12.5 Hz$

Figure 6.10: Global model validation examples. Free-flight measurements versus model-predicted forces computed according to Eq. 6.23, for two flight conditions not used in the modeling process. Cycle averages are also indicated for each force time history (horizontal lines).

are the inclusion of a fling circulation factor to account for unsteady wing-wing interaction, the consideration of specific wing kinematics and geometry, and the consideration of different forward flight velocities. The aerodynamic coefficients in the proposed model structure were computed using parameter estimation techniques and wind tunnel measurements collected on a flapping-wing micro aerial vehicle (FWMAV) test platform. Validation tests were performed with both wind tunnel and free-flight data.

The resulting model was found to predict the lift forces of the test platform accurately, with output correlation coefficients of up to 0.97, and shows that accounting for wing-wing interaction is essential for accurate instantaneous force modeling when such effects are present, and that the proposed approach is effective. The Drag forces are estimated less accurately, with correlation coefficients between 0.04 and 0.90. Better results would require accounting for the tail and using high-accuracy free-flight measurements, but consequently also a more complex model structure. This will be investigated in future research.

The model parameters were found to be either independent of the flight conditions or correlated to these, allowing for a global model to be developed, where the non-constant parameters are a first-order function of the flapping frequency and body pitch attitude. Thus, the same model can be used to represent different operating conditions of a vehicle and, if sufficient data is available, it could be possible to cover the full flight envelope in an analogous way. The global model computed for the test platform is very close to the local models for the flight regimes where the local models were computed. Additionally, validation tests with free-flight data show that the free-flight lift can be predicted with some accuracy also for flight conditions not used in the modeling process. This highlights the potential of the model for control applications.

The proposed model accurately represents a wide range of flight conditions, is computationally simple and requires few measurements (flapping frequency, pitch attitude and forward velocity). Its physically meaningful and yet simple model structure can be easily interpreted and is thus useful to obtain a better understanding of the platform and analyze its properties.

7

CONCLUSION AND RECOMMENDATIONS

7.1 CONCLUSION

Flapping wing micro aerial vehicles (FWMAV) are expected to become much more prevalent in the near future. In order to design the next generation of flight control systems, accurate models will be required in the very near future. Very little is known, however, about dynamics and aerodynamics of flapping wing aircraft, especially in terms of how to physically model the behavior of the flow and the flapping vehicle. This thesis set out to explore the dynamics of a flapping wing micro air vehicle. For the first time, it introduces an end-to-end approach for obtaining FWMAV dynamics models from flight data.

The main research question was:

Research Question

How to develop physically representative dynamic models of clap-and-peel flapping wing micro aerial vehicles using free-flight and wind tunnel experimental methodologies?

This research presents the first rigorous attempt at creating a physically representative dynamic model of a clap-and-peel free-flight capable highly maneuverable FWMAV, from flight data and wind tunnel data, using a system identification approach. Both the system identification process applied to flapping wing flight test data *and* the measurement setup and data pre-processing procedures had to be developed and applied to the DelFly II FWMAV.

As a result, the research in this thesis was split into two parts. The first part focused on creating the different measurement setups, and obtaining accurate aerodynamic forces and moments that act of the platform; the second part concentrated on the development of aerodynamic models using a systematic and physically meaningful approach.

In the first part, an experimental setup was created to test the FWMAV across a multitude of maneuvers, specifically devised to excite the dynamic modes of the platform. Secondly, data processing tools were developed for turning the marker position data into global acting force and moment data. The first step was to combine the marker position data into global linear and rotational accelerations, and accurately reconstruct the states and inputs of FWMAV. This allowed for the characterization of the DelFly's flight envelope. In particular, it was found that it is capable of performing flight at speeds that range from hover to 7 m/s. Its predominant flight regime ranges from hover to 2 m/s, with flap-averaged angle of attack between 83° and 30°. Furthermore, it was found that the typical flapping frequencies for such flight regimes are between 10.3Hz and 13.3Hz.

In order to obtain the global aerodynamic forces and moments acting on the DelFly from the global vehicle accelerations, a kinematics model is required that describes the relative motion of the structural elements of the aircraft. In the literature, very complicated kinematic models are sometimes used, and in this research the applicability of these structures was investigated. For the specific case of the DelFly II, which has a single wing-to-body mass ratio of 1.8%, single rigid body formulations were found to represent the kinematics with great accuracy. Such formulations are simpler to derive and are particularly interesting for passively stable tailed FWMAV designs or flyers with only one active degree-of-freedom per wing, allowing for simpler implementation and identification of acting forces without detrimental loss of information. Furthermore, it was observed that single rigid body formulations are indeed applicable to FWMAVs with four-wings configured in 'X' form and to FWMAVs with two wings with single wing-to-body mass ratios below 8% and 2.8%, respectively. In the same way, the results point to the rise of considerable errors when applying rigid body kinematics to FWMAVs that have larger wing-to-body mass ratios for each of the wing configurations, where multi-body formulations are advised.

Because this was the first time that in-flight data was used to obtained the aerodynamic forces and moments acting on the DelFly, a validation experiment was conducted in a wind-tunnel and vacuum chamber setup. A surprising and far reaching conclusion from the wind-tunnel experiments was that, while this measurement setup is extremely accurate, and perhaps more importantly, repeatable, the experimental setup itself had a very significant influence on the obtained results. It was found that a correct determination of the clamping position was essential when using wind-tunnel direct force measurements to obtain the forces that act on the FWMAV. In particular, despite similarity in the unsteady forces determined along the $\boldsymbol{x}_b$ axis of the ornithopter (X forces), the forces determined along the $\boldsymbol{z}_b$ axis, i.e., the forces along the stroke plane of the wings (Z forces), exhibited dissimilar evolutions for higher flapping frequencies (13.3Hz and 12.5Hz). These differences were concluded to originate from the structural vibrations affecting the wind tunnel measurements, that were caused by the interaction of the flapping forces with the natural modes of the tail of the ornithopter. These effects decrease considerably with the decrement in the flapping frequency, resulting in very similar evolutions of the Z forces between both experimental methods. Furthermore, the differences in the Z forces were also due to the absence of dynamic oscillation of the DelFly in the fixed-base wind tunnel experiments, which were damped in free-flight.

With the validated aerodynamic force and moment data, the second phase of the research could commence. In this second phase, first a flap-averaged dynamics model of the DelFly was identified, and second a physical model of the unsteady sub-flap-cycle forces and moments was created. For the flap-averaged dynamics model a linear system identification approach with a standard decoupled linear time-invariant (LTI) aircraft model structure was used with the aerodynamic dataset. During this phase it was assumed that any flapping effects were averaged out over time. The aerodynamic forces were shown to be modeled with great accuracy in both models, with better results for the *full* model, which revealed correlations between 0.88 and 0.99. Despite the good results obtained for the forces, the models revealed a less accurate approximation to the aerodynamic moments, which points to the need for more complex model structures. Nevertheless, the results of the dynamic simulation point to the use of such models for the design of onboard control systems, given the ability to simulate the flight path of the FWMAV.

For the unsteady nonlinear sub-flap model, a so-called quasi-steady approach was taken. This study further developed existing theory by including a circulatory term for the 'fling' occurring in clap-and-fling force augmentation mechanisms. As a result, the model was found to predict the unsteady lift force acting on the FWMAV for each of the flight conditions with great accuracy. The model was validated using free-flight data at flight regimes different from the conditions used to identify the parameters, with good agreement on the predicted sub-flap forces, hence, resulting in a considerable improvement over existing baseline models. Furthermore, the accuracy of the results of this model suggests that quasi-steady aerodynamic theory can be applied to model flapping flight at conditions were the angle of attack is higher than 25° or the reduced frequency of the flyer is above 0.1.

Combining these results, the main research question can be answered. It was found that position data from a motion capturing facility could indeed be used to obtain global aerodynamic forces and moments working on an FWMAV, provided that the update rate is at least five times higher than the highest frequency content of the aerodynamic forces, and its precision is at least of 0.2mm. The symmetry in the motion of the wings of a clap-and-peel four-wing FWMAV allows for rigid body kinematics to be used to calculate the aerodynamic forces and moments from the position data. Using an LTI system identification approach and standard decoupled model structures, linear flap averaged models of moderate accuracy could be obtained, resulting in a good approximation of forces, suggesting the use for onboard control strategies. Depending on the desired level of fidelity, as well as complexity of the model, it is possible to separate the flap-averaged time-scale aerodynamic forces from the unsteady aerodynamics and develop simpler sub-flap force models using quasi-steady aerodynamic theory. For this case, quasi-steady models that include the fling circulatory term are required for the modeling of the unsteady sub-flap forces, which proved to be accurate for the prediction of the unsteady lift force generated by the flap of the wings, across the flight envelope of the FWMAV.

7.2 RECOMMENDATIONS AND FUTURE WORK

While the results detailed in the previous section were obtained using a single specific FWMAV, the methodology presented in this thesis is applicable to other flapping wing vehicles, although certain choices regarding experimental setup, kinematic model structure selection, and system identification approach may vary depending on the specific platform. In particular, single body kinematic formulations are recommended for FWMAV with: (a) monoplane configuration, light wings (below 2.8% of total body mass) and low flapping frequency (below 20Hz); *or* (b) biplane configuration, (e.g., 'X'-wing) and wing to body mass ratio below 8%. On the contrary, more complex multi-body kinematic formulations are recommended in cases of FWMAVs with higher wing mass or higher flapping frequency, or in the case of FWMAVs equipped with wings that have two or more actively controlled degrees-of-freedom.

The characterization of the forces acting on an FWMAV from free-flight position data measured using an external tracking system should take into account the nature of errors in the data, by assessing the correlation of the residuals obtained using different filtering frequencies. Moreover, it is recommended to assess the accuracy of the position data since it can negate the extraction of the forces and moments for small flyers, where the uncertainty levels can be as large as the forces. As an example, a standard deviation of the position error of the markers above 0.5mm will result in the confidence interval to be as large as the magnitude of the unsteady forces, therefore hindering any reliable force extraction. Furthermore, for ornithopters with less than 30cm of wing span and a total mass below 20 grams, the precision of the position measurements should be higher than ±0.2mm to allow for suitable force reconstructions. In terms of sampling frequency, to conserve the time-resolved unsteady aerodynamic information, it is recommended to still sample the flight at a frequency of at least five times the wing flapping frequency.

It was found that relying solely on the data collected by the external tracking system during free-flight could lead to a misinterpretation of the reconstructed states and lack of information resulting from the Nyquist-Shannon limit, the noise magnification and the low-pass filtering effects of numerical differentiation. Especially for the accelerations, which are obtained from double differentiation of position data, the errors may be considerable. As a result, it is recommended to perform the free-flight tests with onboard logging of the accelerations and angular velocities by means of an inertial measurement unit that is synchronized with the external tracking system information. It is understood, however, that equipping a FWMAV with a data logger requires a considerable maturation of technology. Nevertheless, proceeding towards the development of such onboard capabilities will improve the accuracy of the data, as well as pave the way for the development of automatic controllers for such systems.

In fixed base force measurement techniques, the clamping point should be as close as possible to the aerodynamic and inertial force application point, to reduce the 'arm' between the balance mechanism and the oscillating force. In addition, a pre-assessment of the eigenmodes and eigenfrequencies of the structure of the flyer and consequent comparison with the harmonics of the flapping frequency is recommended before performing the tests.

In terms of system the identification approach, the relation of the flapping frequency and eigenfrequency of the FWMAV has a detrimental effect on the type of aerodynamic theory that can be used. Specifically, if the flapping frequency is of the same order as any of the eigenfrequencies of the flyer, or if the reduced frequency is higher than 0.1 *and* the angle of attack of the wing higher than 25°, numerical methods are recommended, although quasi-steady aerodynamic theory has shown to be able to model the unsteady mechanisms quite accurately if modeled from real data. In contrast, quasi-steady aerodynamic theory is recommended for flapping frequencies that are considerably higher than the principal eigenfrequencies of the flyer, *or* flapping reduced frequencies below 0.1.

To increase the fidelity of the current models of the DelFly II, it is recommended to model the tail and wing/tail interactions to obtain better models of the moments that act on the FWMAV. Additionally, further expanding the aerodynamic model devised in this research to include the ‘clap’ of the wings would allow for a more profound understanding of physical mechanisms of clap-and-peel force generation. Furthermore, future studies can benefit from considering the use of more advanced modeling tools, such as multivariate splines [de Visser et al., 2009], for the identification of more complex models, concentrating on creating global aerodynamic models which are valid on the full flight envelope.

To ease the identification methodology of tailed FWMAVs, it is recommended to separate the time-averaged identification from the unsteady sub-flap oscillatory modeling. This can be done due to the observed decoupling between the time-averaged dynamics, which are determined by the location of the center of gravity and the tail geometry, and the sub-flap dynamics. For tailless designs, this decoupling strategy is not recommended, as the wings are responsible for the control forces and moments, and therefore for the dynamics of the platform at all time-scales.

Future work on system identification using free-flight testing should consider less intense maneuvers, with a deflection of ±10°. This will allow for smoother flight paths and less abrupt dynamic behaviors, while still conserving the dynamic excitation of the DelFly needed for system identification. Moreover, frequency sweep maneuvers should also be tested to assess the impact of such methods on the dynamic response of flapping wing micro aerial vehicles. Furthermore, is recommended that future studies address the analysis of the dynamic stability of the developed models and compare them the results with the real FWMAV. Finally, it is recommended to develop a flight control system based on the models developed in this research and test the model in both a simulated environment, as well as implement the controllers onboard and assess the behavior of the combined system in free-flight.

Appendices

A

MORE RECONSTRUCTED FREE-FLIGHT TESTS

The present appendix presents more results of the different flight path reconstruction techniques applied in Chapter 2. In particular, it presents the results for test #24, which includes two doublet inputs on the elevator, with first deflection down; and the results for test #41 in which two triplet (2-1-1) inputs were performed on the rudder, with the first deflection to the left. It further develops the results, discussing them in the discussion section.

A.1 RESULTS

Both Figures A.1 and A.2 present the respective Figures in the same order: subfigures a) present the 3D trajectory in blue, with a 2D plot in black; Figures b) show the deflection angles of the elevator (top), rudder (middle) and the flapping frequency (bottom); subfigures c) through g) present the reconstructed states, being the Euler angles and attitude angles (*c*), the velocities and aerodynamic angles (*d*), the linear accelerations (*e*), the angular velocities (*f*) and angular accelerations (*g*); subfigures *h)* show the reconstructed aerodynamic forces in the body frame axis (top) and inertial vertical and horizontal axis, with this last one aligned with the direction of flight (bottom); subfigures *i)* present the reconstructed moments. Both the aerodynamic forces and moments were computed using the Eq. 3.1.

The effect of the flapping frequency on the state estimation was assessed by comparing the results obtained using the raw data with the results obtained using different filtering, using a zero-phase lag 3$^{\text{rd}}$ order Butterworth low-pass filter, with different cut-of frequencies. A Power Spectral Density with a window over the time-lapse of 0.5 seconds on each side was also performed to evaluate the frequency peaks. It was found that the

---

This appendix is based the follwing publication: Caetano, J. V., de Visser, C. C., Remes, B. D. W., de Wagter, C., and Mulder, M. (2013c). Modeling a Flapping Wing MAV: Flight Path Reconstruction of the DelFly II. In *AIAA Modeling and Simulation Technologies*, number 2013-4597 highest peaks are around 1Hz and at the flapping frequency. This way a 20Hz cut-off frequency was selected as it is just below the second harmonic of a 10Hz cut-off frequency, which is below the flapping frequency, was also used to compute the states, forces and moments. The difference between the results is presented in subfigures *b), e), f), g)*, and *i)*, which present the states and aerodynamic moments (*i)*) that were computed using a 20Hz (blue) and 10Hz (red) cut-off frequency. The aerodynamic forces did not show a considerable variation between the frequencies.

The first test that is presented here (Figure A.1) consisted of two consecutive doublet inputs on the elevator (with the first input deflecting the elevator down) separated by almost 6 seconds (Figure A.1b) for a slow forward flight regime, with an average velocity of 0.5m/s, corresponding to test #24.

The second test, presented in Figure A.2, comprised a triplet input on the rudder, with the first deflection to the left, in forward flight regime, with an average velocity of 0.8m/s. Both inputs were separated of about 3.5 seconds.

A.2 DISCUSSION

As shown in Figures A.1b and A.2b the flapping frequency does not have a value before second 0.5. This is due to the fact that this input was estimated using a Fourier transform with a window of 1 second around the estimation time, with 0.5 seconds in the past and 0.5 seconds in the future. The square wave are due to the limited resolution, given the discrete sampling frequency.

Figures A.1c and A.2c present the Euler (red) and attitude (blue) angles. The sudden changes of 360° in the ϕ angle (red, top) are due to the fact that, when rotating from the inertial to the body frame (Eq. 2.1), that angle is rotated of $\pm 180°$ as the z axis of the inertial and body frame point in opposite directions. The ϕ_{r_b} represents the corrected roll angle, as if it was measured by an onboard sensor. Also, the corrected yaw angle is presented on the bottom plot of Figure A.1c in blue. The red line, corresponding to the Euler angle ψ jumps due to the inverted flight, when the DelFly $\boldsymbol{x_b}$ axis points in the opposite direction, between $t \in [2.3, 2.7]$ and $t \in [8, 8.5]$.

With respect to force generation, the flapping wings mainly produce thrust, that points in the $\boldsymbol{x_b}$ direction. Its lift and vertical force (in the inertial frame) are generated by the forward motion. This way, the FWMAV has to flap faster around hover regimes to stay aloft, as the lift component is very small, due to the small velocities. The tests presented here fall in this regime and in this case the inputs force the DelFly to lose vertical force, exchanging height for speed in the first instants.

A.2.1 ELEVATOR DOUBLET INPUT

For the flight test #24, with elevator downwards deflection (Figure A.1), the DelFly also accelerates because the thrust vector rotates with the DelFly (pitch angle decreases), having a higher horizontal component. The ornithopter pitches down with the elevator down input and regains altitude with the elevator up deflection, losing velocity and returning to the initial trimmed condition (Figure A.1d). It takes less than 4 seconds to dampen the longitudinal oscillations.

The accelerations present a coherent evolution, when compared to the velocities and position, indicating an acceleration in $\dot{u}$ and $\dot{w}$ (Figure A.1e) at the beginning of the ma-

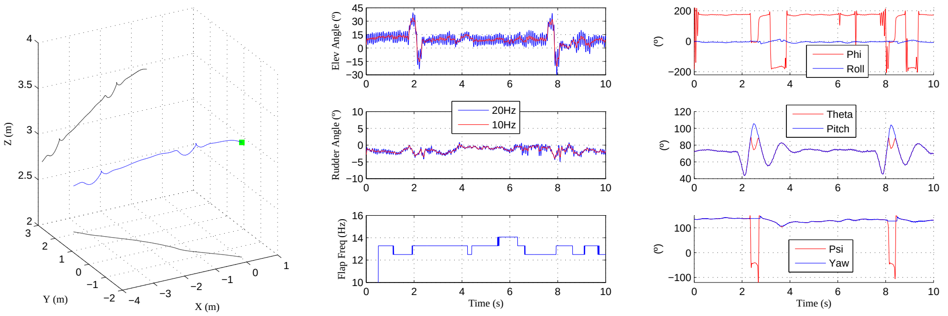

(a) 3D position of the CG (blue); 2D position of the CG, written in (x,y) (black).

(b) Autopilot commanded input deflections: elevator (top); rudder (middle); flapping frequency (bottom), computed with an FFT with a window of 1 second.

(c) Euler (red) and attitude angles (blue).

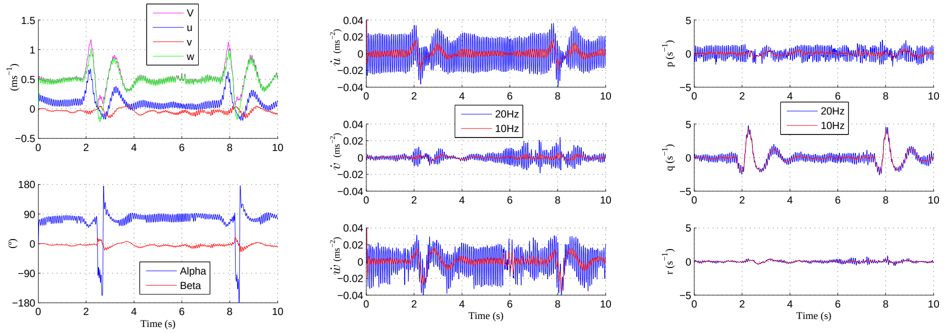

(d) Velocities in the body frame (top) and aerodynamic angles (bottom).

(e) Accelerations in the body frame.

(f) Body angular velocities.

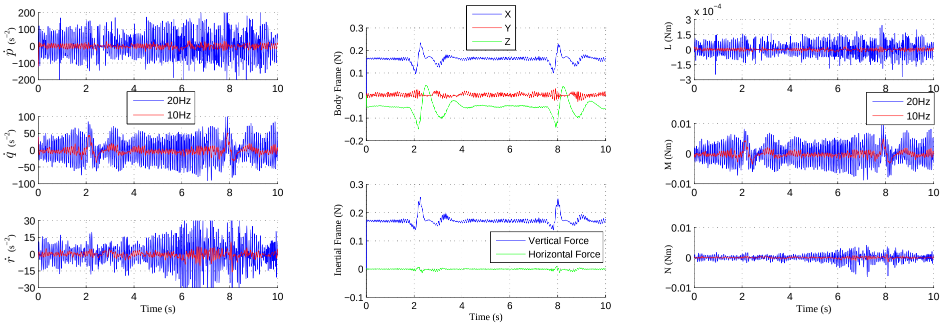

(g) Body angular accelerations.

(h) Aerodynamic forces in the body frame (top) *and* in the inertial frame, with vertical positive up and horizontal positive in the direction of flight/negative if flying inverted (bottom)

(i) Aerodynamic moments computed using the equations of motion presented in Eq. 3.1

Figure A.1: Doublet elevator input test with first input down, in a nose-down maneuver in slow forward flight, test #24.

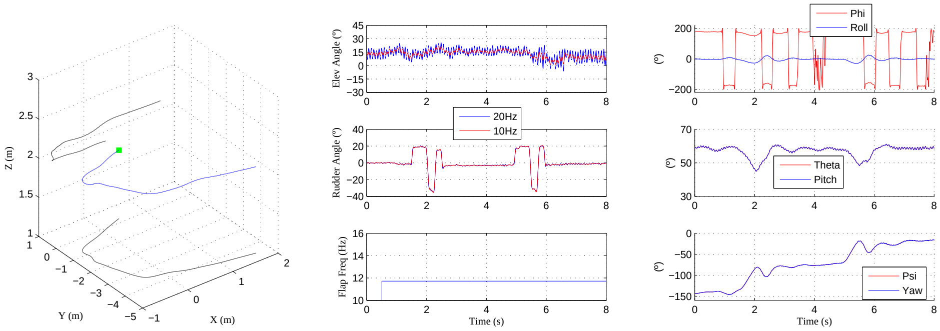

(a) 3D position of the CG (blue); 2D position of the CG, written in (x,y) (black).

(b) Autopilot commanded input deflections: elevator (top); rudder (middle); flapping frequency (bottom), computed with an FFT with a window of 1 second.

(c) Euler (red) and attitude angles (blue).

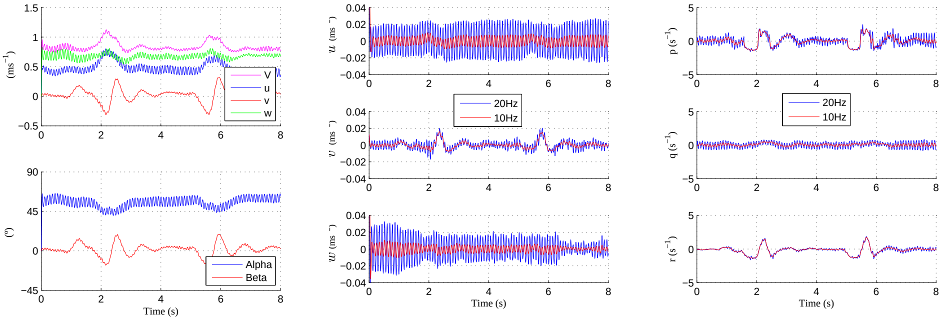

(d) Velocities in the body frame (top) and aerodynamic angles (bottom);

(e) Accelerations in the body frame.

(f) Body angular velocities.

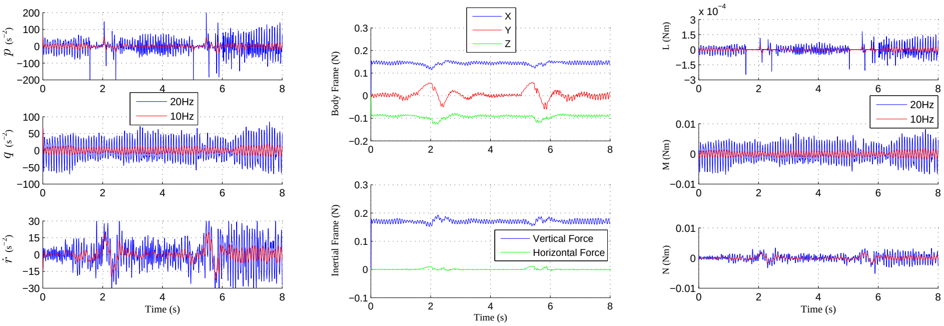

(g) Body angular accelerations.

(h) Aerodynamic forces in the body frame (top) *and* in the inertial frame, with vertical positive up and horizontal positive in the direction of flight/negative if flying inverted (bottom)

(i) Aerodynamic moments computed using the equations of motion presented in Eq. 3.1

Figure A.2: Rudder triplet input test with first deflection to the left in slow forward flight, test #41.

neuver, with a consecutive deceleration due to the pitch angle increase during the elevator upwards deflection.

By zooming around one single input, a longitudinal oscillatory mode was captured, with a period of about 1 second. This mode can be identified in the pitch, pitch rate (q), velocity and aerodynamic angle plots (Figures A.1c, A.1d and A.1f), pointing to a phugoid-like movement. On the other hand it was not possible to identify a faster oscillatory mode (like short-period) that is independent of the flapping frequency. All the faster modes have a period equal to one flap cycle.

The aerodynamic forces are not considerably affected by the filtering, having a similar value when calculated with the raw data. These are mainly affected by the gravity terms for trimmed flight. Around the maneuvers, the terms with q or w highly contribute to the value of the estimations. The remaining 3rd and 4th terms (in Eq. 3.1) do not play a significant role and can even be neglected. The terms in Eq. 3.1 were presented in order of greatness, with the biggest being the first and the smallest the last, when compared to the left side of each equation.

When analyzing the evolution of the forces, these are coherent with the evolution of the states. More specifically, the X and Z forces decrease when the pitch angle decreases, but in the case of the Z force, it increases in absolute value, since a negative force points upwards. Hence, around the maneuver, the X force reaches a minimum at the minimum pitch angle and a maximum at 90° pitch; following an opposite trend, the Z force reaches an absolute maximum at the minimum pitch angle and goes to positive values when the FWMAV is in inverted flight. The Y force seems to not change considerably around the maneuver. However, the results presented in red in Figure A.1h show a loss of data around the maneuver possibly due to the incapability of accurately estimating the roll angle and roll rate for pitch angles between [82,98]°, inherent to the Euler angle estimation method. The vertical force (with respect to the inertial reference frame) has an average value equivalent to the DelFly weight when in trimmed flight, varying around the maneuvers – it decreases to a value below the weight when the DelFly loses height and assumes a higher value when the ornithopter re-gains altitude, indicating a coherent behavior. The horizontal force presents an average value with a magnitude of $3{,}3E^{-4}$N when in trimmed flight, indicating that it produces an horizontal force equivalent to 4 milligrams, which is close to zero, indicating the equilibrium. This force varies around the maneuver in the same way as the X force, decreasing at the first input and increasing with the second input.

Contrary to the forces, the aerodynamic moments are mainly affected by the accelerations, in this case the angular acceleration terms, presented as the first terms of Eq. 3.1. It was found that the remaining moment terms can be neglected, with minor effects on the final results. The L and N moments are not affected by the maneuvers, indicating a decoupling between the longitudinal and lateral/directional oscillations.

A.2.2 RUDDER TRIPLET INPUT

The rudder triplet input test #41 is presented on Figure A.2 indicates a coupling between the lateral and directional axes, in the way that a rudder input induces a rolling and yawing movement. This effect can be seen by comparing the top and bottom plots of Figures A.2c, A.2f and A.2g. However, after rudder deflection input ceases, the oscillations around $\boldsymbol{x_b}$ are fully damped in less than 2 seconds, in as little as 2 periods of 0.9 seconds and the oscillations around $\boldsymbol{z_b}$ are damped in 1.5 periods, as presented in the top and bottom plots of Figures A.2f.

It was also noticed that the coupling between the roll and yaw induces a decrease in the pitch angle for all rudder inputs. This was also verified experimentally as the FWMAV enters an unsteady spiral if the rudder input has a high magnitude or lasts too long. Hence, the small oscillations on X and Z around the input times are due to the decrease in the pitch angle.

In a similar way as the longitudinal input, the aerodynamic forces are mainly affected by the first term of their respective equations, in Eq. 3.1. The second terms only contribute to the forces around the maneuvers, falling close to zero otherwise and the remaining terms can be neglected.

The aerodynamic moment around $\boldsymbol{x_b}$ (L) shows a similar behavior around the maneuvers as the one found in the previous inputs. However, a full spectrum analysis indicates that the rudder deflections acts as a damper in the lateral oscillations influencing estimation of the angular velocity around $\boldsymbol{x_b}$ *(p)* – this effect can still be seen on the top plot of Figure A.2f. The moment around $\boldsymbol{z_b}$ (N) seems to not be well estimated, as the first and longest input on the rudder does not reflect considerable changes on the magnitude of the moment, when compared to the effects of consecutive inputs. However, this could also be due to the fact that the estimation method is mainly influenced by the angular accelerations, which are considerably higher on the second and third inputs, due to the greater change in the states. This was also noted for the other tests, as the second and third rudder inputs generated a bigger N moment than the first input. The M moment, around $\boldsymbol{y_b}$, seems to not have been affected by the rudder inputs, keeping the similar values around the maneuvers.

B

MORE RESULTS OF FORCES AND MOMENTS OBTAINED FROM RIGID AND FLAPPING KINEMATICS

This appendix presents more results of the forces and moments calculated using the kinematic formulations of Chapter 3. It compares the aerodynamic forces and moments obtained from (a) Newton-Euler formulation of a single rigid body kinematic model; and (b) d'Alembert's equations for five coupled rigid bodies for two different flight tests. Test #32 corresponds to a doublet input on the rudder, as described in Chapter 2; Test #25 corresponds to a doublet input on the elevator.

The forces and moments were found to have very similar relative evolutions throughout the several flights. Hence, for objectiveness and ease of comprehension, the results are presented for trimmed flight and two system identification maneuvers: doublet input on the rudder and doublet input on the elevator, with the input duration of $\frac{2}{3}$ seconds ($\frac{1}{3}$ second to each side).

B.1 RESULTS

The aerodynamic forces and moments of 4 seconds of flight are presented in Figure B.1. These were computed using the Newton-Euler single rigid body formulation detailed in Chapter 3, using the flight data of test #32. The states of this flight test are presented in Chapter 2, from Figure 2.10 to Figure 2.12. The aerodynamic forces and moments presented in Figure B.1 present an evolution that is in agreement with the accelerations of Figure 2.12. The force component that varies the most is the Y force; the N

This appendix is based on the follwing publication: Caetano, J. V., Weehuizen, M. B., de Visser, C. C., de Croon, G. C. H. E., de Wagter, C., Remes, B. D. W., and Mulder, M. (2014b). Rigid vs. Flapping: The Effects of Kinematics Formulations in Force Determination of a Free Flying Flapping Wing Micro Air Vehicle. In *International Conference on Unmanned Systems*, pages 949 – 959. IEEE.

moment is the most affected by the input.

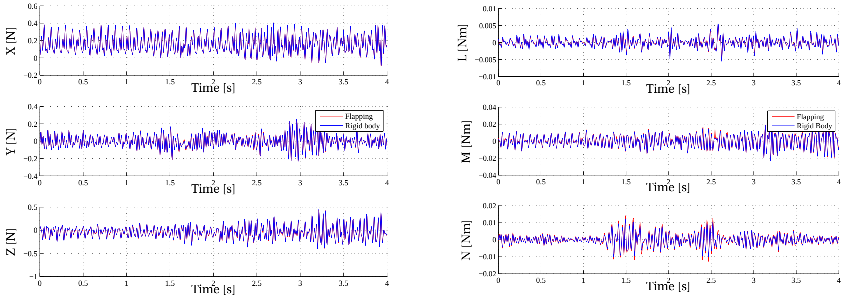

(a) Aerodynamic forces.

(b) Aerodynamic moments.

Figure B.1: Aerodynamic forces and moments calculated using rigid body Newton-Euler equations of motion (blue) and d'Alembert's equations for 5 coupled rigid bodies (red) for test #32, corresponding to a doublet on the rudder with first deflection to the right.

Figure B.2, presented below, shows the evolution of the forces and moments of 4 seconds of flight of flight test #25, which corresponds to a doublet input on the elevator, with first deflection up. The three-dimensional position and the orientation of the DelFly during this maneuver was presented in Figure 2.7a; the respective input commands are presented in Figure 2.7b. As observed, the X and Z forces oscillate more around the trimmed condition.

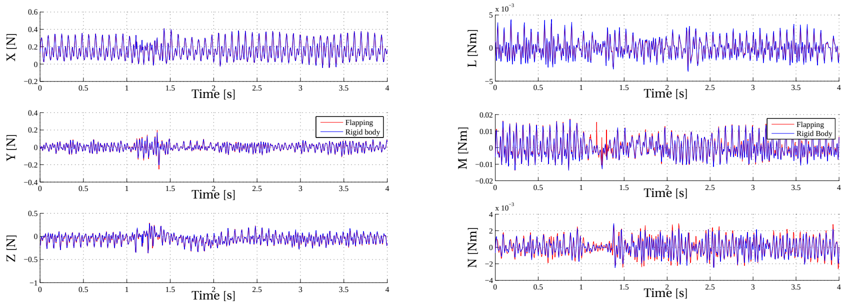

(a) Aerodynamic forces.

(b) Aerodynamic moments.

Figure B.2: Aerodynamic forces and moments calculated using rigid body Newton-Euler equations of motion (blue) and d'Alembert's equations for 5 coupled rigid bodies (red) for test #25, corresponding to a doublet input on the elevator with first deflection up.

B.2 DISCUSSION

There is a dominant oscillatory motion in all states, as well as in the elevator and rudder positions that are induced by the flapping motion described in Figure 2.7a (bottom plot).

The square nature of the flapping frequency (δ_f) observed in Figure 2.7b (top) is due to the limited resolution on the wing angle over a flap cycle. The values correspond to $\frac{200}{15}$Hz and $\frac{200}{16}$Hz, with the denominator being the number of samples per flap cycle.

The rudder deflection input (Figure 2.7b) affects all attitude angles, i.e., the first deflection to the right, induced a roll ϕ_r angle of 50°, a yaw rotation ψ_y of 70° and a pitch (θ_p) variation of 10° downwards; the second deflection, to the left, induced an opposite rotation in all axis, compensating for the first attitude variation. It, however, also aggravated the pitch variation due to the high vertical placement of the rudder with respect to the DelFly's CG, that in this case was of 30mm.

The wing stroke plane angle, that is almost parallel to $\boldsymbol{z_b}$, and the consequent inertia changes around $\boldsymbol{x_b}$ affect mostly the longitudinal states. In particular, the wing flap affects the pitch angle θ_p (Figure 2.10b) that, in turn, will affect the velocity and acceleration along $\boldsymbol{x_b}$ and $\boldsymbol{z_b}$ (Figures 2.11a and 2.12a, respectively), as well as pitch rate p and the pitch acceleration $\dot{p}$ (Figures 2.11b and 2.12b).

The linear and angular velocities, in Figures 2.11a and 2.11b respectively, were also affected by the input. In particular, the lateral velocity v and angular velocities p and r had the biggest oscillations. After the rudder input, the platform returned to its initial flight regime, by dampening the long period oscillations.

The linear and angular accelerations used in the kinematic models are presented in Figures 2.12a and 2.12b, respectively. Comparing these with the respective velocities, one can see that the fast sub-flap oscillations are dominant over the maneuver induced oscillations.

Despite these flap induced oscillations, the evolution of the aerodynamic forces presented in Figures B.1a and B.2a shows that both kinematic derivations lead to very similar aerodynamic forces and moments, even in highly nonlinear maneuvers caused by the doublet on the rudder.

Among the forces, the Z force of the elevator maneuver (Figure 16) had the biggest differences between both methods, while X reveals an almost perfect match. The differences in Z are caused by the deceleration of the wings at the end of the out-stroke, where the flap angle is maximum, which has a bigger influence due to the fact that the stroke plane of the wings is almost parallel to the $\boldsymbol{z_b}$ axis. This results in added pitch inducing forces along $\boldsymbol{z_b}$ which, in turn, induce variations in the pitch moment between both methods, as indicated in Figures B.1b and B.2b.

The higher amplitude of the flapping wing kinematics N moment (Figures B.1b and B.2b) is caused by the added inertia effect of the wings, i.e., the contribution of the four moments of inertia of the wings (Table 3.3) around $\boldsymbol{z_b}$, as a bigger N moment is needed to accelerate more inertia with the same angular acceleration.

Pearson's Correlation Coefficient (PCC) was used to quantify the similarities between both kinematic methods. This method establishes a liner correlation between two signals evaluating the way they vary with respect to their mean and is defined as the covariance (cov) of 2 signals divided by the product of the standard deviation (σ) of each signal (Eq. B.1). Two totally correlated, uncorrelated and negative-correlated signals have a PCC of 1, 0 and -1 respectively.

$$pcc_{F_{rb},F_{flap}} = \frac{\text{cov}(F_{rb}, F_{flap})}{\sigma(F_{rb})\sigma(F_{flap})} \tag{B.1}$$

Table B.1: Pearson's correlation coefficient results for both maneuvers. The forces and moments evidenced a very close form and phase, with correlations always above 0.95.

Forces and Moments	**X**	**Y**	**Z**	**L**	**M**	**N**
Doublet Rudder	0.99	0.99	0.98	0.98	0.99	0.98
Doublet Elevator	0.99	0.99	0.97	0.99	0.97	0.95

The correlation coefficients were found to the be very high, close to 1, for all forces and moments, as indicated in Table B.1, indicating a big linear correlation between the calculated forces and moments.

This study has revealed that simple equations of motion are still applicable to force and moment reconstruction of free flying FWMAVs, for cases where the rocking oscillations are small, in the particular case of ornithopters with 4 wings and also 2 winged ones, whose wings are light and small when compared to the rest of the body. Moreover, these equations should still be able to predict the forces and moments of bird and bat inspired ornithopters, in which the pitch oscillations are dampened by the presence of a tail.

Despite being more complex, detailed multi-body kinematics like the ones described here allow the direct assessment of control forces and moments over the individual wings and motors, which has clear benefits over rigid body formulations. In the present case, a 7^{th} generalized force Q_7 (see Chapter 3) could be calculated, which describes the flapping motor torque. These formulations gain over rigid body equations for FWMAVs that depend on active control of more than 1 DOF of the wings, in the case of insect inspired tailless designs.

Moreover, the use of Quaternions on the flapping formulation has beneficial effects in computational efficiency, as well as in avoiding singularity issues of the Euler angles.

C

COMPLEMENTARY ERROR ANALYSES AND RESULTS

This Appendix contains supplementary material of Chapter 4. In particular (1) the filtering effects of numerical differentiation schemes and (2) the correlation of the residuals in time for one tests performed in the wind tunnel (test #1), previous detailed in Chapter 4.

C.1 FILTERING EFFECTS OF NUMERICAL DIFFERENTIATION SCHEMES

For a generic sinusoidal analog signal ($x(t)=\sin(\omega t)$, where ω is the angular frequency), the time derivative is $\dot{x}=\omega\cos(\omega t)$, the Fourier transform of which is given by [Bahill et al., 1982]:

$$\dot{X}(\omega)=j\omega X(\omega) \tag{C.1}$$

For the digitized version of the signal (x_{d_t}) at a frequency of $f_{daq}=1/\Delta t$, second-order accurate three-point central difference algorithm is used for the calculation of time-derivative of the discrete time-series position and angle data, Eq. 4.10 (in Chapter 4). In order to transform it from the time domain to the frequency domain, the Z-transform was applied: [Bahill et al., 1982]:

$$\dot{X}_{d,c}(z)=\frac{X_d(z)\left(z-z^{-1}\right)}{2\Delta t} \tag{C.2}$$

This appendix includes the suppementary material of the following publication: Caetano, J. V., Percin, M., van Oudheusden, B. W., Remes, B. D. W., de Wagter, C., de Croon, G. C. H. E., and de Visser, C. C. (2015c). Error Analysis and Assessment of Unsteady Forces Acting on a Flapping Wing Micro Air Vehicle: Free-Flight versus Wind Tunnel Experimental Methods. *Bioinspiration & Biomimetics*, 10(5).

Then substituting $z = e^{j\omega\Delta t} = \cos(\omega\Delta t) + j\sin(\omega\Delta t)$ gives:

$$\dot{X}_{d,c}(\omega\Delta t) = \frac{X_d(\omega\Delta t)\, j\sin(\omega\Delta t)}{\Delta t} \tag{C.3}$$

Equations C.1 and C.3 can now be used to assess the ratio of the magnitudes of the calculated and the true derivative. Taking into account that for a properly sampled analog signal (without aliasing), the Fourier transform of the analog signal ($X(\omega)$) is equal to that of the discrete data ($X_{d,c}(\omega\Delta t)$) at the sampling points. Then, the ratio is [Bahill et al., 1982]:

$$\left|\frac{\dot{X}_{d,c}(\omega\Delta t)}{\dot{X}(\omega)}\right| = \frac{\sin(\omega\Delta t)}{\omega\Delta t} \tag{C.4}$$

A similar analysis is now performed for the forward difference algorithm (Eq. C.5) to investigate the frequency limitation effects of the first-order accurate schemes.

$$\dot{x}_t = \frac{x_{t+1} - x_t}{\Delta t} \tag{C.5}$$

Initially, application of z-transform yields:

$$\dot{X}_{d,f}(z) = \frac{X_d(z)\big(z-1\big)}{\Delta t} \tag{C.6}$$

Then substituting $z = e^{j\omega\Delta t} = \cos(\omega\Delta t) + j\sin(\omega\Delta t)$ gives:

$$\dot{X}_{d,f}(\omega\Delta t) = \frac{X_d(\omega\Delta t)\big(\cos(\omega\Delta t) - 1 + j\sin(\omega\Delta t)\big)}{\Delta t} \tag{C.7}$$

By comparing Eqs. C.1, C.3 and C.7, it is clear that forward difference algorithm introduces also a phase difference, whereas central difference algorithm does not have such an effect on the calculated derivative. For the forward difference algorithm, the ratio of amplitudes of the calculated and the true derivative is calculated as follows:

$$\left|\frac{\dot{X}_{d,f}(\omega\Delta t)}{\dot{X}(\omega)}\right| = \frac{\sqrt{2}\sqrt{1-\cos(\omega\Delta t)}}{\omega\Delta t} \tag{C.8}$$

C.2 CORRELATION OF RESIDUALS

Figure C.1 presents the t vs $t+k$ plots of the pitch state residual with varying lags (k) for a flight test with a flapping frequency of 12.5Hz. The correlations appear to be unstructured for most of the lags, except for lag = 16. This corresponds exactly to one period of flap ($200Hz/16/12.5Hz = 1$). As expected, at lag = 32 there is still some correlation between states, as this lag corresponds to having two flap cycles in phase, 32 time steps after the measured point. Contrary to other fixed wing platforms, these correlations will be present in the residuals for a flapping wing or other platforms with cyclic behavior, thus affecting the noise level detection. Nevertheless, for the current study, the noise level has shown to be close to a zero-mean, independent and identically distributed (IID) random variable.

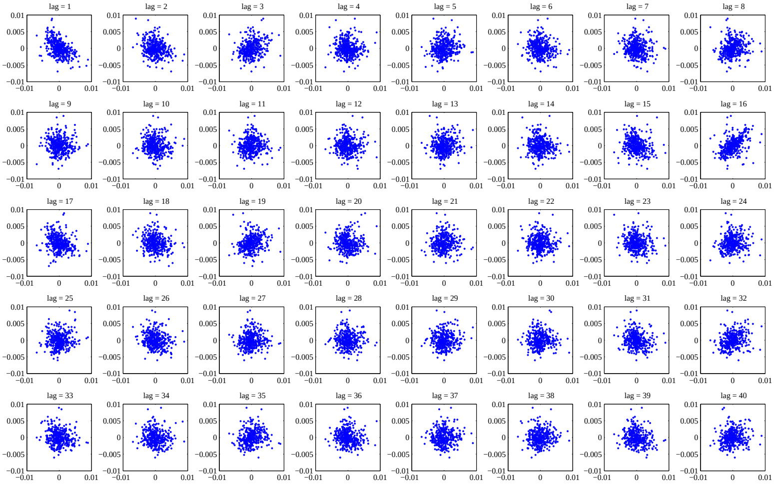

Figure C.1: Graphical correlation of the residuals established at different lags with $l \in [1,40]$ for test #1 of the wind tunnel tests presented in Chapter 4. Correlation in the form of trending was found to at lags in the vicinity of $l = i \times 16$ for $i = 0, 1, 2$.

D

EFFECTS OF FREE-STREAM VELOCITY ON THE UNSTEADY FORCES

The effect of the free-stream velocity on the sub-flap forces acting on the ornithopter is assessed by comparing the evolution of the forces at wind tunnel conditions that replicate those of free-flight *with* the forces obtained with the same pitch angle (θ) and flapping frequency (δ_f) as the respective test, but with no free-stream velocity. Figure D.1 presents the results for four flight conditions that represent the evolution at the four different flapping frequencies that are studied. These results are presented, from left to right, with the decrease in flapping frequency, with real conditions in solid line and zero free-stream with dashed line. Flap angle is shown in gray dash-dotted line. The last sub-figure, Figure D.1e, depicts the evolution of the forces for all four tests that represent the real free-flight conditions.

From the evolution of the X forces, across sub-figures a) to d) of Figure D.1, it is concluded that the free-stream velocity affects the lower flapping frequencies (e.g. 11.7Hz and 10.3Hz) more than the higher frequencies (13.3Hz and 12.5Hz). This is due to two reasons: a) the reduced frequency of the test condition, $k{=}\omega\times\bar{c}/V$, that considerably decreases with the test number due to both the decrease in the flapping frequency (ω) and the increase of the total velocity (V); b) effective velocity component parallel to the $\boldsymbol{x}_b \equiv X$ axis. This latter factor affects the force evolution in the beginning of the flap cycle, corresponding to the fling [Weis-Fogh, 1973] of the wings, because the increase in the velocity along $\boldsymbol{x}_b$ will result in a considerable decrease of the intensity of the leading edge vortex [Percin et al., 2014], which is one of main force generation mechanisms in

---

The contents of this appendix were presented in Caetano, J. V., de Visser, C. C., de Croon, G. C. H. E., and Mulder, M. (2015b). Effects of Eigenmodes, Forward Velocity and Flapping Frequency in Force Generation Mechanisms of a Flapping-Wing MAV. Bali, Indonesia. International Conference on Unmanned Intelligent Systems (ICIUS).

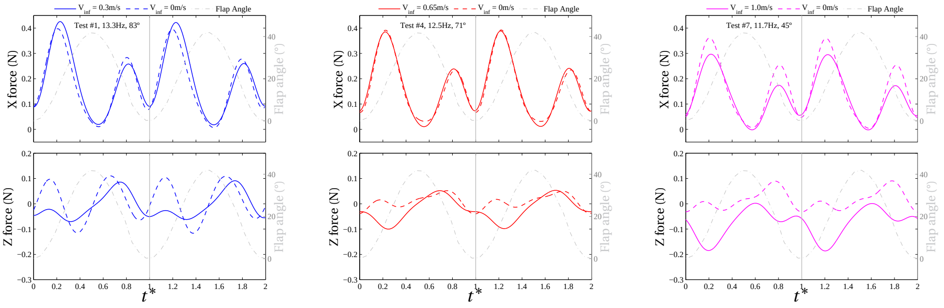

(a) Test #1, δ_f =13.3Hz, V =0.30m/s, θ =83°.

(b) Test #4, δ_f =12.5Hz, V =0.65m/s, θ =71°.

(c) Test #7, δ_f =11.7Hz, V =1.0m/s, θ =45°.

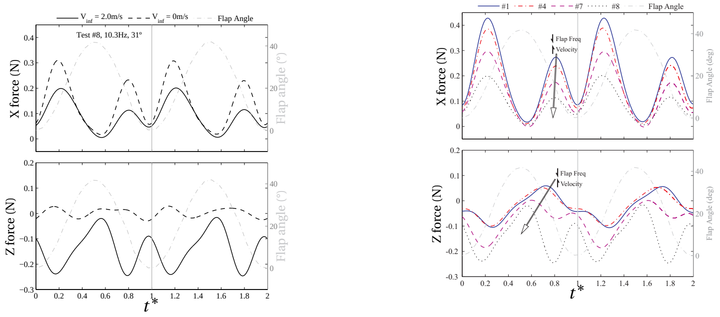

(d) Test #8, δ_f = 10.3Hz, V =2.0m/s, θ =31°.

(e) Tests #1, #4, #7 and #8; arrow indicates decreasing flap frequency and increasing V.

Figure D.1: Evolution of the forces acting on the FWMAV for conditions that represent free-flight (solid lines) compared with the forces obtained with zero free-stream velocity (dashed lines); flap angle is shown in dash-dotted gray line. Test numbers correspond to wind tunnel tests presented in Chapter 4.

clap-and-fling ornithopters (and species) [Weis-Fogh, 1972]. Furthermore, free-stream drag effects, which are more predominant at higher free-stream velocities, add to a) and b) resulting in a smaller net (average) Z force produced in a flap cycle with the presence of forward velocity.

Following a similar analysis for Z as the one performed for the X force, it is observed that, as the free-stream velocity increases, i.e., as the reduced frequency decreases, the cycle net (average) force decreases, becoming more negative – and noting that negative Z is up – results in an increase in the component of Lift force coming from Z. Conversely to what happens in the X forces, the free-stream velocity introduces a phase shift in the Z forces, with the peaks of the force appearing sooner in the flap cycle. This effect results in an apparent rapid decrease of the first peak of the force, at $t^*=0.15$, inverting local maximum to a minimum. A similar effect is also observed in the second peak of the force, occurring at mid in-stroke ($t^* \in [0.6, 0.8]$). Such behavior seems to be induced by the increase in the velocity component along the X force, which forces the camber of the wing to be reduced more rapidly at two time instants: a) beginning of the out-stroke as the in-flow of air into the suction area created between the wings during fling increases; b) beginning of the in-stroke, where the wings are forced to rotate due to stroke reversal. An increase in the free-stream velocity also promotes a considerable increase in peak-to-peak amplitude of the Z forces, e.g., from 0.04N to 0.21N for the test condition #8 (Figure D.1d). This effect is mainly justified by the increase in translational circulation at mid out-stroke (local minimum) due to the maximization of Lift promoted by the free-stream velocity – this mechanism is possible due to the stabilization of wing pitch angle at mid-stroke, i.e. wings reduce their rotation about $\boldsymbol{y_b}$ at half way of the out and in-stroke. For the same reason, the maximum values of the Z force (taking values close to 0N) occur at wing reversal, where the aerodynamic unsteady effects of the flapping dominate due to rapid wing rotation. Worth noting that, except for test #1 (Figure D.1a), for zero free-stream velocity the first peak appears to stay somewhat constant with the varying flapping frequency; this same first peak (first half of out-stroke) of the force cycle is more affected by the presence of free-stream velocity.

Another interesting aspect found in the progression of the sub-flap forces acting on the FWMAV can be observed in Figure D.1e. Here the forces are presented for four tests that replicate the free-flight conditions. The X forces decrease in magnitude (for the reasons detailed before) and maintain their relative phase; conversely, the Z forces change in phase throughout the tests, in the direction identified by the arrow.

E

AERODYNAMIC MODELING: A COMPARISON BETWEEN QUASI-STEADY AND FOURIER SERIES

E.1 QUASI-STEADY AERODYNAMIC MODEL

The forces that act on a single flapping wing are modeled and identified in Appendix D. This model was initially devised by Pesavento and Wang [2004], and extended by Berman and Wang [2007] who combined it with blade-element theory and applied it to a flapping wing with three degrees of freedom. This model is a quasi-2D force model, as the instantaneous forces for each blade-element are in the plane perpendicular to the wing radius (in the span-wise direction). The governing equations are as follows (for further details the reader is referred to Caetano et al. [2015a]):

$$d\boldsymbol{F}_{x_w} = [(\frac{c(r)}{\bar{c}R} M_{wing} + m_{22}) v_{z_w} \dot{\theta} - \rho_f \Gamma v_{z_w} - m_{11} a_{x_w}] dr - d\boldsymbol{F}_x^v \tag{E.1}$$

$$d\boldsymbol{F}_{z_w} = [-(\frac{c(r)}{\bar{c}R} M_{wing} + m_{11}) v_{x_w} \dot{\theta} + \rho_f \Gamma v_{x_w} - m_{22} a_{z_w}] dr - d\boldsymbol{F}_z^v \tag{E.2}$$

$$\Gamma = \frac{1}{2} C_T c(r) |V| \sin 2\alpha + \frac{1}{2} C_R c^2(r) \theta \tag{E.3}$$

The contents of this appendix were presented in Caetano, J. V., Armanini, S. F., de Visser, C. C., de Croon, G. C. H. E., and Mulder, M. (2015a). Data-Informed Quasi-Steady Aerodynamic Model of a Clap-and-Fling Flapping Wing MAV. Bali, Indonesia. International Conference on Unmanned Intelligent Systems (ICIUS).

$$\boldsymbol{F}^{v} = \frac{1}{2}\rho_f c(r)[C_{D_0}\cos^2\alpha + C_{D_{\frac{\pi}{2}}}\sin^2\alpha]|V|(v_{x_w}, v_{z_w})dr \tag{E.4}$$

$$m_{11} = \frac{1}{4}\pi\rho_f b^2, \quad m_{22} = \frac{1}{4}\pi\rho_f c^2(r) \tag{E.5}$$

$$v_{x_w} = r_i\dot{\zeta}\cos\theta_w \quad and \quad v_{z_w} = -r_i\dot{\zeta}\sin\theta_w - dc\dot{\theta}_w \tag{E.6}$$

Eqs. E.1 and E.2 represent the total force acting on a single wing along the $\boldsymbol{x}_w$ and $\boldsymbol{z}_w$ axis, respectively, for each blade element. Eq. E.3 captures the circulatory components of the forces in terms of translational (C_T) and rotational (C_R) circulation. The viscous terms included in Eq. E.4, where C_{D_0} and $C_{D_{\frac{\pi}{2}}}$ are the drag coefficients for zero and 90°angle of attack of the wing. For the current study, the wing was assumed to have a uniform distribution of mass, resulting in the mass terms of Eq. E.5, where b and c are respectively the average thickness (in the $\boldsymbol{z}_w$ direction) and chord of the blade-element.

Relative velocities are defined in Eq. E.6. The total force is computed by integrating the forces on each blade, taking in consideration the wing shape and real flapping kinematics. Except for $C_T, C_R, C_{D_0}, C_{D_{\frac{\pi}{2}}}$ and d, the remaining unknowns are taken from wing kinematics, described in Chapter 3 and Caetano et al. [2015d]. The missing parameters are estimated from the force data as explained in Section E.3. It is worth noting that the present model does not take into account the forward velocity of the FWMAV.

E.2 FOURIER SERIES AERODYNAMIC MODEL

As an alternative to the previously presented quasi-steady aerodynamic model, a Fourier series model was developed. Whilst physical meaning is desirable, for many applications an accurate model of any sort is useful, and in fact even physically-derived aerodynamic models often involve some empirical component. This type of model was considered to provide a useful comparison for the physically-derived model presented in the previous section, but also as a practical solution in its own right.

Experimental data presented before show that the flapping of the wings leads to periodic patterns in the sub-flap aerodynamic force production, particularly in the X component. Hence a trigonometric Fourier series expansion was selected as a model structure to represent the X force over the flap cycle, i.e.,

$$X(t) = a_0 + \sum_{n=1}^{h}\left(a_n\sin(2\pi n f t)\right) + \sum_{n=1}^{h}\left(b_n\cos(2\pi n f t)\right), \tag{E.7}$$

where h is the number of harmonics in the model, f is the fundamental frequency, which is chosen to be equal to the flapping frequency, t is time, and a_n and b_n are the nth Fourier coefficients. Only a single constant term, viz. a_0, is left in the series to avoid redundant parameters. This term is used to model the average of the forces.

In view of the structure of Fourier series, it is logical to select a Fourier series containing the same number of harmonics as are left in the estimation data after filtering. Hence the driving factor in selecting the number of harmonics for the model was the choice of filter cut-off for the estimation data. Fourier series up to the third and fifth harmonic h were initially investigated. The first three harmonics are the most easily recognizable in the measurements and can be identified relatively clearly even in free- flight. Filtering out frequency content above the third harmonic still allows for the main component of the force evolution to be seen, therefore establishing a model for the first three harmonics is already useful. However, in the final instance, a 5^{th} order model was selected, as only with at least five harmonics it becomes possible to capture the clap-and-fling effect. In general more effects can be captured when five harmonics are left in the data. This comes at the cost of a larger number of parameters, however the resulting structure is still manageable and computationally simple. Furthermore, given that the parameters have no physical significance, a larger number of these is not as crucial an issue as it would be in a physical model, in terms of interpretation of the model. By contrast, a higher number of parameters entails a higher chance of overfitting, as reflected in the results (Section E.4). However, the chosen formulation can be considered an acceptable compromise between model accuracy and complexity.

The final model structure contains very limited information on the flight conditions. Whilst the flapping frequency determines the periodicity and phase of the force evolution, its effects on the amplitude are not considered. Information on the flow velocity and angle of attack is not included at all. Hence the only measurement needed to apply this type of model is the flapping frequency, making this model extremely simple and easy to apply, including within a simulation framework.One additional reason for this formulation was the observation that in non-maneuvering flight the time-progression of the X force does not appear to vary significantly with different conditions. Thus, an additional goal in testing this type of model, was to investigate to what extent the same model can be used to represent the X force in different steady flight conditions.

E.3 PARAMETER ESTIMATION METHOD

The unknown parameters in the previously presented model structures (cf. Eqs. 6.12–E.7) were estimated using a maximum likelihood (ML) estimator and an output error approach. This is both a powerful estimator and one that can be applied to complex, nonlinear model structures, including ones that are nonlinear in the parameters. It must be noted that the performance of the estimator is limited by the choice of a model structure and by the availability of free parameters. The estimated parameters only optimize the model fit for the given structure. However, while this bounds the performance of the estimator, it gives some useful insight into the adequacy of the model structure itself. The aim of this study was to evaluate and compare the performance of the proposed model structures, rather than to obtain new, optimal model structure directly from the data.

ML estimation has been treated extensively in the literature [Jategaonkar, 2006; Klein and Morelli, 2006], therefore only a brief overview is provided here. ML estimation consists in maximizing the probability, or likelihood, p of an observation z occurring at a measurement time k, given a set of parameters Θ and measurements x. The cost function for this type of estimation problem is typically formulated as the negative logarithm of the likelihood function, i.e.,

$$J(\boldsymbol{\Theta},\mathbf{R}) = -\ln p(\mathbf{z}|\boldsymbol{\Theta}) = \frac{1}{2}\sum_{k=1}^{N}[\mathbf{z}(k)-\mathbf{y}(k)]^T\mathbf{R}^{-1}[\mathbf{z}(k)-\mathbf{y}(k)] + \frac{N}{2}\ln(\det(\mathbf{R})) + \frac{Nn_y}{2}\ln(2\pi), \tag{E.8}$$

where $\mathbf{R}$ is the measurement noise covariance matrix, N is the number of data samples, n_y is the number of output variables, and $\mathbf{z}(k)$ and $\mathbf{y}(k)$ are the measured and model-predicted outputs, respectively, at measurement point k. The model-predicted outputs are a function of the parameter estimates. Minimizing the above cost function is a non-linear optimization problem that can be solved by iteratively adjusting the model parameters until the difference between model-predicted and measured outputs is minimal according to the chosen convergence criterion.

The noise covariance matrix $\mathbf{R}$ contained in the cost function is generally unknown, but can be estimated in each iteration step using a relaxation approach. This is done by fixing the parameters at the values estimated in the previous iteration step, and minimizing the cost function with respect to $\mathbf{R}$. This yields the following estimate for $\mathbf{R}$ [Jategaonkar, 2006],

$$\hat{\mathbf{R}}=\frac{1}{N}\sum_{k=1}^{N}[\mathbf{z}(k)-\mathbf{y}(k)][\mathbf{z}(k)-\mathbf{y}(k)]^T. \tag{E.9}$$

Substituting Eq. E.9 into the cost function (Eq. E.8) gives the cost at the current iteration, which is used to establish whether the convergence criterion has been met. To estimate a new set of parameters for the following iteration step, the measurement noise covariance matrix estimated from the previous set of parameters using Eq. E.9 is substituted into the cost function, which is then minimized with respect to the parameters. The minimization yields the parameter update step. In this work a Gauss-Newton algorithm was used for the minimization process. Initial guesses for the parameters were based on literature values for the quasi-steady aerodynamic models [Andersen et al., 2005b; Berman and Wang, 2007] (Table E.1), and obtained using linear regression for the Fourier models.

For the present estimation work, the output equations can be directly inferred from the aerodynamic models in Sections III.E and III.E. In fact, although the evolution of the aerodynamic forces is a dynamic process, given that measurements of all required variables were obtainable, there was no need to include any dynamics in the estimation process. Rather, the output is a direct function of the input, and can be directly computed from the measurements at each time step.

The output z for both models is the aerodynamic force X, which is in each case a function of a different set of parameters and measurements. In the Fourier series models, the parameters to be estimated are the Fourier coefficients in Eq. E.7, i.e.

$$\Theta_{Fourier}=\left[\, a_0\ a_1\ \dots\ a_5\ b_1\ b_2\dots b_5 \right], \tag{E.10}$$

these parameters bear no physical meaning, and simply yield a mathematical description of the output. The required input measurements are the flapping frequency, constant over the cycle for the wind tunnel tests, and the non-dimensional cycle time t. The output equation is given by Eq. E.7.

In the quasi-steady model the parameters to be estimated are [Caetano et al., 2015a],

$$\Theta_{QS}=\left[\, C_T\ C_R\ d \right]. \tag{E.11}$$

Initially two additional parameters, C_D and $C_{D_{\frac{\pi}{2}}}$ were also estimated. However, while the model-predicted output was fairly accurate, implausible values were estimated for these

Table E.1: Initial guesses for the parameters in the quasi-steady model, based on values in the literature [Andersen et al., 2005b; Berman and Wang, 2007]. In the final model, the parameters C_{D0} and $C_{D\frac{\pi}{2}}$ were fixed at the values given in the table; the remaining parameters were estimated.

Parameter	Initial value before estimation
C_T	1
C_R	1.6
d	0.2
C_{D0}	0.05
$C_{D\frac{\pi}{2}}$	0.2

two parameters, and it was therefore decided to fix them at literature-based values, and only estimate the parameters given in Eq. E.11, to maintain as physically realistic a result as possible.

The meaning of the parameters has been discussed in Section E.3, and the output equation is obtained from Eqs. 6.12 and 6.13. Note that the equations are given for a single blade element, therefore obtaining the actual output requires integrating the forces over the full span. For this model, the required measurements are the flap angle and its derivative, the wing pitch angle and its first and second derivatives, and the flapping frequency. All of these measurements were obtainable from the wind tunnel experiments.

E.4 RESULTS AND DISCUSSION

The two models were evaluated in terms of their effectiveness in representing the measured data and in statistical terms but also, in the case of the physically-derived model, in terms of the plausibility of the obtained parameter values. In the interest of clarity, only four test cases are shown, viz. the same ones as discussed earlier. They differ in flapping frequency as well as in flow velocity and angle of attack. Results show the total force generated by all four wings. f Figure E.1 shows the model-predicted X force for each test case, in comparison with the corresponding wind tunnel measurements. Measurements filtered at 40Hz and at 67Hz are shown, to underline different effects, and both the quasi-steady and the Fourier series models are presented on the same plots, to facilitate their comparison. The corresponding statistical metrics quantifying the performance of each model are presented in Table E.2, whilst the parameter estimates can be found in Tables E.3 and E.4. The quasi-steady model is discussed in detail in Chapter 6, therefore only the salient points are highlighted here to enable a better comparison.

Both models are capable of capturing the main component of the force evolution, albeit to a different extent. The quasi-steady model is fairly effective in replicating the lower-frequency content in the measurements, in all test cases. The model-predicted values display a good agreement with the measurements, and the overall shape of the force evolution is captured well, with the second peak in each cycle being lower than the first. Particularly in comparison with the more heavily filtered (40Hz cutoff) data,

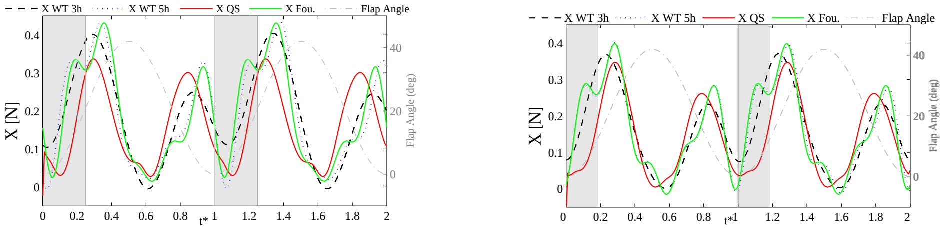

(a) Test # 1.

(b) Test # 4.

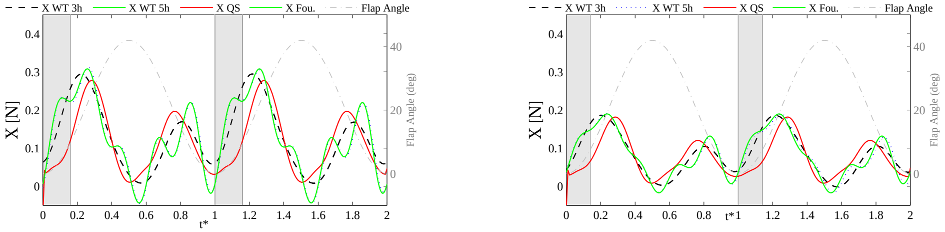

(c) Test # 7.

(d) Test # 8.

Figure E.1: Wind tunnel (WT) *X* force measurements versus *X* forces predicted by quasi-steady (QS) and Fourier models, for test cases #1, #4, #7, #8. Wind tunnel measurements are shown with filtering after the 3$^{\text{rd}}$ harmonic (3h) and after the 5$^{\text{th}}$ harmonic (5h).

Table E.2: Statistical evaluation of computed models, based on estimation data

	Quasi-steady model			**Fourier model**		
Test #	RMS[N]	R2	corr.coeff.	RMS[N]	R2	corr.coeff.
1	0.022	0.478	0.740	0.005	0.998	0.999
2	0.018	0.515	0.768	0.003	0.997	0.999
3	0.017	0.608	0.819	0.003	0.999	1.000
4	0.017	0.614	0.821	0.006	0.997	0.998
5	0.016	0.585	0.798	0.007	0.996	0.998
6	0.017	0.548	0.797	0.037	0.921	0.960
7	0.014	0.563	0.787	0.005	0.998	0.999
8	0.010	0.519	0.752	0.004	0.999	0.999

Table E.3: Parameters estimated from each set of estimation data, for the quasi-steady model.

param.	test #1	test #2	test #3	test #4	test #5	test #6	test #7	test #8	avg.	std.
C_T	2.560	2.020	3.090	3.471	2.556	3.033	2.703	3.330	2.795	0.497
C_R	-0.042	-0.172	-0.145	0.112	0.221	0.683	0.050	0.165	0.109	0.287
d	0.352	0.412	0.369	0.354	0.291	0.255	0.317	0.358	0.333	0.047

Table E.4: Parameters estimated from each set of estimation data, for the Fourier series model

param.	test #1	test #2	test #3	test #4	test #5	test #6	test #7	test #8	avg.	std.
a_0	0.130	0.083	0.145	0.165	0.172	0.191	0.161	0.161	0.151	0.033
a_1	0.071	0.046	0.070	0.084	0.097	0.116	0.088	0.083	0.082	0.021
b_1	0.039	0.030	0.053	0.054	0.038	0.013	0.047	0.050	0.040	0.014
a_2	-0.008	0.000	-0.007	-0.032	-0.024	-0.105	-0.008	-0.039	-0.028	0.034
b_2	-0.085	-0.053	-0.107	-0.107	-0.092	-0.045	-0.100	-0.100	-0.086	0.024
a_3	0.002	0.005	0.003	-0.007	-0.005	-0.027	-0.006	-0.012	-0.006	0.010
b_3	-0.024	-0.014	-0.033	-0.031	-0.013	0.009	-0.028	-0.032	-0.021	0.014
a_4	0.003	0.009	0.016	0.032	0.001	-0.046	0.006	0.022	0.005	0.023
b_4	-0.023	-0.011	-0.008	-0.020	-0.042	-0.023	-0.032	-0.027	-0.023	0.011
a_5	0.046	0.022	0.038	0.023	0.015	-0.048	0.022	0.010	0.016	0.028
b_5	-0.030	0.003	-0.014	-0.049	-0.051	0.010	-0.036	-0.041	-0.026	0.023

where the unsteady effects are less visible, there is a good agreement. However, the force evolution is not fully replicated. In particular, unsteady effects are not accounted for in the model, and it can for instance be observed that the clap-and-fling effect is omitted. The clap-and-fling effect can be visualized in the data filtered at the 5$^{\text{th}}$ harmonic, where it leads to an additional force peak at the start of the flap cycle. Comparing this to the model, it is clear that the model only appears to capture the second peak, i.e. the peak occurring after the clap-and-fling peak. In the more heavily filtered data, the clap-and-fling peak is no longer visible, however its effect is evident in the phase shifting of the first force peak, which incorporates the first two peaks of the less filtered data. Thus, whilst the force evolution in the more filtered data has the same shape as in the model, in the model the first peak of each cycle is phase shifted due to the neglecting of clap-and-fling.

In spite of this shortcoming, which is a consequence of the model definition and was thus expected, the performance of the model can be considered relatively satisfactory, with output correlations up to 0.8 and R2 values up to 0.6 (Table E.2). The adequate performance is particularly noteworthy in view of the small number of estimated parameters, which suggests that the underlying model structure is suitable. The estimation of platform-specific aerodynamic parameters rather than their theoretical derivation or literature-based calculation, ensures closeness to the real system and extracts the best possible solution from the chosen model structure.

It becomes clear that the Fourier series models can achieve a much higher accuracy than the quasi-steady models, for all test conditions considered here. For the Fourier series-based models, the agreement between estimated and measured forces is remarkable, with the former almost perfectly replicating the latter. This behavior is highlighted by the corresponding metrics: the residual errors are extremely low, approximately one order of magnitude smaller than in the quasi-steady case, whilst the output correlation coefficients and R2 values are close to 1. The marked periodicity in the force evolution is clearly well represented by this type of model structure. Furthermore, the model is not limited by physical assumptions and hence can also capture unsteady effects. It can be observed that the clap-and-fling peak is reproduced effectively. The high accuracy also comes at a low computational cost and although the number of parameters is higher than in the quasi-steady case, the model structure is very simple and easy to implement.

However, the Fourier series models also present a number of limitations. Whilst the

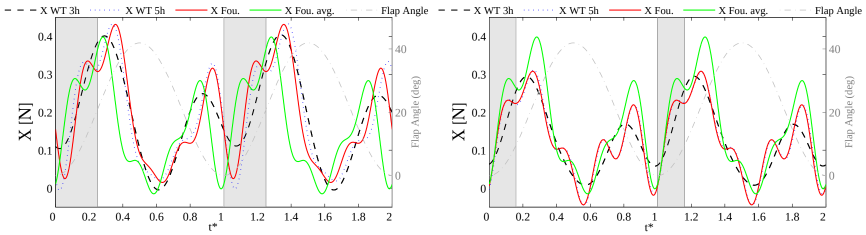

(a) Test # 1

(b) Test # 7

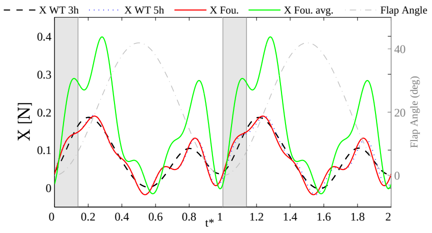

(c) Test # 8

Figure E.2: Wind tunnel (WT) X force measurements versus model-predicted X forces. Evaluation of the Fourier model obtained in a central part of the flight envelope (test #4, cf. Figure E.1b) as a representative model to describe the X force in all test conditions. Being the chosen reference average case, test # 4 is not shown here.

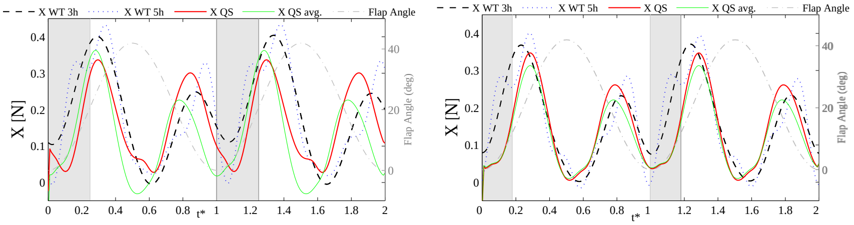

(a) Test # 1

(b) Test # 2

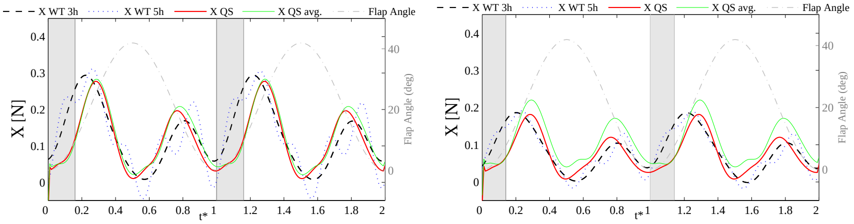

(c) Test # 7

(d) Test # 8

Figure E.3: Wind tunnel (WT) X force measurements versus X forces predicted by quasi-steady (QS) models. Evaluation of average quasi-steady model obtained by averaging each parameter over the values estimated from all 8 datasets.

output match is indeed very accurate, the models are highly connected to the test condition they were estimated in. The only physical information contained in these models is the effect of the flapping frequency on the phase, whereas all other effects of different test conditions cannot be considered. This implies that each model is indeed highly accurate, but only in the test condition it was estimated for, and that these models cannot be easily extended to cover different flight conditions.

Computing an average model from the separate Fourier models obtained in different test conditions is not effective or justifiable, as each combination of parameters applies only to that particular test condition and it is predominantly the parameters themselves that account for the differences between different test conditions. Different combinations of parameters can lead to the same outcome, so that the parameters cannot be considered separately and the models can only be considered as single entities. This is reflected in the often significant variation between estimates for the same parameter obtained from different datasets. Furthermore, given that the separate parameters cannot be attributed any physical meaning, a comparison between estimates for the same parameter obtained from different datasets is meaningless.

One possibility to develop a global model with this approach, would be to assume that the same approximate force evolution occurs at all test conditions. Figure E.2 shows that applying the same model (in this case, the model estimated for test condition # 4, which can be considered representative for the 'central part' of the flight envelope) to different test conditions is in some cases acceptable, but in others inadequate. In particular, the residual RMS appears to increase with the distance of the considered test condition from that the model was estimated in, ranging from 2% to over 50% (Figure E.4).

Clearly, although within a range of more typical flight conditions, the forces generated are fairly similar and the same model can be applied with reasonable accuracy, as soon as larger variations in conditions are introduced, this approach is no longer sufficient. Thus, whilst the Fourier series models are potentially highly accurate, their range of applicability is limited.

In this regard, the quasi-steady formulation offers a clear advantage. Whereas the Fourier models can be considered useful tools, but not a source of information, the quasi-steady model retains a clear connection to the real system and can provide insight and understanding, even considering the significant assumptions and simplifications it involves. This allows for an interpretation of obtained results and for application of the model for analysis purposes. Moreover, it implies that the model can be adapted to different test conditions.

Similarly, it was found that the parameter estimate values are in a plausible order of magnitude and for two of the three estimated parameters, viz. C_T and d, very similar values are estimated from different datasets. This firstly indicates an effective estimation process and lends credibility to the result, and secondly suggests that a global model of this form can be obtained and applied to all test conditions with good results. In fact, given that the model contains information on the test conditions it is being applied in, it should not be necessary to change the parameters to adapt the model to a specific flight condition.

To test this, an average model was computed by taking the mean of each parameter over all test cases. The model was applied in all test conditions and found to have a reasonably good performance, as illustrated in Figure E.3, so that it can be considered, in first approximation, a global model. The RMS remains within a narrow range (4.5%-6%, cf. Figure E.4) for all cases. The significant variation in C_R over the different test cases, which flows into the averaging process, may be affecting the model's performance to some extent, however this effect seems small. Given the satisfactory overall result it seems that C_R is not a dominant parameter and has a relatively small impact on the final outcome. Nonetheless, this effect merits further investigation.

In global terms, the use of a quasi-steady averaged model thus appears to be more effective and reliable than the use of one of the Fourier models as a global model. However, the Fourier models retain the advantage of a higher achievable accuracy and the inclusion of unsteady effects. For applications such as basic simulation, the small changes between different test conditions can be considered less important, and here the Fourier models would provide a more realistic simulation than the simplified quasi-steady ones.

E.5 CONCLUSION

Two different models for the aerodynamics of a flapping-wing flyer were presented and compared. The first was based on quasi-steady aerodynamic modeling, while the second was a 5^{th}-order Fourier series expansion. The parameters within the models were estimated using wind tunnel data and system identification methods. The models were applied to model the X force of the DelFly, a clap-and-fling FWMAV, and evaluated, particularly in comparison to each other.

It was found that the quasi-steady model can represent a significant component of

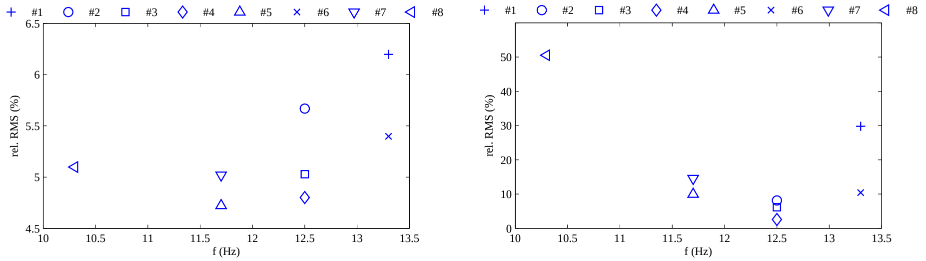

(a) Quasi-steady average model

(b) Fourier series average model

Figure E.4: Residual RMS of the ‘average’ quasi-steady and Fourier series models, respectively, when applied to each dataset (test #1–test #8). In view of the different modeling approaches, the average quasi-steady model is computed by averaging each parameter over all test cases, whereas the *average* Fourier model is the model estimated for test condition # 4, considered representative for the ’central part’ of the flight envelope.

the X forces (relative RMS <9%), and is a useful basic description despite its inability to capture unsteady effects such as clap-and-fling. Using experimental data to estimate model parameters is an effective way of adapting the model to the platform and increasing the accuracy, while the fairly satisfactory results obtained using a very small number of parameters suggest that the model structure is adequate for the vehicle considered. Although this formulation has a limited accuracy, it has the advantage of being easily adapted to different flight conditions. An averaged model was found to provide a reasonably accurate description of the FWMAV over the full flight envelope, which is useful for quick global modeling that requires basic but not highly accurate sub-flap simulation. Thanks to its physical significance, the model is also applicable for conceptual analysis and investigations.

By contrast, the Fourier models were found to yield a highly accurate description of each test condition, including unsteady effects. However they depend entirely on the parameters to capture differences between different flight regimes, and therefore cannot be adapted to different conditions. In particular, the use of the same model to describe different conditions was found to be effective only within small regions of the flight envelope. This type of model is useful for simulation and control in limited parts of the flight envelope, but a more wide-ranging application would require either a form of scheduling to combine separate models, or the inclusion of additional information on the flight conditions in the model structure.

Due to their different properties, the models are better suited for different applications. However both have a useful level of accuracy, and are theoretically and computationally very simple. A more accurate description using physical models would require the explicit inclusion of the clap-and-fling effect. This could be done based on first principles, which however would require significant simplification for a practical solution to be obtained, or alternatively, the quasi-steady model could be combined with a Fourier series component accounting only for the unsteady effects.

F

EXPLANATION OF FINAL PROCESSED FREE-FLIGHT DATA, INCLUDING STATES, INPUTS, FORCES AND CODE

F.1 DESCRIPTION

A very light automatic Flapping Wing Micro Air Vehicle (FWMAV) equipped with eight retro-reflective markers (see Figure F.1) was flown extensively in a high accuracy position tracking chamber [1]. The test chamber (Figure F.2) had a total flyable volume of (21x17x7.6)m^3 and was equipped with 36 4-megapixel Vicon T40 cameras and 24 16-megapixel T160 cameras, which allowed for position tracking accuracies higher than ±1 mm. Here, a set of 168 flight tests were conducted to record the position of the aerial robot, at 200Hz, across a multitude of system identification maneuvers that covered the full flight envelope of the robot. These maneuvers, which consisted of step, doublet and triplet inputs on the control surfaces of the robot, were carefully designed to excite its full range of dynamics. Each maneuver was performed three times by the autopilot, guaranteeing repeatability and accuracy on the inputs, and consequently, on the collected data.

In flapping-wing flight, the position of the center of gravity of the platform will influence its flight regime. In this regard, the center of gravity was placed at four different locations along the robot body frame to cover all the flight regimes, from hover to fast forward flight.

The contents of this appendix were as README file for the publication: in Caetano, J. V., de Wagter, C., Ruijsink, R., Remes, B. D. W., Beran, P. S., and de Visser, C. C. (2016). Free-flight Data of a Flapping Wing Micro Air Vehicle for System Identification. *IEEE Transactions on Robotics*, (submitted).

[1] μAVIARI flight chamber of the U.S. Air Force Research Laboratory.

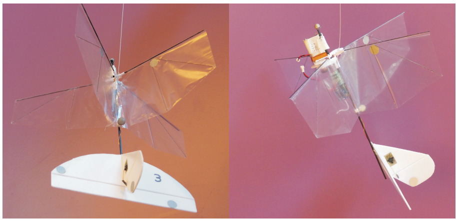

Figure F.1: Micro robot used for data collection.

Figure F.2: Image of flight chamber.

The data are composed of 168 Matlab loadable files organized by maneuver and flight speed. This data are divided in three main folders: i) Position Data; ii) States and outputs; iii) Code. Each data folder is divided in four sub-folders, per configuration of the center of gravity.

The 'Position Data' folder has the position in space of the eight retro-reflective markers that define the FWMAV. This data can be used to obtain flight dynamic and aerodynamic models of the FWMAV, using your own system identification and modeling techniques; The 'States and outputs' folder includes the aerodynamic forces and moments, Euler and attitude angles, the linear and angular velocities and accelerations of the FWMAV, the flap angles and respective wing flap velocities and accelerations and the aerodynamic angles. The 'Code' folder contains the Matlab files with the code needed to compute the data in folder 'States and output' from the 'Position Data'.

Furthermore, this information is guaranteed to be error-free and has the potential to contribute to other studies that focus on, e.g., aerial robot stability analysis, development of controllers, nonlinear dynamic inversion, aerodynamic modeling, robot design and onboard sensor development, as demonstrated in Caetano et al. [2013a, 2014a, 2015d].

F.2 SIZE

The total size of the data and code is of 259Mb.

F.3 PLATFORM AND ENVIRONMENT

The data in folders i) and ii) mentioned above can be loaded to any Matlab software after 2011. Previous versions may not be fully compatible. The code uses in-built Matlab functions compatible with Matlab version R2012b. Other versions might need an update of these functions. Microsoft Office Excel or compatible .xlsx reader should be used to open the `Flight Test Description.xlsx`. The code was tested in Windows operating system (OS) desktops and laptops. Nevertheless, no incompatibilities are expected with other OS, if Matlab versions are respected.

F.4 MAJOR COMPONENT DESCRIPTION

F.4.1 EXCEL SHEET AND DATA CONTENT

The geometric, material, inertial and kinematic characteristics of the robotic vehicle are carefully tabulated in the article to enable readers to synthesize the system level model to which the flight data corresponds. Moreover, file `0_Main_Flight_Test_Description.xlsx` contains the detailed description of the inertia and geometric properties of the FWMAV per configuration – each configuration is separated by a different spreadsheet. Each spreadsheet contains the description of the system identification maneuvers of each of the flight tests, presenting the following information:

i. Number of the test, which corresponds to the test numbering in the data folders;

ii. The overall quality of each test, numbered from 3 to 5 (files with a quality of 1 or 2 were not considered for publishing), with 5 indicating the highest overall quality of the data;

iii. Description of the test, indicating a summary of the test maneuver or flight conditions;

iv. Average velocity of the FWMAV during the flight test, in m/s;

v. Average flapping frequency of the FWMAV during the flight test, in Hz;

vi. Number of missing data points, corresponding to time instants that the tracking chamber did not record the position of the FWMAV;

vii. Time correspondence of the missing data points, in seconds;

viii. Percentage of usable information, determined from the ratio $(1-\frac{missingpoints}{totalinitialpoints})$;

ix. Length of file in seconds.

F.4.2 DATA FILES AND FOLDERS

The dataset is divided in three folders:

i. ‘Position Data’, divided in four folders, per configuration, which contain:

   a. Matlab loadable functions containing information about three dimensional position of the eight retro-reflective markers placed on the FWMAV, recorded by the external tracking system at 200Hz. This data was treated to certify error free positioning. Worth noting that the tracking system is not able to track the position of the FWMAV at all times, resulting in missing points in time, as described above.

   b. Each position data file is a `struct` with a field name for each marker coordinate, along the (x_I, y_I, z_I) inertial reference frame, using the following nomenclature:

      - `Time` – timesteps measured at 200Hz;
      - `Nose` – Nose marker
      - `LW` – Left wing marker
      - `RW` – Right wing marker
      - `TE` – Wing Trailing Edge central marker
      - `Hstab` – Horizontal stabilizer marker
      - `Elev` – Elevator marker

   - `Vstab` – Vertical Stabilizer marker
   - `Rud` – Rudder marker

ii. 'States and Outputs', divided in four folders, per configuration, which contain:

   a. Principle Moments of Inertia of the FWMAV, along the body axes: (I_{xx}, I_{yy}, I_{zz});
   b. Position data, corresponding to position East, North and Height: `(Pe,Pn,H)`
   c. Flap angle and rotational velocity of the wings: `RW_angle` [rad]; `LW_angle`[rad]; `flap_freq`[Hz]; `Flap_rate`[rad/s]; `Flap_acc` [rad/s^2]
   d. Control surface deflection angles: `d_elev`[rad]; `d_rud`[rad];
   e. Euler and attitude angles: Euler `(phi,theta,psi)`; Attitude `(roll,pitch,yaw)`;
   f. Linear and angular velocities and accelerations in the robot body frame, determined using three different in-time differentiation schemes: linear velocities `(u,v,w)`, norm `V`; linear accelerations `(u_dot,v_dot,w_dot)`; angular velocities `(p,q,r)`; angular accelerations `(p_dot,q_dot,r_dot)`;
   g. Aerodynamic angles of attack α and side-slip β measured from the CG of the FWMAV, considering the CG velocities `(u,v,w)`;
   h. Aerodynamic forces acting on the FWMAV: acting along the body axes `(X,Y,Z)`; acting along the relative wind reference frame `(Lift; Thrust)`;
   i. Aerodynamic moments acting on the FWMAV: acting along the body axes `(L,M,N)`;
   j. Accuracy of the position data, which is a function of position within the chamber and acceleration of the robot: `Errors`, identified by `er` before the name of the variable;
   k. Subscripts: `b` body axes to body axes differentiation of the velocities or accelerations, instead of using Euler angle based differentiation; `2P` forward or backward central differences differentiation of the velocities or accelerations; `3P` three-point central differences differentiation of the velocities or accelerations; `5P` five point stencil or Lagrange differentiation of the velocities or accelerations; `d` indicates when a variable is in degrees instead of radians, whether [deg] or [deg/s].

iii. 'Code', including 20 Matlab `.m` files that compute all the variables mentioned in point 'ii.' from the data in 'i'. To run the code the user only needs to run `0_Main_Flight_Path_reconstruction.m` and typeset the values of the user selectable variables:

   - `vector_of_tests` – array with the number of the flight tests to be computed in a single run. The code loops through the array until all tests have been computed;
   - `plot_Figures` – if 1 will plot a set of figures with the states;
   - `savefile` – set to 1 to save the workspace of variables for each test; if set to 1 user must select correct save path (below);
   - `StatesSavePath` – Path of the variables to be saved;

- `Fp, Fst, Fs` – Forward-backward zero-lag filter parameter selection. `Fp` for start of the stop band in [Hz]; `Fst` for end of stop band in [Hz]; `Fs` is the sampling frequency.
- `Filter_1, Filter_2, Filter_3` - different points along the code where filtering can be applied. Set to 1 to filter according to the parameters set above. Detailed in `.m` file.
- `check_inverted_flight` - Set to 1 if test corresponds to 'elevator up' deflection, to attitude pitch angles greater than 90°;
- `useExactUncertCalc` – set to 1 to determine the Errors/Uncertainty in the computed states per time-step – takes considerably more time; set to 0 for errors determined using a sample of the flight test; Values may differ of a maximum of 10%.
- `Rud` – Rudder marker

The following `.m` files are called by the `0_Main_Fligh_Path_reconstruction.m` or subroutines:

- `Robot_Properties` – loads the FWMAV geometric, mass and inertia properties;
- `Var_ini` – Initializes the variables and allocated memory;
- `Rotation_Matrix` – Computes the rotation matrices from the inertial reference frame to the body reference frame;
- `Marker_Uncertainty_Analysis` – Analyses of the marker uncertainty that will be used to compute the errors in the final states;
- `Attitude_Angles_Quaternions` – Computes the Euler and attitude angles and the Quaternions;
- `Determine_control_inputs` – Computes the deflection angles of the control surfaces;
- `Linear_Vel_Accel` – Compute the linear velocities and accelerations;
- `Angular_Vel_Accel` – Compute the angular velocities and accelerations;
- `Forces_Moments` – Compute the aerodynamic forces and moments;
- `Save_States` – Save the states and variables in the path introduced in `StatesSavePath`.
- `Uncertainty_Calc` – Determine the uncertainty affecting the states, using a sample of the data (select using `useExactUncertCalc = 0`);
- `Uncertainty_Calc_Exact` – Determine the uncertainty affecting the states using the entire flight test (select using `useExactUncertCalc = 1`);
- `filterDesign` – Design the filter, a Chebyshev type II forward-backward filter, which does not introduce phase lag on the data;
- `Plot_euler_rates_compare_betw_methods` – Plot the Euler angles, rates and compare between differentiation methods;

- `Plot_Trajectory_States` – Plot the trajectory, velocity, pitch, flapping frequency and control surface states;
- `ErProp1` – Numerical error propagation for a function, used in `Uncertainty_Calc`;
- `PropError` – Analytical error propagation for a function, used in `Uncertainty_Calc`;
- `FFError2Errors` – Used to create the variable `Errors` from pre-existing variables;

F.5 DETAILED SET-UP INSTRUCTIONS

The data is stored in Matlab `.m` files. It is meant to be loaded to Matlab version posterior to 2010. An `.xlsx` compatible software should be used to interpret each file test and relate to the maneuver that was performed. The data can be used in two complementary ways:

a. 'Position Data' only, which the user can use in-house kinematic formulations, select different filtering and differentiation techniques to compute the forces and moments acting on the FWMAV;

b. 'States and Outputs', which include the states (position, velocities, accelerations), uncertainty and the post-processed filtered aerodynamic angles, forces and moments to feed to system identification routines or modeling approaches.

F.6 DETAILED RUN INSTRUCTIONS

Each file in the 'Position Data' folder can be called directly or loaded in Matlab and used according to the variable description.

The data in 'States and Outputs' is computed using the Matlab routine `0_Main_Flight_path_reconstruction.m`. This data can be recomputed to include different FWMAV inertia properties, filter parameters, differentiation techniques or reference frame transformations by changing the user selectable variables, as explained in F iii.

The information contained in the files in 'States and Outputs' can be directly used as inputs to a model, or loaded to Matlab, as it contains all the states and variables needed as inputs to a model.

F.7 OUTPUT DESCRIPTION

On the one hand, the data provided can be directly used for modeling and system identification techniques. On the other hand, the data also allows for considerable flexibility, as different kinematic models, differentiation techniques and filtering designs can be used to re-compute the states of the FWMAV during the flight tests.

The code in 'Code' folder uses the 'Position Data' information to compute the variables in 'States and Outputs' `0_Main_Flight_path_reconstruction.m` the user can re-compute the states as well as the aerodynamic forces and moment and save them directly on a preselected folder. Different sets of figures can be plotted as auxiliary means of comprehension of the flight tests.

New data can be generated according by changing the user selectable parameters, as explained in F iii.

F.8 CONTACT INFORMATION

For further information, please contact: Joao V. Caetano at `jvcaetano@gmail.com`.

BIBLIOGRAPHY

Abbott, I. H. A. and Doenhoff, A. E. V. (1959). *Theory of wing sections : including a summary of airfoil data.* Dover Publications, New York.

Andersen, A., Pesavento, U., and Wang, Z. J. (2005a). Analysis of transitions between fluttering, tumbling and steady descent of falling cards. *Journal of Fluid Mechanics*, 541:91–104.

Andersen, A., Pesavento, U., and Wang, Z. J. (2005b). Unsteady aerodynamics of fluttering and tumbling plates. *Journal of Fluid Mechanics*, 541:65–90.

Anderson, M. L. and Cobb, R. G. (2014). Implementation of a Flapping Wing Micro Air Vehicle Control Technique. *Journal of Guidance, Control, and Dynamics*, 37(1):290–300.

Ansari, S., Zbikowski, R., and Knowles, K. (2006). Aerodynamic modelling of insect-like flapping flight for micro air vehicles. *Progress in Aerospace Sciences*, 42(2):129–172.

Armanini, S. F., Caetano, J. V., de Croon, G. C. H. E., de Visser, C. C., and Mulder, M. (2016a). Quasi-steady aerodynamic model of clap-and-fling flapping mav and validation using free-flight data. *Bioinspiration & Biomimetics*, 11(4):046002.

Armanini, S. F., Caetano, J. V., de Visser, C. C., de Croon, G. C. H. E., and Mulder, M. (2016b). Aerodynamic Model Identification of a Clap-and-Fling Flapping-Wing MAV: a Comparison between Quasi-Steady and Black-Box Approaches. In *AIAA Atmospheric Flight Mechanics Conference.*

Armanini, S. F., de Visser, C. C., de Croon, G. C. H. E., and Mulder, M. (2015). Time-Varying Model Identification of Flapping-Wing Vehicle Dynamics Using Flight Data. *Journal of Guidance, Control, and Dynamics*, 11(4).

Arora, N., Gupta, A., Sanghi, S., Aono, H., and Shyy, W. (2014). Lift-drag and flow structures associated with the clap and fling motion. *Physics of Fluids*, 26(7).

Baek, S. S. (2011). Autonomous ornithopter flight with sensor-based behavior. *Univ. California, Berkeley, Tech. Rep. UCB/EECS-2011-65.*

Baek, S. S., Bermudez, F. L., and Fearing, R. S. (2011). Flight control for target seeking by 13 gram ornithopter. In *IEEE Int. Conf. Intelligent Robots and Systems.*

Baek, S. S. and Fearing, R. S. (2010). Flight forces and altitude regulation of 12 gram i-bird. In *IEEE RAS and EMBS International Conference on Biomedical Robotics and Biomechatronics (BioRob)*, pages 454–460.

Bahill, A. T., Kallman, J. S., and Lieberman, J. E. (1982). Frequency Limitations of the Two-Point Central Difference Differentiation Algorithm. *Biological Cybernetics*, 4:1–4.

Baruh, H. (1999). *Analytical Dynamics*. McGraw-Hill Higher Education, New York, NY, first edition.

BBC (2015). Ten lost giants from earths past.

Bejgerowski, W., Ananthanarayanan, A., Mueller, D., and Gupta, S. K. (2009). Integrated product and process design for a flapping wing drive mechanism. *Journal of Mechanical Design*, 131(6):061006.

Bennett, L. (1977a). Clap and fling aerodynamics-an experimental evaluation. *Journal of Experimental Biology*, 69(1):261–272.

Bennett, L. (1977b). Clap and fling aerodynamics-an experimental evaluation. *Journal of Experimental Biology*, 69(1):261–272.

Berman, G. J. and Wang, Z. J. (2007). Energy-minimizing kinematics in hovering insect flight. *Journal of Fluid Mechanics*, 582:153–168.

Bevington, P. R. and Robinson, D. K. (2003). *Data Reduction and Error Analysis for the Physical Sciences*. McGraw-Hill, New York, NY, third edition. ISBN 0-07-247227-8.

Bohm, G. and Zech, G. (2010). *Introduction to Statistics and Data Analysis for Physicists*. DESY, 1 edition. ISBN: 3935702418.

Bolender, M. A. (2009). Rigid multi-body equations-of-motion for flapping wing MAVs using Kane equations. In *AIAA Guidance, Navigation, and Control Conference*, number 2009-6158.

Bomphrey, R. J., Lawson, N. J., Harding, N. J., Taylor, G. K., and Thomas, A. L. R. (2005). The aerodynamics of Manduca sexta: digital particle image velocimetry analysis of the leading-edge vortex. *The Journal of Experimental Biology*, 208(Pt 6):1079–94.

Box, G. E. P., Jenkins, G. M., and Reinsel, G. C. (2008). *Time Series Analysis: Forecasting and Control*. Wiley, fourth edition. ISBN 978-0-470-27284-8.

Brockwell, P. J. and Davis, R. A. (2006). *Time Series: Theory and Methods*. Springer, second edition. ISBN 0-387-97429-5.

Bruggeman, B. (2010). Improving flight performance of DelFly II in hover by improving wing design and driving mechanism. Master's thesis, Delft University of Technology, http://www.delfly.nl/?site=Publications&menu=&lang=en.

Caetano, J. V., Armanini, S. F., de Visser, C. C., de Croon, G. C. H. E., and Mulder, M. (2015a). Data-Informed Quasi-Steady Aerodynamic Model of a Clap-and-Fling Flapping Wing MAV. Bali, Indonesia. International Conference on Unmanned Intelligent Systems (ICIUS).

Caetano, J. V., de Visser, C. C., de Croon, G. C. H. E., and Mulder, M. (2015b). Effects of Eigenmodes, Forward Velocity and Flapping Frequency in Force Generation Mechanisms of a Flapping-Wing MAV. Bali, Indonesia. International Conference on Unmanned Intelligent Systems (ICIUS).

Caetano, J. V., de Visser, C. C., de Croon, G. C. H. E., Remes, B. D. W., de Wagter, C., Verboom, J. L., and Mulder, M. (2013a). Linear Aerodynamic Model Identification of a Flapping Wing MAV Based on Flight Test Data. *International Journal of Micro Air Vehicles*, 5(4):273–286.

Caetano, J. V., de Visser, C. C., Remes, B. D. W., de Wagter, C., and Mulder, M. (2013b). Controlled flight maneuvers of a Flapping Wing Micro Air Vehicle: a step towards the DelFly II Identification. In *AIAA Atmospheric Flight Mechanics Conference*, number 2013-4843.

Caetano, J. V., de Visser, C. C., Remes, B. D. W., de Wagter, C., and Mulder, M. (2013c). Modeling a Flapping Wing MAV: Flight Path Reconstruction of the DelFly II. In *AIAA Modeling and Simulation Technologies*, number 2013-4597.

Caetano, J. V., de Wagter, C., Ruijsink, R., Remes, B. D. W., Beran, P. S., and de Visser, C. C. (2016). Free-flight Data of a Flapping Wing Micro Air Vehicle for System Identification. *IEEE Transactions on Robotics*, (submitted).

Caetano, J. V., Percin, M., de Visser, C. C., van Oudheusden, B., de Croon, G., de Wagter, C., Remes, B. D. W., and Mulder, M. (2014a). Tethered vs. Free Flight Force Determination of the DelFly II Flapping Wing Micro Air Vehicle. In *International Conference on Unmanned Systems*, pages 842–847. IEEE.

Caetano, J. V., Percin, M., van Oudheusden, B. W., Remes, B. D. W., de Wagter, C., de Croon, G. C. H. E., and de Visser, C. C. (2015c). Error Analysis and Assessment of Unsteady Forces Acting on a Flapping Wing Micro Air Vehicle: Free-Flight versus Wind Tunnel Experimental Methods. *Bioinspiration & Biomimetics*, 10(5).

Caetano, J. V., Weehuizen, M. B., de Visser, C. C., de Croon, G. C. H. E., de Wagter, C., Remes, B. D. W., and Mulder, M. (2014b). Rigid vs. Flapping: The Effects of Kinematics Formulations in Force Determination of a Free Flying Flapping Wing Micro Air Vehicle. In *International Conference on Unmanned Systems*, pages 949 – 959. IEEE.

Caetano, J. V., Weehuizen, M. B., de Visser, C. C., de Croon, G. C. H. E., and Mulder, M. (2015d). Rigid-Body Kinematics Versus Flapping Kinematics of a Flapping Wing Micro Air Vehicle. *Journal of Guidance, Control and Dynamics*, 38(12).

Chirarattananon, P. and Wood, R. J. (2013). Identification of flight aerodynamics for flapping-wing microrobots. In *IEEE International Conference on Robotics and Automation (ICRA)*, pages 1381–1388. IEEE.

Cooter, R. J. and Baker, P. S. (1977). Weis-fogh clap and fling mechanism in locusta. *Nature*, 269(5623):53–54.

De Clercq, K. M. E., de Kat, R., Remes, B. D. W., van Oudheusden, B. W., and Bijl, H. (2009). Aerodynamic Experiments on DelFly II: Unsteady Lift Enhancement. *International Journal of Micro Air Vehicles*, 1(4):255–262.

de Croon, G. C. H. E., de Clercq, K., Ruijsink, R., Remes, B. D. W., and de Wagter, C. (2009). Design, aerodynamics, and vision-based control of the DelFly. *International Journal of Micro Air Vehicles*, 1(2):71–97.

de Croon, G. C. H. E., de Weerdt, E., de Wagter, C., Remes, B. D. W., and Ruijsink, R. (2012). The appearance variation cue for obstacle avoidance. *IEEE Transactions on Robotics*, 28(2):529–534.

de Croon, G. C. H. E., Groen, M. A., de Wagter, C., Remes, B. D. W., Ruijsink, R., and van Oudheusden, B. W. (2012). Design, aerodynamics and autonomy of the DelFly. *Bioinspiration & Biomimetics*, 7(2):025003.

de Visser, C. C., Chu, Q., and Mulder, J. A. (2009). A new approach to linear regression with multivariate splines. *Automatica*, 42(12):2903–2909.

Demoll, R. (1919). Zuschriften an die Herausgeber. Der Flug der Insekten und der Vogel. *Die Naturwissenschaften*, 27:480–482.

Deng, S., Percin, M., van Oudheusden, B., Remes, B., and Bijl, H. (2014). Experimental investigation on the aerodynamics of a bio-inspired flexible flapping wing micro air vehicle. *International Journal of Micro Air Vehicles*, 6(2):105–116.

Dickinson, M. H., Lehmann, F.-O., and Sane, S. P. (1999). Wing Rotation and the Aerodynamic Basis of Insect Flight. *Science*, 284(5422):1954–1960.

Dietl, J. M. and Garcia, E. (2008). Stability in ornithopter longitudinal flight dynamics. *Journal of Guidance, Control and Dynamics*, 31(4):1157–1162.

Dietl, J. M. and Garcia, E. (2013). Ornithopter optimal trajectory control. *Aerospace Science and Technology*, 26:192–199.

Dietl, J. M., Herrmann, T., Reich, G., and Garcia, E. (2011). Dynamic modeling, testing, and stability analysis of an ornithoptic blimp. *Journal of Bionic Engineering*, 8(4):375–386.

Dudley, R. (2000). *The Biomechanics of Insect Flight: Form, Function, Evolution.* Princeton University Press. ISBN: 9780691094915.

Edwards, R. H. and Cheng, H. K. (1982). The separation vortex in the weis-fogh circulation-generation mechanism. *Journal of Fluid Mechanics*, 120:463–473.

Ellington, C. P. (1978). *The aerodynamics of normal hovering flight: three approaches.* Cambridge University Press.

Ellington, C. P. (1984a). The aerodynamics of hovering insect flight. i. the quasi-steady analysis. *Philosophical Transactions of the Royal Society of London. B, Biological Sciences*, 305(1122):1–15.

Ellington, C. P. (1984b). The aerodynamics of hovering insect flight. iii. kinematics. *Philosophical Transactions of the Royal Society of London. Series B, Biological Sciences*, 305(1122):41–78.

Ellington, C. P. (1984c). The aerodynamics of hovering insect flight. iv. aeorodynamic mechanisms. *Philosophical Transactions of the Royal Society of London. Series B, Biological Sciences*, 305(1122):79–113.

Ellington, C. P. (1984d). The aerodynamics of hovering insect flight II. Morphological Parameters. *Philosophical Transactions of the Royal Society of London. Series B, Biological Sciences*, 305(1122):17–40.

Ellington, C. P. (1984e). The aerodynamics of hovering insect flight V. A Vortex Theory. *Philosophical Transactions of the Royal Society of London. Series B, Biological Sciences*, 305(1122):115–144.

Ellington, C. P. (1999). The Novel Aerodynamics of Insect Flight: Applications to Micro-Air Vehicles. *Journal of Experimental Biology*, 202:3439–3448.

Ellington, C. P., van den Berg, C., Willmott, A., and Thomas, A. (1996). Leading-edge vortices in insect flight. *Nature*, 384(19/26):626–630.

Etkin, B. and Reid, L. D. (1996). *Dynamics of Flight: Stability and Control.* Jonh Wiley & Sons, Inc., 3rd edition.

Fearing, R., Chiang, K., Dickinson, M., Pick, D., Sitti, M., and Yan, J. (2000). Wing transmission for a micromechanical flying insect. In *Proceedings of IEEE International Conference on Robotics & Automation*, pages 1509–1516, San Francisco. IEEE.

Festo (2013). Festo fwmav. online. accessed: 21 May 2016.

Gebert, G. and Gallmeier, P. (2002). Equations of motion for flapping flight. In *AIAA Atmospheric Flight Mechanics Conference and Exhibit*, number 2002-4872.

Gogulapati, A. and Friedmann, P. (2011). Approximate aerodynamic and aeroelastic modeling of flapping wings in hover and forward flight. In *AIAA Structures, Structural Dynamics and Materials Conference*, number 2011-2008, Denver, Colorado, USA. AIAA.

Grauer, J., Ulrich, E., Jr., J. H., Pines, D., , and Humbert, J. S. (2011). Testing and system identification of an ornithopter in longitudinal flight. *Journal of Aircraft*, 48(2):660–667.

Grauer, J., Ulrich, E., Jr., J. H., Pines, D., and Humbert, J. S. (2010). System identification of an ornithopter aerodynamic model. In *AIAA Atmospheric Flight Mechanics Conference*, number 2010-7632.

Graves, R. (1955). *The Greek Myths. ISBN 0-14-007602-6.*, volume 92 - Daedalus and Talus. Penguin Books. ISBN 0-14-007602-6.

Groen, M. (2010). PIV and force measurements on the flapping-wing MAV DelFly II. Master's thesis, Delft University of Technology.

Groen, M., Bruggeman, B., Remes, B., Ruijsink, R., van Oudheusden, B., and Bijl, H. (2010). Improving flight performance of the flapping wing MAV DelFly II. In *International Competition and Conference on Micro Air Vehicles*. IMAV.

Guinness Book of Records (2008). The smallest camera plane. http://www.guinnessworldrecords.com/world-records/7000/smallest-camera-plane.

Hedenstrom, A. and Johansson, L. C. (2015). Bat flight aerodynamics, kinematics and flight morphology. *Journal of Experimental Biology*, 218(5):653–663.

Henningsson, P. and Bomphrey, R. J. (2011). Time-varying span efficiency through the wingbeat of desert locusts. *Journal of The Royal Society Interface*.

Hines, L., Campolo, D., and Sitti, M. (2014). Liftoff of a motor-driven, flapping-wing microaerial vehicle capable of resonance. *IEEE Transactions on Robotics*, 30(1):220–232.

Hines, L. L., Arabagi, V., and Sitti, M. (2011). Free flight simulations and pitch and roll control experiments of a sub-gram flapping-flight micro aerial vehicle. In *Proceedings - IEEE International Conference on Robotics and Automation*, Shanghai, China.

Hsiao, F. Y., Yang, T. M., and Lu, W. C. (2012). Dynamics of flapping-wing MAVs: Application to the tamkang golden snitch. *Journal of Applied Science and Engineering*, 15(3):227–238.

Jategaonkar, R. (1997). Art and science of system identification. Techreport, DLR.

Jategaonkar, R. (2006). *Flight Vehicle System Identification A Time Domain Methodology*. AIAA Progress in Astronautics and Aeronautics, Reston, VA, USA.

Jones, R. (1939). The unsteady lift of a finite wing. Technical Report 682, NACA, January.

Jones, R. (1940). The unsteady lift of a wing of finite aspect ratio. Technical Report 681, NACA.

Kang, C., Aono, H., and Cesnik, C. E. (2011). Effects of flexibility on the aerodynamic performance of flapping wings. In *6th AIAA Theoretical Fluid Mechanics Conference*, number 2011-3121, Hawaii. AIAA.

Karasek, M., Hua, A., Nan, Y., Lalami, M., and Preumont, A. (2014). Pitch and roll control mechanism for a hovering flapping wing mav. *International Journal of Micro Air Vehicles*, 6(4):253–264.

Kawamura, Y., Souda, S., Nishimoto, S., and Ellington, C. (2008). Clapping-wing micro air vehicle of insect size. In Kato, N. and Kamimura, S., editors, *Bio-mechanisms of Swimming and Flying*, pages 319–330. Springer Japan.

Keennon, M., Klingebiel, K., and Won, H. (2012). Development of the nano hummingbird: A tailless flapping wing micro air vehicle. In *50TH AIAA Aerospace Sciences Meeting incl. New Horizons Forum and Aerospace Exposition*, number AIAA 2012-0588, pages 1–24.

Keshavan, J. and Wereley, N. M. (2007). Design and development of a high frequency biologically inspired flapping wing mechanism. In *48th AIAA/ASME/ASCE/AHS/ASC Structures, Structural Dynamics, and Materials Conference, Structures, Structural Dynamics, and Materials Conference*, number 2007-1789. University of Maryland, AIAA.

Khan, Z. A. and Agrawal, S. K. (2005). Wing Force and Moment Characterization of Flapping Wings for Micro Air Vehicle Application. In *Proceedings of the American Control Conference*, volume 3, pages 1515–1520. IEEE.

Kim, D.-K., Lee, J.-S., Lee, J.-Y., and Han, J.-H. (2008). An aeroelastic analysis of a flexible flapping wing using modified strip theory. In *Proceedings SPIE 6928, Active and Passive Smart Structures and Integrated Systems*, volume 6928. SPIE.

Kim, J. H., Park, C. Y., Jun, S., Chung, D. K., Kim, J. R., Hwang, H. C., Stanford, B., Beran, P., Parker, G., and Mrozinski, D. (2012). Flight test measurement and assessment of a flapping micro air vehicle. *International Journal of Aeronautical and Space Sciences*, 13(2):238–249.

Klein, V. and Morelli, E. A. (2006). *Aircraft System Identification: Theory And Practice*. AIAA Education Series, Reston, VA.

Kolomenskiy, D., Moffatt, H. K., Farge, M., and Schneider, K. (2011). The Lighthill-Weis-Fogh clap-fling-sweep mechanism revisited. *Journal of Fluid Mechanics*, 676:572–606.

Korotkin, A. I. (2009). *Added Masses of Ship Structures*, volume 1 of *88*. Springer Netherlands, 1 edition.

Kramer, M. (1932). Die Zunahme des Maximalauftriebes von Tragflugeln bei plotzlicher Anstellwinkelvergrosserung (Boeneffekt). *Z. Flugtech Motorluftschiff*, 23:185–189.

Laboratory, U. S. A. F. R. (2015). Micro air vehicle integration and application research institute laboratory training plan. Technical Report 88ABW-2015-0842, AFRL.

Lapa, A. (1928). *Aviacao Portuguesa*. Libanio da Silva, Lisbon.

Lee, J.-S. and Han, J.-H. (2012). Experimental study on the flight dynamics of a bio-inspired ornithopter: free flight testing and wind tunnel testing. *Journal of Smart Materials and Structures*, 21.

Lehmann, F.-O. (2007). When wings touch wakes: understanding locomotor force control by wake–wing interference in insect wings. *Journal of Experimental Biology*, 211(2):224–233.

Lehmann, F.-O. and Pick, S. (2007). The aerodynamic benefit of wing–wing interaction depends on stroke trajectory in flapping insect wings. *Journal of Experimental Biology*, 210(8):1362–1377.

Lehmann, F.-O., Sane, S. P., and Dickinson, M. (2005). The aerodynamic effects of wing–wing interaction in flapping insect wings. *Journal of Experimental Biology*, 208(16):3075–3092.

Lentink, D. and Dickinson, M. H. (2009). Rotational accelerations stabilize leading edge vortices on revolving fly wings. *Journal of Experimental Biology*, 212(16):2705–2719.

Lighthill, M. J. (1973). On the weis-fogh mechanism of lift generation. *Journal of Fluid Mechanics*, 60:1–17.

Lim, G., Shkarayev, S., Goff, Z., and Beran, P. (2012). Studies of flight kinematics of ornithopters. In *International Competition and Conference on Micro Air Vehicles*. IMAV 2012.

Lin, C.-S., Hwu, C., and Young, W.-B. (2006). The Thrust and Lift of an Ornithopter's Membrane Wings with Simple Flapping Motion. *Aerospace Science and Technology*, 10(2):111–119.

Ma, K., Chirarattananon, P., Fuller, S. B., and Wood, R. J. (2013). Controlled flight of a biologically inspired, insect-scale robot. *Science*, 340(6132):603–607.

Malne, R. E. and Iliff, L. W. (1986). Agard flight test techniques series identification of dynamic systems - appliatons to aircraft part 1: The output error approach. Printed.

Malolan, V., Dineshkumar, M., and Baskar, V. (2004). Design and development of flapping wing micro air vehicle. In *42nd AIAA Aerospace Sciences Meeting and Exhibit, 5 - 8 January, Reno, Nevada*.

Maniar, G., Randall, R., Shkarayev, S., Goff, Z., and Beran, P. (2012). Kinematics of free-flight ornithopters. In *AIAA Aerospace Sciences Meeting including the New Horizons Forum and Aerospace Exposition*, number 2012-0666. AIAA.

Mao, S. and Xin, Y. (2003). Flows around two airfoils performing "fling and subsequent translation" and "translation and subsequent clap". *Acta Mechanica Sinica*, 19(2):103–117.

Marble, A. E., Member, S., and Intyre, C. M. M. C. (1981). Comparison of Digital Algorithms Used in Computing the Derivative of Left Ventricular Pressure. (7):524–529.

Mazaheri, K. and Ebrahimi, A. (2011). Experimental investigation on aerodynamic performance of a flapping wing vehicle in forward flight. *Journal of Fluids and Structures*, 27(4):586–595.

Mettler, B. F. (2010). Extracting micro air vehicles aerodynamic forces and coefficients in free flight using visual motion tracking techniques. *Exp. Fluids*, 49:557–569.

Miller, L. A. and Peskin, C. S. (2005). A computational fluid dynamics of 'clap and fling' in the smallest insects. *Journal of Experimental Biology*, 208(2):195–212.

Miller, L. A. and Peskin, C. S. (2009). Flexible clap and fling in tiny insect flight. *Journal of Experimental Biology*, 212(19):3076–3090.

Mueller, T. J. (2001). *Fixed and Flapping Wing Aerodynamics for Micro Air Vehicle Applications*. American Institute of Aeronautics and Astronautics. Print ISBN 978-1-56347-517-7.

Muniappan, A., Baskarand, V., and Duriyanandhan, V. (2005). Lift and thrust characteristics of flapping wing micro air vehicle (mav). In *43rd AIAA Aerospace Sciences Meeting and Exhibit - Meeting Papers*. AIAA.

Nachtigall, W.and Rothe, H. (1982). Nachweis eines „clap-and-fling-Mechanismus“ bei der im Windkanal fliegenden Haustaube. *J. Ornithol.*, 123(4):439–443.

Nagai, H., Isogai, K., Fujimoto, T., and Hayase, T. (2009). Experimental and numerical study of forward flight aerodynamics of insect flapping wing. *AIAA Journal*, 47(3):730–742.

Nakata, T., Liu, H., and Bomphrey, R. J. (2015). A cfd-informed quasi-steady model of flapping-wing aerodynamics. *Journal of Fluid Mechanics*, 783:323–343.

Nakata, T., Liu, H., Tanaka, Y., Nishihashi, N., Wang, X., and Sato, A. (2011). Aerodynamics of a bio-inspired flexible flapping-wing micro air vehicle. *Bioinspiration & Biomimetics*, 6.

Nguyen, Q.-V., Chan, W. L., and Debiasi, M. (2014). Design, Fabrication, and Performance Test of a Hovering-Based Flapping-Wing Micro Air Vehicle Capable of Sustained and Controlled Flight. In *International Micro Air Vehicle Conference and Competition*, Delft, The Netherlands.

Nguyen, Q.-V., Chan, W. L., and Debiasi, M. (2015). An insect-inspired flapping wing micro air vehicle with double wing clap-fling effects and capability of sustained hovering. In *SPIE Proceedings Bioinspiration, Biomimetics and Bioreplication*, volume 9429, pages 94290U–94290U–11. SPIE.

Nguyen, Q. V., Truong, Q. T., Park, H. C., Goo, N. S., and Byun, D. (2010). Measurement of Force Produced by an Insect-Mimicking Flapping-Wing System. *Journal of Bionic Engineering*, 7:S94–S102.

Noda, R., Nakata, T., and Liu, H. (2014). Effects of wing deformation on aerodynamic performance of a revolving insect wing. *Acta Mechanica Sinica*, 30(6):819–827.

Norberg, R. A. (1972a). Flight characteristics of two plume moths, alucita pentadacty/a l. and orneodes hexadactyla l. (microlepidoptera). *Zoologica Scripta*, 1(5):241–246.

Norberg, R. A. (1972b). The pterostigma of insect wings an inertial regulator of wing pitch. *Journal of Comparative Physiology*, 81(1):9–22.

Norberg, R. Å. (1975). *Swimming and Flying in Nature: Volume 2*, chapter Hovering Flight of the Dragonfly Aeschna Juncea L., Kinematics and Aerodynamics, pages 763–781. Springer US, Boston, MA.

Noyon, T. A., Tay, W. B., van Oudheusden, B., and H., B. (2014). Effect of chordwise deformation on unsteady aerodynamic mechanisms in hovering flapping flight. *International Journal of Micro Air Vehicles*, 6:265–277.

Oppenheimer, M. W., Doman, D. B., and Sigthorsson, D. O. (2011). Dynamics and Control of a Biomimetic Vehicle Using Biased Wingbeat Forcing Functions. *Journal of Guidance, Control, and Dynamics*, 34(1):204–217.

Orlowski, C. T. and Girard, A. R. (2011). Modeling and simulation of nonlinear dynamics of flapping wing micro air vehicles. *AIAA Journal*, 49(5):969–981.

Orlowski, C. T., Girard, A. R., and Shyy, W. (2010). Four wing flapping micro air vehicles - dragonfies or X-wings? In *AIAA Guidance, Navigation, and Control Conference*, number AIAA 2010-7707, Toronto, Ontario, Canada.

Percin, M., Eisma, H., van Oudheusden, B., Remes, B., Ruijsink, R., and de Wagter, C. (2012a). Flow Visualization in the Wake of the Flapping-Wing MAV 'DelFly II' in Forward Flight. In *AIAA Applied Aerodynamics Conference*. AIAA.

Percin, M., Eisma, H. E., de Baar, J. H. S., van Oudheusden, B. W., Remes, B., Ruijsink, R., and de Wagter, C. (2012b). Wake reconstruction of flapping-wing MAV DelFly II in forward flight. In *International Micro Air Vehicle Conference and Flight Competition, July 2012, Braunschweig, Germany.*

Percin, M., Hu, Y., van Oudheusden, B., Remes, B., and Scarano, F. (2011). Wing flexibility effects in clap-and-fling. *International Journal of Micro Air Vehicles*, 3:217–227.

Percin, M. and van Oudheusden, B. (2015). Three-dimensional flow structures and unsteady forces on pitching and surging revolving flat plates. *Experiments in Fluids*, 56(2).

Percin, M., van Oudheusden, B., Eisma, H., and Remes, B. (2014). Three-dimensional vortex wake structure of a flapping-wing micro aerial vehicle in forward flight configuration. *Experiments in Fluids*, 55(9).

Pesavento, U. and Wang, Z. J. (2004). Falling paper: Navier-stokes solutions, model of fluid forces, and center of mass elevation. *Physical Review Letters*, 93(14):144501–1 – 144501–4. The American Physical Society.

Peters, D. (2008). Two-dimensional incompressible unsteady airfoil theory - an overview. *Journal of Fluids and Structures*, 24:295–312.

Pfeiffer, A. T., Lee, J.-S., Han, J.-H., and Baier, H. (2010). Ornithopter Flight Simulation Based on Flexible Multi-Body Dynamics. *Journal of Bionic Engineering*, 7(1):102–111.

Phillips, W. F., Hailey, C. E., and Gebert, G. a. (2001). Review of Attitude Representations Used for Aircraft Kinematics. *Journal of Aircraft*, 38(4):718–737.

Polhamus, E. C. (1971). Predictions of vortex-lift characteristics by a leading-edge suctionanalogy. *Journal of Aircraft*, 8(4):193–199.

Pornsin-sirirak, T. N., Tai, Y. C., Ho, C. M., and Keennon, M. (2001). Microbat: A palm-sized electrically powered ornithopter. In *Proceedings of NASA/JPL Workshop on Biomorphic Robotics*, pages 14–17.

Prosser, D. (2011). Flapping wing design for a dragonfly-like micro air vehicle. Master's thesis, Rochester Institute of Technology. Accessed from http://scholarworks.rit.edu/theses/5804.

Randall, R., Kumar, R., and Shkarayev, S. (2012). Bio-inspired design of micro ornithopters with emphasis on locust hindwings. In *International Competition and Conference on Micro Air Vehicles, IMAV 2012*. IMAV.

Rayner, J. M. V. (1979a). A vortex theory of animal flight. part 1. the vortex wake of a hovering animal. *Journal of Fluid Mechanics*, 91:697–730.

Rayner, J. M. V. (1979b). A vortex theory of animal flight. part 2. the forward flight of birds. *Journal of Fluid Mechanics*, 91:731–763.

Reissner, E. and Stevens, J. E. (1947a). Effect of finite span on the air load distributions for oscillating wings i aerodynamic theory of oscillating wings of finite spans. Technical Report 1194, NACA.

Reissner, E. and Stevens, J. E. (1947b). Effect of finite span on the air load distributions for oscillating wings ii methods of calculation and examples of application. Technical Report 1195, NACA.

Rose, C. and Fearing, R. S. (2014). Comparison of ornithopter wind tunnel force measurements with free flight. In *2014 IEEE International Conference on Robotics & Automation (ICRA)*, pages 1816–1821. IEEE.

Sane, S. P. (2003). The aerodynamics of insect flight. *Journal of Experimental Biology*, 206(23):4191–4208.

Sane, S. P. (2011). Steady or unsteady? uncovering the aerodynamic mechanisms of insect flight. *Journal of Experimental Biology*, 214(3):349–351.

Sane, S. P. and Dickinson, M. H. (2001). The control of flight force by a flapping wing: lift and drag production. *The Journal of Experimental Biology*, 2626:2607–2626.

Sane, S. P. and Dickinson, M. H. (2002). The aerodynamic effects of wing rotation and a revised quasi-steady model of flapping flight. *The Journal of Experimental Biology*, 205(Pt 8):1087–96.

Shalizi, C. R. (2013). *Advanced Data Analysis from an Elementary Point of View*. Cambridge University Press.

Shkarayev, S. and Maniar, G. (2012). Experimental and computational modeling of the kinematics and aerodynamics of membrane flapping wings. In *50th AIAA Aerospace Sciences Meeting including the New Horizons Forum and Aerospace Exposition*, number 2012-1208, Nasville, Tennessee. AIAA.

Spedding, G. R. and Maxworthy, T. (1986). The generation of circulation and lift in a rigid two-dimensional fling. *Journal of Fluid Mechanics*, 165:247–272.

Stevens, B. L. and Lewis, F. L. (2003). *Aircraft Control and Simulation.* Jonh Wiley & Sons, Inc., 2 edition. p. 110.

Su, W. and Cesnik, C. (2010). Nonlinear aeroelastic simulations of a flapping wing micro air vehicle using two unsteady aerodynamic formulations.

Sun, M. and Tang, J. (2002). Unsteady aerodynamic force generation by a model fruit fly wing in flapping motion. *Journal of Experimental Biology*, 205(1):55–70.

Sunada, S., Kawachi, K., Watanabe, I., and Azuma, A. (1993). Fundamental analysis of three-dimensional 'near fling'. *Journal of Experimental Biology*, 183(1):217–248.

Taha, H. E., Hajj, M. R., and Beran, P. S. (2014). State-space representation of the unsteady aerodynamics of flapping flight. *Aerospace Science and Technology*, 34:1–11.

Taha, H. E., Hajj, M. R., and Nayfeh, A. H. (2012). Flight dynamics and control of flapping-wing MAVs: a review. *Nonlinear Dynamics*, 70:907–939.

Tay, W. B., van Oudheusden, B. W., and Bijl, H. (2015). Numerical simulation of a flapping four-wing micro-aerial vehicle. *Journal of Fluids and Structures*, 55:237–261.

Taylor, G. K. and Thomas, A. L. R. (2003). Dynamic flight stability in the desert locust schistocerca gregaria. *The Journal of Experimental Biology*, 206(16):2803–2829.

Theodorsen, T. (1935). General theory of aerodynamic instability and the mechanism of flutter. Technical Report 496, NACA.

Tijmons, S., de Croon, G., Remes, B., De Wagter, C., Ruijsink, R., van Kampen, E.-J., and Chu, Q. (2013). Stereo vision based obstacle avoidance on flapping wing mavs. In Chu, Q., Mulder, B., Choukroun, D., van Kampen, E.-J., de Visser, C., and Looye, G., editors, *Advances in Aerospace Guidance, Navigation and Control*, pages 463–482. Springer Berlin Heidelberg.

van den Berg, C. and Ellington, C. P. (1997). The three dimensional leading edge vortex of a hovering model hawkmoth. *Philosophical Transactions of the Royal Society of London B: Biological Sciences*, 352(1351):329–340.

van den Berg, C. and Rayner, J. M. (1995). The moment of inertia of bird wings and the inertial power requirement for flapping flight. *The Journal of Experimental Biology*, 198 (8):1655–1664.

Verboom, J. L., Tijmons, S., De Wagter, C., Remes, B., Babuska, R., and de Croon, G. C. H. E. (2015). Attitude and altitude estimation and control on board a flapping wing micro air vehicle. In *2015 IEEE International Conference on Robotics and Automation*, pages 5846–5851. IEEE.

Wagner, H. (1925). *Uber die Entstehung des dynamischen Auftriebes von Tragflugeln.* VDI-Verl.

Wang, C. and Eldredge, J. (2013). Low-order phenomenological modeling of leading-edge vortex formation. *Theoretical and Computational Fluid Dynamics*, 27(5):577–598.

Wang, Z. J. (2000). Two dimensional mechanism for insect hovering. *Physical Review Letters*, 85:2219–2219.

Wang, Z. J. (2005). Dissecting insect flight. *Annual Rev. Fluid Mechanics*, 37:183–210.

Weis-Fogh, T. (1972). Energetics of hovering flight in hummingbirds and in drosophila. *Journal of Experimental Biology*, 56:79–104.

Weis-Fogh, T. (1973). Quick estimates of flight fitness in hovering animals, including novel mechanisms for lift production. *Journal of Experimental Biology*, 59:169–230.

Weis-Fogh, T. (1975). *Flapping flight and power in birds and insects, conventional and novel mechanisms*, volume 2. Springer US.

Whitney, J. P. and Wood, R. J. (2010). Aeromechanics of passive rotation in flapping flight. *Journal of Fluid Mechanics*, 660:197–220.

Wood, J. (1970). A Study of the Instantaneous Air Velocities in a Plane behind the Wings of Certain Diptera Flying in a Wind Tunnel. *Journal of Experimental Biology*, 52(1):17–25.

Wood, J. (1972). An Experimental Determination of the Relationship between Lift and Aerodynamic Power in Calliphora Erythrocephala and Phormia Regina. *Journal of Experimental Biology*, 56(1):31–36.

Wood, R. J. (2008). The first takeoff of a biologically-inspired at-scale robotic insect. *IEEE Tranactions on Robotics*, 24(2):341–347.

WSU (2012). Wright State University Center for Excellence in Micro Air Vehicle Research. `http://cecs.wright.edu/mav/`.

Wu, J. C. and Hu-Chen, H. (1984). Unsteady aerodynamics of articulate lifting bodies. In *2nd Applied Aerodynamics Conference, Fluid Dynamics and Co-located Conferences*.

Zbikowski, R. (2002). On aerodynamic modelling of an insect like flapping wing in hover for micro air vehicles. *Philosophical Transactions of the Royal Society of London A: Mathematical, Physical and Engineering Sciences*, 360(1791):273–290.

Zheng, L., Hedrick, T., and Mittal, R. (2013). A comparative study of the hovering efficiency of flapping and revolving wings. *Bioinspiration & Biomimetics*, 8(3):036001.

ACKNOWLEDGMENTS

The last four years will be kept in my memory as some of the most rewarding and enthusiastic years of my life. Pursuing a Ph.D. degree at Delft University of Technology has allowed me to experience life in the Netherlands, be part of the Dutch culture and, above it all, gain profound scientific knowledge in the areas of flapping wing micro aerial vehicles and system identification in one of the best Universities in the world. Despite the fact that this research was carried by myself, over the course of 4 years, its impact and relevance to the scientific community was more pronounced due to the contributions of inspiring people who have guided, motivated and inspired me.

I would like to express my highest gratitude and respect to my promotor, Prof. Dr. ir. Max Mulder, for the unconditional support and motivation, since the first day. You have been inspirational and highly motivational. I will never forget your words, wise advices and passionate discussions, that always made me feel happy about the results and conclusions of the research and made me feel capable of being a better researcher. Additionally, I thank you for the challenging scientific discussions, that allowed me to consider new perspectives and approaches to the research. More importantly, you were by my side during this journey, not only during the time I was in Delft, but also the long periods I spend in Portugal. Thank you.

It is with great pleasure that I address the following words of appreciation to my co-promotor, Dr. ir. Coen de Visser. Not only were you always available for challenging and productive scientific discussions, but you went above your duties, outside of your office hours and professional goals to support and guide me throughout the dissertation. Almost like a good premonition, we first met when I was sitting on what would be your office, when you returned to TUDelft. Ever since then, you have demonstrated to be one of the most inspirational people one person can meet. Thanks to your profound scientific knowledge and elevated emotional intelligence you were always able to ask the best questions and transmit the highest level of confidence in my research. I will forever be grateful for your time, teachings, words and motivation.

I would also like to express my gratitude and appreciation to my daily advisor, Dr. Guido C. H. E. de Croon, for your teachings and orientation. You were always present when needed, and have further motivated me to supersede myself, both at a scientific and writing level. You are a fantastic advisor and your advising skills are proven in the large number of high impact scientific publications that stem from your guidance.

A special word to ir. Bart Remes, ir. Christophe de Wagter, and ir. Rick Ruijsink for your support over the course of the entire research. Your knowledge and innovative thinking have molded the technology implemented on the DelFly, making it possible to perform the calibrated maneuvers for system identification purposes, which were at the core of the research.

A profound thank you to the Portuguese Fundação para a Ciência e Tecnologia for the grant SFRH/ BD / 80374 / 2011, without which it would not have been possible.

A special thank you to the Portuguese Air Force Academy Major General Serôdio Fernandes and Major General Joaquim Borrego for the opportunity of perusing the Ph.D. research abroad and for allowing me to dedicate two and a half years to this project.

A warm appreciation to Coronel António Costa, Coronel José Santiago, Coronel Armando Barros, Lieutenant Coronel Maria Matos for the unconditional support, wise words and motivation. It has been great to be commanded by you. You have shown the ability to motivate and appreciate your subordinates and are, without doubt, fantastic Officers of the Portuguese Air Force.

A special and particular word of appreciation to Coronel José Morgado, Lieutenant Coronel Maria Nunes, Major Aurélio Santos, Major Carlos Silva, Major Paula Gonçalves, Captain Tiago Oliveira, Captain Gonçalo Cruz for, not only, having assured my duties during the time I was away from Portugal, but most importantly for the excellent work they have developed, pushing the borders of research in Unmanned Aerial Systems at the Portuguese Air Force.

To Captain Luis Pereira, who joined me on this adventure in Delft and witnessed the intensity of the work. Thank you for your support, motivation and help. You were always present when needed and always had excellent suggestions, not only for the Ph.D. dissertations, but also for life.

To Mustafa Perçin, who is one of the best researchers I ever came across, for the interesting discussions and support throughout the project. More importantly, thank you for the teachings, wonderful menus and contact you provided me with the Turkish culture, as well as for helping me in those constant house changes.

Jaime, Tommaso, Sophie, Jan Comans, Jan Smisek, Daan, Dyah, Maarten, Rolf, Matěj, Kirk, Sjoerd, Peng, you have been a fantastic and *gezellig* group of friends who I look up to very much. The times we spent together were absolutely remarkable and will, forever, be kept in my memory and heart. Thank you for your help, motivation and constant good mood, transmitting the best work 'athmosphere' one could long for.

To Mafalda, Milene, Saumya, Nicoletta, Amber, Raj, Rúben, René, Bob and Iñigo for welcoming me in your fantastic group, as well as for the marvelous and *gezellig* moments we shared together, between Royal parties, Wonderlands, Austrian endeavors and growing families.

Thank you to Guida, Bas, Tomás, Emílio, Rosa Ana, Vicente, Paula, Ana, Sofia, Ricardo, Francisco, Duarte, Cristiane, Paul, Teresa, Gabriel, Sandra, Miguel, Francisco, Pedro, Christa, Ralph, Benjamin, Christian, Maya, Gregor, Peter and Mark for being such wonderful, amusing and supportive friends. You have changed our feeling towards the experience of living abroad and have marked our lives forever, in the best way possible.

To Luis Levy Lima, one of the greatest artists I know, for all the cheerful and enthusiastic comments and for the cover designs.

Saving the best for last, I address the following words to Christoph, Claire, Aurelia and Harald Kofler. You have been the most fantastic serendipity I have ever experienced. I cannot put in words how much you mean to me and Susana. You have showed me (us) real love and have made us a part of your family. We will forever long to be with you and will always keep you in our hearts. To CK, I dedicate this dissertation to you, for your support, motivation and for always cheering me and making me believe that it would be possible. You are the best younger brother one can have.

Family is the best and most treasured value one can have. Family reminds you of what is important, cheers you, loves you and supports you unconditionally. My family has done that and much more. To my Mother Estela, my father José, my Sister Carina and Nephew Bernardo I address my deepest, caring and loving appreciation to what you have done for me. This dissertation is the culmination of all the support, unconditional love and personal investment you put in me. This dissertation has made it all make sense. Thank you, I love you.

My biggest, most profound and felt words of appreciation are to my, soon-to-be, wife, Susana. You are, beyond doubt, the most well intentioned, heart-loving, comprehensive and motivational – in short, best – person I know. You inspire me every day to be better, to be kinder, to love more and to live more. As expressed in the beginning of this book, I dedicate this dissertation to You, Susana, since it is my strongest belief that I would not have done it without you – I love you.

CURRICULUM VITÆ

14.05.1984	Born in Funchal, Madeira, Portugal.

EDUCATION

2012–2016	Ph.D., Aerospace Engineering Delft University of Technology, Delft, The Netherlands
2015	Unmanned Aerial System Operator Course
2009–2010	M.Sc., Aeronautical Engineering Portuguese Air Force Academy, Sintra, Portugal
2011	Commanding Officer Course, Air Force
2010	2010: Systems Engineering Course, Oporto University

PROFESSIONAL EXPERIENCE

2008–present	Portuguese Air Force Research Center UAV developer and operator, Sintra, Portugal
2012–2016	Delft University of Technology Ph.D. Researcher, Delft, The Netherlands
2009–2013	Northern Atlantic Treaty Organization Researcher for NATO Research and Technology Organization in Unmanned Aerial Systems, Worldwide
2010–2012	Superior Institute of Education and Sciences Invited Lecturer, Lisbon, Portugal
2008	Directorate for Maintenance of Weapons Systems Junior Manager of F-16 Fighter Engine fleet, Lisbon, Portugal

Honors and Awards

2015	Best Scientific Article in International Conference on Unmanned Intelligent Systems
2012	Medal of Exceptional Service
2011	FCT Doctoral Fellow in Flapping Wing MAV Modeling
2003-2005	Student of the Year, Best Overall Student Portuguese Air Force Academy
2002	Student of the year, Madeira Island Best Overall Student 3^{rd} place – 9.6 / 10

LIST OF PUBLICATIONS

JOURNALS

6. **Caetano, J. V.**, de Wagter, C., Ruijsink, R., Remes, B., de Visser, C.C., Beran, P., and de Croon, G.C.H.E. (2016). Free-flight data of a Flapping-Wing Micro Air Vehicle for System Identification. *IEEE Transactions on Robotics*, (submitted).

5. Armanini, S.F., **Caetano, J.V.**, de Croon, G.C.H.E., de Visser, C.C., and Mulder, M. (2016a). Quasi-steady aerodynamic model of clap-and-fling flapping MAV and validation using free-flight data. *Bioinspiration & Biomimetics*, 11(4):046002.

4. **Caetano, J. V.**, Percin, M., van Oudheusden, B. W., Remes, B. D. W., de Wagter, C., de Croon, G.C.H.E., and de Visser, C.C. (2015c). Error analysis and assessment of unsteady forces acting on a flapping wing micro air vehicle: Free-flight versus wind tunnel experimental methods. *Bioinspiration & Biomimetics*, 10(5).

3. **Caetano, J. V.**, Weehuizen, M. B., de Visser, C. C., de Croon, G.C.H.E., and Mulder, M. (2015d). Rigid-Body Kinematics Versus Flapping Kinematics of a Flapping Wing Micro Air Vehicle. *Journal of Guidance, Control and Dynamics*, 38(12).

2. **Caetano, J. V.**, de Visser, C. C., de Croon, G. C. H. E., Remes, B., de Wagter, C., Verboom, J. L., and Mulder, M. (2013a). Linear Aerodynamic Model Identification of a Flapping-Wing MAV Based on Flight Test Data. *International Journal of Micro Air Vehicles*, 5(4):273–286.

1. Matos,M. d.M., **Caetano, J. V.**, Morgado, J. A. P., and Sousa, J. B. d. (2015). *From Research to Operations: The PITVANT UAS Training Experience*, pages 2525–2560. Chapter Handbook of Unmanned Aerial Vehicles. Springer Netherlands, Dordrecht.

CONFERENCE PROCEEDINGS

9. Armanini, S. F., **Caetano, J. V.**, de Visser, C. C., de Croon, G. C. H. E., and Mulder, M. (2016b). Aerodynamic Model Identification of a Clap-and-Fling Flapping-Wing MAV: a Comparison betweenQuasi-Steady and Black-Box Approaches. In *AIAA Atmospheric Flight Mechanics Conference*.

8. **Caetano, J. V.**, Armanini, S. F., de Visser, C. C., de Croon, G. C. H. E., and Mulder, M. (2015a). Data-Informed Quasi-Steady Aerodynamic Model of a Clap-and-Fling Flapping Wing MAV. Bali, Indonesia. *International Conference on Unmanned Intelligent Systems (ICIUS)*.

7. **Caetano, J. V.**, de Visser, C. C., de Croon, G., and Mulder, M. (2015b). Effects of eigenmodes, forward velocity and flapping frequency in force generation mechanisms of a flapping-wing MAV. Bali, Indonesia. *International Conference on Unmanned Intelligent Systems (ICIUS)*.

6. **Caetano, J. V.**, Percin, M., de Visser, C. C., van Oudheusden, B., de Croon, G., de Wagter, C., Remes, B. D. W., and Mulder,M. (2014a). Tethered vs. Free Flight Force Determination of the DelFly II FlappingWingMicro Air Vehicle. In *International Conference on Unmanned Aircraft Systems (ICUAS)*, pages 842–847. IEEE.

5. **Caetano, J. V.**, Weehuizen, M. B., de Visser, C. C., de Croon, G. C. H. E., de Wagter, C., Remes, B. D. W., and Mulder,M. (2014b). Rigid vs. Flapping: The Effects of Kinematics Formulations in Force Determination of a Free Flying Flapping Wing Micro Air Vehicle. In *International Conference on Unmanned Systems (ICUAS)*, pages 949 - 959. IEEE.

4. **Caetano, J. V.**, de Visser, C. C., Remes, B. D. W., de Wagter, C., and Mulder, M. (2013b). Controlled flight maneuvers of a Flapping Wing Micro Air Vehicle: a step towards the DelFly II Identification. In *AIAA Atmospheric Flight Mechanics Conference, number 2013-4843*.

3. **Caetano, J. V.**, de Visser, C. C., Remes, B. D. W., de Wagter, C., and Mulder, M. (2013c). Modeling a Flapping Wing MAV: Flight Path Reconstruction of the DelFly II. In *AIAA Modeling and Simulation Technologies*, number 2013-4597.

2. **Caetano, J. V.**, Verboom, J. L., de Visser, C. C., de Croon, G., Remes, B. D. W., de Wagter, C., and Mulder, M. (2013d). Near-Hover Flapping Wing MAV Aerodynamic Modelling - a linear model approach. In International Conference and Competition on Micro Air Vehicles. IMAV.

1. Durst, P. J., Gray, W., Nikitenko, A., **Caetano, J. V.**, Trentini,M., and King, R. (2014). A Framework for Predicting theMission-Specific Performance of AutonomousUnmanned Systems. In IEEE/RSJ International Conference on Intelligent Robots and Systems, pages 1962 – 1969, Chicago, USA. IEEE.